LA-4075-MS

LOS ALAMOS SCIENTIFIC LABORATORY
of the
University of California
LOS ALAMOS • NEW MEXICO

Status Report of the

LASL Controlled Thermonuclear Research Program

for 12-Month Period Ending October 31, 1968

UNITED STATES
ATOMIC ENERGY COMMISSION
CONTRACT W-7405-ENG. 36

This LA...MS report presents the status of the LASL Controlled Thermonuclear Research Program. Previous annual status reports in this series, all unclassified, are:

LA-3628-MS
LA-3831-MS

This report, like other special-purpose documents in the LA...MS series, has not been reviewed or verified for accuracy in the interest of prompt distribution.

Printed in the United States of America. Available from
Clearinghouse for Federal Scientific and Technical Information
National Bureau of Standards, U. S. Department of Commerce
Springfield, Virginia 22151
Price: Printed Copy $3.00; Microfiche $0.65

Distributed January 15, 1969

LA-4075-MS
UC-20, CONTROLLED
THERMONUCLEAR PROCESSES
TID-4500

LOS ALAMOS SCIENTIFIC LABORATORY
of the
University of California
LOS ALAMOS • NEW MEXICO

Status Report of the
LASL Controlled Thermonuclear Research Program
for 12-Month Period Ending October 31, 1968

TABLE OF CONTENTS

INTRODUCTION

(J. L. Tuck)

On November 21, 1968, shortly after the end date of the period covered by this report, construction started on the Scyllac building.

The continuous flow z-pinch is a concept proposed by A. I. Morozov in 1967. It was discovered experimentally and elucidated independently at LASL in 1968 by J. Marshall and A. A. Newton. The concept is as follows: Consider a z-pinch consisting of a continuous source of low-β plasma at some large radius, which flows slowly, hydromagnetically and adiabatically, into the axis. The resulting plasma distribution is automatically neutral to interchange and the pinch is therefore $m = 0$ neutrally stable. This work is reported together with a demonstration of greatly increased longevity (of order 50 μsec) in a z-pinch by this method. The incidence of shocks in a continuous pinch for flows of finite speed, not discussed by Morozov, is being studied by B. Suydam and R. L. Morse at Los Alamos.

This provides a new and promising addition to the possibilities for stabilizing a z-pinch discussed in this report last year.

If dynamic stabilization should turn out to be essential on the Scyllac toroidal θ-pinch, then some experiments are reported here which suggest that it will be effective and less difficult to apply than had been predicted.

FAST Z-PINCH

(J.N. DiMarco and L.C. Burkhardt)

Introduction

The fast z-pinch experiment developed from a consideration of why z-pinches have not produced temperatures of the same order of magnitude as some of the θ-pinch experiments. If, for the moment, the method of coupling into the plasma is excluded, then there should not be any fundamental difference between a z-pinch and a θ-pinch during the initial implosion phase. The z-pinch remains intact for a few μsec which should be long enough for the formation of a high-temperature plasma. Calculations[1] of the electrode effect on the z-pinch indicate that thermal conduction to the electrodes should limit the electron temperature. But, thermal conduction along magnetic field lines to the wall of the discharge tube can take place in the θ-pinch. It may be just this effect that limits the electron temperature in the θ-pinch experiments.[2] The Scylla IV θ-pinch has attained ion temperatures in the range 5 to 10 keV while the electron temperature is ~200-300 eV.[3]

In considering the differences between the θ- and z-pinches it was observed that none of the z-pinch experiments performed to date have achieved the initial electric fields that are generated, for example, in the Scylla IV θ-pinch experiment. This excludes an experiment in which high electric fields were obtained but no attempt was made to confine the plasma.[4] (The peak current was of the order of 75 kA.) The importance of the electric field can be noted in the context of the snowplow model.

The term $\dot{B}$ is used in the following equations rather than the equivalent electric field on the surface of the sheath because it is difficult to determine the electric field applied in the z-pinch experiments due to a lack of sufficient detail in the literature. In almost all cases, however, a current wave form is available from which $\dot{B}$ may be calculated.

The snowplow model predicts the initial sheath velocities for the z-pinch and θ-pinch as:

z-pinch

$$\left.\frac{dr}{dt}\right)_{t=0} = -r_0 \left(\frac{\dot{B}^2}{\mu_0 \rho r_0^2}\right)_{t=0} \frac{\int_0^t t^2/K dt}{(1-K^2)} .$$

θ-pinch

$$\left.\frac{dr}{dt}\right)_{t=0} = -r_0 \left(\frac{\dot{B}^2}{\mu_0 \rho r_0^2}\right)_{t=0} \frac{\int_0^t t^2 K dt}{(1-K^2)}$$

where ρ = plasma mass density, r_0 = radius of the discharge tube, $K = r/r_0$, and $B = \dot{B}t$; the θ-pinch is approximated by an infinite solenoid.

An approximate solution to these equations can be obtained by substitution of a power series expansion for K. The results are:

z-pinch

$$\frac{dr}{dt} = -r_0 \, [\phi t + \frac{11}{30} \phi^3 t^3]$$

θ-pinch

$$\frac{dr}{dt} = -r_0 \, [\phi t - \frac{1}{30} \phi^3 t^3],$$

where

$$\phi = \left(\frac{\dot{B}^2}{3\mu_0 \rho r_0^2}\right)^{\frac{1}{2}} .$$

For the present purposes, the second term in the expansion can be neglected. Computer calculations indicate that this approximation is accurate to ~ 10% during the first 25% of the sheath radial motion for both the z- and θ-pinches.

If shock heating of the plasma followed by adiabatic compression of the heated plasma is the mechanism that results in the high-temperature plasma observed in the θ-pinch, then the data in Table 1 show that none of the z-pinch experiments has achieved initial velocities that are comparable to the Scylla experiments, except for the experiment by Heflinger.[4] In that experiment high sheath velocities (equivalent to ~1.8 keV for H) were observed that are consistent with prediction of the model.

The θ-pinch experiments differ as far as the peak magnetic field, length of coil, preionization, and technique of measuring the ion temperature, so that the parameter $\dot{B}/\sqrt{\rho}$ cannot be expected to apply to these experiments in detail. In spite of these differences, there is what appears to be a scaling of the reported ion temperature with increasing values of the parameter. The reported temperatures are as follows: Pharos 0.9 keV; R. L. Bingham 5 keV; ISAR I 3.7 keV; Scylla IV 3-7 keV.

It is therefore required to perform an experiment that can achieve high initial sheath velocities and will be capable of supplying sufficient current so that the plasma can be contained until the formation of instabilities. The following section will present the experimental technique being developed at LASL for this extremely fast z-pinch experiment.

Magnetic Energy Storage

Introduction

Magnetic energy storage has an inherent advantage over electrostatic energy storage in that, for practical systems, the energy density of a magnetic field can be larger than that of an electrostatic field. This allows the energy to be stored in a small volume close to the load so that a system can be designed having extremely low inductance between the energy source and the load. Since the rate at which energy can be supplied to the load depends on $\dot{I}$ (where $\dot{I} = V/L$), there is a possibility of obtaining extremely fast energy transfer. Equivalent $\dot{I}$'s can be obtained with electrostatic energy storage techniques, but to achieve a source inductance comparable to that of a magnetic energy storage system requires the parallel combination of a large number of capacitors, spark gap switches, and coaxial cables, all operating at high voltage; the insulation needed then increases the parasitic inductance.

Table 1.

	$\dot{I}$ 10^{12} A/sec	r_o cm	$\dot{B}$ 10^{10} G/sec	ρ μ	$\left(\frac{\dot{B}^2}{\rho}\right)^{\frac{1}{2}}$ 10^9 G/sec-$\mu^{\frac{1}{2}}$	Ref
Z-PINCHES						
S. Berglund, et al.	0.5	14	0.3	10	.95	5
L.A. Arstimovich, et al.	0.15	10	0.3	10	.95	6
H.A. Bodin and J.A. Reynolds	~ 1.0	7.5	2.7	320	1.5	7
R.E. Dunway and J.A. Phillips	~ 0.13	3.5	0.74	100	0.74	8
H.A. Bodin, et al.	0.45	7.5	1.2	30	2.2	9
V.S. Komel'Kov	1.4	9.5	2.9	100	2.9	10
D.C. Hagerman and J.W. Mather	~ 0.7	5	~ 2.8	70	3.3	11
L.O. Heflinger and S.L. Leonard	8.0	0.635	260	2×10^{16} ions/cm^3	140	4
θ-PINCHES						
Pharos		5.25	1.15	30	2.1	12
Cariddi		9.0	1.0	25	2.0	13
R.J. Belitz, et al.		5.25	2	25	4	14
R.L. Bingham, et al.			1.4	10	4.4	15
H.A.B. Bodin, et al.		5.0	2.0	10	6.3	16
Scylla I		2.7	6.6	85	7.15	17
Scylla III		4.1	5.0	85	5.32	18
Scylla IV		5	4.0	10	13	3
Isar I		5.3	2.8	5	12.5	19
Our Proposed Experiment	~ 5	5	~ 20	~ 10	~ 63	

The utilization of the magnetic energy storage technique requires the development of a switch that will pass a current of the order of 10^6 A and then will open in a fraction of a microsecond. In addition, the switch must be able to withstand voltages ≥ 50 kV. Various techniques for opening inductive circuits have been reported in the literature.[20-23] The essence of this switching technique is the use of a metallic fuse which is caused to vaporize. The change from the solid to vapor state results in a change in resistance; if this change is large enough to reduce the current substantially, then the fuse can be considered to be a switch. For the switch to remain open, the metallic vapor must be prevented from becoming ionized.

The fuse is inserted in series with a capacitive discharge circuit and the fuse opening is timed to occur at peak current; the resulting $\dot{I}$ will cause large voltages to be developed across the inductive components of the circuit. If a load, having a series spark gap switch set to conduct

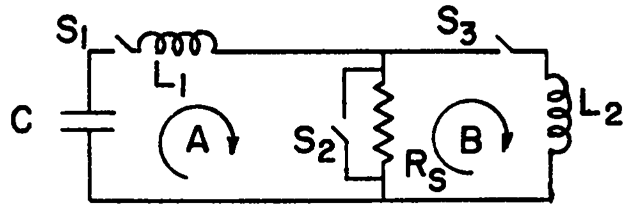

Fig. 1. Simplified schematic of magnetic energy storage system.

when the fuse voltage reaches some predetermined value, is placed across the fuse, then the initial $\dot{I}$ in the load circuit will be determined by the fuse voltage and load inductance. Since a load inductance of the order of 5-10 nH is feasible, and voltages of ~ 50 kV can be developed across the fuse, an $\dot{I}$ of the order of 0.5-1.0 x 10^{13} A/sec can be obtained.

The switching technique developed by Early and Martin[21] has been used and this report presents some of the results of experiments for maximizing the voltage developed across the fuse and determining the opening current as a function of the fuse dimensions. A comparison with theoretical predictions is also presented.

Basic Circuit Theory

The circuit of the magnetic energy storage system is shown in Fig. 1. The time dependence of the switch resistance has been replaced by a step function. Initially switches S_1 and S_3 are open and S_2 is closed. The capacitor bank is charged to the desired voltage and switch S_1 is closed. Current starts to flow in circuit A, with amplitude and period determined as usual for an LC circuit. When the current in circuit A reaches its peak value, switch S_2 is opened and then switch S_3 is closed. The voltage developed across the switch resistance now causes a current to flow in circuit B. The current in the two circuits can be expressed in the following way.

I. Before S_2 is opened.

$$I_A = I_{A_0} \sin \frac{2\pi}{\sqrt{L_1 C}} \; t \; .$$

II. S_2 is opened and S_3 closed at peak current. The current transfer can be expressed by

$$I_B = \left(\frac{L_1}{L_1 + L_2}\right) I_{A_0} \left(1 - e^{-\frac{R_s}{L_3}(t-t_c)}\right) ,$$

where

$$L_2 = \frac{L_1 \; L_2}{L_1 + L_2} \quad ,$$

and t_c = time at which S_2 is opened and S_3 closed. Upon taking the time derivative, the following expression for $\dot{I}$ is obtained:

$$\dot{I}_B = I_{A_0} \frac{L_1}{L_1 + L_2} \left[\frac{R_s}{L_3} \exp\left(- \frac{R_s(t-t_c)}{L_3}\right)\right] .$$

Since the switch voltage at time $t = t_c^+$ is $I_{A0}R_s$, this result can be written as

$$\dot{I}_B = \left(\frac{V_s}{L_2}\right)_{t \,=\, t_c} \left(\exp - \frac{R_s(t-t_c)}{L_3}\right) \quad .$$

A rapid transfer of current into the load requires a large fuse voltage and small load inductance and, in addition, the fuse resistance must be of a suitable order of magnitude to match the time scale of the experiment. For example, if L_2 = 10 nH and L_1 = 40 nH, then L_3 = 8 nH. For one e-folding time of 50 nsec the fuse resistance must be 0.16 Ω.

Theory of Switch Operation

Details of the physical principles of the fuse operation are given by Maisonnier, et. al.[22] To compare the LASL results with those of Maisonnier requires the definitions

$$a = \frac{\sqrt{2}}{\pi} \gamma \int_{e_0}^{e_1} \frac{1}{\rho} \, de, \tag{1}$$

and

$$b = \frac{1}{\gamma e_v} .$$

The fuse is considered to be on the verge of opening when enough energy has been supplied to heat the fuse to the temperature at which vaporization will take place. The energy input to the fuse can be related to its resistance, cross section, and the current in the circuit by

$$S^2 = \frac{\int_0^t I^2 \, dt}{\frac{\pi}{\sqrt{2}} k_1 a} \qquad (2)$$

where S = cross section of fuse, I_0 = capacitor discharge current, γ = mass density of fuse, ρ = resistivity of fuse, e = internal energy per unit mass of the fuse, and k_1 is explained below.

The integration over the internal energy is carried to the point of vaporization of the fuse and does not include the heat of vaporization. The correction factor k_1 is included to account for the difference between the handbook values of the physical properties of the fuse and those obtained during the extremely fast heating that takes place in these experiments. The equation is also known as the action integral equation.[24]

The parameters of a and b for four metals are quoted in Table 2; the data for copper have been added to those given by Maisonnier.[22]

Table 2.

Metal	a	b
Ag	3.9×10^{16}	4×10^{-11}
Au	3×10^{16}	3.5×10^{-11}
Al	2.2×10^{16}	3.5×10^{-11}
Cu	5.9×10^{16}	2.1×10^{-11}

Experimental Apparatus

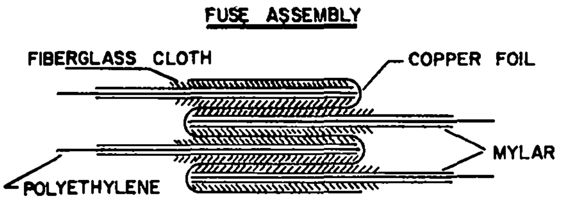

Fig. 2. Schematic of fuse.

The fuse is shown schematically in Fig. 2. The design follows the pattern outlined by Early and Martin[21] with the addition of polyethylene sheets which were required to maintain the integrity of the package during the discharge. The fuse package is inserted between a parallel plate transmission line and then the entire assembly is clamped in a hydraulic press. The number of "folds" refers to the number of active folds of the foil; for example, Fig. 2 shows a 3-fold fuse. The portion of foil located at the top and bottom of the package, being in contact with the parallel plate transmission line, does not vaporize.

Since the voltage characteristics of the fuse are investigated, the current is not transferred into a load. This means that all of the energy stored magnetically will be dissipated in the fuse, requiring the mechanical containment of ~ 10 g TNT energy equivalent.

The capacitor bank consists of 20, 15-μF 20-kV capacitors, the maximum stored energy being 60 kJ. Each capacitor is switched with an ignitron which then couples into a parallel-plate transmission line through a total of 60, 3-m long RG-8 cables. The parallel-plate transmission line consists of a header, to receive the coax cables, which then tapers down to rectangular plates 20-cm wide and 17-cm long with the fuse package located at one end. The rectangular plates are separated by 2 cm so that most (~ $\frac{2}{3}$) of the 40 nH inductance of the circuit is in this region. This partially isolates the large voltage that develops across the fuse from the capacitor bank and coaxial cables.

The resistive voltage probe is located 12 cm from the fuse package and it consists of 10, 1-kΩ 2-W carbon resistors connected to a 50-Ω coaxial cable. The resistors are placed in a plexiglass tube which is filled with transformer oil. Capacitive compensation is accomplished by an Al hat connected to the top of the probe which extends partially down around the outside of the plexiglass tube. The probe is found to have a rise time of ~ 10 nsec with ~ 10% overshoot. Amplitude calibration of the probe is accomplished with a Marx bank pulse-charge system having a period of 9 μsec; it has been found to be linear to 90 kV.

The voltage across the fuse is obtained from that measured at the probe position corrected for the inductive voltage drop between the probe and fuse. The following techniques are used to determine the inductance between the probe position and the fuse: A plate of copper is substituted for the fuse and the voltage at the probe position is compared to the voltage on the capacitor bank. With the total inductance of the system known, the inductance between the probe and fuse location is then calculated. A second determination is made by measuring the probe voltage and $\dot{I}$ with the copper plate in place. There is 10% agreement between these techniques and the value of inductance calculated from the geometry of the system. Since the inductive voltage between the probe and fuse amounts to at most 25% of the fuse voltage, a 10% error in determining the inductive voltage accounts for less than 2.5% error in the fuse voltage.

The current and $\dot{I}$ are measured with a Rogowski probe placed around one transmission line and constructed so that the measured rise time of the probe is < 10 nsec.[25] Integration is performed with a passive integrator that is down 3 dB from ideal response at 30 MHz.

Experimental Results

Since the purpose of the first phase of these experiments is to obtain the conditions under which the voltage across the fuse is a maximum, the current is prevented from transferring into a load. This condition pertains to all of the data discussed below.

It is convenient to consider the fuse characteristics by dividing the time history into two steps. The first step requires an energy input sufficient to bring the fuse to a state at which vaporization just starts. At this point the fuse is considered to be on the verge of opening. The second step requires the addition of energy to the fuse to cause vaporization to occur. The fuse is then considered to be in the process of opening.

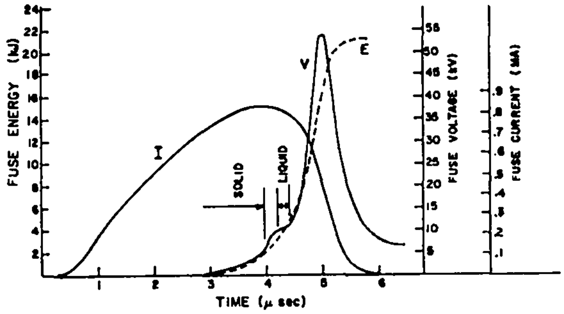

Fig. 3. Characteristics of fuse as function of time.

This history can be illustrated by reference to Fig. 3 which presents the current, voltage across the copper fuse (0.8-mil thick, 15-cm long, 15.3-cm wide), and the energy input to the fuse obtained by mechanically integrating the product of the fuse voltage and current. In addition, the time dependence of the physical state of the fuse is obtained by comparison of the internal energy required, from handbook values, with the experimentally determined energy input.

The history referred to above can now be demonstrated by comparison of the physical state of the fuse with the voltage. The solid-to-liquid transition results in a relative change in resistance of 2.1 according to the handbook. The corresponding jump in the voltage is in good agreement with the phase change and the relative resistance change is calculated from the data to be ~ 1.8. The end of the first step is postulated to occur at the time when enough energy has been deposited into the fuse to heat it to the point where vaporization should start, with a corresponding rapid increase in the resistance. A comparison with the voltage trace shows it is at just this time that there is a rapid increase in the voltage across the fuse.

With this definition of opening time, Eq. 2 can be solved by mechanical integration of the measured current and the solution can be compared with the observed opening time. Figure 4 presents the results of this comparison; the triangles are obtained by mechanically integrating the current and assuming $k_1 = 1$, whereas the boxes and solid circles are the experimentally observed

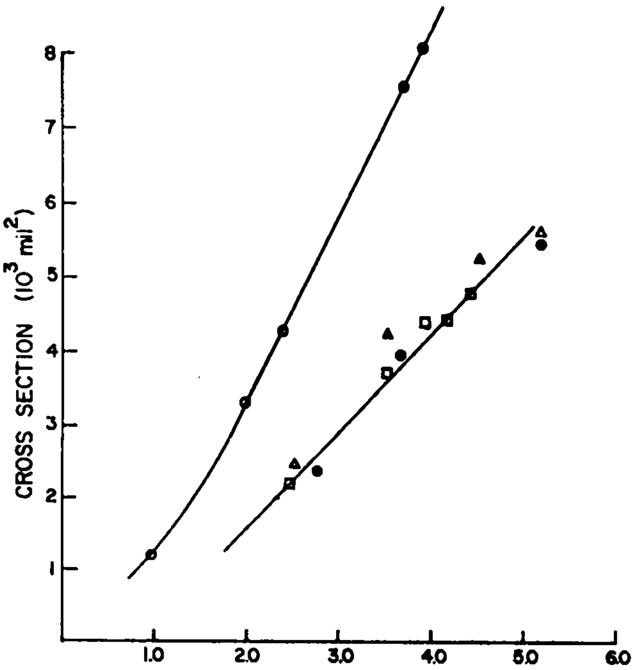

Fig. 4. Fuse cross section vs opening time.

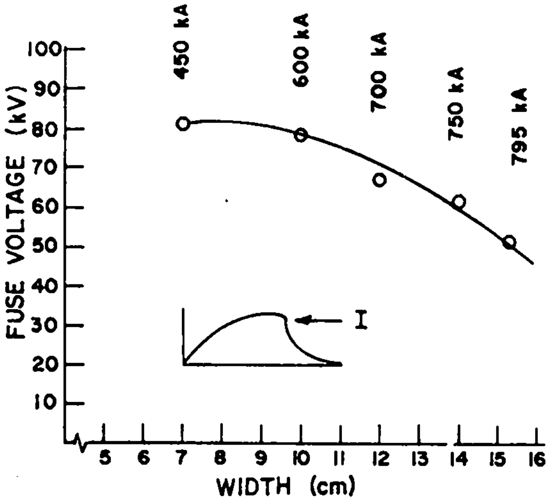

Fig. 5. Fuse voltage vs fuse width.

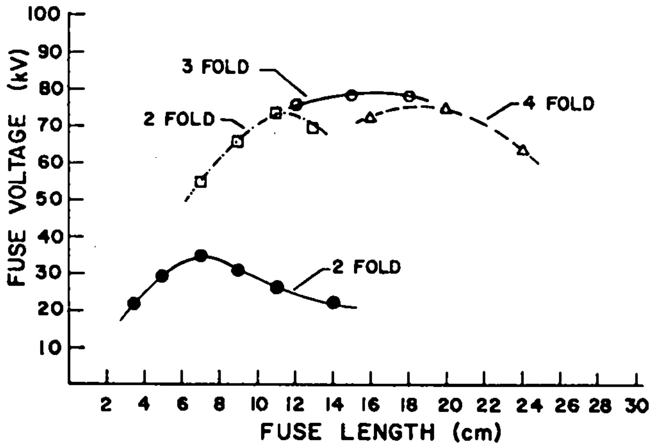

Fig. 6. Fuse voltage vs fuse length.

opening times. The boxes present the data for a 0.8-mil thick foil and the solid circles for a 2.0-mil foil; both were 15-cm long. The open circles represent the results of using Eq. 2 to calculate the cross section of the foil.[22] If a correction factor of $k_1 \approx 2$ is applied to this calculation it would predict the actual experimental data. This correction factor is not due to a discrepancy between the handbook values of the physical properties of the material and those obtained under conditions of rapid heating as previously reported;[22] rather, it results from the properties of the circuit. The experiment shows that, at the current densities used, a correction factor is not required. The need for a correction factor does arise, however, when the current density in the fuse exceeds $\sim 3 \times 10^7$ A/cm^2 as observed in other experiments.[26,27]

The second stage, during which the maximum voltage occurs, will now be considered. The fuse voltage as a function of the fuse width is shown in Fig. 5; The fuse was of copper 0.8-mil thick and 15-cm long. The capacitor bank was charged to 14 kV. The current values indicated are those just before the fuse "opens". It is seen that the maximum voltage does not occur at the time of maximum current but rather at times less than the quarter period of the circuit oscillation. Figure 6 presents the fuse voltage as a function of fuse length. The results are grouped by the value of the capacitor bank voltage: the lower curve is obtained with 7.5 kV and a 5-cm wide copper foil, and the upper curve with 14 kV and a 10-cm wide copper foil. In both cases the copper is 0.8-mil thick. The folds referred to in the figure indicate the number of active layers of fuse material (cf. Fig. 2 for a 3-fold package). Those points plotted with a square box indicate that a restrike takes place; that is, the current is reduced to a low but still detectable value (~ 50 kA).

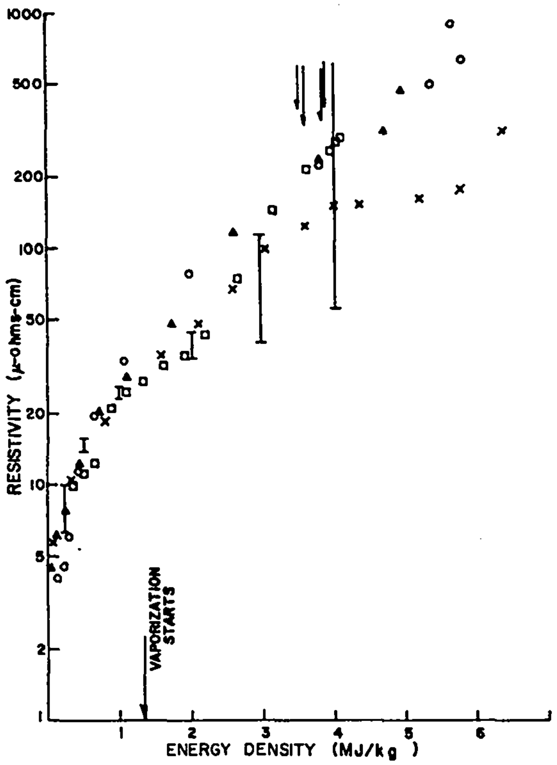

Fig. 7. Fuse resistivity vs fuse length for different cross sections.

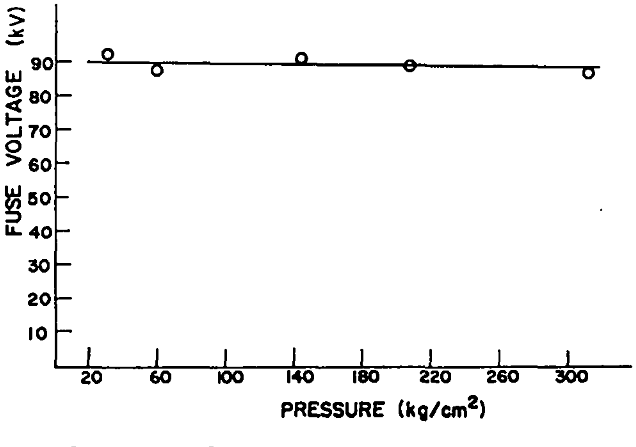

Fig. 8. Fuse voltage vs pressure.

Figure 7 is a plot of the copper fuse resistivity as a function of the energy per unit mass deposited in the fuse for different fuse widths and thicknesses; the capacitor voltage was 14 kV. The results compare favorably with the exploding wire work up to about 3.5 MJ/kg. Again the highest current density (4.04×10^7 A/cm^2 represented by x in the figure) shows the same type of deviation experienced with exploding wires in that an excess energy is delivered to the fuse when compared to the energy required to account for the observed resistivity. The occurrence of peak voltage is indicated by the vertical arrows. For all the cases analyzed this arises when the energy density in the fuse reaches a value of 3.7 MJ/kg. The spread of ± 5% is less than the experimental error, estimated to be 20%. Also, the resistance is approximately the same at the time of peak voltage for the three copper foils of 0.8-mil thickness.

In all cases discussed above the fuse package is subjected to a force of 21,800 kg applied with a hydraulic press. The pressure on a 3-fold package of 15-cm length and 14-cm width is 320 kg/cm^2. Figure 8 shows that no effect on the fuse voltage is observed by varying the pressure from 26.8 to 310 kg/cm^2. The copper fuse was 0.8-mil thick, 15-cm long, and 14-cm wide; the capacitor voltage was 17.5 kV.

A test to determine the effect of the presence of the fiberglass is performed by assembling a 3-fold fuse package without the fiberglass. The fuse voltage is reduced by a factor of $\frac{1}{2}$ to $\frac{2}{3}$, and the fuse package is destroyed. The overpressure is sufficient to result in an approximate doubling of the gauge pressure of the hydraulic press, an effect not encountered when using fiberglass.

Discussion

The effect of folding the fuse material as well as the role played by fiberglass cloth and pressure applied to the fuse package can be ascertained by using Eq. 1 to compare the results with those of Maisonnier et al.,[22] who used a thin foil without folds, and also with the results of work on exploding wires, since this equation predicts the behavior of the latter up to the time of opening.[5] In Fig. 4, the predicted values of the opening time are obtained from Eq. 1, using handbook values of the physical properties and mechanically integrating the experimentally observed current (with the correction factor in Eq. 2 taken equal to 1.0). The figure also shows the result obtained from Eq. 2 by considering the circuit to be ideal and integrating the undamped sinusoidal current. In this case to fit the experimental data $k_1 \approx 2$. The agreement between the experimental data and the prediction of Eq. 2 is considered to be very good, since the technique of obtaining the integral in Eq. 2 by squaring the measured current followed by mechanical integration has an estimated accuracy of 20%. Therefore, circuit damping cannot be neglected when evaluating Eq. 2, and this equation does predict the observed opening time when using the handbook values for the physical constants.

In considering the fuse voltages shown in Fig. 3, it is to be noted that if the length of the fuse is sufficient to prevent restrike, making the fuse wider reduces the voltage developed across the fuse, even though the fuse current and the amount of energy stored inductively increases.

To explain the voltage dependence upon length, given in Fig. 6, it is seen that for fuse length shorter than 15 cm the voltage increases with length, and also restrikes (denoted by boxes) are observed. This suggests that the maximum electric field the fuse vapor can withstand without restriking is ~ 6 kV/cm. To the right of the peak voltage the longer fuse requires more energy for vaporization to take place, resulting in increased dissipation of the inductively stored energy. For example, as shown in Fig. 3 a copper fuse 15.3-cm wide, 0.8-mil thick, and 15-cm long requires 5330 J to raise its temperature to the point at which vaporization commences, and an additional 10,700 J is required by the time of peak voltage. The 5330 J is supplied from the capacitor bank during the long current rise of 3-5 µsec, whereas the 10,700 J is transferred rapidly so most of it must be stored inductively. Since the energy stored inductively for this example is found experimentally to be 12,200 J, almost all of the inductive energy is dissipated in the fuse. Of the inductive energy remaining at the time of peak voltage (4080 J), 2580 J is supplied by the capacitor bank.

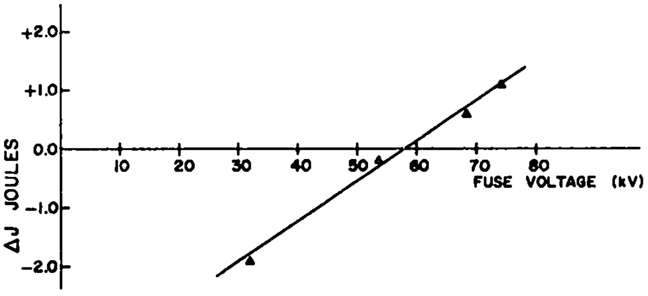

Fig. 9. Dependence of fuse voltage on inductively stored energy.

Mechanical integration of the current trace to obtain the change in voltage on the capacitor bank during the time from the beginning of vaporization to the maximum voltage shows that the capacitor bank has supplied 2400 J during this period, in agreement with the energy balance obtained above. This dependence of voltage upon the inductively stored energy is shown in Fig. 9 where the difference between the maximum energy stored inductively and the energy required at peak fuse voltage is plotted against the peak fuse voltage for four different fuse cross sections. More inductively stored energy is required to produce the higher voltages.

To attempt to maximize the efficiency of the circuit, so that peak voltage will occur when the minimum amount of energy has been dissipated in the fuse, requires an analytic expression for the dependence of the fuse resistance on the circuit parameters. One model[28] that attempts to predict the resistance differs from the experimentally determined value by a factor of 4 at the time of peak voltage.

In a second phase of the experiment, current is transferred into a load of constant inductance by means of a switch that consists of a number of layers of 2-mil thick polyethylene. The load inductance is calculated to be 40 nH and the resulting current transfer is consistent with the equations developed from circuit theory. When transfer takes place at the time of peak fuse voltage, the maximum energy transferred into the load is ~ 8% of the maximum energy stored inductively in the primary circuit. These efficiencies are much lower than the theoretically predicted efficiency of 50% when $L_1 = L_2$, because of the requirement of waiting until the peak voltage is developed across the fuse. If the transfer into the load is accomplished before peak voltage, less energy is dissipated in the fuse and the transfer improves. The current transfer is similar to that observed by others[21,22] with the initial $\dot{I}$ being of the order of 2×10^{12} A/sec. Unfortunately, there is considerable variation in the breakdown voltage obtained with the dielectric switch. Rather than try other techniques of initiating breakdown in a dielectric switch, it has been decided to use an illuminated spark gap switch. Tests with such a switch indicate very reproducible breakdown voltage (~1%). Use of this switch will add inductance and thereby reduce $\dot{I}$. It is felt that this sacrifice in $\dot{I}$ is worth the advantage gained in having a reproducible voltage.

It is planned to use this technique of magnetic energy storage to develop strong shocks in a plasma using the z-pinch geometry.

Conclusion

By using the technique of exploding fuses to interrupt a current and thereby transfer the inductive energy into a load, it is possible to achieve a rapid transfer of energy. Voltages as high as 90 kV are measured, which when working into loads of the order of 10 nH inductance, would result in $\dot{I}$ of the order of 10^{13} A/sec. Up to the time at which vaporization of the fuse takes place the properties of the fuse can be predicted with the model and follows closely the work done with exploding wires at the same current densities. Therefore, folding the foil and compressing it between fiberglass does not noticeably affect the behavior of the fuse when compared with exploding wires. For short lengths of fuse the voltage is determined by the maximum electric field that the fuse can withstand (~ 6 kV/cm). For long lengths of fuse, the maximum voltage that can be produced across the fuse decreases as the length is increased; such behavior is associated with the amount of energy required to vaporize the fuse.

If current transfer is to take place at the time of peak voltage, the efficiency at which energy is transferred to the load compared to the magnetic energy stored at the time of peak current is low, being on the order of 8%. In spite of such low efficiency this system affords the definite advantage of achieving very rapid transfer of energy.

References

1. M. G. Haines, Proc. Phys. Soc. (G.B.) pt. 3 77, 643 (1961).
2. T. S. Green, et al., Phys. Fluids, 10, 1663 (1967).
3. W. E. Quinn, et al., Plasma Phys. and Cont. Nuc. Fusion Res. (IAEA Vienna, 1966) Vol. 1, p. 237.
4. L. O. Heflinger and S. L. Leonard, Phys. Fluids, 4, 406 (1960).
5. S. Berglund, et al., Nucl. Inst. 1, 233 (1957).
6. L. A. Artsimovich, et al., J. Nucl. Energy II, 4, 213 (1957).
7. H. A. B. Bodin, et al., Nucl. Fus., 1, 54 (1960).
8. R. E. Dunaway and J. A. Phillips, J. Appl. Phys. 29, 1137 (1958).
9. H. A. B. Bodin and J. A. Reynolds, Engineering, p. 538, Oct. 25, 1957.
10. V. S. Komel'kov, Sov. Phys., JETP, 35, 10 (1959).
11. D.C. Hagerman and J. W. Mather, Nature, 181, 226 (1958).
12. A. C. Kolb, et al., Plasma Phys. and Cont. Nucl. Fus. Res. (IAEA Vienna, 1966) Vol. 1, p. 261.
13. U. Ascoli-Bartoli, ibid., Vol. 1, p. 275.
14. R. J. Belitz, et al., ibid., Vol. 1, p. 287.
15. R. L. Bingham, et al., Vol. 1, p. 301.
16. H. A. B. Bodin, et al., ibid., Vol. 1, p. 193.
17. K. Boyer, et al., Phys. Rev., 119, 831 (1960).
18. E. M. Little, et al., Nucl. Fus. Suppl. 2, 497 (1962).
19. C. Andelfinger, et al., Plasma Phys. and Cont. Nuc. Fus. Res. (IAEA Vienna, 1966), Vol. 1, p. 249.
20. G. S. Janes and H. Koritz, Rev. Sci. Instr., 30, 1032 (1959).
21. H. C. Early and F. J. Martin, ibid., 36, 1000 (1965).
22. Ch. Maisonnier, J. G. Linhart, and C. Gouilan, ibid., 37, 1388 (1966).

23. D. B. Thomson, et al., Proc. of the APS Topical Conf. on Pulsed High-Density Plasmas, LA-3770, 1967, Paper H-3.

24. G. W. Anderson and F. W. Nielson, Vol. I Exploding Wires, W. G. Chace and H. K. Moore (eds.) Plenum Press, New York (1959).

25. J. Cooper, Plasma Phys. (J. Nucl. Energy Part C), 5, 285 (1963).

26. F. H. Webb, Jr., et al., Vol. II, Exploding Wires, W. G. Chace and H. K. Moore (eds.) Plenum Press, New York (1962).

27. R. J. Reithel and J. H. Blackburn, Vol. II, Exploding Wires, W. G. Chace and H. K. Moore, (eds.) Plenum Press, New York (1962).

28. T. J. Tucker, J. Appl. Phys. 32, 1894 (1961).

COLUMBA

(J.A. Phillips, P.R. Forman, A.Haberstich, H.J. Karr, A.E. Schofield)

Simple Z-Pinches

Deuterium and argon discharges in the Columba experiment have been examined with an axial Mach-Zehnder interferometer. As interferograms give only the line density averaged down the line of sight parallel to the axis, small scale fluctuations are not seen. Side-on image converter photographs of the discharge were therefore taken simultaneously. These photographs were obtained through the pyrex discharge tube at a right angle to the z axis. The results are shown in Fig. 10 and 11.

With deuterium (Fig. 10) the z-pinch breaks up into a series of blobs with a characteristic wavelength of ~ 2 cm; there is a pronounced necking down (~ 1 mm radius) of the discharge between the blobs. If all the discharge current (~ 60 kA) passes through these filaments the current density is high ~ 2 mA/cm^2. Argon (Fig. 11) shows the same general pattern but the discharge does not neck down as tightly.

It is clear from the side-on photographs that the pinch is far from equilibrium during late times and a comparison of the experimental radial density profiles with theory (e.g., a Bennett distribution) should not be attempted.

Superposition of Z-Pinch on θ-Pinch Plasma

The Columba experiment was constructed to see if the plasma created by a θ-pinch could be further compressed and heated by the addition of a strong z-current. The initial fear that the z-current would not flow on the plasma but rather on the discharge tube wall has been allayed. Image converter pictures taken with a quartz discharge tube show no evidence for $m = 0$ instabilities for the combined θ- and z-pinched plasma; $m = 1$ instabilities are present, however, and their growth rates have been measured. Modifications

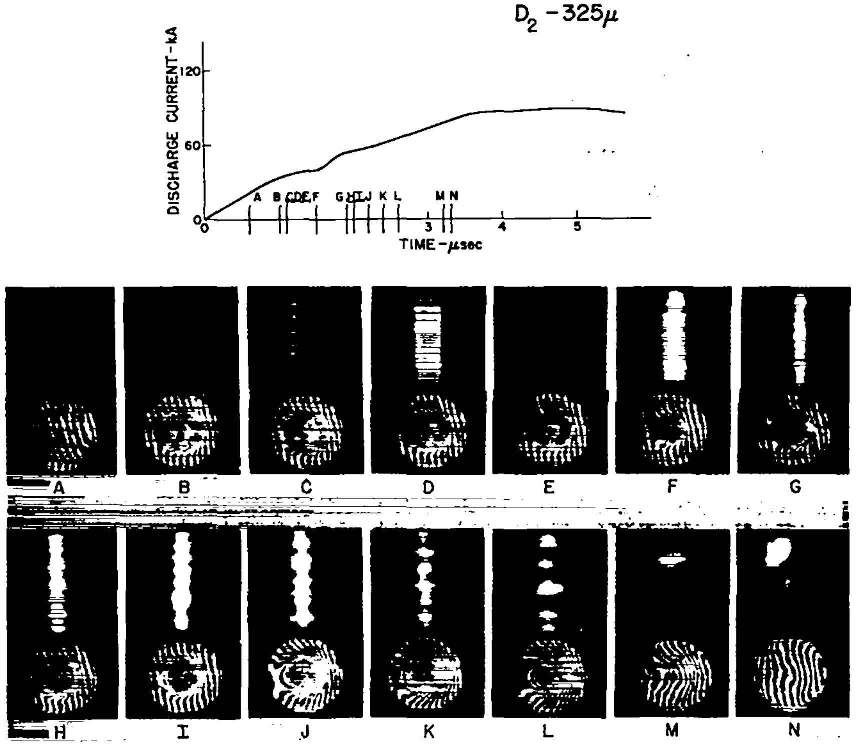

Fig. 10. Side-on image converter photographs and axial Mach-Zehnder interferograms for a deuterium pinch.

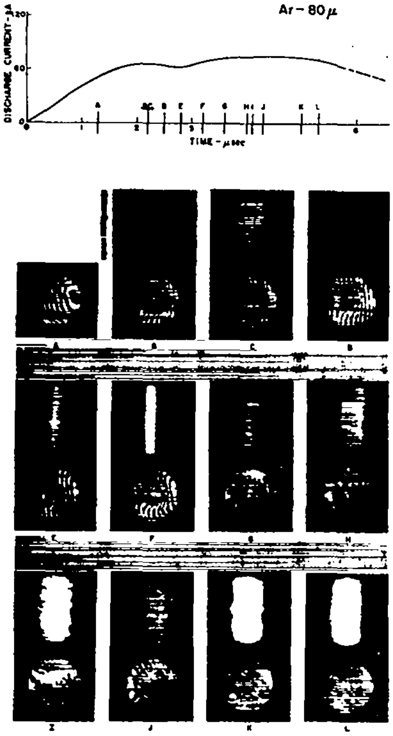

Fig. 11. Side-on image converter photographs and and axial Mach-Zehnder interferograms for an argon pinch.

of the machine are in progress to see if these instabilities can be suppressed by dynamic stabilization.

The Columba experiment has been adequately described previously.[1] It is a 28-cm long θ-pinch upon which it is possible to apply an axial current of up to 500 kA. Because of difficulties in ionizing and breaking down the gas the experiment was initially operated on the second half-cycle of the θ-pinch.

Figure 12 shows streak photographs taken down the axis of the discharge tube across a diameter with the system operated on the second half-cycle of the θ-pinch. The initial deuterium gas pressure was 0.1 torr. The θ-pinch field passes through zero at the end of the first half-cycle at t = 0. The initial implosion of the discharge and the subsequent radial oscillations of the plasma are quite apparent. From a study of the period of these oscillations and a knowledge of the strength of the magnetic field, B, the line mass, M (mass for unit length), can be found from the relation[2]

$$\tau = 2\pi (M/B^2)^{\frac{1}{2}} \delta ,$$

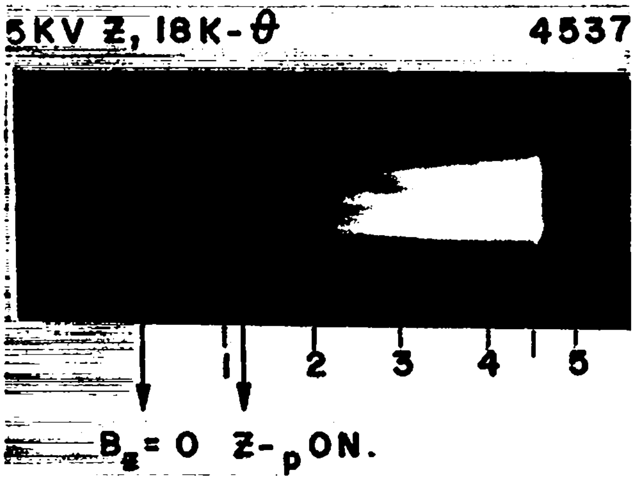

Fig. 12. Axial streak photograph of θ-pinch discharge.

where δ depends on the compression of the plasma column and on the radial distribution.

The results show: (1) At early times, ~ 0.8 μsec after t = 0, most of the gas is swept up by the θ-pinch. (2) At later times the line mass increases over the initial line mass filling, showing that the θ-pinch has trapped a reversed magnetic field and that the plasma column compresses axially.

The existence of trapped reversed fields inside the plasma column has been confirmed by means of a Mach-Zehnder interferometer. Figure 13 shows a number of interferograms taken down the axis of the tube at various times in the discharge. Each picture represents a separate discharge. In this series of shots the z-pinch was fired 1.2 μsec after the first zero of the θ-pinch. Δt_ℓ, on the figure, indicates the time at which the laser recording the interference pattern was fired. For each time there are two cases shown: (1) θ-pinch only (2) θ- plus z-pinch. Below each interferogram is a plot of the average density profile. As can be seen the plasma column is hollow.

The most remarkable characteristic of the second half-cycle operation is demonstrated in Fig. 13. At 2.4 μsec there is ample plasma on the axis yet 0.3 μsec later the plasma is essentially gone. Diamagnetic loops were placed just outside the ends of the θ-pinch coil to see if the plasma was being lost axially. This indeed seems to be the case. At the time of plasma loss, strong signals appear on these coils as if plasma were excluding flux from the loops. On a few occasions, the sense of the signal was reversed as if the plasma was carrying flux with it.

X-rays emitted by the discharge were examined using a double absorber geometry for the time-resolved measurement of the plasma electron temperature.[3] The detector had two channels with Be foil absorbers; one had a thickness of 10.7 mg/cm^2 (thin foil) and the other of 24.7 mg/cm^2 (thick foil). In Fig. 14 the effect is indicated of a z-current on the x rays seen by the detector with the thin Be foil. Zero time is the start of the second half-cycle of the θ-pinch current and the initiation of the z-current is indicated by an arrow. With a late start of the z-current (Trace No. 4682), the x-ray signal starts at 1.1 μsec and then falls smoothly, as also observed with θ-pinch alone. As the z-pinch is fired earlier, this peak in the x-ray signal is quenched at ~ 2.0 μsec in No. 4673, at ~ 1.5 μsec in No. 4680, and is absent in No. 4703. It is not clear why the onset of the z-pinch current quenches the x rays. In Fig. 15 the ratio of the two x-ray signals is expressed as an electron temperature. In all three cases, at ~ 3.0 μsec there is a peak in the electron temperature at about the time for the loss of plasma.

To eliminate the possibility of a trapped reversed field as an energy source for the rapid loss of plasma associated with second half-cycle operation, the Columba device has been modified to achieve the first half-cycle operation. An initial preionization z-current of about 10 kA lasting ~ 10 μsec has been added. A B_z field bias bank, which provides an essentially constant axial magnetic field of 6 kG of either polarity, has also been installed. With these modifications, the first half-cycle of the θ-pinch produces a dense, pinched plasma. With reverse bias field, the pinch is not hollow apparently due to annihilation of the bias field during the formative stages of the pinch. The catastrophic loss of plasma with the z-pinch at 2.4-2.6 μsec previously found with second half-cycle operation does not occur. As late as 3.5 μsec, as much plasma remains in the central region as with the θ-pinch alone.

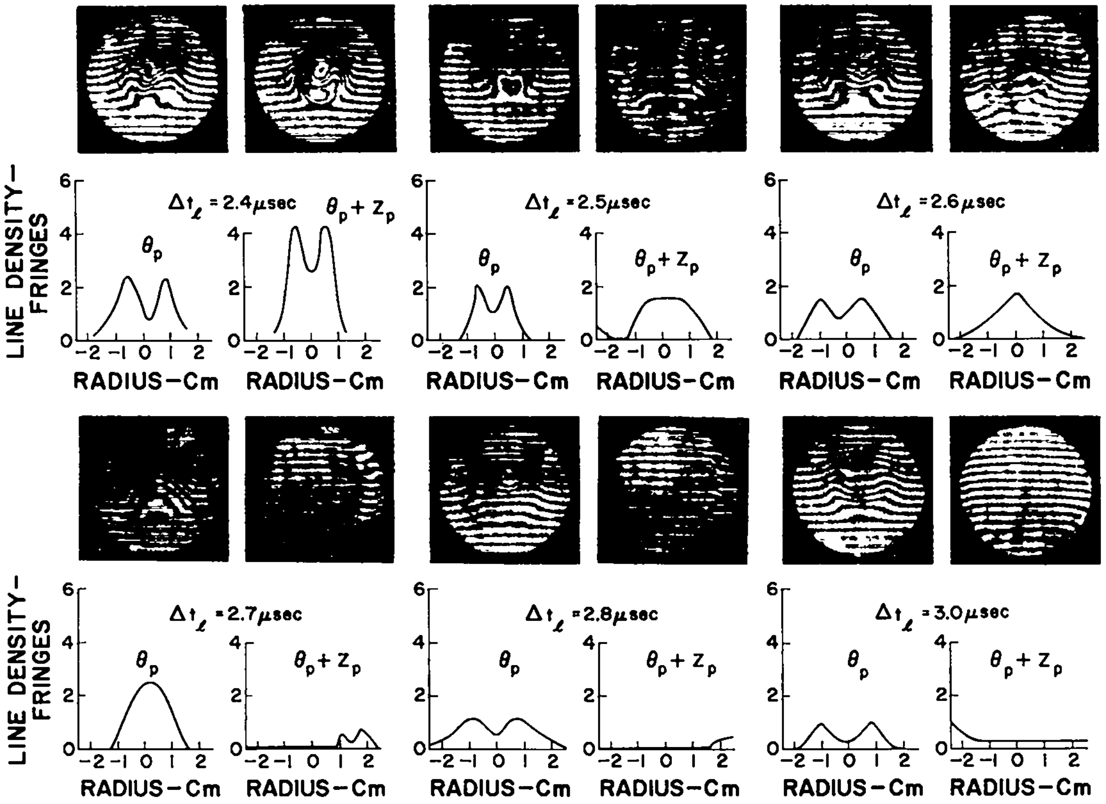

Fig. 13. Axial Mach-Zender interferograms of second half-cycle plasma.

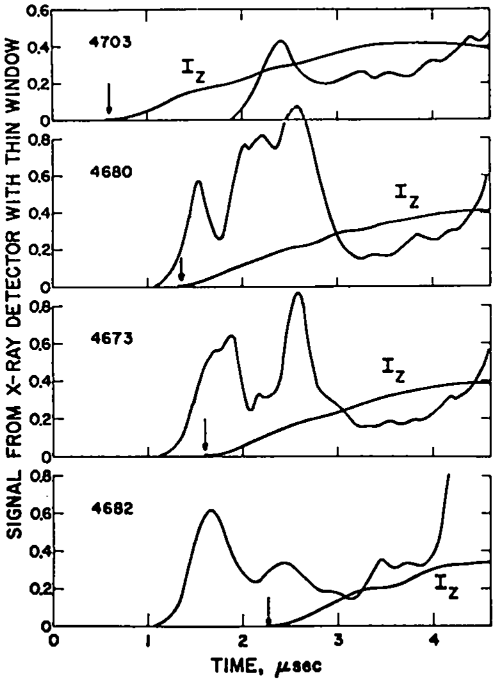

Fig. 14. Signal from thin-window x-ray detector.

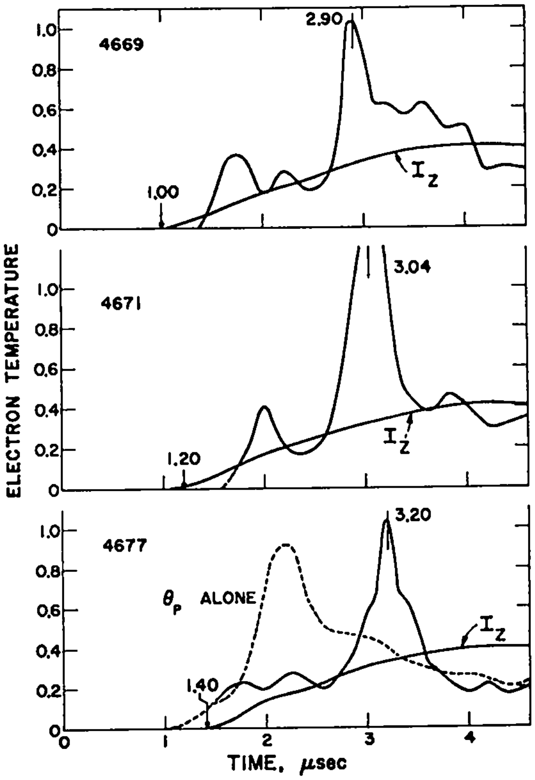

Fig. 15. Electron temperature vs time.

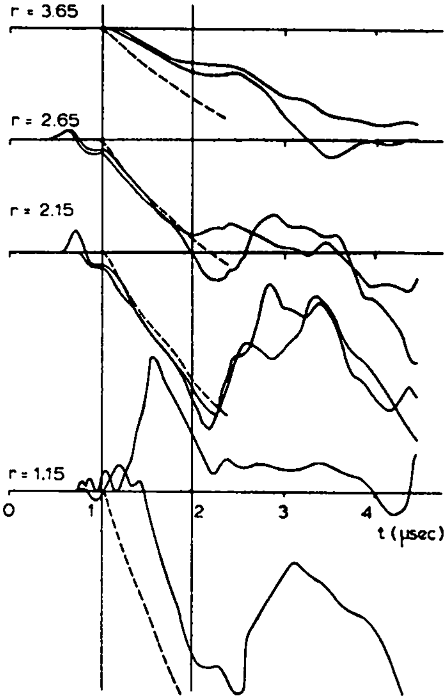

Fig. 16. Probe traces showing radial dependence of azimuthal field.

An attempt was made to determine to what extent the z-current was flowing on the plasma column created by the θ-pinch. A small radially movable probe was built to measure the radial dependence of the azimuthal magnetic field inside the discharge tube. The probe was located during these measurements 7 mm beyond the end of the θ-coil. In Fig. 16 are shown probe traces recorded at four different distances from the tube axis. The trace marked r = 3.65 corresponds to a position 0.5 cm outside the discharge tube; the other traces are for positions inside the discharge. The reproducibility of the traces up to 2 μsec is taken as evidence that the discharge is centered, in agreement with other measurements. Use was made of the total I_z recorded to predict the strength of the azimuthal magnetic field at the radius of the probe, assuming a 1/r dependence. These fields are represented by dashed curves in Fig. 16. The discrepancy occurring at r = 3.65 can be partially justified by the discrete structure of the return bars. The agreement between the 1/r dependence and the probe traces at r = 2.65 and 2.15 is quite satisfactory, indicating that I_z current detaches from the wall of the discharge tube very early, if not at all times, during the first part of the z-pinch and flows along the plasma created by the θ-pinch.

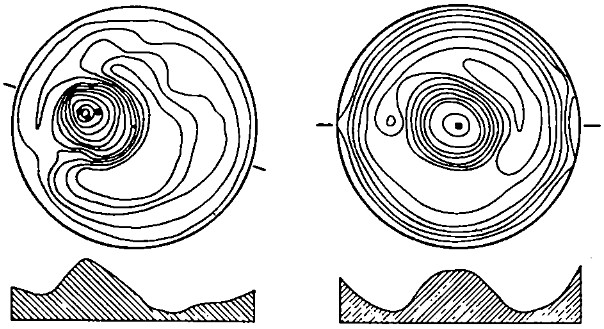

Fig. 17. Comparison of Mach-Zender interferograms with observed position of the I_z current.

To determine the m = 1 stability of the pinch a technique was developed to determine the center of gravity of the z-current at three different positions along the axis of the discharge. The details and results of this measurement are given in the next section. Figure 17 indicates the excellent agreement that was obtained between the center of gravity of the z-current as measured by these coils (represented by the squares on the figure) and the position of the plasma column as determined by the Mach-Zehnder interferometer (shown are contours of constant density). The plasma at large radii that appears on the Mach-Zehnder interferograms has been shown, in a separate experiment, to be due to electrode effects and is not related to the plasma column. On the right is seen a case, early in time, where the plasma column is still centered. On the left, later in time, the column has moved off axis. This is taken as further evidence that the z-current is flowing on the plasma column.

References

1. CTR Status Report for period ending Oct. 31, 1967, LA-3831-MS.
2. T.S. Green, Phys. Fluids 6, 864 (1963).
3. F.C. Jahoda, et al., Phys. Rev. 119, 843 (1960).

RADIAL STABILITY OF THE PINCH IN THE COLUMBA EXPERIMENT

(A. Haberstich and P. R. Forman)

The Columba experiment, described above, consists of superimposing a strong z-current on a plasma preheated by a θ-pinch. The objective is to produce a denser and hotter plasma than would be possible with a θ-pinch alone.

If a sharp boundary model is assumed, such a configuration is theoretically unstable. The most dangerous mode, according to Kruskal and Shafranov, is the m = 1 mode. One of the reasons for building the Columba machine was to see if this mode does indeed develop in a hot z-pinch. The measurements reported here have been devised to throw light on this matter.

The m = 1 instability is expected to produce a helical displacement of the z-pinch current. The experimental method used consists in measuring changes in the azimuthal magnetic field distribution due to this displacement. The perturbation is detected by means of three sets of sensing coils located at midplane, as well as 9.5 cm above and below midplane of the machine. Each set consists of two strings of sensing coils, such as those shown on the right side of Fig. 18.

This configuration is designed to perform a discrete Fourier analysis of the azimuthal magnetic field distribution. The output of each string is proportional to the sum of the individual coil signals. As indicated in the figure, the coil sensitivities marked 10, 14, etc., go like the cosine of the azimuth for the upper string, and like the sine of the azimuth for the other.

Each string is essentially an 8-coil system, the two missing coils having zero sensitivity. The time-integrated output of such N-coil systems is given by

$$V_C = C\frac{N}{2}\left[a_1 + \sum_{\ell=1}^{\infty}\left(a_{\ell N-1} + a_{\ell N+1}\right)\right]$$

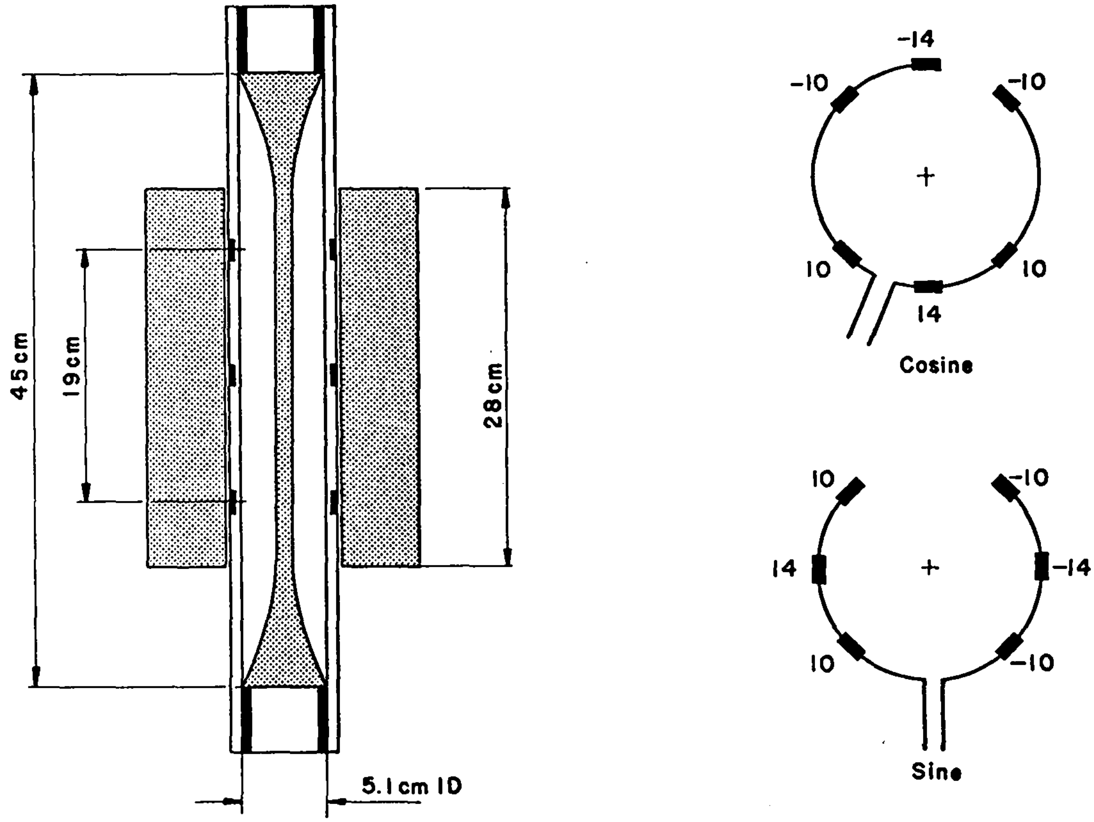

Fig. 18. Cut along discharge tube of the Columba experiment and sensing-coil configuration.

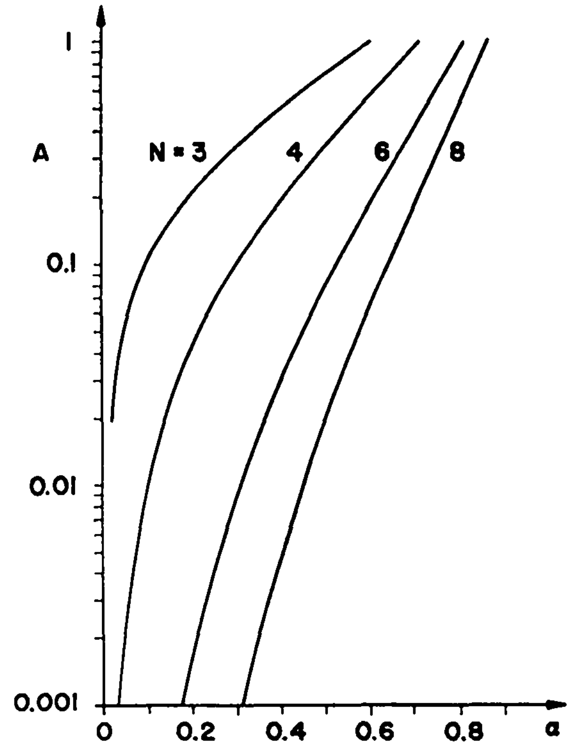

Fig. 19. Aliasing error as function of normalized position ($\alpha = r/R$) of a filamentary current.

for the cosine coils, and

$$V_S = C\frac{N}{2}\left[b_1 + \sum_{\ell=1}^{\infty}(b_{\ell N-1} + b_{\ell N+1})\right]$$

for the sine coils. The Fourier-coefficients a_k and b_k are given by

$$\begin{matrix} a_k \\ b_k \end{matrix} = \frac{\mu_0}{\pi R^{(k+1)}} \iint J_z\, r^k \begin{matrix} \cos \\ \sin \end{matrix} (k\theta)\; r\, dr\, d\theta .$$

In these expressions, $J_z(r,\theta)$ is the z-current density, R is the radius of the inner wall of the θ-pinch coil, and C is a constant dependent on the design of the coils.

The sum appearing in the expressions for V_C and V_S is an aliasing term due to the discreteness of the analysis. If this term is neglected for the time being, it is found that V_C and V_S become proportional to the x and y components of the first moment of J_z.

The proportionality between sensing-coil signal and position of the discharge is perturbed, for large radial displacements, by the emergence of the aliasing term. The relative magnitude of this perturbation is plotted in Fig. 19, for a filamentary current at position (r,0). The 8-coil configuration is seen to remain linear within 10% up to a radial displacement of 0.6 times the wall radius. The linear range of a conventional 4-coil system, by comparison, is only about half as large.

Turning now to the stability measurement, Fig. 20 shows a typical result obtained at a z-bank voltage of 15 kV. The large circles correspond to the inner wall of the discharge tube. The small circles indicate the position of the center of gravity of the current, at the three axial positions and at ten consecutive times during the discharge. The z-pinch is applied 1.1 μsec after the θ-pinch and the plasma column of radius 0.9 cm is seen to become unstable ~0.7 μsec after initiation of the z-pinch. The plasma first moves towards the wall almost as a straight column. Once the eccentricity reaches 1.5 cm, the column goes into a helix in the direction of the magnetic field.

Measurements carried out at 5 and 10 kV showed essentially the same behavior. The angular displacement between the two extreme axial positions rarely exceeded 45°, indicating a wavelength larger than 150 cm. The z-pinch remained stable at these lower voltages for up to 1.1 μsec.

A comparison between these measurements and end-on Mach-Zehnder interferograms was given in Fig. 17. The left side of the figure shows a plasma column on its way towards the wall. The two results are seen to be in good agreement. Furthermore, the interferogram confirms the small angular dispersion of the plasma column during the initial stage of the instability.

By knowing the time dependence of the eccentricity , the growth rate, ν, of the instability can be calculated. Results for delayed z-pinches at z-bank voltages of 5-15 kV are shown in Fig. 21.

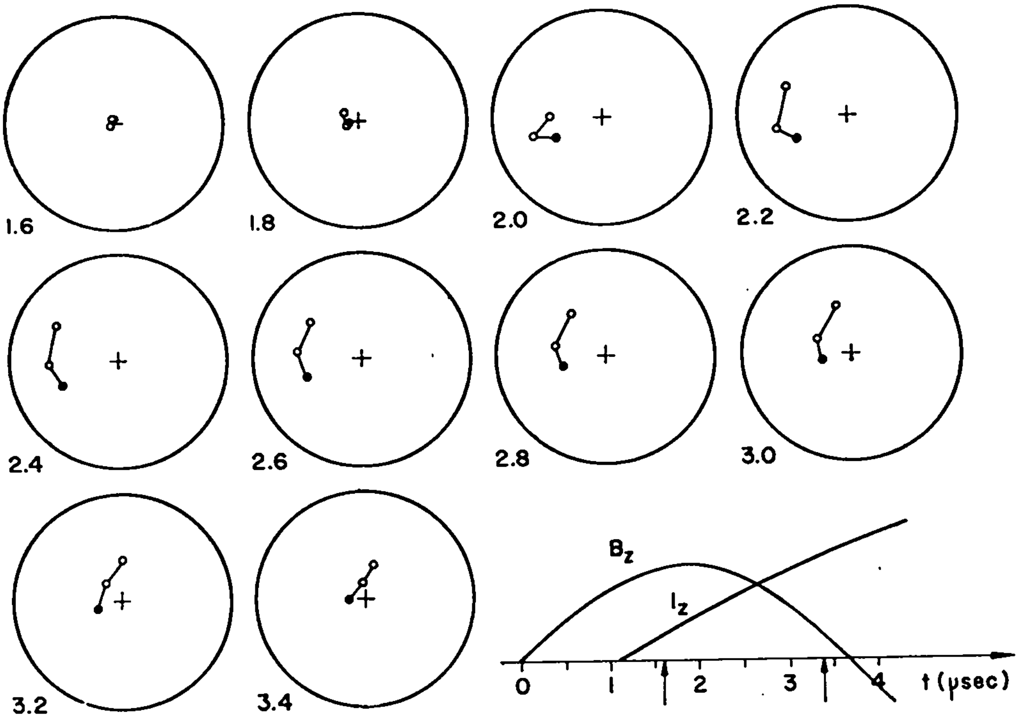

Fig. 20. Observed position of z-current vs time.

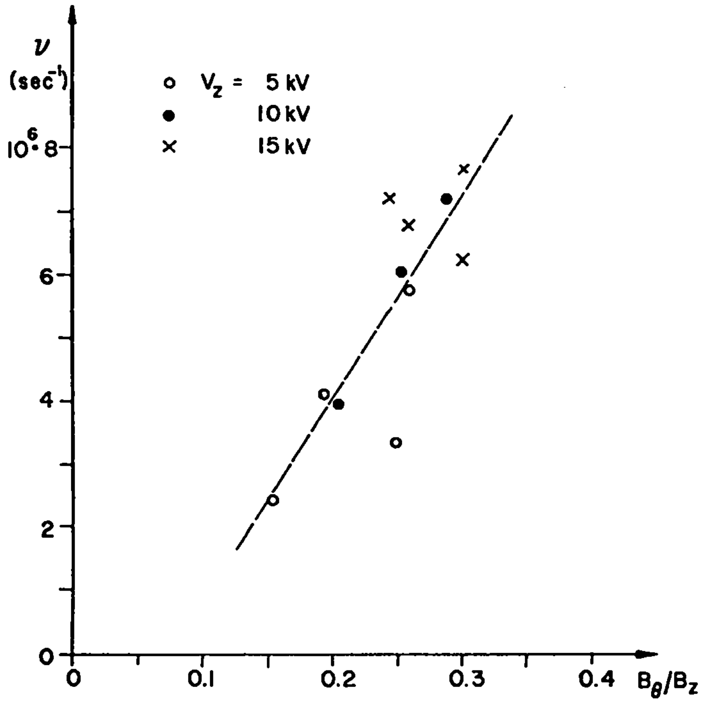

Fig. 21. Growth rate vs B_z/B_θ.

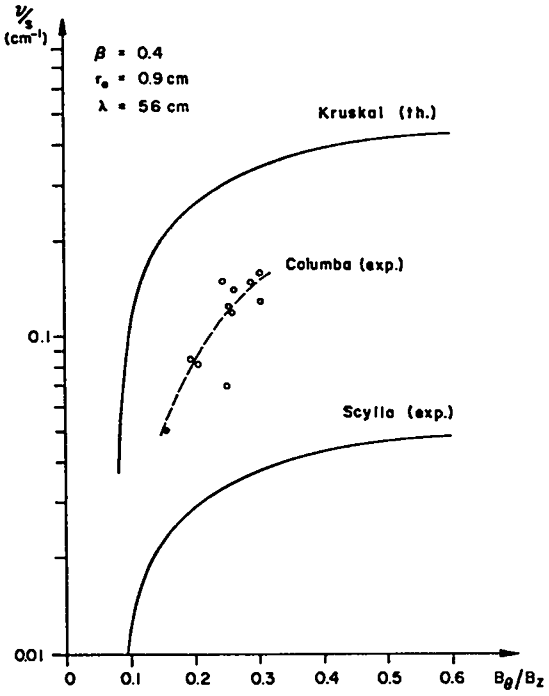

Fig. 22. Normalized growth rate (ν/s) vs B_z/B_θ.

The e-folding time is seen to range between 0.5 and 0.125 μsec. The 5-, 10-, and 15-kV results overlap, indicating a one-to-one correspondence between growth rate and B_θ/B_z. Similar measurements, carried out with simultaneous z- and θ-pinches (screw pinch), gave comparable growth rates.

The experiment described above is reminiscent of a Scylla experiment, in which a quasi-constant z-current is superimposed on a θ-pinch.[1] The Scylla group observed an m = 1 instability with wavelength twice the length of their machine and growth rate 1/9 the Kruskal-Shafranov value.

To compare the growth rates in the present work with the Scylla data, Kruskal's equation[2] has been solved numerically for a wavelength of twice the length of the Columba machine. The result, normalized to the sound speed s, is represented by the upper curve in Fig. 22. The growth rate to be expected from the Scylla results, i.e., 1/9 the theoretical value, is represented by the lower curve. It should be noted that the Scylla experiments were carried out at values of B_θ/B_z smaller than 0.25; the remainder of the curve has not been verified.

The growth rate observed in Columba is seen to be larger than in Scylla but still about three times slower than the Kruskal value. More recent results on Scylla IV indicate a growth rate 1/5 the theoretical value.[3] This is comparable to the Columba growth rate.

Conclusion

A method has been developed to measure the m = 1 stability of the Columba pinch from the outside of the discharge tube. The plasma column becomes m = 1 unstable at 0.7-1.1 μsec after initiation of the z-current with a wavelength longer than 150 cm. The growth rate of the instability is comparable to the latest Scylla IV results, but still about three times slower than the Kruskal value for a wavelength of twice the length of the machine. The discrepancy is believed to be due in part to the idealized current and density distributions assumed in the theory.

References

1. E. M. Little, et al., Paper CN-24/K-2. Third IAEA Conference on Plasma Phys. and Cont. Nuc. Fusion Res., Novosibirsk, 1968.

2. M. D. Kruskal et al., Phys. Fluids, 1, 421 (1958).

3. K. S. Thomas, et al., Paper 1A-4, Annual Mtg. Amer. Phys. Soc., Div. of Plasma Physics, Miami Beach, 1968.

SUMMARY OF THE PULSED PLASMA GUN PROGRAM

(I. Henins and J. Marshall)

The primary purpose of the program has been to develop a pulsed coaxial plasma gun with a large output of hot thermonuclear plasma. Presumably this plasma would be used for injection into some containment device. However, the process of trying to understand the gun behavior and the adaptability of the experiment have led into slightly different directions during the past year.

First, the removal of the outer electrode allows the study of the "snowplow" discharge in an ambient gas filling as initially reported in the last annual report (LA-3831-MS, p. 39). These experiments were extended and a paper was prepared for publication in cooperation with R. L. Morse and T. D. Butler, who have developed a theoretical model and performed particle-in-cell computer simulation calculations for comparison with the experimental data. A discussion of the work is presented later in this report.

Another interesting investigation has been the continuous flow pinch. This developed from the observation of the relatively stable pinch which persists in front of the gun for rather long periods of time after the plasma emerges. In cooperation with A. A. Newton of the Culham Laboratory, this has led to a study of the phenomenon with the aim of understanding it, and improving those plasma properties which might be of thermonuclear interest. Various aspects of the continuous flow pinch are discussed in the following three sections.

Other developments, primarily of a technological nature, have been made as necessary. One of these is the high-pressure fast gas valve. This was needed to make it possible to put the desired gas loads in the large gun (1.02-m long, 6.4-cm diam inner electrode, 17.1-cm diam outer electrode) used in the experiments. A paper on the valve has been submitted for publication to the Review of Scientific Instruments and is included in a later section of this report. Another development of this type is the adaptation of the holographic interferometer to the large field of view (25-cm diam) needed in these experiments. This interferometer is discussed in detail in the Snowplow Discharge section of this report. The solid dielectric switch development was discussed in the last annual report (LA-3831-MS, p. 43), and a paper on it has now been published.[1]

Reference

1. I. Henins, J. Marshall, Rev. Sci. Instr. 39, 1481 (1968).

THE CONTINUOUS FLOW PINCH INVESTIGATION

(I. Henins, J. Marshall, A.A. Newton)

Introduction

The continuous flow pinch is a phenomenon which appears to allow the achievement of very large plasma densities at thermonuclear temperatures in z-pinch configurations without the usual $m = 0$ (sausage link) instability. It differs conceptually from the usual z-pinch in that there is no boundary between plasma on the inside and containing magnetic field on the outside. Instead there is a continuous gradation from dense, high-temperature, high-β plasma near the axis to tenuous, low-temperature, low-β plasma at large radii. The distribution of density and temperature is maintained by continuous flow of plasma and magnetic flux inward, balanced by flow outward along the axis.

In principle, the lifetime of the pinch could be indefinitely long, but the containment time for Lawson criterion purposes is the flow time of an average ion along the pinch after compression. Neutral stability against $m = 0$ by hydromagnetic interchange modes is predicted in the simplest steady flow model. In practice it appears to be possible to attain positive interchange stability by inversion of the distribution, i.e., by having a larger than normal plasma pressure at large radii. No means are presently available for assessing the problem of the $m = 1$ instability except that experimental continuous flow pinches, encountered beyond the muzzle of a coaxial gun, are usually free of it for long times, and recover from $m = 1$ displacements if they develop at early times.

The continuous flow pinch shares the property of z-pinches in general that magnetic pressures can be employed which are far beyond the strength of materials. It also has the advantage that the containment field energy is transformed into the plasma energy during the compressional flow, so that no parasitic energy is required for the containment field. If a reactor could be built on this principle, the hot plasma escaping after the containment time would be led away from the confinement region in a natural manner so as not to damage the walls. In principle, also, the walls in the containment region can be far from the plasma so as not to suffer excessively large neutron loads.

The Coaxial Gun

Perhaps the best way of introducing the continuous flow pinch is to point out that it could be a coaxial gun, modified so as to provide a steady (or nearly steady) flow of plasma and magnetic flux out through its muzzle. A coaxial gun usually consists of two long concentric cylindrical electrodes, separated at one end by an insulator and opening at the other into a large evacuated volume. The terminals, which are separated by the insulator, can be connected by a switch to a high-voltage capacitor bank. A pulsed valve admits gas to the interelectrode space, and, after a suitable delay for gas to spread along the gun barrel, the switch is closed, connecting the bank to the terminals . The resulting high-current discharge is driven away from the terminals hydromagnetically. It does not, however, drive the gas load ahead of it through the muzzle but rather pushes most of it aside leaving it stagnated against the outer electrode. The gas which has been left behind along the gun barrel is mixed with a substantial amount of magnetic flux by mechanisms which are not fully understood. The magnetic piston carries a plasma with it partly because of gas distribution conditions which are empirically optimized through adjustment of gas inlet position and delay after admission. All of the plasma in the gun is magnetized with a B_θ field at the time the discharge reaches the muzzle, and all of the magnetic field on the gun side of the insulator carries at least some plasma. The plasma emerging from the gun is the result of the expansion through the muzzle of this magnetized plasma. The so-called "fast plasma" is the result of the expansion of the magnetic piston part of the field, the part which carries only a tenuous plasma. The "slow plasma" is the result of the expansion of the less magnetized, denser plasma which was left behind against the outer electrode.

Qualitative Description of the Phenomenon

The continuous pinch phenomenon in the gun results from the flow of magnetized plasma over the end of the center electrode. Suppose that the B_θ magnetized plasma between the gun electrodes is in radial equilibrium as a moderately low-β plasma, i.e., that most of the pressure is magnetic. The plasma-field mixture exerts an inward pressure on the inner electrode where the B_θ field is bounded by an axial current. As the plasma and field flow over the end of the electrode, the support provided by it is removed. The current bounding the field must now be carried by the plasma, and the result is an inward force which drives the plasma toward the axis. Assume for the purposes of the model that the plasma is a perfect conductor, so that the number of ions and electrons in a tube of flux is a constant. As the tube of flux moves inward its volume decreases. (In a $B_\theta = 2I/r$ field the volume of a tube containing one Maxwell of flux is $v = 2\pi r/B = \pi r^2/I$). The magnetic energy density in the field however varies as $1/r^2$ so that the magnetic energy of the tube is independent of radius. The plasma energy, however, grows because of the compression. The result is that the β of the plasma rises, and, if the inward flow is carried far enough, nearly all of the pressure is due to the plasma.

Morozov Model

Flow systems of this kind have been treated theoretically by A. I. Morozov[1] by means of a hydromagnetic Bernoulli equation

$$V_a^2 + \frac{V^2}{2} + \frac{C^2}{\gamma-1} = \text{const.},$$

where V_a = Alfvén speed $(\sqrt{B^2/4\pi\rho})$, C = speed of sound $(\gamma p/\rho)$, and V = streaming speed of the plasma. The equation is derived on the assumption that the plasma is nonresistive, adiabatic in the sense that the particles follow $E \times B$ guiding center drift motion, and that the plasma conforms adiabatically and isotropically to the changing volume of a tube of flux.

The three terms in the Bernoulli equation can be transformed one into the other by suitable flow patterns. For example, where a streamline approaches the axis, the Alfvén velocity or magnetic energy term becomes negligible. If at the same time the streaming velocity term can be kept small by somehow throttling the flow, the plasma density and temperature can be raised by large factors from their values at the source. The maximum factor by which the density can be raised is given by

$$\frac{n}{n_o} = \overline{\frac{2(\gamma-1)}{\gamma\,\beta_o}}^{\,\frac{1}{\gamma-1}} ,$$

whereas the maximum temperature is

$$T_{max} = \frac{\gamma-1}{\gamma}\,\frac{B_o^2}{k4\pi n_o} .$$

If the compressed plasma near the axis is allowed to flow out into a large volume, it will expand so that its thermal energy and the magnetic energy associated with it are both negligible compared to its streaming energy. This corresponds to complete dominance of the first term in the Bernoulli equation. The streaming energy per particle will now be $\frac{1}{2} mV^2 = B_o^2/4\pi n_o$. At this point in the flow the density is small because of the expansion and the plasma is probably not of immediate thermonuclear interest.

The Slow-Fast Model

This model of the continuous flow pinch was developed at LASL in ignorance of the work of Morozov.[1] It includes no inertial effects and is one-dimensional, assuming purely radial flow of plasma and flux, with a flux sink at the axis. It is described in the next section (p. 28). Its only virtue, compared to the more sophisticated treatment of Morozov, is that, since it includes no inertial effects, it describes a static equilibrium and it is immediately obvious that the situation is neutrally stable against m = 0 hydromagnetic instability. This follows from the reversible adiabatic compression assumed in the model. Any two tubes of flux, complete with attached plasma,

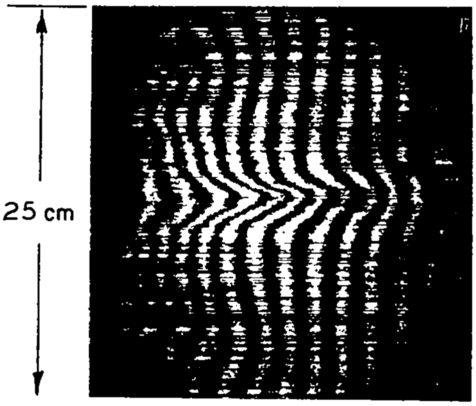

Fig. 23. Interferogram of deuterium plasma pinch in front of gun muzzle.

can in principle be interchanged without altering the system at all. This means that such a perturbation produces no change of energy, and is therefore neutrally stable.

Observations with Coaxial Guns

For a number of years it has been known that a z-pinch configuration of current extends beyond the muzzle of a coaxial gun, and that it is remarkably stable, showing no violent fluctuations in voltage and current. For a little more than a year work has been proceeding at Los Alamos with a scaled-up coaxial gun driven by large, rather inductive, capacitor banks. Much larger gas loads have been used than before, this being a natural scaling requirement of the move toward higher energy. In addition the technique of holographic interferometry has been applied to the emergent plasma. Taken together, these factors have led to the direct observation of the gun muzzle pinch. The example in Fig. 23 is for a deuterium plasma pinch in front of the gun muzzle at 55 μsec after breakdown; the first plasma emerges at ~ 15 μsec. The 3.2-cm^3 plenum was filled to 500 psig; the 2800-μF capacitor bank was charged to 10 kV and the firing delay was ~ 400 μsec after valve opening.

Under appropriate conditions the pinch is found to be grossly stable over periods of about 100 μsec and to have densities of several times 10^{17} /cm^3, both in deuterium and argon. Plasma temperatures and streaming energies are in the region of about 100 eV although they can be varied over wide ranges. Spectroscopically, the pinch is observed to show only the lines of the injected gas (no copper from the electrodes is found). The current in the muzzle pinch is considerably less than that along the center electrode well within the gun. In addition, it decreases rather rapidly with increasing distance from the gun. The current decrease is due to expansion through the muzzle and away from it. The expansion involves plasma acceleration, due mostly to $\vec{J} \times \vec{B}$ forces, and the current required to do this flows radially out of the pinch and returns to the outer electrode, thus decreasing the current in the pinch.

Muzzle pinches observed with argon and deuterium gas injection both show gross stability over long periods, although unstable behavior is found under some conditions. It appears that with argon the plasma column of the pinch is smaller in diameter and more turbulent, i.e., with a lumpier appearance as viewed photographically or by interferometer. The smaller diameter is probably due to more resistive behavior in argon where a great deal of energy can be dissipated in line radiation. The resistance leads to flux annihilation at the axis and enhanced hydromagnetic drift inward toward the flux sink.

Shock Waves

The edge of the muzzle pinch is frequently sharper than would be expected from the simple adiabatic flow theory. This may be due in part to a standing shock wave which has appeared in a hydromagnetic particle-in-cell computation.[2] Some of the results are shown in Fig. 24; the problem is started with a cold isomagnetic plasma load on a 1/r B_θ field filling the space between the electrodes. After some time, the system achieves a nearly steady state with a plume of high-velocity, hot plasma streaming along the axis. A shock wave bounds this plume, apparently resulting from supersonic implosion against the axis.

Flux Annihilation

The detailed shape of the muzzle pinch must also be affected by resistive flux annihilation, as mentioned above. Measurements of the

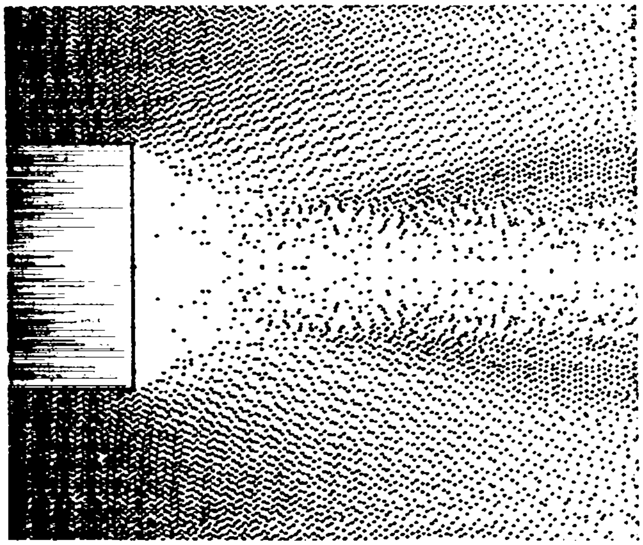

Fig. 24. Calculation of plasma configuration in the gun muzzle pinch (made by T. D. Butler, J. L. Cook, and R. L. Morse[2]).

magnetic field carried with the flow of plasma in the pinch indicate that the plasma is substantially demagnetized as compared with its state inside the gun barrel. In addition, total flux flow measurements made with electric probes show that with argon about ⅜ of the flux emerging from the gun muzzle disappears into the first 20 cm or so of muzzle pinch.

In ordinary resistive hydromagnetic systems, magnetic flux can be shown to be conserved except at singularities of a particular type, namely, where a resistive current bounds a magnetic field zero. The axis of a z-pinch is an example of such a singularity. Thus in a resistanceless flow pinch the streamlines of hydromagnetic flow, which are identical to the streamlines of flux flow and of plasma flow, never reach the axis, but first approach it and then later recede. In a resistive continuous flow pinch, many of the streamlines of flux flow are seen to terminate on the axis. The reason they do so is the presence of electrical resistance and this implies a departure from hydromagnetic behavior. Thus the plasma flow is not identical with the flow of flux, particularly near the axis. However, at larger radii, where the current density is much smaller, the behavior remains reasonably hydromagnetic. No computations have yet been made that include resistive effects. At present it is not even clear as to whether resistance makes the pinch more or less stable. It can be shown that, at least on the average, it has no effect on the amount of energy delivered to a particle.

Plasma Flow Experiments

The Mather type of dense plasma focus (DPF) machine[3] resembles a coaxial gun very closely in shape. The outstanding difference between the devices is that the plasma focus is operated with a static gas filling at relatively high pressure (~ 5 torr), whereas the coaxial gun operates with fast valve gas injection. In addition, a DPF device is said to operate "better" with the positive electrode at the center. Coaxial guns, on the other hand, produce a more useful plasma stream with the negative electrode at the center. One reason is that the trajectories of individual ions in a negative center electrode gun approximate the guiding center motion of the hydromagnetic plasma assumed in flow theory. Ion trajectories with positive center electrode would be expected to be directed initially outward away from the axis, so as to produce a much less focused stream. It is not clear why higher neutron yields are produced in a DPF machine with positive center electrode, but grossly the behavior is nearly independent of polarity. Higher gas density and relatively smaller ion gyro radius presumably allow the plasma to behave more nearly like an ideal hydromagnetic fluid than in a gun.

The Snowplow Experiment

The continuous pinch process may also be involved in the pinch of the "snowplow" discharge experiments (p. 35). There it is found that the magnetic field disturbance, created by the snowplow spilling over the end of the electrode and pinching, propagates toward the terminals at a finite Alfvén speed. From this it is inferred that the snowplow is somewhat leaky. By combining it in one particular case with the magnetic field value at the surface of the electrode, the plasma mass density is calculated to be about 1/200 of the initial filling density. This remaining plasma should be thoroughly magnetized, and thus the plasma and magnetic flux flow into the pinch is a more-or-less sustained process and, according to Morozov, should compress to a high density. The question then is whether or not this might also be the process responsible for the high densities observed in the DPF experiments.

The Mather Experiment

Detailed measurements have been made by J. W. Mather et al., of the angular distribution of neutron energies in their DPF machine.[4] The measurements have been interpreted to indicate that the neutrons are produced by approximately thermal distribution of deuterons with a streaming velocity > 10^8 cm/sec. At the same time the neutron pulse lasts for ~ 0.1 μsec. These observations and conclusions are in agreement with those of other experimenters. It appears that it is very difficult to reconcile these observations with anything but a sustained flow model. Furthermore, in the admittedly different experiment described above, the plasma required for sustained flow is present and the flow exists.

Other Gun Experiments

Exploratory experiments have been made with the idea of seeking to improve the stability and density of the continuous flow pinch observed beyond a coaxial gun muzzle. The central idea has been modification of the plasma source. The design of coaxial guns was partially optimized to produce the maximum possible amount of fast plasma. The parameters arrived at in this way are not necessarily optimum for continuous pinch operation. It would be desirable to operate a continuous source of low-β plasma with an "isomagnetic" distribution; isomagnetic is a word coined by Morozov to indicate that every Weber or Maxwell of flux carries the same amount of plasma. Low β is required because of the inverse relationship between initial β and final density after compression. A source which might be applicable is the "deflagration" process which apparently has been observed in a coaxial gun by D. Y. Cheng.[5] Attempts have been made to duplicate Cheng's results in modifications of his gun geometry, but they have not yet been successful. Apparently in Cheng's system there is a breakdown on the downstream side of a puff of injected gas which burns away at the gas so as to drive a high-velocity, tenuous plasma out through the muzzle. A relatively steady source has been achieved, feeding on continuous flow through the gas valve, but apparently there were relaxation oscillations in the discharge which produced an unsteady plasma source and sausage-type instabilities in the pinch. A number of other things have been tried, but so far no conclusive results have been achieved.

The Continuous Flow Pinch as a Reactor

It is not yet clear if the continuous flow pinch can make a thermonuclear reactor, but there are interesting possibilities. The most obvious way of making a reactor is to use the self-field of the pinch alone for containment, and to make the pinch long enough so that the ions, at their streaming speed out along the axis, remain in the pinch for the time required to satisfy the Lawson criterion. Suppose the streaming speed is assumed to be equal to the speed of an ion with the energy kT. Then, a density of $10^{20}/\text{cm}^3$ could be achieved, the streaming time would have to be at least 10^{-8} sec. At 10 keV this would require the pinch to be 1 m long. The assumption that the streaming velocity is equal to the thermal speed may be unduly pessimistic. If it can be slower, the pinch need not be so long.

In principle, a given density can be achieved at any desired value of the pinch current, simply by varying the density and temperature of the plasma at the source. The diameter of the pinch, however, will be proportional to the current, since the same plasma pressure requires the same containment field. Thus, a total pinch current which is increased by a factor ten, for instance, will be carried in a plasma column having 100 times the area or the resistive voltage drop will be reduced by a factor of 10. This will reduce the accumulation of plasma in the pinch because of resistive flux annihilation and may contribute to stability.

In the coaxial gun version of the continuous flow pinch, the pinch current falls off rapidly with increasing distance from the gun muzzle. This is due to axial acceleration and presumably can be overcome by control of the flow pattern. One possibility is to restrict the flow away from the gun muzzle by a poloidal magnetic field as generated for instance by a coil coaxial with the pinch. Another is to use inward radial flow from an extended source at large radius. Presumably the axial flow would be outward at each end diminishing in velocity to zero at the center. A coaxial coil around each end of the pinch could be used to restrict the flow to a smaller radius. A practical difficulty here is that it is not known how to make the plasma source.

Control of m = 1 instability, if it is serious in the continuous flow pinch, must wait for a better knowledge of the instability. In principle, the same methods of stabilization are available as for an ordinary z-pinch, but more knowledge is needed in this connection.

References

1. A. I. Morozov, Zh. Tekh. Fiz., 37, 2147 (1967) [Sov. Phys. - Tech. Phys., 12, 1580 (1968)].
2. T. D. Butler, et al., "Proc. APS Topical Conference on Numerical Simulation of Plasma, Los Alamos, Sep. 1967," LA-3990, Paper C-6.
3. J. W. Mather, Phys. Fluids, 8, 366 (1965).
4. J. W. Mather, et al., Bull. Am. Phys. Soc., Ser. 2, 13, 1542 (1968)(Abstract).
5. D. Y. Cheng, ibid., Ser. 2, 13, 1560 (1968) (Abstract).

THE CONTINUOUS FLOW PINCH

(J. Marshall and A. A. Newton)

Recent experiments with a coaxial gun, firing into vacuum and using pulsed gas injection half way along the center electrode, have demonstrated the existence of a dense, stable pinched plasma column in front of the gun which is sustained for periods of more than 100 μsec.[1] It is remarkable that, although probe measurements of the current distribution show this to be a z-pinch, which is known to be unstable to the m = 0 mode, no such unstable behavior at the boundary is observed. Within the pinch there is some turbulent structure. A model is proposed here to account for the heating, sustainment, and stability of the pinch.

The investigations have shown the plasma in the column to be flowing away from the gun and to originate from a B_θ magnetized plasma produced and left behind between the gun electrodes by a high-current electrical discharge. It corresponds to the "slow plasma" from the gun, comprises most of the gas admitted by the valve, and carries about half of the streaming energy. It succeeds the "fast plasma," the component usually considered to be of primary interest in gun studies.

The significant part of the flow, for the present purpose, is radially inward, and occurs when the plasma "falls off" the end of the inner electrode. If there were no means for removal of high-pressure plasma, accumulating near the axis because of this flow, the flow would be only momentary. Expansion away from the gun along the axis provides a sink, however, and the spillover process continues until all of the stored plasma and flux have been exhausted from the interelectrode space.

Thus a one-dimensional model of inward flow is constructed assuming a sink for plasma and magnetic flux at the axis, and a steady source for both at some outer radius; J is considered to be purely axial so that B is azimuthal. Ideal M.H.D. flow is assumed, so that the plasma density, n, varies with field and radius as

$$n = \frac{NB}{2\pi r} , \qquad (1)$$

where N, the number of particles per unit flux, is conserved. If the flow is slow and steady, pressure balance takes the form

$$\frac{d}{dr}(nkT) + JB = 0. \qquad (2)$$

Furthermore, isentropic compression is assumed, so that

$$T/T_o = (n/n_o)^{\gamma-1}, \qquad (3)$$

where the suffix zero denotes a value at the source radius, r_o. There is a problem here as to what value of γ should be used, since the compression is somewhat anisotropic, and the anisotropy varies with radius. Qualitatively, the results are independent of the value of γ within reasonable limits.

If J and B are related by Maxwell's equations, Eqs. 1-3 may be combined to give

$$\frac{dB}{dr} = -\frac{B}{r}\left(\frac{1 - AB^{\gamma-2}\,r^{-\gamma}}{1 + AB^{\gamma-2}\,r^{-\gamma}}\right), \qquad (4)$$

where

$$A = 2\gamma\, N\, kT_o\,(r_o/B_o)^{\gamma-1}.$$

Integration then yields

$$rB(\gamma-1 + Ar^{-\gamma}\,B^{\gamma-2}) = \text{constant}.$$

It is of interest to note that the ultimate temperature is related to the field energy/particle at the source, i.e.,

$$kT_{max} = \frac{B_{\theta o}^2}{4\pi n_o}\,\frac{\gamma - 1}{\gamma}.$$

An equivalent statement is that

$$C_s^2 = (\gamma - 1)\,V_{ao}^2,$$

where C_s is the ultimate sound speed and V_{ao} the Alfvén speed at the source. The ultimate density is given by

$$n_{max} = n_o\left[\left(\frac{2(\gamma-1)}{\gamma\beta_o}\right)\right]^{\frac{1}{\gamma-1}}. \qquad (5)$$

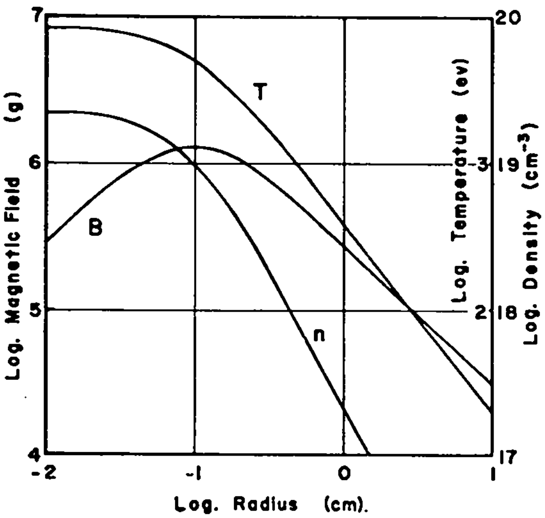

Fig. 25. Computed density, temperature, and magnetic field for a pinch with a slow, steady inward flow.

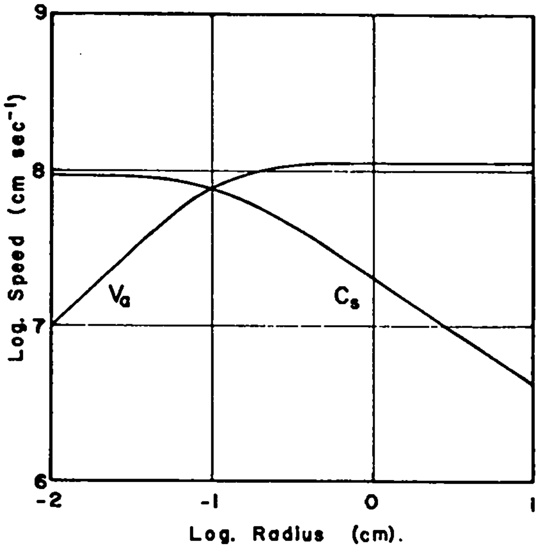

Fig. 26. Computed radial distribution of sound and Alfvén speeds corresponding to Fig. 25.

Typical distributions of density, temperature and magnetic field for $\gamma = 5/3$ are shown in Fig. 25. The numbers have been chosen to correspond to possible conditions in a dense plasma focus machine. The growth of C_s at the expense of V_a is shown in Fig. 26.

Inclusion of inertia in Eq. 2, i.e., by adding $(\rho V)(\partial V/\partial r)$ in this case, gives an additional term in the denominator of Eq. 4, namely, $-4\pi\rho_o V_o^2 r_o B_o/rB^3$. The singularities obtained suggest a standing shock. A two-dimensional numerical model[2] reveals a shock which corresponds qualitatively to some of the observations made in this work.

Morozov[3] has studied the two-dimensional plasma flow in axisymmetric systems by means of a hydromagnetic analogue of the Bernoulli equation. When his treatment is specialized to slow, one-dimensional flow the results are identical with those given above. However, the possibility of shocks was not considered.

The existence of a shock is important because its appearance invalidates Morozov's (and the present) calculations of a continuous flow pinch as a thermonuclear device. With a shock, a high temperature is still obtained but the large compression, which is an essential feature of such a device, falls short of that predicted by Eq. 5.

A feature of the continuous flow pinch is its neutral stability to m = 0 interchanges when the flow is slow and steady. Neutral stability against flutes is implied by the reversibility and steady flow of the model. Thus, if any two tubes containing equal magnetic flux and numbers of particles are exchanged, there is no change in the total energy of the system. This is consistent with the general criterion for stability against interchange[4]

$$\frac{dP}{dv} + \frac{\gamma P}{v} > 0 , \qquad (6)$$

where v is the volume per unit flux. With N constant everywhere, Eq. 6 reduces to

$$\Gamma = \frac{1}{P}\frac{dP}{dr} - \frac{\gamma}{\rho}\frac{d\rho}{dr} > 0. \qquad (7)$$

In the isentropic case $\Gamma = 0$ and the stability is neutral.

It follows from Eq. 7 that heat conduction and radiation cooling of the central regions induce stability whereas dissipative heating has the opposite effect. A suitable distribution of N can ensure stability in real cases at the expense of steady flow. That the flow may sweep away a perturbation before it grows to significant amplitude is clearly beneficial, but only for short systems.

It is concluded that the foregoing explains qualitatively the production of the slow component from the coaxial gun and accounts for the sustained stable pinch observed. Similarity with the dense plasma focus suggests that the "paradox" noted by Mather[5] may be explained in an analogous manner.

It is clear that conditions for continuous flow pinching are not optimized in the gas-injected gun and occur fortuitously through broadening of the initial current sheet in the plasma focus. If means were provided to replenish the plasma magnetic field mixture convected into the pinch, then the pinched column could be sustained for much longer times.

W. Riesenfeld, I. Henins, and D. Henderson contributed to the discussion of the work described above.

References

1. I. Henins and J. Marshall, Bull. Am. Phys. Soc., Series 2, 13, 878 (1968)(Abstract).
2. T. D. Butler, J. L. Cook, and R. L. Morse, Proc. APS Conf. on Numerical Simulation of Plasma, LASL Report, LA-3990, Paper C6, 1968.
3. A. I. Morozov, Soviet Phys.-Tech. Physics 12, 1580 (1968). Proc. Third I.A.E.A. Conf. on Plasma Phys. and Cont. Nucl. Fusion Res., Novosibirsk, 1968.
4. I. B. Bernstein, et al., Proc. Roy Soc. A 244, 17 (1958).
5. P. J. Bottoms, et al., Proc. Third I.A.E.A. Conf. on Plasma Phys. and Cont. Nucl. Fusion Res., Novosibirsk, 1968.

THE CONTINUOUS FLOW PINCH AS A THERMONUCLEAR REACTOR

(A. A. Newton)

Introduction

In the work of A. I. Morozov[1] it can be seen how the magnetic Bernoulli equation may be used in the description of the properties of ideal M.H.D. flows. Large and predetermined increases in density and temperature can be expected. The possibility is examined here of using these effects to make a thermonuclear reactor.

As indicated earlier in this Report, the plasma column somewhat resembles a z-pinch, although there are special differences, viz., the distributions of pressure and density. These appear to suppress the dangerous m = 0 instability, at least in the simplest model. In the experiments of Morozov and those made at LASL, the plasma is observed to be stable; hence, ideal stability will be assumed in what is to follow. In addition, it is assumed that the flow channel can be constructed in such a manner as to suppress any shock effects akin go those predicted by R. L. Morse.

Technological considerations, such as the durability of electrode surfaces, will be assumed to be favorable.

Concept

As presently conceived, the Continuous Flow Pinch Reactor comprises three regions. First, there is a chamber where neutral gas is fed in and ionized in an azimuthal magnetic field to produce the low-β plasma-field mixture. Neutral gas and electrical energy are continuously fed in to make a continuous supply of the mixture.

Then the plasma streams from the low-β region to a second region where it is compressed and heated. Densities and temperatures are sufficient to generate thermonuclear reactions. Finally, the plasma flows to a third region where its energy is mostly in streaming motion for recovery by some mechanism unspecified.

The effective lifetime τ of an ion in the pinch is the time spent flowing through the high-density region and it is this time which must be used when Lawson's containment criterion is applied.

It is visualized that the flow pinch will be sustained indefinitely. If it is necessary to use pulse operation, the supposition is made that one pulse will last many ion transit times so that energy expended in setting up and disassembling the pinch can be neglected. Clearly if the latter energy is not negligible then the criteria have to be revised to take this fact into account.

Scaling Laws

Scaling Laws can be obtained through the application of Lawson's criterion using the ideal M.H.D. Bernoulli effect. At the end of this section there is given a qualitative discussion of the effects of radiation loss, diffusion, and microstability.

The reactor comprises three regions: (i) An inlet where low temperature, low-β magnetised plasma is generated. It has a density n_1 and a magnetic field $B_1 \sim 2I_1/R_1$ where I_1 is the current in the central electrode of radius R_1. In the Bernoulli equation (appropriate to this special case $V = V(V_r, V_z)$, $B = B(B_\theta)$)

$$V_a^2 + \frac{C^2}{\gamma-1} + \frac{V^2}{2} = U = \text{constant} \qquad (1)$$

(see p. 24 for definitions), the first term is dominant, i.e.,

$$U = V_{a_1}^2 = \frac{I_1^2}{\pi\rho_1 R_1^2} \qquad (2)$$

where $\rho_1 = m_i n_1$.

(ii) The plasma flows and compresses into a high-temperature, high-density region where a thermonuclear yield is obtained. Here $V_a \to 0$ so that

$$U = \frac{C_2^2}{\gamma-1} + \frac{V_2^2}{2} . \qquad (3)$$

The flow and thermal terms will be taken as equal; the density compression ratio is then

$$\lambda = \frac{\rho_2}{\rho_1} = \left[\frac{V_{a_1}^2}{C_1^2}\,(\gamma-1)\right]^{\frac{1}{\gamma-1}} \left(\frac{1}{2}\right)^{\frac{1}{\gamma-1}} , \qquad (4)$$

where the factor $(\frac{1}{2})^{\frac{1}{\gamma-1}}$ arises from flow and thermal terms being equal.

At this time the physics determining the length L of this region is uncertain, and so it is chosen to be

$$L = \alpha R_o . \tag{5}$$

Then the reaction time is

$$\tau = \frac{L}{V_2} = \frac{\alpha R_1}{C^2} \left(\frac{\gamma-1}{2}\right)^{\frac{1}{2}} . \tag{6}$$

(iii) The flowing plasma enters a final region in which the energy is all in flow, i.e.,

$$\frac{V_3^2}{2} = U, \tag{7}$$

and is recovered by means as yet unspecified.

Lawson Criteria

The Lawson criteria require the temperature and the containment parameter to attain certain (starred) values, i.e.,

$$T = T^*, \quad (n\tau) = (n\tau)^*.$$

The equivalent form

$$C_2 = C^*, \quad (\rho_2 \tau) = (\rho\tau)^* \tag{8}$$

will be used here. The current and density are now determined through Eq. 2 and 6, i.e.,

$$\frac{I_1^2}{\pi \rho_1 R_1^2} = \frac{2C^{*2}}{\gamma-1} \tag{9}$$

and

$$\frac{\alpha R_1 \gamma \rho_1}{C^*} \left(\frac{\gamma-1}{2}\right)^{\frac{1}{2}} = (\rho\tau)^* . \tag{10}$$

If α and R are given, then

$$I_1^2 = \frac{(\rho\tau)^* C^{*3} R_1}{\alpha\lambda} \pi \left(\frac{2}{\gamma-1}\right)^{\frac{3}{2}} \tag{11}$$

and

$$\rho_1 = \frac{(\rho\tau)^* C^*}{\alpha \lambda R_1} \left(\frac{2}{\gamma-1}\right)^{\frac{1}{2}} \tag{12}$$

must be chosen to satisfy the Lawson criteria.

Mass and Energy Fluxes

The mass flux through the device can be estimated by using the pressure balance relationship

$$\frac{2}{\gamma}\left(\frac{B^2}{8\pi}\right)_{max} = (nkT)_{max} \approx \frac{I_2^2}{\gamma\pi R_2^2} \approx \frac{\rho_2 C^{*2}}{\gamma} \tag{13}$$

to find the value of R_2 approximately. Then the mass flux is

$$\Gamma = \pi \rho_2 R_2^2 V_2 = \frac{I_2^2}{C^*} \left(\frac{2}{\gamma-1}\right)^{\frac{1}{2}} =$$

$$\delta^2 \frac{(\rho\tau)^* C^{*2} R_1}{\alpha\lambda} \pi \left(\frac{2}{\gamma-1}\right)^2 \tag{14}$$

with the assumption $I_2 = \delta I_1$.

The energy flux is

$$W = \left[\frac{C^{*2}}{\gamma-1} + \frac{V_2^2}{2}\right] \Gamma = \delta^2 \left(\frac{2}{\gamma-1}\right)^{\frac{3}{2}} I^2 C^* =$$

$$\delta^2 \frac{(\rho\tau)^* C^{*4} R_1}{\alpha\lambda} \left(\frac{2}{\gamma-1}\right)^3 \pi . \tag{15}$$

The driving emf can be found to be

$$\mathcal{E} = \frac{W}{I} = \delta^2 \frac{(\rho\tau)^{*\frac{1}{2}} C^{*\frac{5}{2}} R_1^{\frac{1}{2}}}{\alpha^{\frac{1}{2}} \lambda^{\frac{1}{2}}} \pi^{\frac{1}{2}} \left(\frac{2}{\gamma-1}\right)^{\frac{9}{4}} \tag{16}$$

and the dynamic resistance

$$R_{dyn} = \frac{W}{I^2} = \delta^2 C^* \left(\frac{2}{\gamma-1}\right)^{\frac{3}{2}} . \tag{17}$$

This is the resistance seen by the power source looking into the device.

Compression Ratio

The compression ratio λ merits some discussion. There is an upper limit, since $V_a \sim C^*$ which is fixed and C_1 has a minimum value since the plasma must be fully ionized. Even so C^{*2}/C_1^2 may be $\sim 10^4$.

Also, the compression ratio is sensitive to γ, particularly as $\gamma \to 1$. A change of γ from 2 to 5/3 can make a factor ~ 10 increase in maximum values of λ. This suggests that in practice the device may not exhibit a unique or well-defined λ.

Aspect Ratio

The physics determining the aspect ratio is not known at present. Experiments suggest $\alpha \sim 1$-10 is feasible. The scaling laws suggest much higher values, i.e., $\alpha \sim 100$-1000, would be more useful.

To raise α, Marshall and Morozov have advocated a B_z guide field. However, no significant gain would be expected from having a magnetic channel unless $B_z \sim B_\theta$. In this case much of the advantage of a continuous pinch reactor is lost since B_z is limited by practical considerations and αR_0 turns out to be rather large. (Morozov calls this device the "Prolyototron" or literally "fly-through-tron").

Numerical Examples

Typical numbers appropriate to a D-T mixture for the Lawson criteria are

$$n\tau = 10^{14}\ \text{cm}^{-3}\ \text{sec} \qquad T = 10^{4}\ \text{eV}$$

or

$$(\rho\tau)^{*} = 4 \times 10^{10}\ \text{g cm}^{-3}\ \text{sec},$$

$$C^{*} = 0.895 \times 10^{8}\ \text{cm sec}^{-1}.$$

For the calculations, γ is taken as 5/3 or 2 and the temperature of the cold gas corresponds to $C_1 = 1.414 \times 10^{6}$ cm sec^{-1}. The resulting parameters of the flow pinch are given in Table 3.

The extreme sensitivity to γ is illustrated there being one and a half orders of magnitude difference in λ for the two cases chosen. The importance of achieving a high aspect ratio to α is also apparent.

Table 3

Parameters of a Flow Pinch Satisfying $n\tau = 10^{14}$ cm^{-3} sec, $T = 10^{4}$ eV

	$\gamma = 5/3$	$\gamma = 2$
λ	2.55×10^{5}	4.01×10^{3}
I	$1.35 \times 10^{5}\sqrt{R_1/\alpha}$ emu	$7.98 \times 10^{5}\sqrt{R_1/\alpha}$
ρ_1	$2.43 \times 10^{-7}/\alpha R_1$ g cm^{-3}	$1.26 \times 10^{-5}/\alpha R_1$
Γ	$3.56 \times 10^{2}\,\delta^{2} R_1/\alpha$ g sec^{-1}	$1.02 \times 10^{4}\,\delta^{2} R_1/\alpha$
W_f	$8.5 \times 10^{18}\,\delta^{2} R_1/\alpha$ erg sec^{-1}*	$1.6 \times 10^{20}\,\delta^{2} R_1/\alpha$
$\mathcal{E}$	$6.3 \times 10^{13}\,\delta^{2}\sqrt{R_1/\alpha}$ emu	$2 \times 10^{4}\,\delta^{2}\sqrt{R_1/\alpha}$
R	$4.65 \times 10^{8}\,\delta^{2}$ emu	$2.53 \times 10^{8}\,\delta^{2}$

*i.e., $850/\alpha R$ kMW

Radiation

To test for the importance of radiation, a system with large α is assumed; then radiative cooling is only important in the jet. A figure of merit is defined by

$$\chi_1 = \frac{P_R \tau}{P/(\gamma-1)}$$

which is the ratio of radiated energy to the internal plasma energy

$$P_R = k\,\rho_2^{2}\,C^{*}$$

for pure bremsstrahlung ($k = 1.21 \times 10^{16}$ erg cm^{2} g^{-2}). It then follows, using $\gamma p/\rho = C^{*2}$, that

$$\chi_1 = \frac{\gamma(\gamma-1)\,k(\rho\tau)^{*}}{C^{*}} \quad .$$

Upon inserting numbers, it is found that

$$\chi_1 \approx 0.06 \quad \text{for } 10\ \text{keV} \quad n\tau = 10^{14}$$

$$\chi_1 \approx 0.4 \quad \text{for } 20\ \text{keV} \quad n\tau = 10^{15}$$

so that radiation is a feature which ought to be included for reactor calculations. In particular its effect may be manifest through $\lambda(\gamma)$.

Diffusion

To assess the importance of diffusion, the ohmic and dynamic resistances of the plasma column are compared, i.e.,

$$\chi_2 = \frac{R_{\text{ohmic}}}{R_{\text{dynamic}}} \quad .$$

Now $R_{\text{ohmic}} \sim \alpha R_1 \eta/\pi R_2$ and R_{dynamic} has already been calculated. Thus

$$\chi_2 = \frac{\eta \alpha \lambda}{\delta^2 C^* R_1} \quad \frac{1}{\pi} \left(\frac{\gamma - 1}{2} \right)^{\frac{5}{2}} .$$

For negligible diffusion it is required that $\chi_2 \ll 1$ which imposes an upper limit on $\alpha / \delta^2 R_1$. To obtain representative numerical values $\eta = 10^8$ emu/$T_e^{\frac{3}{2}}$ (eV) is used. Then

$$\frac{\alpha}{\delta^2 R_1} \ll 170 \text{ cm}^{-1} \quad \text{for } \gamma = 5/3$$

and

$$\frac{\alpha}{\delta^2 R_1} \ll 4000 \text{ cm}^{-1} \quad \text{for } \gamma = 2.$$

Microstability

A particular microinstability, viz., the excitation of ion acoustic waves which leads to an enhanced resistivity, is excited if the electron drift velocity, u, exceeds a characteristic speed $(kT_e/m_i)^{\frac{1}{2}}$. Now

$$u \sim \frac{j}{ne} \sim \frac{I_2}{Ne} \sim \frac{m_i}{e} \quad \frac{I_2}{\pi \rho_2 R_2^2}$$

and

$$\left(\frac{kT_e}{m_i} \right)^{\frac{1}{2}} \sim C^* / \gamma^{\frac{1}{2}} .$$

So that the criterion $\gamma u^2 < C^{*2}$ for the excitation of the waves becomes

$$\frac{\alpha}{\delta^2 R_1} < \frac{(\rho\tau)^* C^* e^2 \pi}{\lambda \gamma m_i^2} \left(\frac{2}{\gamma - 1} \right)^{\frac{3}{2}}$$

i.e.,

$$\frac{\alpha}{\delta^2 R_1} < 22 \text{ cm}^{-1} \quad \gamma = 5/3$$

$$\frac{\alpha}{\delta^2 R_1} < 1590 \text{ cm}^{-1} \quad \gamma = 2.$$

It follows that if the criteria for microstability are met then there should be no risk of diffusion.

Wall Loading

There is an upper limit to the energy flux incident on a reactor wall, which is one of the technological constraints in reactor design. A continuous flow pinch can have a metal wall. The energy flux incident on the wall of radius $R_w = \epsilon R_2$ which bounds the second (reacting) region is

$$F = \frac{W}{2\pi R_2} = \frac{1}{2m_i^2} \rho_2^2 <\sigma V> Q^* \frac{\pi R_2^2}{2\pi R_2} ,$$

where $<\sigma V> Q^*$ is the product of reaction rate and energy release. Making use of previous scaling laws, it is found that

$$F = \left[\frac{<\sigma V> Q^* C^{*\frac{1}{2}} (\rho\tau)^{*\frac{1}{2}}}{4 m_i^2 \lambda^{\frac{1}{2}}} \left(\frac{2}{\gamma - 1} \right)^{\frac{3}{2}} \right] \frac{\delta}{\epsilon R_1 \alpha^2} .$$

Inserting the numerical values $<\sigma V> = 10^{-16}$ cm^3 sec^{-1}, $Q^* = 2.26 \times 10^{-12}$ J, the result for $\gamma = 5/3$ is

$$F = 2.6 \times 10^{13} \frac{\delta}{\epsilon R_1 \alpha^2} \text{ W cm}^{-2}.$$

The upper limit to F is presently $\leqslant 10^3$ W cm^{-2} which constrains

$$\frac{\epsilon R_1 \alpha^2}{\delta} \geqslant 2.6 \times 10^{10} \text{ cm}^2 .$$

To see the restrictions imposed by wall loading, assume $\epsilon/\delta \sim 26$, $\gamma = 5/3$. Now to keep the power W_f within reasonable bounds, say 10^9 W (this is the electrical input power) it is necessary that $R_1/\alpha \sim 10^{-3}$ cm. Moreover, the machine must be a reasonable length say $\alpha R_1 \sim 10^4$ cm. Thus $R_1 \sim 3$ and $\alpha \sim 3 \times 10^3$ which leaves the result a factor of 3×10^2 short of the above criterion.

These difficulties might be overcome with pulsed wall loading.

Pulsed Wall Loading

Consider a pulse of duration $\mu\tau$. The energy received by the wall is

$$E_w = \mu\tau F = \left[\frac{<\sigma V> Q^* C^* (\rho\tau)^{*2}}{2 m_i^2 \lambda^{\frac{1}{2}} (\gamma - 1)} \right] \frac{\mu\delta}{\epsilon\alpha} .$$

The radius is now removed from the criterion. Numerically for $\gamma = 5/3$

$$E_w \approx 3 \times 10^5 \frac{\mu\delta}{\epsilon\alpha} \text{ J cm}^{-2} \text{ per pulse.}$$

A certain upper limit to E_w is that at which the walls melt e.g., when $E_w \sim 10^5$.

The wall loading criterion has now been freed from an R_1 dependence. Moreover the energy balance will be less favorable, requiring inclusion of terms for setting up and disassembling the plasma on the energy balance sheet.

Conclusion

The foregoing attempt to assign scaling laws is of course only approximate and it is clear that some detailed computational model will be required to obtain more realistic numerical results. The situation with regard to diffusion and microstability appears to be good. Radiation cooling is also not severe if the plasma is pure.

However, a number of points have been neglected, e.g., conduction heat loss and the all-important alpha-particle heating. The former being across field transport is difficult to calculate directly.

Reference

1. A. I. Morosov, Zh. Tekh. Fiz., 37, 2147 (1967) [Sov. Phys. - Tech. Phys., 12, 1580 (1968)]

COAXIAL SNOWPLOW DISCHARGE

(T.D. Butler, I. Henins, F.C. Jahoda,
J. Marshall, R.L. Morse)

Introduction

Since the advent of coaxial plasma accelerators some years ago, numerous studies have been made to determine the characteristics of the plasma produced. Studies have centered on both the puffed gas mode[1-6] of operation as well as on the static filling mode.[7-16]. There has been much discussion of the results and many are left unexplained by available theory.

For the static-filled operational mode, gas at uniform density and temperature fills the space between two cylindrical coaxial electrodes that are separated at one end by an insulator and are open at the other end. When a capacitor bank is discharged through the gas-electrode system, an axially symmetric current sheet forms at the surface of the insulator at the breech end of the accelerator. The sheet propagates axially along the electrode to the open end by means of a $\vec{J} \times \vec{B}$ force leaving in its wake a rarefield region permeated with an azimuthal magnetic field. Lovberg[12] studied this phase of the dynamics extensively using schlieren photography. Upon reaching the end of the electrode, the sheet diffracts around it and implodes on the axis forming a pinch. This latter phase of the dynamics has been investigated by Mather[13,15] and is called the dense plasma focus.

The primary purpose of this work is to investigate the dynamical plasma distribution in the accelerator. Both experiment and theory are used with each complementing the other to aid in the understanding of the problem. In addition, an evaluation of the applicability of the theoretical models to the problem is made by comparing their predictions with experiment.

Previous investigations have raised specific questions concerning the plasma properties and distribution in the accelerator, and some light has been shed on the problems. For example, Keck[10], Lie, et al.[14], and others have indicated that significant differences in the distrubution occur as a result of an interchange in polarity. In these cases, the negative center electrode experiments produce distributions that differ more from the conventional "snowplow" theoretical predictions than do distributions formed using a positive center electrode. This is not the result found in the present work. Good agreement between experiment and theory is obtained although the experiments were performed only with negative polarity.

The experimental setup differs from those usual in accelerator studies. As mentioned above, an outer cylindrical electrode surrounding the inner one has provided the current return in previous work. The outer electrode obstructs the radial flow of plasma in the devices and hampers the diagnostics during the time interval when the sheet propagates along the electrode. Lovberg[12] and Mather[13,15] have carried out studies with a perforated electrode that mitigates these problems. In the present work, the outer cylindrical electrode has been eliminated altogether and replaced by an unobstructive current return. This allows the use of the various diagnostics in all phases of the discharge.

Experimental Arrangement

General Description

The experiment was set up in a large vacuum tank, ~ 120-cm i.d. and 200-cm long, which can be pumped to a base vacuum of $< 10^{-7}$ torr by a combination of pumps capable of creating a relatively oil-free vacuum. The work was performed with static gas fillings to various pressures within a factor 50 up or down from 1 torr. Pressures were measured, depending on the range, with a trapped McLeod gauge or a precision diaphragm gauge. A large number of shots could be taken on one gas filling with no observable change in the time history or photographic appearance of the discharge. The gas was changed, however, at frequent intervals to avoid the possibility of contamination. The tank is provided with appropriate ports for probes, photography, and straight-through laser illumination for interferometry (Fig. 27).

The energy storage system is an adaptation of existing capacitor banks. The normal gun bank uses variable numbers of 14-μF, 20-kV capacitors each with a low-inductance ignitron switch mounted on its terminals, and up to six low-inductance cables from each capacitor to the gun terminals. Typically the bank has less than 10-nH inductance as seen by the load. For some of the present experiments eight of these capacitors were used, and for some 16. With dense gas fillings, it was necessary to increase the amount of stored energy beyond the capability of the normal gun bank by paralleling this bank with relatively high-inductance banks normally employed for operating pulsed magnetic field coils. A nominal 140 kJ of bank energy with an inductance of about 0.3 μH was used. The gun bank was left connected in parallel with this much larger energy source so as to reduce the large voltage transients otherwise accompanying the current break when the snowplow discharge spilled over the end of the electrode.

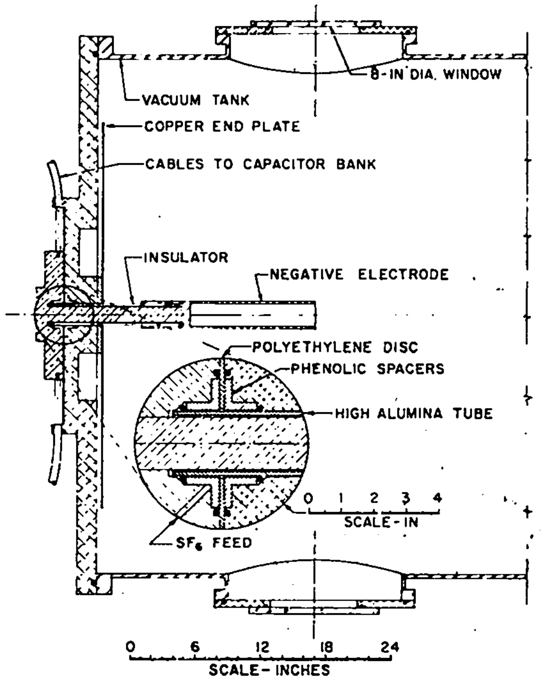

Fig. 27. Experimental arrangement for plasma gun studies.

In all cases a negative voltage was applied to the electrode. The cables connect to a pair of parallel flanges at the gun terminal with a sheet of polyethylene between them for insulation. The

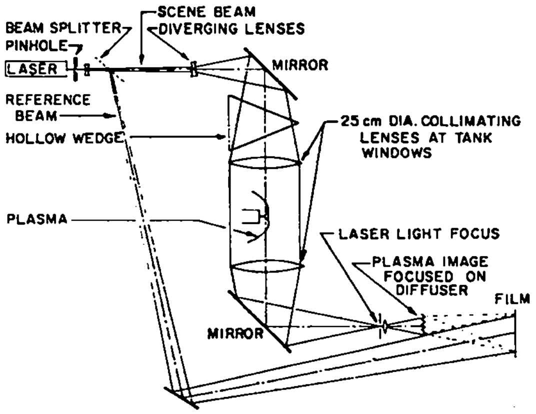

Fig. 28. Optical system for holographic interferometry (not to scale).

electrical insulator through the tank vacuum wall is a tube of high-alumina ceramic ~ 5-cm diam. To make the joint between the flat polyethylene insulator and this tube, phenolic "hat" insulators are used in a space pressurized to ~3 atm SF_6. The feed to the snowplow electrode passes through the ceramic tube, and the electrode overlaps it inside the tank so as to protect its end from the discharge. The gas discharge starts along the outer surface of the insulator tube and is then driven outward hydromagnetically in an inverse pinch configuration. As a general rule, there was no trouble with this design in the sense that a good clean hydromagnetic behavior was obtained with a variety of gases from a few mtorr to 50 torr.

The electrode is made of ordinary copper tubing 6.35-cm diam with ~ 3-mm wall thickness. The end is left open to a considerable depth (> 20 cm) to avoid current concentration on the end; during operation with a closed end, such concentration resulted in enormous amounts of light, presumably from evaporated copper. The low light level achieved with the open end allows optical observation of behavior after collapse over the end of the electrode; this would have been difficult or impossible otherwise. Also it does not affect the theoretical interpretation of the collapse in a very serious way.

For most of the experiments the current return was to a copper sheet covering the inside of the end of the tank. The shape of this positive electrode varied somewhat, and in some cases it was left out completely, the current returning directly to the aluminum alloy end plate. The shape or material of the return electrode would be expected to make little difference to the behavior of the system, and this appears to be the case.

Holographic Interferometry

The diagnostic technique of holographic interferometry is relatively new and has been used at LASL in studies of the θ-pinch.[17] However, certain modifications were necessary in order to adapt the technique to the larger field of view and increased plasma self-luminosity in the present work. The primary advantage is that holographic interferometers are much simpler to apply to the present problem than a Mach-Zehnder interferometer, while giving equivalent results.

A diagram of the optical system (not to scale) is shown in Fig. 28. The light source is a rotating mirror Q-switched ruby laser, TRG Model 104A operated at ~ 460 J input and with a pulse duration of ~ 30 nsec. In order to improve the spatial coherence, only a part of the laser light is selected by passing it through a 0.5-mm diam pinhole; this makes the light slightly divergent as a result of diffraction. The divergence is increased by a negative lens and the beam is separated with a beam splitter into a scene beam and a reference beam. The former is enlarged with a second negative lens to fill a 25-cm diam collimation lens just in front of a glass window in the tank. The laser light passing through the plasma is then parallel, and just fills another glass window on the other side of the tank.

A second 25-cm diam lens refocuses the light on a small-aperture diaphragm; this combination permits all the laser light to pass while letting through only a very small fraction of the plasma luminosity. An additional lens behind the diaphragm then forms an image of the plasma location on a ground-glass diffuser plate. This imaging counteracts the refractive bending effects due to density gradients. In order to reduce the temporal coherence required of the laser the reference beam is set up to have about the same mean optical path length (within ~ 1 cm) as the scene beam. The film used is Kodak High Definition Aerial Safety Film, Type SO-243.

Briefly, holographic interferometry consists of the superposition of two successive holographic exposures on the same photographic plate.[18] For the first exposure the Q-switched laser is fired without plasma. On the next exposure, which may be up to several minutes later, the laser is synchronized with a discharge of the machine, so that phase shifts of varying amounts are introduced in parts of the field of view, depending on plasma refractivity. When the hologram from the developed plate is reconstructed, the two separately recorded images of the diffuser interfere with each other to produce a fringe structure that delineates successive contours of 1 wavelength optical path difference.

If the plate is exposed to two successive laser shots with no plasma on either one, some fringes may appear because of random vibrations which move the optics in the system slightly. These fringes are generally straight and of random orientation. In practice it is convenient to overwhelm the random fringes by changing the gas (hydrogen or air) in a hollow glass wedge in the scene beam between shots. This introduces a closely spaced set of parallel fringes across the field with a known sense of optical path length gradient. The effect of the random fringes is then only a slight change in spacing or orientation of this background and the interpretation of fringe shifts introduced by plasma is unambiguous.

Theoretical Description

Basic Assumptions

In order to simulate the experiments, use has been made of two mathematical models which apply to two-dimensional flow; one is analytic whereas the other is numerical time-dependent. Each has its basis in the following assumptions: (1) the continuum hydromagnetic equations are applicable for describing the flow field; (2) the plasma conductivity is infinite so that the driving current flows in a thin layer separating the plasma and magnetic field; (3) the magnitude of the current is constant in time.

The basis for the fluid approximation (1) is that, for the densities and temperatures considered, the effective ion-ion[20] and ion-neutral[21] mean free paths are short compared to the thickness of the shock layer. Assumption (2), perfect conductivity at the piston interface, can be justified if classical field diffusion in the plasma[22] is assumed, but the possibility of anomalous diffusion leaves the basis for this assumption mostly experimental. The external circuit parameters were adjusted to some extent to cause only a slow variation of current flow to occur near the time when most of the plasma measurements were made. Hence, the mathematically convenient constant current assumption is not too strained.

The Analytic Model

The analytic model in the cylindrically symmetric snowplow discharge helps in understanding the gross features of this phenomenon. The model applies to the class in which the center electrode is infinitely long. The shock is assumed to be very thin and all effects that are directly related to the thickness are treated as small corrections to the vanishing shock thickness approximation. If it is assumed that a stationary solution exists in a frame moving axially with the shock, then the resulting time-independent system of equations (see below) has only one physical solution.

The (r,z) cross section of the shock surface described by this solution is a curved line (see Fig. 29) which starts normal to the electrode surface at the point of contact and quickly bends away from the direction of shock propagation with increasing radius. In this time-independent picture the radius and radius of curvature of the shock increase monotonically with arc length along with surface. In the shock frame the undisturbed gas flows uniformly in the z direction toward the shock. When the gas strikes the shock surface its momentum is altered and it is carried along by the flow in the shocked layer.

The flow is everywhere outward along the surface, starting with zero velocity at the electrode and increasing with increasing radius. It is because of this uniformly outward flow that for most purposes an outer electrode is at best unnecessary. When this pattern of flow is viewed in the lab frame it is seen that an element of shocked layer forms at the electrode surface and is pushed first straight ahead in the z direction and then increasingly outward away from the electrode, accumulating mass as it goes. Hence, the name "snowplow" is particularly appropriate.

In the shock frame the stationary equations of the thin shocked layer are

$$\frac{B_o^2 r_o^2}{8\pi r^2} - \rho u^2 \cos^2\theta + \frac{\sigma V^2}{2\pi r}\frac{d\theta}{ds} = 0 \tag{1}$$

$$\frac{d}{ds}(V\sigma) = 2\pi r u \rho \cos\theta \tag{2}$$

$$\frac{d}{ds}(V^2\sigma) = 2\pi r u^2 \rho \cos\theta \sin\theta - 2\pi r \delta \frac{dP}{ds} \tag{3}$$

$$\frac{d}{ds}(V\epsilon) = \frac{2\pi r u}{\gamma} \cos\theta \left(\frac{\rho}{2}\right) \left[u^2 \cos^2\theta + (u \sin\theta - V)^2 - u_c^2\right] + \frac{2\pi r \delta}{\gamma}\frac{dP}{ds}, \tag{4}$$

where

s = arc length along the shock from the electrode

r_o = the electrode radius

B_o = B_θ field at r_o behind the shock

ρ = mass density of gas ahead of shock

u = flow velocity of undisturbed gas (negative of axial shock velocity)

θ = angle made by shock surface with local radius

V = velocity of flow in shocked layer

σ = mass per unit arc length (integrated over angle around the center axis)

ϵ = internal energy per unit arc length

u_c = critical u velocity at which the kinetic energy of an incoming gas molecule equals its ionization energy

γ = ratio of specific heats (5/3 here)

δ = thickness of shocked layer

P = pressure in the shocked layer.

Equations for δ and P are needed to make the set complete. From $P = nkT = (\gamma-1)\,\epsilon/2\pi r\delta$, where $\epsilon/2\pi r\delta$ is the internal energy per unit volume, it follows that

$$\delta = (\gamma-1)\,\epsilon/2\pi r P.$$

There are three contributions to pressure in the shocked layer; the magnetic pressure on the back

$$P_B = \frac{B_\theta^2}{8\pi} = \frac{B_o^2 r_o^2}{8\pi r^2},$$

the snowplow pressure on the front

$$P_S = \rho u^2 \cos^2\theta,$$

and the effective pressure caused by the centrifugal force from the plasma flow in the curved shocked layer

$$P_C = \frac{\sigma V^2}{2\pi r}\frac{d\theta}{ds}.$$

Equation 1 is just

$$P_B + P_S + P_C = 0.$$

The value of the internal pressure, P, will be taken to be the average of the front and back pressures, i.e.,

$$P = (P_B + P_S)/2.$$

This completes the set of equations describing the thin, stationary shocked layer. Equations 2 and 3 describe conservation of mass and momentum, respectively. Equation 4 describes the creation, absorption, and transport of internal energy. The first term on the right side gives the rate of production of internal energy on impact of the cold gas on the shock; the second term gives the rate of decrease of internal energy due to expansion during flow in the shocked layer. These equations appear somewhat different from the Rankine-Hugoniot relations because of the singularity of the model but in fact contain all of the same physics that survives in this limit.

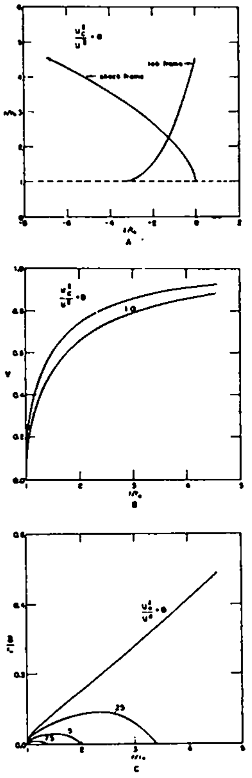

Fig. 29. Results of the steady-flow analytic model; A shows the shock configuration, B gives the flow velocity; and C the thickness of the shocked layer. (See text for details.)

If internal energy and pressure are disregarded and the centrifugal force term is dropped from Eq. 1, the remaining set of equations can be integrated analytically.[11]

This analytic result clearly resembles the physical solutions of the complete set of equations, but the thickness, δ, is lost and the lab frame characteristics are noticeably different. Since the purpose of this work is a comparison of theory and experiment, numerical solutions of the complete set are presented. These equations must be integrated starting at the singular point $s = 0$, $\delta = 0$, where $V = 0$ and $\sigma = 0$. When the equations are expanded about this singular point, the leading terms of θ, V, and σ, which are all proportional to $s^{\frac{1}{2}}$, are used to start the numerical integration.

Figure 29A shows the shock profile and the lab frame stream line (all other stream lines differ only by a z displacement), for the case of no internal cooling by ionization. (In Fig. 29 all dimensions are relative to the electrode radius, r_0.)

The effect of ionization cooling on these curves is almost negligible. The reason is apparent from Fig. 29B which shows the velocity of flow in the shocked layer, V, for zero and for total ionization cooling. Clearly the relative difference is small; the major contribution to V is from the oblique impact of unshocked material on the shocked layer, and not from pressure gradients within the layer. Since the only effect of internal energy on the shape of the shock is through V in the centrifugal force pressure term, the effect of changing ionization energy should then be expected to be small.

Figure 29C shows the predicted shocked layer thickness in units of the electrode radius for several values of ionization energy. On the curves for $u_c > 0$, δr_0 drops to zero at the same radius, indicating that, at this point and beyond, ionization cooling has reduced the internal energy, and therefore the layer thickness, to zero. This happens at large radii because the normal incidence velocity, and therefore the production of internal energy per unit incident mass, is less at larger radii whereas the ionization energy per unit mass remains the same.

Numerical Model

For the time-dependent model, a two-dimensional compressible hydrodynamics computing technique has been modified to include the effects of the magnetic pressure. The Particle-in-Cell[16,19] method is used because of its ability to calculate fluid flow in the presence of free surfaces. The fluid-magnetic field interface is treated as a free surface with an applied pressure representing the magnetic field pressure.

The Particle-in-Cell (PIC) method uses an Eulerian mesh of cells with Lagrangian particles to describe the fluid. The flow region of interest is subdivided into rectangular cells forming the computing mesh. Each cell is characterized by certain average values of the flow variables, such as pressure, density, specific internal energy, and velocities, in the two directions. The partial differential equations of motion are approximated by finite difference equations related to the mesh.

At the beginning of a problem, initial values of the flow variables are specified for each cell, together with the boundary conditions that govern flow behavior at mesh boundaries. The calculation proceeds in two phases. Accelerations are computed in the first phase neglecting the transport terms in the equations. From these are determined the cell velocities. In the second phase, the Lagrangian particles are moved with local fluid velocities. The movement of the particles makes up for the neglect of the transport terms because the particles carry along local values of momentum and energy.

In the calculations reported here, the fluid is assumed to be inviscid and non-heat-conducting with the flow confined to the radial and axial directions. The fluid is represented by a polytropic gas equation of state

$$P = (\gamma - 1) \rho \mathcal{E} ,$$

in which $\mathcal{E}$ is the specific internal energy. For an ideal gas, $\mathcal{E}$ is proportional to the absolute temperature. The calculations have been made for $\gamma = 5/3$, assuming that the fluid in the shock layer is completely ionized and dissociated.

The effect of the magnetic field is simulated by prescribing that, in an empty cell, the pressure is given by

$$P = \frac{B_o^2 r_o^2}{8\pi r^2} ,$$

where the zero subscript refers to the conditions at the electrode and r is the cell radius.

The boundary conditions are such that the electrode boundaries are rigid walls, whereas the radials and end boundaries of the mesh are continuative outflow ones. Through these boundaries, plasma is permitted to leave the computing region with minimal signal propagated into the mesh.

Initially, the gas is of uniform density, at rest, and cold with the exception of one cell at the intersection of the left boundary and the electrodes. This cell is void of particles and thus is assumed to be permeated with an azimuthal magnetic field. The initial pressure gradient generated by the field drives a shock into the fluid followed by a plasma-field interface.

Space limitations in the computer dictate that the calculations simulate the problem with a considerably shorter electrode than is used in the experiments. However, this is not a serious limitation because it is found that before the calculated shock layer has traveled a distance r_o along the electrode, it reaches a steady-state velocity. This result is based on the assumption of constant driving current. From the experiments, the driving current is found to vary rather slowly when the actual sheath traverses the region covered in the calculations. It is in this region, then, that the constant-current assumption is best satisfied.

After the sheath has reached a steady velocity, the dynamics in the vicinity of the electrode are independent of sheath position, and the calculations correspond closely to the equilibrium model.

When the sheath diffracts around the end of the electrode, again the calculations differ from experiment. The experimental electrode is hollow whereas the calculations consider it solid. This is not a serious difference because the sheath in the experiment is found to diffract around the end and remain attached to the inner surface, cutting the plane of the end normally. The free-slip, rigid boundary condition in the calculation does in fact have this same symmetry. In contrast, Mather[15] has found that the sheath, upon diffracting around the end of a solid electrode, drags along that surface. This effect is not included in the calculations because of the free-slip condition at that boundary.

The nature of the magnetic driving pressure on the interface accelerates the sheath until it implodes on the axis (see Fig. 30). When this occurs the plasma is compressed to a region so small that there are only one or two cells in the radial direction to resolve the flow. Fine structure cannot be discerned in this region. The calculated results exhibit only mean flow quantities averaged over a cell. Since fluid mass, momentum, and energy are conserved, however, the mean flow is represented accurately and the subsequent dynamics closely resembles that seen in the experiment.

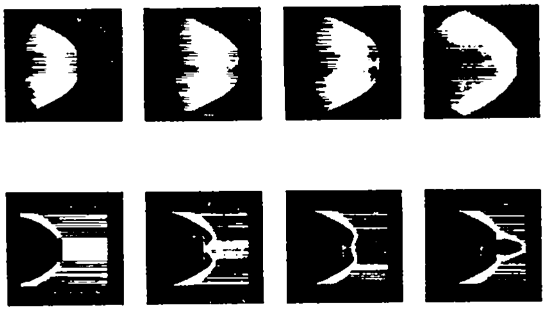

Fig. 30. Image-converter photographs (above) and PIC calculations (below).

Results and Comparisons

The discharge was photographed over a wide range of filling pressures, times, and currents with a fast image-converter camera. The studies were made most thoroughly with deuterium gas, and to some extent with argon. A typical series of photographs is seen in the upper part of Fig. 30; they were obtained using a 10-nsec exposure time for a discharge in deuterium at 2.0-torr filling pressure with a current just before spill over of 400 kA. The figure shows the luminous sheath at four different stages of the dynamics together with the corresponding PIC results. The latter are cylindrical cross-sectional plots of the Lagrangian particle positions at each time.

The first frame in Fig. 30 shows the luminous sheath as it moves along the inner electrode. In succeeding frames are seen the diffraction around the end, the pinch on the axis, and the bubble formation, respectively. This behavior is typical of the results over much of the pressure range covered. The luminous sheath usually has a sharp, smooth outer surface and intersects the electrode approximately at right angles. Some luminosity is visible on the electrodes, but this is usually weak compared to the sheath itself. Approximately at the time the sheath reaches the axis visibly, a burst of neutrons is produced in deuterium gas. The visible light from the pinch then disappears and the almost hemispherical bubble grows from the end of the pinch.

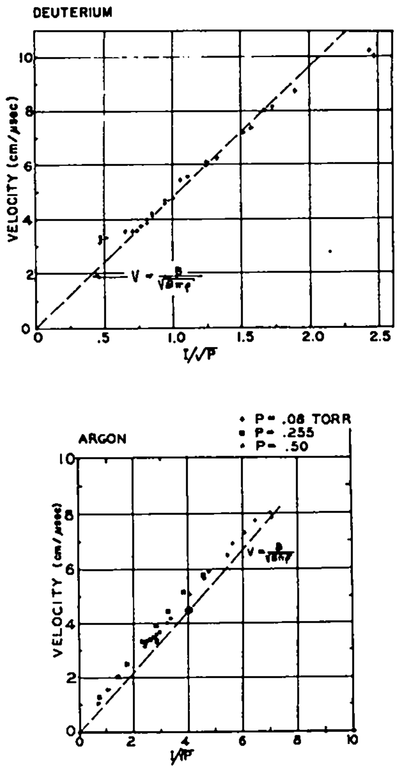

Fig. 31. Comparison of observed and calculated sheath velocities.

There is seen to be good agreement between experiment and theory over the time period of Fig. 30. In the last frame, however, the calculated bubble is not as hemispherical as the photographed one; this matter will be discussed later.

Extensive experimental data have been collected for the phase of the dynamics when the sheath translates axially along the electrode. Since this is the region where both theoretical models apply, the validity of the models can be ascertained by comparing the theoretical predictions with experiment.

Figure 31 summarizes the comparisons of snowplow model velocities with those measured in the experiments with deuterium and argon. In deuterium, the velocity was changed by changing the pressure, whereas in argon the gas pressure was set and the current changed by varying the voltage. Sheath velocities were determined by focusing two photomultiplier telescopes at points 10 cm apart on the electrode and determining the transit interval from oscilloscope traces. Results

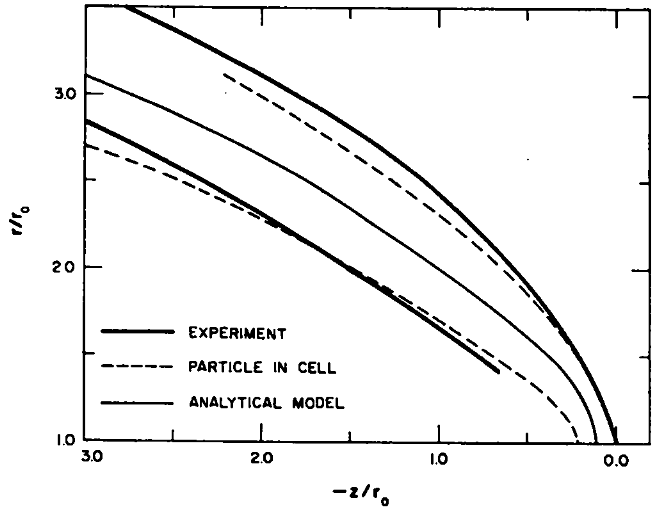

Fig. 32. Comparison of experimental sheath shape with calculations.

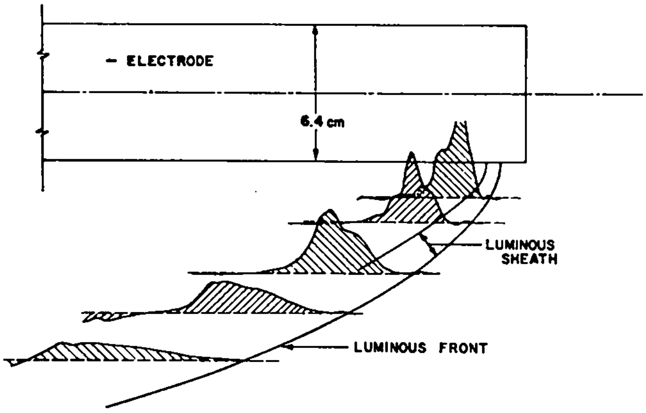

Fig. 33. Radial current density distribution at five positions.

from different shots are plotted against $I/\sqrt{P}$, where I is the current. This ratio is proportional to $B_0/\sqrt{\rho_0}$. The predicted velocities are given by the dashed lines which lie reasonably close to the experimental points, thus providing a justification for the theoretical approach for the equilibrium model.

Another comparison with experiment for the theoretical models is found in Fig. 32, which shows the sheath shape during the equilibrium phase. The heavy solid lines are taken from the holographic interferometry data of Fig. 36A for a discharge in deuterium at 0.45 torr filling pressure. The experimental field-plasma interface is the position of the magnetic piston as given in Fig. 37. The dashed lines represent the shock front and back interface, respectively, as determined from a PIC calculation. The light solid line is the shape predicted by the analytical model.

The experimental shape and PIC results agree well over the range shown. The PIC data give a narrower sheath with a more sharply diverging shock front than does the experiment. The analytical model follows closely the experimental shape and PIC calculations, with the shape agreeing better with the latter than the former.

The thickness predicted by the analytical model is not shown, because it is not in agreement with observation; the thickness given in Fig. 29C is too small. This discrepancy stems from the approximation of zero sheath width at the electrode surface. A more realistic treatment of the dynamics near the electrode demands a significant width there with correspondingly greater thickness everywhere downstream.

The magnetic field distribution in the vicinity of the sheath is obtained by means of magnetic probes. Figure 33 is a composite display of the results of magnetic probing at five different radii superimposed on the outline of the luminous sheath. The discharge occurred in deuterium at 0.43 torr filling pressure and a 240 kA current with a measured velocity of 10^7 cm/sec. The data were taken with a pair of small probes that fitted inside 3-mm o.d. glass tubing. The signal was displayed unintegrated and, thus, represents the magnetic field change at the probe position. Under the conditions of the measurement, the velocity of the front was essentially constant and therefore the probe signal is proportional to radial current density. By multiplying the time base on the oscilloscope by the sheath velocity, plots of the radial current density as a function of z were obtained and are displayed in the figure. Each probe measurement was correlated accurately in time with an image-converter photograph in which the relative positions of the probe and the luminous front could be seen clearly.

The photographs indicate a sharp break in luminosity on the interior of the visible sheath.

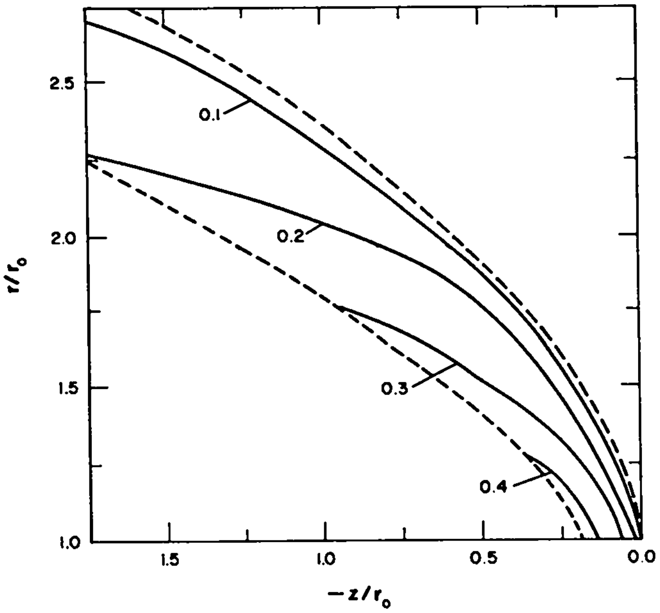

Fig. 34. Calculated isotherm contour plots within sheath in equilibrium phase.

Most of the current is found to flow behind the luminous region, implying that the luminosity is due to the gas dynamic shock ahead of the magnetic field region. Interferometer results show that the plasma density is small in the region where the current flows. Thus, to a large extent the field is excluded from the plasma in the sheath. The traces at the larger radii go negative in value although it is unlikely that the current does so. This is due to experimental error ; the probe signals are small at these positions and the probes themselves are poorly shielded because of their small size.

In Fig. 34 are seen the calculated isotherm contour plots of the sheath as it moves with the equilibrium velocity along the electrode. The dashed lines represent the shock front and the plasma-field interface, respectively. The solid lines are the isotherms (lines of constant specific internal energy). The shock front and interface positions are determined from the particle plots whereas the contours are obtained from the print-outs of the specific internal values. It is seen that the temperatures decline from a maximum at the field-plasma interface near the surface of the electrode to lower values toward the shock front and away from the electrode. At a given radius, the highest temperatures always occur at the interface.

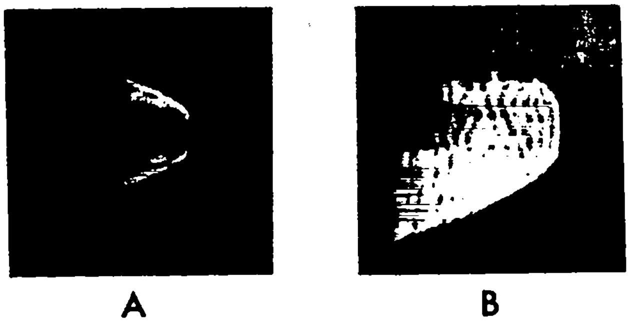

Fig. 35. Photographs of snowplow discharge in D_2 at 30 torr (A) and Ar at 0.09 torr (B).

The contour 0.4 corresponds to a thermal energy of 56 eV for deuterons in a sheath with velocity of 10^7 cm/sec. This plot shows that dissociation and ionization of deuterium in the sheath is expected to be complete for the ranges shown in the figure. But since a decline in temperature is observed with increasing distance along the sheath, these processes may not be complete in all regions of the sheath. The results are taken from a calculation with 16 cells across the electrode radius. Another calculation with 8 cells across the radius produced slight changes in the positions of the contours, but there were no significant modifications. Thus, no attempt has been made to adjust the contours for a zero-cell size extrapolation.

A departure from the smooth, sharp appearance of the sheath is noted for experiments carried out with deuterium at filling pressures significantly greater than 1.0 torr. Such a case is shown in Fig. 35A, where the filling pressure was 30 torr with a 500 kA current. The luminous sheath is streaked and does not have the usual paraboloidal shape. Another departure is observed with argon at 0.09 torr filling pressure as seen in Fig. 35B; the current was 420 kA. This sheath, while retaining a paraboloidal shape, has ripples on its surface.

The full explanation of these phenomena is not certain. However, one contributing factor is present in both cases: the temperatures in the sheath produced by the gas dynamic shock are not expected to be high enough to accomplish complete ionization of the gas. With deuterium at 30-torr filling pressure, the front velocity is lower by a

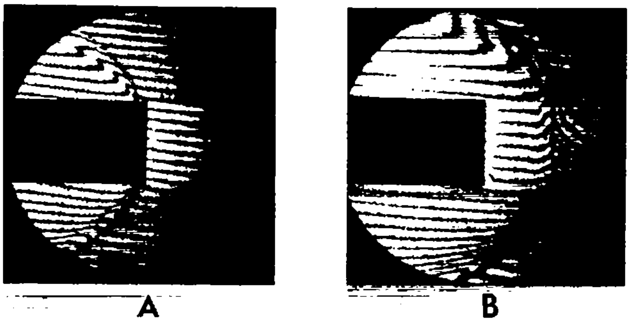

Fig. 36. Interferograms of snowplow discharge in D_2 at 0.45 torr (A) and 1.10 torr (B).

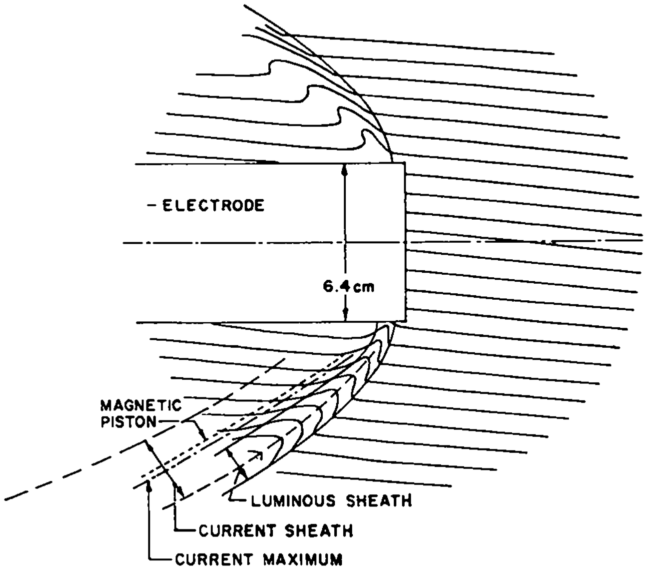

Fig. 37. Tracings of interference fringes of Fig. 36A with outlines of luminous sheath and current from Fig. 33.

factor of ∼ 3 than for the 2.0-torr case with 400 kA driving current. Since the specific internal energy scales as the square of the velocity, a decided effect is expected in the degree of ionization and conductivity of the sheath. For argon, the ionization energy is quite large, and again the degree of ionization is expected to be lower than for the 2.0-torr deuterium. With lower ionization and conductivity, the magnetic field boundary is more diffuse, and the snowplow will not be as effective. This is believed to alter the sheath appearance.

Typical interferograms showing the plasma distribution at two different phases of the dynamics for deuterium at two different filling pressures are given in Fig. 36. Frame A shows the fringe shifts for the sheath before it diffracts around the end for a 0.45-torr filling pressure (190 kA current). Frame B displays the fringe shifts for the sheath and bubble after the pinch has formed on the axis for 1.10-torr pressure (200 kA current). Quantitative information concerning electron density has not been extracted from these integrated densities because of the uncertainties of an Abel inversion. The situation at 1.10-torr pressure is further complicated because the electron density gradient is very high and the fringes cannot be followed through the front.

For 0.45 torr, the fringes can be followed through the front and tracings of these are seen in Fig. 37. In addition, the outlines of current and luminous sheaths in Fig. 33 are superimposed on the fringes. The position of the magnetic piston is determined by integrating the current density traces, then obtaining the magnetic pressure profile, and defining the position as the locus of points of half-maximum of these profiles.

A qualitative comparison has been made of these fringe shift data with a PIC calculation. A traverse through the sheath at a radius of 1.5 r_o to a point midway into the sheath produces a fringe shift deduced from the calculations that agrees to within a factor of 1.5 with the experimental shift, the calculated shift being the greater. This is consistent because the calculations show a narrower sheath with a higher density than the experiments in Fig. 32.

Rapid changes in the terminal current are seen to occur when the sheath reaches the end of the electrode and implodes on the axis. Typical oscillograms of the terminal current are shown in Fig. 38. The data are taken from two different shots with deuterium at 0.45-torr filling pressure. Trace (a) shows the overall history of the current; it depicts the initial current buildup and the sudden decrease associated with the rapid change in the inductance of the system when the pinch forms. Trace (c) shows the current behavior on an expanded time scale for the pinch phase, with the corresponding scintillator neutron signal as trace (b).

There are two bursts of neutrons for the shot recorded. Sometimes there is only one burst, but frequently there are two or more separated by

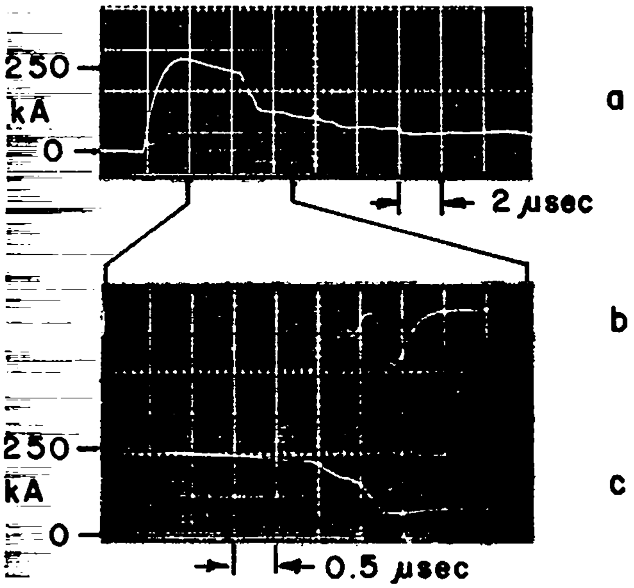

Fig. 38. Oscillograms of snowplow discharge in deuterium; (a) terminal current, (b) scintillator neutron signal, (c) terminal current. Trace (a) is from a different discharge than (b) and (c).

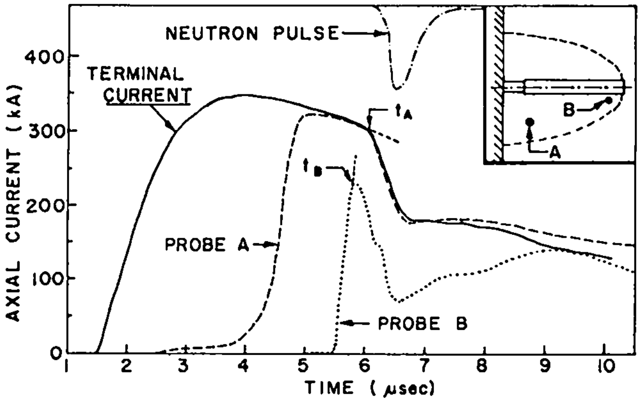

Fig. 39. Current and neutron pulse history from a discharge in deuterium.

a few tenths of a μsec. Each burst is associated with a sudden decrease in current. The implication is given that the electromagnetic energy is converted to heat energy in the pinch and a burst of neutrons is produced.

Figure 39 summarizes the data for the terminal current, the axial current obtained by use of magnetic probes, and the neutron pulse for a discharge in deuterium at 0.50 torr. A single neutron pulse was recorded. The inset indicates the relative positions of the two probes. The sudden decrease in axial current resulting from spillover at the end occurs earlier in the probe near the tip than it does in the probe near the terminals. These data provide some information on the plasma density in the magnetic field region inside the current sheath. The disturbance takes ~0.25 μsec to travel the 45-cm distance between probes. This implies an Alfvén velocity, $V_a = B/\sqrt{4\pi\rho}$, of 1.8×10^8 cm/sec in a magnetic field of ~19 kG (the field at the surface of the electrode where the velocity is highest). Assuming a uniform plasma density in this region, the derived density is 9×10^{-10} g/cm^3, a value two orders of magnitude less than the initial filling density. This gives further indication that the snowplow action is quite effective.

Quantitative experimental information from the diagnostics is difficult to obtain after the sheath reaches the end of the electrode. The PIC calculations provide additional information that helps to explain the dynamics during this phase of the problem. The radial collapse velocity of the plasma-field interface is readily available from the calculations. In Fig. 40 is plotted the scaled radial position of that interface as a function of the scaled time; τ is given in units of time necessary for the sheath to travel a distance r_o when moving with equilibrium velocity and τ_e is the time in the same units at which the interface reaches the end of the electrode. The final slope of the curve yields a velocity ~ 4.5 times the equilibrium velocity, in agreement with the measurements of Mather.[23] The temperatures estimated at collapse time using this radial collapse velocity are > 20 times larger than those in the equilibrium sheath.

In addition to the collapse velocity, the calculations give insight into the processes taking place during the pinch and "bubble" formation phases. The phased implosion along the axis as a result of the collapsing curved sheath forms an axial filament ~ 2 r_o in length in a time increment $\Delta\tau = 0.15$ unit (i.e., 0.5 μsec for a sheath velocity of 10^7 cm/sec and $r_o = 3.18$ cm). The length here assumes symmetry about the end plane of the hollow electrode. High pressures in the filament produce an axial gradient that accelerates the plasma, forming a jet. The tip of the jet expands upon penetrating the collapsing sheath front and forms the bubble.

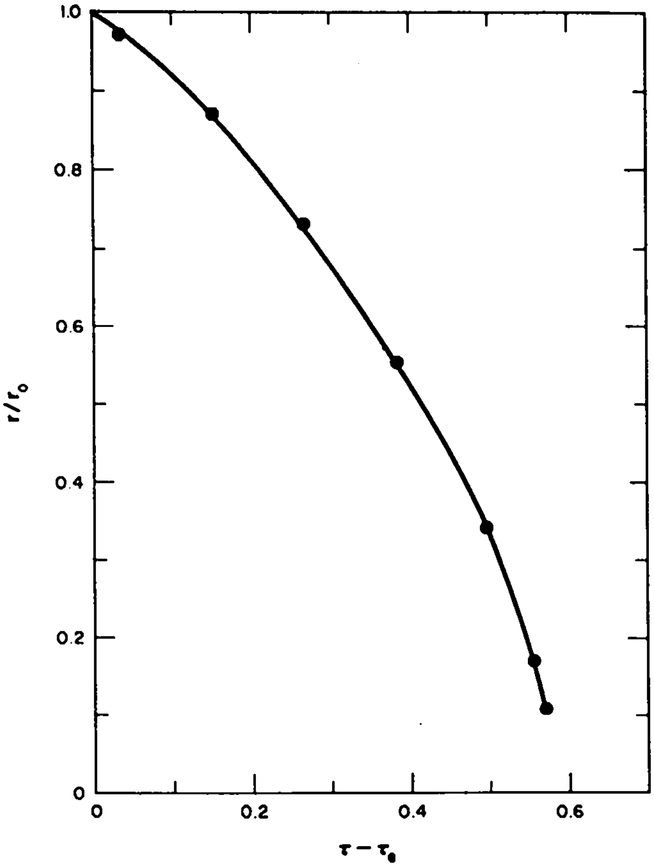

Fig. 40. Radial position of the plasma-field interface vs scaled time.

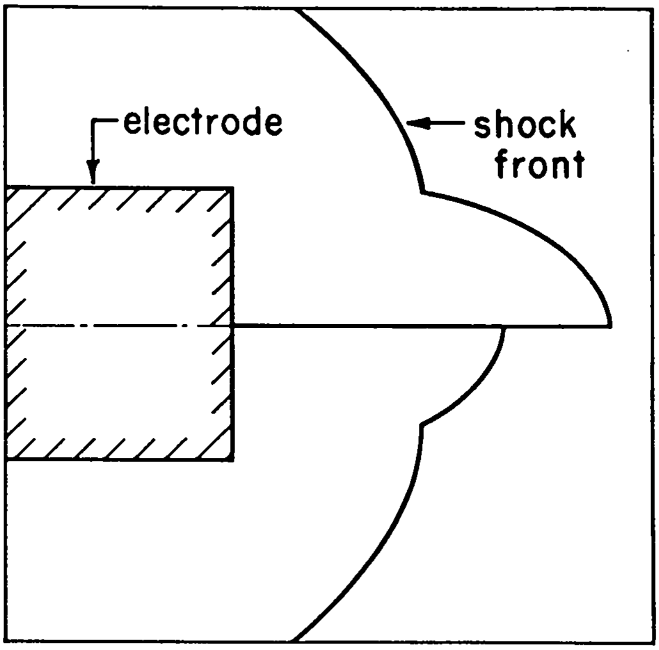

Fig. 41. Shock front outlines of sheath and bubble at same time from two-PIC calculations.

As mentioned earlier, the bubble shape in the final frame of Fig. 30 differs from the experimental one. The difference results from the calculational assumption of constant driving current throughout the phases of collapse and bubble formation. Experimental current traces show a sharp decrease in terminal current at collapse time, a violation of the constant current assumption. This is apparently caused by the large increase of inductance with decreasing pinch radius. In order to determine the effect of this on the calculated results, two calculations were performed that were identical except that in one the current was set to zero at collapse time. The results are summarized in Fig. 41. The upper portion of the figure shows the outline of the shock front on both the sheath and the bubble for the constant-current case. The lower portion shows this outline at the same relative time for the calculation with no current after collapse time. Whereas the sheath itself is unaffected by the change at this time in the calculation, the bubble in the latter case lags behind in both radial and axial expansion and is more hemispherical in shape. The experimental current traces do not show the current vanishing, but the observed shape is more closely approximated by the calculation with no driving current after collapse.

As a further indication that the numerical description of the bubble formation is approximately correct, it is noted that the calculated bubble intersects the sheath, trapping plasma at the intersection and creating a ring of high-density plasma. This region of high density is also clearly seen in the interferogram of Fig. 36B, where a portion of the bubble is shown with large fringe shifts in the region of the intersection.

Conclusions

Removal of the outer electrode from the coaxial plasma accelerator permits the use of a variety of diagnostics for investigating the plasma distribution. The dynamical distribution is clearly seen using image converter photography and the holographic interferometry technique.

The luminosity of the plasma sheath as it propagates along the electrode is found to be produced mainly by the gas dynamic shock wave. In most cases studied, the sheath is smooth and well defined with most of the current flowing behind the luminous region. However, two cases are presented in which the smooth, sharp appearance is not in evidence. The full reason for this change is not known, but analysis of the modified PIC results shows that ionization may not be complete for the plasma in the sheath, resulting in a low conductivity, a more diffuse current layer in the sheath, and insufficient snowplowing at the interface.

The sheath spills over the end of the electrode and pinches on the axis. With deuterium filling, a burst of neutrons is produced at this time. Subsequent dynamics show a rapidly expanding hemispherical bubble formed at the end of the pinch.

Comparisons of the predictions of the theoretical models with experiment have demonstrated the applicability of fluid models in plasma research involving high-density plasmas. The analytical model predicts the shape and qualitative properties of the sheath during the equilibrium phase of the dynamics.

The plasma distribution calculated with the modified PIC model compares favorably with experiment for all phases of the dynamics. This is an indication that further quantitative studies can be made with this technique. The model could be further enhanced by adding the following straightforward refinements: (1) allowing a finite plasma conductivity with a diffusing magnetic field, (2) coupling the circuit equations to the magnetogas-dynamic equations, (3) zoning the mesh finer in the vicinity of the z-pinch, and (4) using a more realistic equation of state for the plasma.

References

1. J. Marshall, Phys. Fluids 3, 134 (1960).
2. L. C. Burkhardt and R. H. Lovberg, ibid., 5, 341 (1962).
3. J. Marshall and T. F. Stratton, Nuclear Fusion Supplement Part 2, 663 (1962).
4. J. W. Mather, Phys. Fluids Suppl. 7, S28 (1964).
5. J. Marshall and I. Henins, Plasma Phys. and Cont. Nucl. Fusion Research (International Atomic Energy Agency, Vienna, 1966) p. 449.
6. R. D. Butler, J. L. Cook, and R. L. Morse, Proc. APS Topical Conf. on Computer Simulation of Plasma, LASL Report LA-3990, Paper C-6, 1968.
7. R. M. Patrick, Phys. Fluids 2, 589 (1959).
8. N. H. Kemp and H. E. Petschek, ibid., 2, 599 (1959).
9. P. J. Hart, ibid., 5, 38 (1962).
10. J. C. Keck, ibid., 5, 630 (1962).
11. F. J. Fishman and H. E. Petschek, ibid., 5, 632 (1962).
12. R. H. Lovberg, ibid., 8, 177 (1965).
13. J. W. Mather, ibid., 8, 366 (1965).
14. T. N. Lie, et al., ibid., 10, 1545 (1967).
15. J. W. Mather and P. J. Bottoms, ibid., 11, 611 (1968).
16. T. D. Butler and J. L. Cook, ibid., 11, 2286 (1968).
17. F. C. Jahoda, R. A. Jeffries, and G. A. Sawyer, Appl. Optics 6, 1407 (1967).
18. L. O. Heflinger et al., J. Appl. Phys. 37, 642 (1966).
19. A. A. Amsden, LASL Report LA-3466 (1966).
20. L. Spitzer, Jr., "Physics of Fully Ionized Gases," Interscience Publishers, 1962.
21. S. C. Brown, "Basic Data of Plasma Physics," MIT Press, 1967. 2nd ed. pp.43, 72.
22. C. L. Longmire and M. N. Rosenbluth, Phys. Rev. 103, 507 (1956).
23. J. W. Mather, private communication.

A PULSED GAS VALVE FOR FAST TIMEABLE HIGH PRESSURE OPERATION

(I. Henins and J. Marshall)

Introduction

A need exists in plasma experiments for a pulsed valve capable of the admission of known amounts of gas into an evacuated system in times short compared to those required for molecules to move across the system. A typical application is in the feed to a coaxial plasma gun where it is desirable to fill the space between the gun electrodes with gas, while the rest of the system remains at high vacuum. In the past, the amount of gas required has been modest (1 cm^3-atm, for example) and several types of valve have been suitable. Some of these have been operated by mechanical hammers[1], some have been driven electromagnetically[2,3], and a precisely timeable valve driven by thermal expansion of a metal tube after pulsed electrical heating has been developed at LASL[4]. Many of the electromagnetically operated valves have relied on the reproducibility of a short open time as a means of determining the amount of gas admitted. For the present purpose, however, it has been found preferable to do this by a plenum, which is filled slowly between shots to a definite pressure, and completely emptied when the valve is opened. The requirement for repeatability with such a valve is simply that the speed of opening be fast enough so that minor variations do not affect the emptying time appreciably relative to other functions of the experiment.

The simplest valve to build and operate has been one held shut with a spring and opened with a hammer blow. A hammer is not normally precisely timeable in advance, but when hammer contact precedes all other experimental events, a timing signal can be generated by electrical contact between hammer and the valve stem, so that electronic delay systems can initiate electrical discharges at approppropriate times. An additional delay of a few hundred μsec between hammer contact and valve opening is introduced by sonic delay in the steel valve rod. For cases in which the valve must be synchronized with other equipment, such as the rotating prism in a Q-spoiled laser, it has been possible to use a hammer driven by an electrically exploded foil.

The need has arisen in the development of high-energy plasma guns, however, for a valve capable of the admission of much larger amounts of gas, up to several hundred cm^3-atm. It does not appear to be desirable simply to increase the size of the valve plenum, while filling it to the same pressure as before (1-3 atm), because this increases the emptying time. The alternative of increasing the plenum pressure was inapplicable in existing valves because they are usually held shut against gas pressure by elastic forces which are overcome by the actuating impulse. To seal against higher plenum pressures, these forces must be increased. Therefore, both the opening impulse and subsequent reclosing impact would be more violent and likely to be destructive.

The valve described here is adapted to high gas pressure operation because it is kept closed by a large force which is removed to open it. Thus, the plenum can be small and can have relatively fast emptying time. The opening rate is comparable to or faster than that realizable with a mechanical hammer. There is no possibility of damage during reclosure, since the valve does not slam closed again after opening, but is closed slowly just before the next operation.

Principle of Operation

The rapid motion required for fast opening derives from energy stored elastically in an axially compressed nylon rod. A hydraulic jack is used to exert about 200 atm pressure which compresses the rod by about 0.7% from its original length. The force also makes a good gas seal between the far end of the nylon and the mouth of the plenum, with no additional gasketing being necessary. To open the valve, the force of the jack is removed suddenly by destroying an expendable support. This is done in a timeable way by electrically exploding a wire passed through a hole along its axis.

With the compressive force nearly instantaneously removed from one end of the nylon rod, a rarefaction wave moves along it at the speed of sound, $c = \sqrt{E/\rho}$, where E is the elastic modulus in dynes/cm^2, ρ is the density in g/cm^2, and c is in cm/sec. Ahead of the wave, the rod remains compressed and at rest. Behind the wave the compression has been removed and that part of the rod is moving with uniform axial velocity toward the place formerly occupied by the support. If the rod is L cm in length, the time for the rarefaction wave to travel its length is L/c sec. The length of the rod was shortened by the applied pressure p by an amount $\Delta L = pL/E$. At the instant when the rarefaction wave has reached the other end of the rod, the entire rod has been returned to a state of zero compression, and has therefore returned to its original length. The velocity of the near (support) end is then the change of length due to the compression divided by the time for the wave to travel the length of the rod

$$V = \frac{\Delta L}{L/c} = \frac{pL}{EL}\sqrt{\frac{E}{\rho}} = \frac{p}{\sqrt{E\rho}} = \frac{p}{c\rho}. \qquad (1)$$

It is seen that, as might be expected, the velocity is proportional to the released pressure. It also varies inversely with the density, but somewhat less obviously it varies inversely with the velocity of sound in the rod. To achieve high velocities, the rod should be made of a material capable of withstanding large compressive forces, but with a low density and a low sound velocity. Plastic materials such as nylon are ideal for the purpose. In order for the valve to remain closed against plenum pressure the compressional force in the rod must be greater than the force exerted against the end of the rod by the gas pressure in the plenum. Since the area of the plenum is less than that of the rod, a rod compression pressure equal to the gas pressure should be adequate. It would appear then that for gas pressures under 300 atm, nylon has sufficient strength. Tool steel could produce the same velocities, but would require something like 23 times the pressure necessary for nylon. If gas pressures up to 600 atm were needed, tool steel might be more appropriate. A simplified diagram of the valve design is shown in Fig. 42.

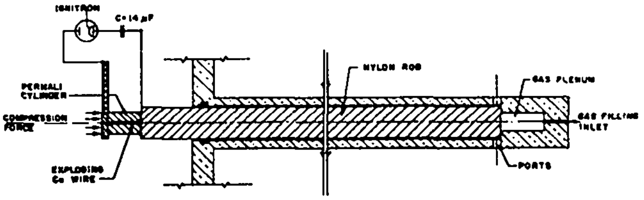

Fig. 42. Simplified diagram of valve.

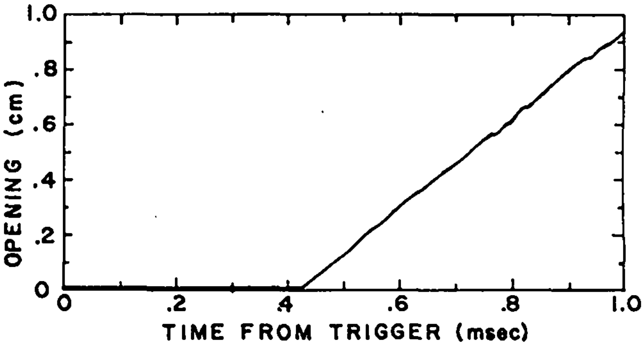

Fig. 43. Optical measurement of motion of far end of nylon rod. (Fluctuations are due to photon statistics.)

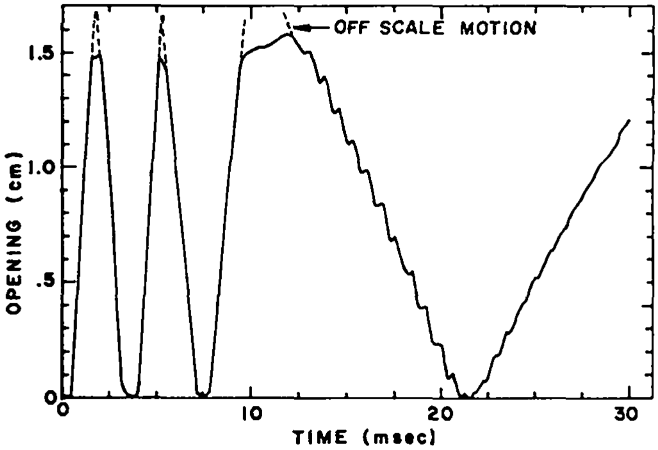

Fig. 44. Slow sweep oscillogram of same signal as in Fig. 43.

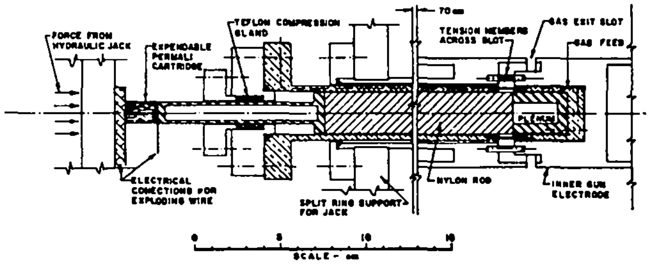

Fig. 45. Diagram of working valve.

Model Measurements

A working model with no valve, but including a plastic rod with a hydraulic jack to apply pressure to it, was made and instrumented optically, to check that actual operation would be as predicted. A number of methods for removing the compressive force from the rod were considered, and some involving breakable glass supports were tested to some extent; however, the present method proved most satisfactory. It uses an expendable Permali (phenolic impregnated wood) cylinder which is shattered by an electrically exploded wire. In order to keep the rod from buckling under compression, it was encased in a loosely fitting metal tube, which was in tension when force was applied to the rod. The force on the rod was determined by measuring the cylinder pressure of the jack. A slit system was attached to the far end of the rod from the removable support, illuminated, and observed with a photomultiplier so as to give an output signal approximately linear with rod position. Typical results are shown in Fig. 43; they apply to a rod of 68.2-cm length, 18.67-mm diam, compression force 7.86 x 10^8 dynes, and opening rate 16.5 m/sec. The oscilloscope sweep started at trigger time of the exploding wire ignitron. On the time scale of the oscilloscope trace, the removal of the support is nearly instantaneous, although it has a ~ 60-μsec delay. After an appropriate delay for sound transit time, the far end of the rod experiences a very large acceleration to a full velocity of 16 m/sec. No comparable observations of far end motion have been made on a working valve because of inaccessibility. The slower sweep in Fig. 44 shows the rod to bounce several times from the jack platen. This is felt to be undesirable in a valve and therefore has been eliminated in the working design.

From these oscillograms the measured velocity of sound in nylon and the speed of motion of the rod are 1.63 x 10^3 m/sec and 16.5 m/sec, respectively. By using the observed sound velocity, the measured compressive pressure (2.87 x 10^8 dynes/cm^2), and the measured density of nylon (1.15 g/cm^3), Eq. 1 gives a rod velocity of 15.3 m/sec. This appears to be in satisfactory agreement with the observed velocity.

Working Valve Design

A working valve design is shown in Fig. 45. Complication results from the necessity to feed gas to a plenum beyond the valve opening, the need for a labyrinth to protect the valve seal from the high current gun discharge, and the desirability to have a removable plenum for maintenance and volume changes. Gas is fed through hypodermic tubing to the part of the inner assembly beyond the opening. A small O-ring seals the gas feed to the bottom of the plenum which is held in place by three small screws. Eighteen 3-mm diam stainless steel tension members, hard-soldered across the exit slot, support the muzzle end of the center electrode, carry current, and take the tension necessary to compress the 2.5-cm diam nylon valve rod. The compression force is transmitted to the rod through a stainless steel plunger, which passes through a Teflon compression gland vacuum seal. The friction of this sliding seal is sufficient to damp the motion of the rod before it bounces on the jack platen during operation. This same friction also reduces the effective change of compressive force responsible for valve operation, but even so the motion remains fast enough for practical purposes.

The expendable cartridge which relieves the compression is cut from 1.27-cm diam Permali rod in ~2-cm lengths. The cartridge is destroyed by the explosion of a 0.25-mm diam copper wire passed through a 1.8-mm diam hole drilled through the cartridge along its axis. The wire is bent over at the ends to make electrical contact; the hole is sealed with a dab of modeling clay and filled with water using a hypodermic syringe. The water provides coupling between the wire explosion and the Permali and possibly also adds additional expanding gas. Permali is chosen because its wood grain structure, parallel to the axis, allows it to shatter into suitably fine filaments for complete and reliable removal of support. The cartridge has not been tried without a water filling; presumably it would still disintegrate, but less rapidly.

Contact to the explodable wire is provided, on one end by a strip of metal foil, and on the other by a metal plate fastened to a phenolic jack

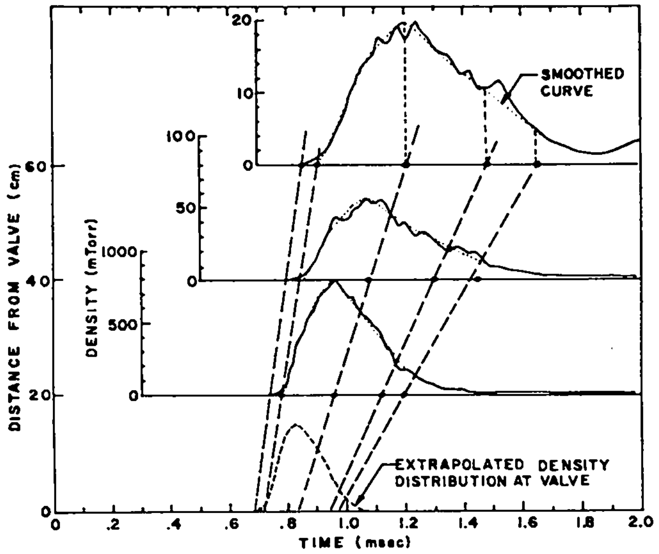

Fig. 46. Time-resolved gas density measurements at various distances from the valve.

platen. A 15-μF capacitor, charged to 10 kV, and ignitron switched, is used to explode the wire . The explosion produces a considerable amount of fine high-velocity shrapnel which has the appearance of being fine splinters of the wood from the Permali. Protection is placed around the cartridge to prevent damage to surrounding equipment. Observations of near-end rod motion indicate that the compressive force is suddenly relieved ~ 60 μsec after ignitron trigger time.

A 5-ton hydraulic truck jack is used to compress the rod. It is provided with a pressure gauge and is normally operated at 100-atm oil pressure, which produces a compressive force of 1.2 tons. The nylon rod has a 2.5-cm diam so that the compressive pressure is 2.4×10^8 dynes/cm^2, giving a calculated rod velocity of 11.6 m/sec. The observed velocity is ~ 7 m/sec, presumably because of friction in the vacuum seal and mass loading by the stainless steel plunger.

Performance

The emptying time of the valve has been investigated with a 6AH6 fast ion gauge[5]; the results are summarized in Fig. 46. The opened gauge tube was mounted on a sliding probe stem, so that it could be placed in a variety of positions along the axis of a large vacuum tank (1.2-m diam, 3.1-m long). The gauge was oriented so as to allow as nearly as possible direct flow into the interelectrode spaces. The valve was mounted as shown in Fig. 45 in the gun electrode assembly at the center of the tank, with the axis of the tank lying in the plane of the annular gas exit slot. The ion gauge signal is not perfectly smooth, but is modulated by an irreproducible turbulent flutter. However, if a reasonably smooth curve is drawn through the signals obtained at various distances, features, such as first appearance, peak density, and half-density times, appear to relate to each other as though the molecules were moving from the valve in straight lines with unique velocities at any point in time and space. This is consistent with the assumption that the gas has cooled during its expansion through the valve opening, so that its temperature is very low compared to the streaming molecular energy. In any case it allows a reasonable extrapolation back to the valve position and an estimate of the emptying time, as has been done in the figure.

Measurements were made with two different plenum volumes at two pressures with deuterium, which is the gas expected normally to be admitted with the valve. The emptying time depends on plenum pressure and volume, being shorter at high pressure, and longer with a large plenum volume. The valve cannot be conveniently tested by itself without the surrounding electrode structure but it is believed that the empyting time is more a result of the protective labyrinth than of the speed of withdrawal of the nylon valve stopper. With a 1-cm^3 plenum, the emptying time is ~ 200 μsec with 35-atm deuterium pressure, and 320 μsec with 3.5 atm. With a 10-cm^3 plenum it is 770 μsec with 3.5-atm filling pressure .

The flow beyond the gas exit slot is highly supersonic and shock waves are frequently observed, particularly at high plenum pressures. No attempt has been made to study these shocks.

References

1. J. Marshall, in "Plasma Acceleration," S.E. Kash, ed., Stanford University Press, 1960, p.61.
2. B. Gorowitz, et al., Rev. Sci. Instr. 31, 146 (1960).
3. E. Knapp and A. Williams, LASL Report, LA-2978 (1963).
4. I. Henins and J. Marshall, U.S. Patent No. 3281324.
5. J. Marshall, Ref. 1, p. 62.

CROSS FIELD INJECTION

(J.E. Hammel, A.R. Sherwood, R.W. Kewish)

Introduction

The question of how a collisionless plasma stream enters a transverse magnetic field arose after the first experiments on transverse injection were performed several years ago. Simple MHD theory does not allow a collisionless plasma to go into the field from zero field. The possibility of anomalous resistivity providing a sufficiently short penetration time to agree with observation is unlikely since the minimum resistivity needed would be of the order of a hundred Ω-m.

In the past, a steady-state solution to the entry problem has been considered because of the experimentally observed fast stream 1 to 2 m in length flowing more or less uniformly in the high-field region. Models have been tried utilizing the nonadiabatic motion in the low magnetic field at the entrance. A steady state flow of this type does not seem easy to attain (see p.112 of this Report).

Most previous measurements on the injected stream have been made well inside the field volume. In the present experiments an attempt is made to find the E-field in the region of the vacuum field null where the stream first encounters the magnetic field.

Nitrogen Plasma Stream

The first measurements were made with nitrogen as the working gas; first, because the visible light might give a view of the path of the fast plasma (fast hydrogen plasma is invisible), and, second, the heavier ion might expand the nonadiabatic region in which the entry takes place. Image-converter pictures were taken and the amount of light produced by the fast plasma during the longest exposure (1 μsec) was again so small that no flow pattern could be recorded. The light from a magnetic probe placed in the stream was clearly visible. An array of ten electric probe pairs was used to obtain the E-field pattern. Direct interference with the plasma stream is avoided by placing the probe pairs outside the stream. The probe connection with the plasma stream is along a magnetic field line with the usual assumption being made that $E_{\parallel} = 0$ for the time scale of interest. Several array configurations were used and two of these are shown in Fig. 47. The arrangement in Fig. 47(a) has the first vertical probe pairs placed at the vacuum magnetic field null. The E-field measured along the null by these three pairs was essentially zero. The pair indicated by β off the null showed a small signal.

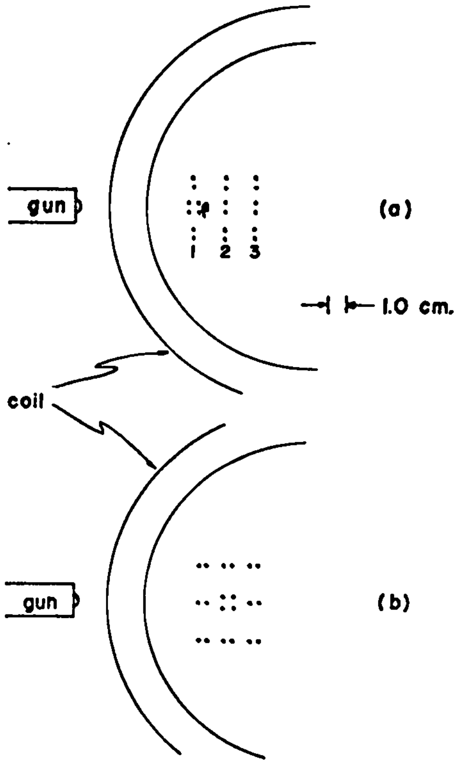

Fig. 47. Arrangements of ten electric probe pairs. (a) Vertical probes, (b) horizontal probes.

Since $\dot{B} \approx 0$ even in the entry region, curl E = 0 implies E-fields along the stream direction with opposing directions on opposite sides of the stream. The horizontal probes in Fig. 47 (b) were placed in a position to measure these fields along the flow direction. Probe signals taken from the opposite sides of the stream are shown in Fig. 48(a) and (b). For fields well below the cutoff (~10 kG) these signals are on the average what is expected from curl E = 0 and E = 0 at the null. The probe on the lower side has a signal (Fig. 48(b)) which starts "negative" and rapidly changes to the expected direction. An effect which is in agreement with these signals is a preliminary

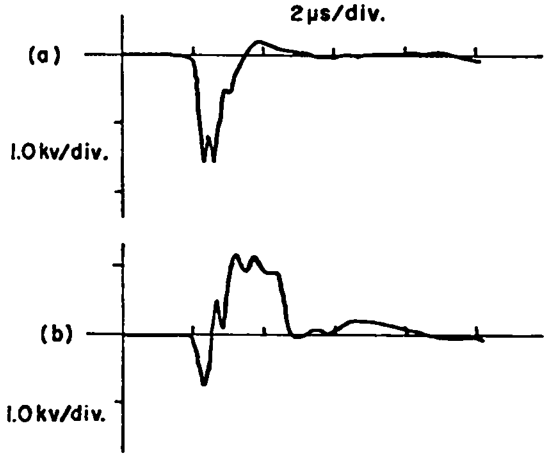

Fig. 48. Electric probe signals from horizontal probes: (a) upper probe, (b) lower probe, in N_2.

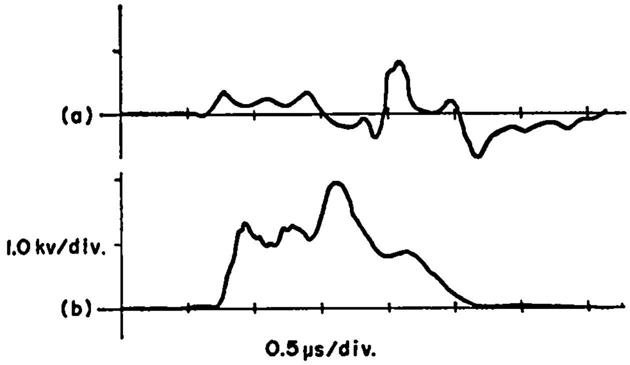

Fig. 49. Electric probe signals of vertical component of E; (a) where magnetic field first encountered, (b) well inside the field, in D_2.

field which arises from the ions going ahead of the electrons when the field is first encountered by the stream. This field then flips over into the field configuration which is the E-field of the drifting stream. The top probe signal remains unidirectional as it should (Fig. 48(a)) , according to this effect.

Deuterium

The gas in these preliminary experiments was changed to deuterium since the properties of the deuterium plasma are much better known from previous experience. Again the probe pairs placed to intersect the null gave a zero E-field and the pair downstream from the null gave a significant signal. A search was made for a reversal of the lower probe signal such as that seen with nitrogen but no evidence of this could be found.

The probe arrangement shown in Fig. 47(a) has a much larger effective separation than the 2.5-cm physical spacing, since distances must be mapped along the magnetic field lines into the plane of the plasma stream. This makes the effective probe separation 18 cm between probe sets 1 and 2,and 7 cm between probe sets 2 and 3. It is found that the fine structure of the E-field signal cannot be correlated from one probe to the next over these large distances. In fact, the character of the signal changes from an oscillating, highly structured signal at the probe just off the null to a sharply rising, somewhat rectangular pulse of about 2-µsec duration at the position 3. Figure 49 illustrates this effect with (a) the signature at Position 1 and (b) at Position 3.

A series of runs was then initiated with an actual probe separation of 0.5 cm. With this close separation, the structure of the voltage pulse could be followed as the stream moved past successive probes. The development of the sharply rising front could be traced from the rather oscillatory beginnings. These data are still being examined for more detail.

I. Henins and J. Marshall at LASL found it to be of great value to measure the flow of flux past a probe pair by integrating the voltage signal with time. It was suggested that the flux flow signals might be more easily interpreted than those of voltage with their large amount of structure. The voltage signals between far points of the probe array in Fig. 50 were integrated. Figures 51 and 52 show the results of these measurements for two cases. A positive signal is a flux flow through the probe pair into the volume defined by the field lines connected to the array ($E_{\parallel} = 0$ is assumed). It is found that the sum of the voltage around the array is zero at all times within 10%. At fields below 7 kG the flow was that shown in Fig. 51. At fields above 7 kG a typical flow is that shown in Fig. 52. The low-field result shows a net flow in the front and sides and out the back of the array. The high-field data are more difficult to interpret and it

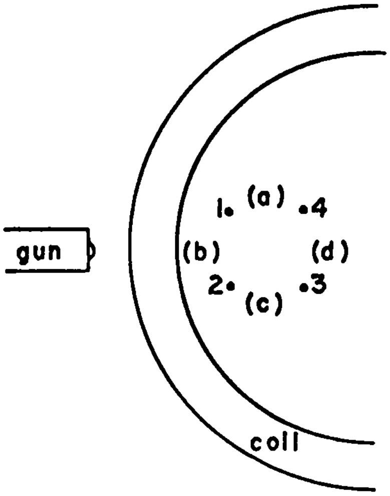

Fig. 50. Probe array for magnetic flux flow measurement. The integrated voltage signal is measured between (a) 4,1; (b) 1,2; (c) 2,3; (d) 3,4.

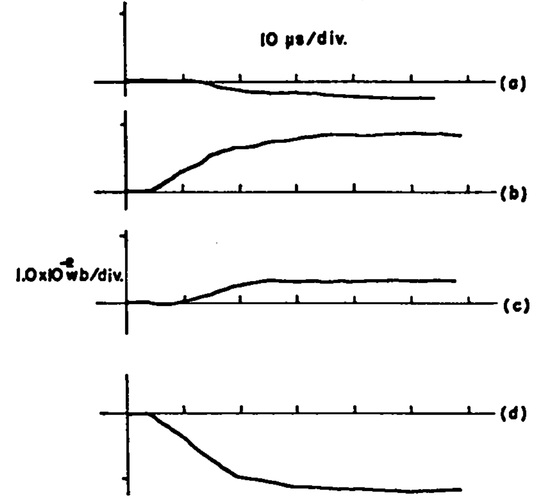

Fig. 51. Examples of flux flow (integrated voltage) between probe pairs for B = 3.4 kG.

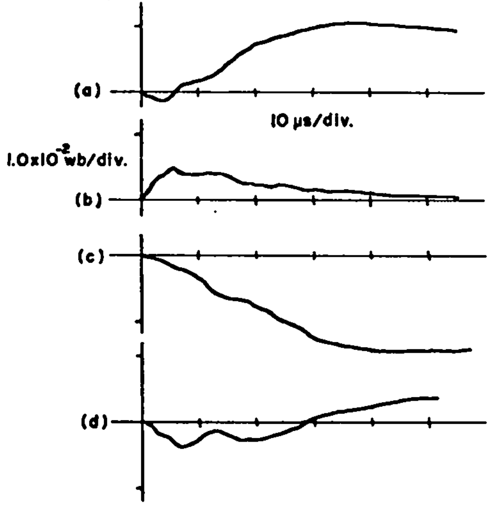

Fig. 52. Examples of flux flow for B = 8.7 kG.

appears that the stream is deflected and the signal in the array is an eddy outside the main stream.

A general survey of the results to date shows the following:

1. Zero E-field along the magnetic field null.

2. Width of the stream decreases with field strength. The stream narrows very rapidly as it penetrates the field.

3. The E-field given by the probe which intersects the stream well inside the field is a more-or-less rectangular pulse lasting 1.5 to 2 μsec. In contrast, the fields near the null and at the edge of the stream are much more ill-defined and oscillate with frequencies up to 10 MHz.

4. With B ≤ 7 kG the integrated signals from the four-point array are such as would be expected from the stream flowing across the magnetic field and compressing as it goes into the higher field region. At high fields the data seemed to indicate large deflections of the main stream with eddies or vortices.

Even though the stream appears to take on the character of a steady flow inside the field, it is probably important that the stream does not appear as a steady flow in the region of the vacuum field null. It is hoped that careful analysis of the data obtained with closely-spaced probes will indicate the development of these flow patterns.

J. Marshall contributed to the discussions and W. B. C. Smith assisted with the experiments.

QUADRUPOLE INJECTION EXPERIMENT WITH INNER CONDUCTORS FED THROUGH MAGNETICALLY SHIELDED SUPPORTS

(D. A. Baker, J. E. Hammel, R. W. Kewish, L. W. Mann, A. R. Sherwood)

Introduction

The design study of the quadrupole injection experiment described in the previous CTR Status Report (LA-3831-MS, p. 45) was completed and construction is well under way. The details of the computational methods, the considerations involved in the design of the main quadrupole fields, and the calculations used to design the dipole guarded current fields are all covered in the aforementioned report.

Final Quadrupole Field Design

The constraints listed in LA-3831-MS had to be relaxed somewhat chiefly because of engineering and strength of material considerations. The final quadrupole geometric configuration was designed so as to maximize the number of gyroradii in the $\int d\ell/B$ stable region subject to the following revised constraints.

1. The maximum field along the injection path must be greater than 7 kG and less than 10 kG. The lower value is such as to exclude the low-energy plasma from the machine and to insure that the injected plasma is stopped after passing the field null. The upper value was chosen because present coaxial guns will not penetrate higher fields.

2. The maximum field must be no larger than 40 kG; this restriction stems from limitations on strength of materials.

3. Total field energy is less than 1.7 MJ; this is the energy readily available in the experimental area.

4. The current per turn in each of two-turn coils is less than 0.75 MA. Experimental tests on the current junctions which feed the coils indicate this is an upper limit. In view of the technical difficulties associated with electrically floating the capacitor bank, it was decided to feed the coils in parallel. This eliminated the series feed constraint of having equal current in both conductors.

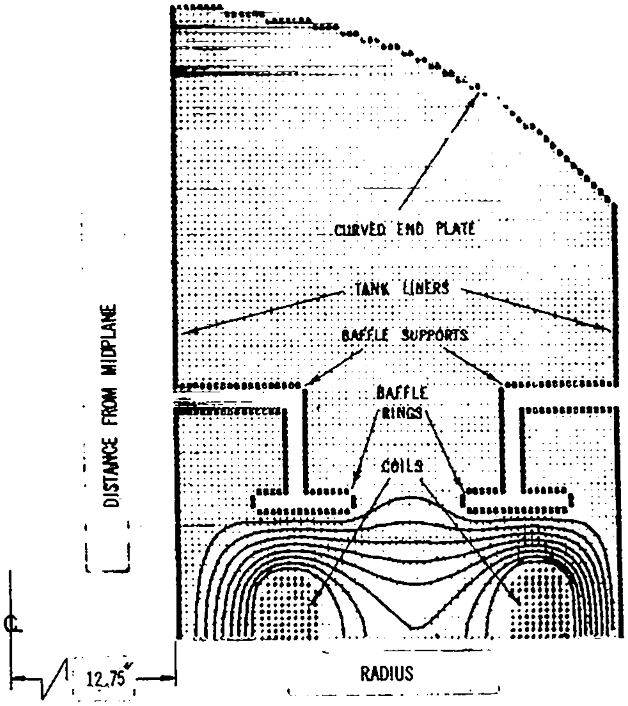

Fig. 53. Final field configuration for quadrupole injection experiment.

5. The coil thickness is not less than $2\frac{5}{8}$ in. This was based on preliminary estimates of mechanical coil strength.

6. The space between the coil and the "equal flux line" should exceed $\frac{5}{8}$ in. (dipole cross-over width). The equal flux line is defined as the line that provides the same $\Delta\psi$ between itself and the separatrix as there is between the separatrix and the $\int d\ell/B$ stable line.

7. The actual mechanical design places a minimum of about 2.5 cm on each dipole leg diameter. This requirement with a force-free condition on the dipole puts a constraint on the ratio of the coil current I and the bridge field B.

The optimum design was determined by trial and error computer calculations and represents the best of the many configurations that were tried. Table 4 gives the final machine dimensions and associated physical parameters of interest. The criteria were all met satisfactorily, but minor engineering changes dictated slightly different dimensions for certain conductors. As a result, the cross-feed criterion (6) were not quite met.

TABLE 4

FINAL QUADRUPOLE DESIGN

Field Energy	0.81 MJ
Turns/Coil	2
Number of gyro-radii across stable region	5.5 (2.5 keV deuterons)
Injection field	7.3 kG
Maximum field inner coil	40.0 kG
" " outer coil	24.1 kG
Field inner bridge at the separatrix	32.4 kG
" outer " " "	19.6 kG
Current/turn, inner coil	0.61 MA
" " outer "	0.41 MA
Space allowed for inner dipole X-feed (computer)	0.60 in.
Space taken for inner dipole X-feed (actual)	0.625 in.
Space allowed for outer dipole X-feed (computer)	0.50 in.
Space taken for outer dipole X-feed (actual)	0.625 in.
Max. inner coil dipole leg diam. (computer)	1.24 in.
Inner coil dipole leg diam. (actual)	1.12 in.
Max. outer " " " (computer)	1.30 in.
Outer dipole leg diam. (actual)	1.12 in.
Inner coil dipole separation	1.65 in.
Outer " " "	1.72 in.
Inner liner O.D.	25.5 in.
Outer " I.D.	73.0 in.
Inner coil inside diam.	34.3 in.
Outer coil outside diam. (computer)	67.1 in.
Outer coil outside diam. (actual)	67.05 in
Coil thickness (computer)	2.92 in.
Coil thickness (actual)	2.875 in.
Baffle rings	
Gap to inner coil (computer)	3.65 in.
Gap to inner coil (actual)	3.72 in.
Gap to outer coil (computer)	3.28 in.
Gap to outer coil (actual)	3.36 in.
Width of inner baffle ring	5.47 in.
Width of outer baffle ring	5.84 in.
Thickness (computer)	1.18 in
Thickness (actual)	1.00 in.

Figure 53 shows the boundaries, mesh points, and flux lines as obtained from the computer for the final design. The conductors, called baffles in Fig. 53, are parasitically-driven, field-shaping rings to increase the amount of $\int d\ell / B$ stable flux. The supports are well removed from the main field region so that diagnostic viewing ports may be introduced into them without appreciably perturbing the field. This increase in the stable region was made at the expense of having multiple mirror bridges. The machine is designed so that the geometry of the field-shaping conductors may be changed if these mirrors prove to be a major disadvantage.

Mechanical Design

Considerable effort has been expended, in cooperation with R. Dike, to develop a mechanical design for the quadrupole device based on the computer field design. Parts of this mechanical design (not showing, for example, the baffle rings) are indicated in Fig. 54 and a more detailed sketch is given in Fig. 55.

Each coil is both supported and fed by a single pair of dipole feed elements. Each dipole is in series with its coil, so that the coil current itself provides the magnetic field that shields the dipole. To provide strength for supporting the coils, the diameter of the dipole elements is $1\frac{1}{8}$ in. The dipole separation is then determined by applying the force-free condition to a thin-wire model as explained in LA-3831-MS, (pp. 48-49), except that in the final design the spatial variation of the background magnetic field was taken into account so that the dipoles are "average force-free." For a given background field and a given number (λ) of gyro-radii from ψ_{crit} to the separatrix, a condition on the current producing the background field results from the fixed diameter of the dipole elements combined with the condition that the number of gyro-radii between the dipole field null and the surface of a dipole element be equal to or larger than λ. This condition on the current is the I/B ratio condition which was used in the computer design.

As can be seen in Fig. 54, the dipoles pass out through slots in the liners and through

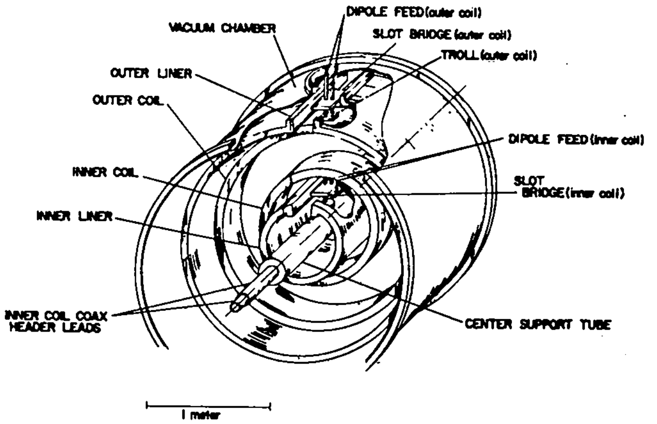

Fig. 54. Schematic diagram of quadrupole coil dipole field and support system.

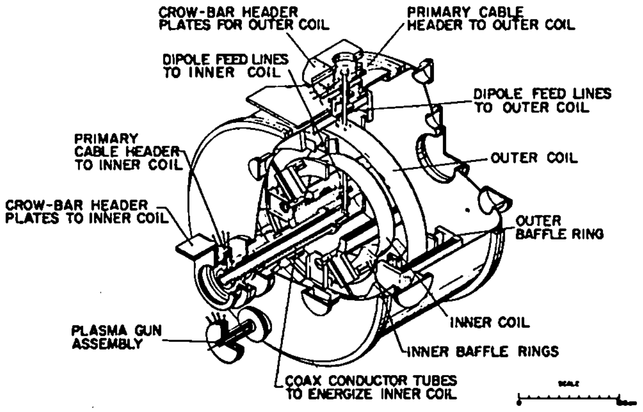

Fig. 55. Schematic diagram of quadrupole injection experiment design.

"slot bridges" to the exterior. There are two possible advantages to this configuration. First, the holes to allow the dipole to pass through the liner are moved farther away from the containment region and so the perturbation of the magnetic field in the containment region due to these holes is reduced. Second, the dipole null lines now pass out of the main plasma region before they strike a wall (at a presently unknown position); therefore, if the plasma leaks out along these null lines, it may be possible to minimize the effect on the main plasma body of the results of the leaking plasma hitting the wall by means of a shield of some sort.

The foregoing configuration is based on the suggestion by J. Marshall that the wall of the liner can be moved to a larger radius without affecting the interior field so long as it remains on flux surfaces which are an extension of the interior geometry. The application of this concept is not straightforward. For example, the extension of the cylindrical outer flux surface is across a separatrix. Studies of experimental conductor arrangements on a resistor analog board and probe studies of three-dimensional models were employed to determine the dimensions of the conductors. There is a perturbation of the magnetic field in the region where the baffle ring meets the slot in the liner. In the model this perturbation was < 5% in what is anticipated to be the region of stable flux.

There are in this design several high-current-density joints involved in connecting the coils through the dipole elements and through coaxial leads to the external headers. Proposed current joints were tested at 750 kA, and although many failed for various reasons, a satisfactory tapered joint was found that carried 750 kA for 200 shots without evidence of damage and also a satisfactory collet joint which showed only slight signs of damage after the same test. These two joints, then, were incorporated into the design.

Much of the design of the quadrupole coils was checked by the construction and testing of a ($\sim \frac{1}{2}$ scale) prototype coil, and as a result several critical points in the design were changed. Of these, a redesign to strengthen the crossover between turns was probably most important. The prototype coil itself failed under the loading of a 600-kA current on the third shot. The fiberglass and epoxy potting procedure to be used on the actual coils was tested on the prototype and found to be satisfactory. The flux smoothing copper shroud with a Micalex insulator in its gap was used as the outer container of the epoxy pour. As expected, this shroud proved to be effective in smoothing out the field irregularities due to the nonideal structure of the coil.

Except for the two coils, the major components and most of the smaller components have been fabricated, and construction of the device is under way. The outer coil is presently being fabricated, but the inner coil is still being delayed by a problem relating to strength of materials. As mentioned above, the failure of the prototype coil at the design current of the inner coil prompted some redesigning of the coils. Even so, in the case of the inner coil it is necessary either to turn to an aluminum alloy of higher strength than the usual Type 6061-T6 or to limit the current to about 75% of the listed design current. A program is now under way for testing welds in an aluminum alloy (Type 7039-T64) of higher strength to see if it can be used for the inner coil.

A further problem related to the coil design is the electrostatic shield. The purposes of this outermost layer of the coil are to shield the plasma from the ohmic electric field produced in the coil and to prevent large electric fields from appearing across the insulator in the shroud. A flame-sprayed preparation of titanium dioxide, with a surface resistivity of ~ 700 Ω per square, appears to be a promising material for this purpose. At present difficulty is being experienced with breakdowns in the insulation coating that separates the titanium dioxide shield from the copper shroud.

MONTE CARLO AND COMPUTER PLASMA SIMULATION STUDIES OF THE INHIBITION OF END LOSS FROM A θ-PINCH BY NONADIABATIC "ROUGH" MAGNETIC WALLS

(J. L. Tuck)

A combination of uniform magnetic field, with its manifest advantages for stable plasma confinement in the direction transverse to the field, with some effective check of the free flow of plasma in the direction along the field, could be of appreciable help in the achievement of net power from a thermonuclear reaction. Monte Carlo studies[1] of particles escaping from a $\beta = 1$ θ-pinch, having a sharp plasma-field boundary equipped with multiple small perturbations, have indicated that cumulative nonadiabatic effects can be promoted. The plasma model studied was probably too simple to be altogether valid for a real plasma; plasma loss reductions which resulted were surprisingly large. Static perturbations, which would be simple to apply, reached a factor of ten in reduction of loss, whereas moving perturbations reached a factor of 100. The latter would be complicated to apply but could conceivably be used additionally to heat plasma and force it up to the density gradient.

A far more sophisticated (but still approximate) study is now beginning to yield results. By using a previously developed computer simulated θ-pinch plasma model of R. L. Morse[2], with appropriately modified magnetic field, 13,000 particles are followed at high β, the magnetic field being computed self-consistently. Electrons are assumed to maintain space charge neutrality at all points. The systems studied so far, with their losses at two-thirds characteristic time are:

1.	Open-ended θ-pinch (smooth walls)	4000
2.	Open-ended θ-pinch (smooth walls) plus mirror	3400
3.	Open-ended θ-pinch (rough walls) (stationary)	2800
4.	Open-ended θ-pinch (rough walls) (moving)	2400

1 characteristic time = 2 x pinch length/mean thermal speed (= 2.8 μsec in Scylla IV) = 100 time steps ≡ 3 h computing time on CDC 6600. The loss rates per time step at t = 67 are 59, 22, 24, and 28, respectively.

Adequate description of the plasma distribution required 20 steps in the radial direction and 100 steps in the longitudinal direction. Although this corresponds to a shorter system than had been found necessary for a 10-fold loss reduction in the previous calculation, it was needed to keep the computation cycle time down to feasible values. Consequently, the loss rate reductions to be expected are not large. The table given above shows the number of particles lost after 67 time steps (~ 2.3 characteristic time). The results are in the expected order. The computed loss rate for Case 1 at early times is in excellent agreement with theory for a rigid pipe with reflecting walls and, interestingly, thereafter falls below theory, presumably on account of the development of self-mirrors.

Case 3, if its performance continues, should give the required 10-fold reduction of loss rate, for a 6-fold length extension or a total length of 160 radii. This would be quite practical. Motion pictures of the printouts exhibit waves and bunching phenomena which may repay further study.

Mathematical plasma physics is notoriously difficult; the problems it has attacked in many cases have had to be taken far from reality in order to yield solutions. Few expect a mathematical description of all the behavior of a real confined plasma with its wave interactions, plasma boundary resonances, wall resonances, radiative interactions, etc., to become available in the near future. The art of computer plasma simulation is still in its infancy. In this report, it is applied in a simplified way to a complicated system which would probably not easily be treated by mathematical analysis. It would be idle to pretend that the predictions made here are exact, and they may, in fact, turn out to be no closer to reality than those made by more familiar approximations. However, they are likely to improve, and the approximations are different.

References

1. J. L. Tuck, Phys. Rev. Letters 20, 715 (1968).
2. R. L. Morse, Proc. APS Topical Conf. on Pulsed High Density Plasmas, Sept. 1967, LA-3770, Paper F-3.

LINEAR θ-PINCH EXPERIMENTS ON SCYLLA IV RELATED TO THE STABILITY OF THE SCYLLAC TOROIDAL θ-PINCH

(E. M. Little, A. A. Newton,
W. E. Quinn, and F. L. Ribe)

Introduction

The 15-m Scyllac θ-pinch[1,2,3] is a high-β plasma experiment to be operated initially with a straight coil and subsequently as a torus with a 5-m major-diameter. For the second stage, configurations are being explored which use, in addition to the zero-order longitudinal field B_e, superimposed first-order transverse components to neutralize the toroidal drift. These may be either azimuthal (B_θ) as in the screw pinch or periodic along the torus (B_δ) to produce a bumpy, or "M and S"[4,5] configuration. In both cases there are gross instabilities, and these must be suppressed by oscillating the transverse field (dynamic stabilization). Alternatives under consideration are: (a) an oscillating screw pinch[2] with B_θ varying, (b) time varying or moving bumps[6] with B_δ varying, and (c) static bumps with B_δ fixed but B_θ oscillating[2,7]. Of these three, (c) seems preferable, since the dynamic stabilization power and frequency are least. Moreover, the longitudinal current, which may stimulate microinstabilities[8], is less than in (a).

The theory of this approach is outlined below; it shows how the Haas-Wesson instability[9] inherent in a bumpy plasma column can be stabilized. Experiments are reported with a 1-m θ-pinch on the instabilities induced by quasistatic B_δ and B_θ, the plasma density distribution with quasistatic and oscillating B_θ, and the plasma resistance in the oscillating case.

Theoretical Considerations

Forces Acting on a Bumpy Plasma Column and the M and S Toroidal Equilibrium

Recently it has been shown[5] that the M and S, high-β plasma equilibrium in a toroidal

θ-pinch can be realized by adding periodic multipolar magnetic fields which produce excursions of the plasma radius r about its equilibrium value a given by

$$r - a = \sum_{\ell} a\delta_{\ell} \cos \ell\theta \sin kz. \tag{1}$$

Here z is the coordinate along the plasma axis, θ is the azimuth about that axis, and $2\pi/k$ is the wavelength of the multipolar field. The basic principle involves only the $\ell = 0$ (bumpy) and $\ell = 1$ (wavy) excursions. The $\ell = 0, 1$ combination produces a uniform transverse force per unit length in the direction of maximum bumpiness given by

$$F_1 = \beta(3 - 2\beta)(B_e^2/8)k^2 a^3 \delta_o \delta_1, \tag{2}$$

where β is the ratio of plasma pressure to the external magnetic pressure. A toroidal plasma column of large aspect ratio $(R/a >> 1)$ has an outward (curvature) force per unit length given by $F_R = \beta B_e^2 a^2/4R$. Equilibrium is obtained with $F_1 = F_R$; i.e., when $2(\delta_0\delta_1)^{-1} = (3 - 2\beta)k^2 aR$. Typical values for the projected Scyllac toroidal θ-pinch are: $a \approx 1$ cm, $R \approx 250$ cm, $ka \approx 0.3$, $\delta_0 \approx \delta_1 \approx 0.25$, $B_e \approx 100$ kG and $\beta \approx 0.8$ (on axis).

Gross Instability of an Axisymmetric Bumpy High-β Plasma Column

The bumpy plasma column required for M and S equilibrium possesses net unfavorable curvature and is therefore unstable. The gross stability of straight bumpy, high-β plasma columns has been studied[9,10] for displacements of the form $\xi(z) = \xi_m(z) \cos m\theta$. Since it has been found experimentally in the present work (and by others[11]) that the m = 1 mode, which involves little ballooning or z dependence, is dominant, and modes with $m \geq 2$ are not seen, the treatment is confined to m = 1 for the present.

The m = 1 growth rate can be derived from considerations[7] like those of Eq. 2. When an axisymmetric column with bumpiness δ_0 is displaced from the axis of symmetry by an amount ξ_1, there results an $\ell = 1$ component of surface distortion given by

$$\delta_1 = 2\xi_1(\delta_0/a)(1 - \beta)/(2 - \beta)$$

for $ka << 1$. Upon substituting into Eq. 2, the destabilizing m = 1 force per unit length of plasma column is given by

$$F_\delta = \frac{\beta(1 - \beta)(3 - 2\beta)}{(2 - \beta)} (B_e^2/4)k^2 a^2 \delta_o^2 \xi_1$$

$$\equiv h_\delta^2 (B_e^2 a^2/4)\xi_1, \tag{3}$$

where h_δ is an "effective wavenumber".

Effects of a Steady Longitudinal Current on the Plasma Column

The Kruskal-Shafranov (KS) Modes

When a longitudinal current I_z is applied, the magnetic lines at the plasma surface become helical with pitch wavenumber

$$\mu = 2I_z/a^2 B_e \tag{4}$$

at the plasma surface. It is then appropriate to consider helical displacements of the form $\xi_m \cos m(\theta - hz)$; consideration is again limited to the m = 1 mode. In the presence of a conducting wall (inner surface of the θ-pinch compression coil) of radius b, and for μa, ha, μb, hb, $a/b << 1$ the transverse force per unit length of plasma column is

$$F_{KS} = \left[- (2 - \beta)h^2 + 2h\mu - 2\mu^2 (a^2/b^2)\right](B_e^2 a^2/4)\xi_1. \tag{5}$$

The threshold of instability for a mode of wavenumber h (the Kruskal limit) is given by

$$\mu_K = (2 - \beta)h/2, \tag{6}$$

neglecting the last (wall effect) term of Eq. 5 since it is small.

The m = 1 Helical Mode Driven by Bumpiness

Provided that μka^2 is of the same order as δ_0 and $\mu << k$, the only effect of the longitudinal current[7] is to replace θ by $\theta_0 + \mu z$ in Eq. 1, where θ_0 is the azimuth of a field line at z = 0. The equation of motion for a helical displacement ξ_1 of pitch h is

$$\rho_\ell \ddot{\xi}_1 - F_\delta - F_{KS} = 0, \qquad (7)$$

where ρ_ℓ is the plasma line density. If it is assumed that $\xi_1 = \xi_{10} e^{\nu t}$, the growth rate ν is given by

$$\nu^2 = \left[- (2 - \beta)h^2 + 2h\mu - 2\mu^2 (a^2/b^2) + h_\delta^2\right] v_A^2, \qquad (8)$$

where

$$v_A^2 \equiv \left[B_e^2 a^2/4\rho_\ell\right].$$

Dynamic Stabilization by Means of an Oscillating Longitudinal Current

The destabilizing $F_\delta + F_{KS}$ force can be neutralized when the current I_z is alternated; i.e., $I_z = I_o \cos \omega t$ (correspondingly $\mu = \mu_o \cos \omega t$). Setting $\zeta = \omega t/2$, Eq. 7 assumes the Mathieu form; the solutions are stable (first stability zone) when

$$h_\delta^2 < (2 - \beta)h^2 < h_\delta^2 + \omega^2/4v_A^2$$

and

$$\omega^2 > 4\left[(2 - \beta)h^2 + h\mu_o - h_\delta^2\right] v_A^2. \qquad (9)$$

Here the wall-effect term has been neglected. If $h \approx \mu_o$, condition 9 requires I_o to be of the order of 10 kA ($\mu_o \approx 0.1$ k) and the minimum frequency $\omega/2\pi$ to be in the range of 1-2 MHz to stabilize the effects of δ_o for Scyllac parameters.

EXPERIMENTAL MEASUREMENTS

Apparatus and Measured Plasma Properties

The plasmas used in the present experiments were generated by the 560-kJ, 1-m Scylla IV θ-pinch operated in the "low-pressure" regime[12]. The time history of B_e is that of one half-cycle of a sinusoid with an amplitude of 90 kG and a quarter period (rise time) of 3.7 μsec. The discharge conditions of most of the measurements were as follows. Deuterium filling pressure = 20 to 100 mtorr and zero bias field (B_o = 0). Near peak compression the plasma column has a length ℓ of ~ 80 cm, a radius of ~ 1 cm, density n on axis varying from ~ 5 x 10^{16}/cm^3 to 1.2 x 10^{17}/cm^3, β on axis 0.8,[13] kT_e ~ 300 eV, and kT_i varying from ~ 2.0 keV to ~ 0.5 keV. The plasma corresponding to 20-mtorr filling pressure is essentially collisionless (ion-ion mean free path $\lambda_{ii} \approx 150$ cm), whereas that at 100 mtorr is much less so ($\lambda_{ii} \approx 3$ cm).

Observation of the m = 1 Instability with a Single Axisymmetric Bump

Apparatus

In an extension of the work reported earlier,[3] an effort was made to apply the bump "adiabatically," i.e., after the initial plasma implosion which forms the plasma column during the first ~ 0.5 μsec of the discharge. Two methods were used. In the first a series coil diverted magnetic field from a 7.6-cm central section of the main coil through 1.2-cm gaps, causing a fractional decrease $\Delta B_e/B_e$; values of 0.11 and 0.21 were obtained for the latter, corresponding to series coil diameters of 6.35 cm and 10.2 cm (compression coil = 10.3 cm diam). The generation of the bump was delayed by means of carbon cylinders of 0.95-cm wall thickness and 6.03 and 9.68 cm o.d. which were inserted into the series coils. The resistivity of the carbon cylinders, η = 1.78 x 10^{-2} Ω-cm, was such that their flux-penetration time provided the delay. The bump could be eliminated by inserting an aluminum cylinder in place of the carbon one.

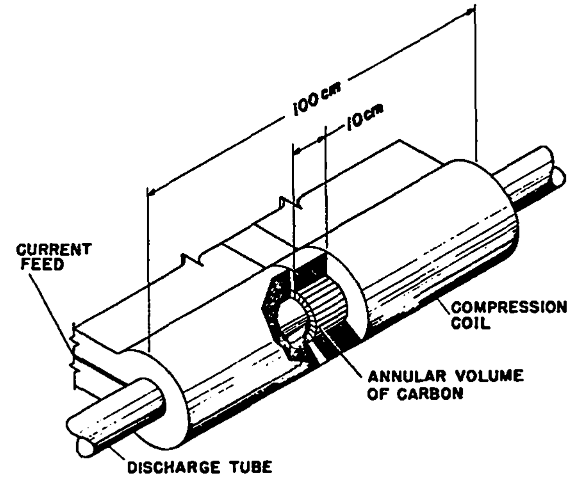

Fig. 56. Method for producing single $\ell = 0$ bump adiabatically in a Scylla IV θ-pinch.

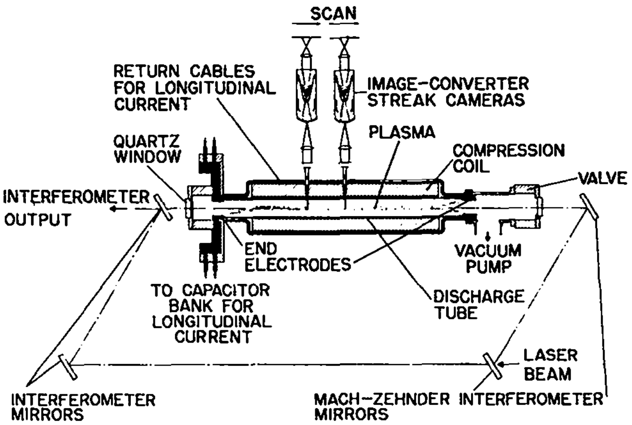

Fig. 57. Scylla IV θ-pinch with end electrodes, image-converter camera, and interferometer.

In the second method (Fig. 56) magnetic lines are diverted into an annular volume of 6.52-cm length and 1.29-cm radial thickness in the compression coil wall to give $\Delta B_e/B_e = -0.25$. The delay is provided by flux diffusion into an array of trapezoidal Inconel X-750 steel tubes of 0.025-cm wall thickness, having $\eta = 1.22 \times 10^{-4}$ Ω-cm. Plasma motion was observed by two streak cameras viewing perpendicular to the plasma axis, one in the midplane and the other 20.3 cm away, and by a Mach-Zehnder interferometer aligned parallel to the plasma axis (Fig. 57).

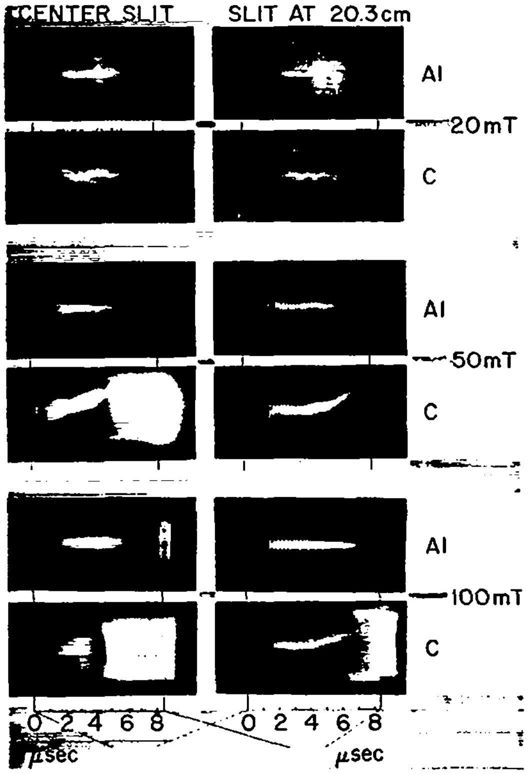

Fig. 58. Streak photographs of Scylla IV plasma with and without 21% $\ell = 0$ bump at different filling pressures ($B_0 = 0$).

Results Obtained with the Series Coils

Streak camera photographs are shown in Fig. 58 for no bias field. With no bump (Al cylinder in series coil) the plasma remains on axis, except for some sideways motion, or "wobble," seen at 20-mtorr filling pressure, p_0. The end loss is also visible as a narrowing of the plasma diameter toward the end of the streak photograph. At this pressure, application of the bump (C in series coil) is found to result only in an enhancement of the wobble. At the two higher pressures, however, the plasma in the midplane is seen to move sideways and to hit the discharge-tube wall. The sideways motion begins later at the 20.3-cm axial position. (The barred structure in these photographs is a feature of the image converter, not the plasma). Reduction of the end loss is also seen as the filling pressure is raised.

The application of bias field caused a qualitative change in the occurrence of the sideways plasma motion. With $B_0 = -780$ G, $\Delta B_e/B_e = -0.21$, and $p_0 = 20$ mtorr the plasma moved to the wall at the midplane in the same time as at $p_0 = 50$ mtorr, $B_0 = 0$.

It is concluded that this is the $m = 1$ instability driven by F_δ as observed earlier.[11]

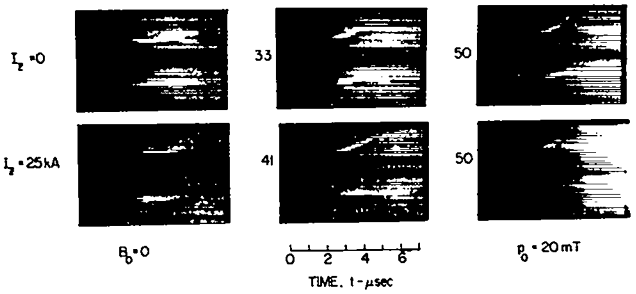

Fig. 59. Streak photographs at midplane of Scylla IV for $B_0 = 0$ and various maximum values of quasisteady I_z; $p_0 = 20$ mtorr.

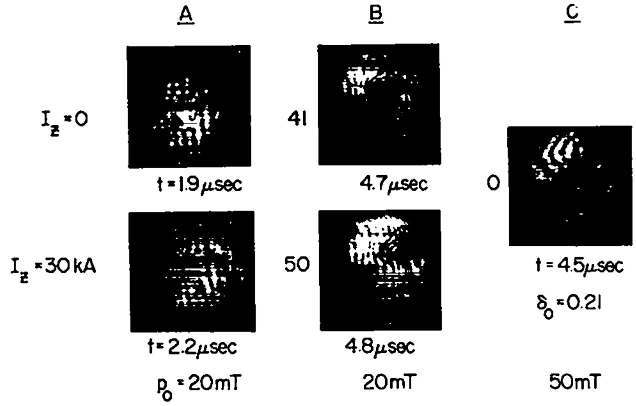

Fig. 60. Interferograms. A: without and with I_z ($B_0=0$, $\delta_0=0$); B: with fully developed transverse motion resulting from I_z ($B_0=0$, $\delta_0=0$); C: with fully developed transverse motion resulting from $\ell=0$ magnetic bump with $I_z = 0$ ($B_0=0$).

At $p_0 = 50$ and 100 mtorr the growth rate is in agreement with theory[10], but the absence of the instability at low pressure is not accounted for. However, the plasma length ℓ is sufficiently small that v_A/ℓ and v_i/ℓ (v_i = ion thermal velocity) are comparable to the growth rate ν. This contrasts with the Culham experiments, carried out with an 8-m long plasma which was well isolated from end effects.

Effect of Quasisteady Longitudinal Current with $\delta_0 = 0$

Transverse Plasma Motion

The experimental arrangement was that shown in Fig. 57. A 5-μF capacitor was used to drive I_z, which was applied about 1 μsec after the main compression field and had a quarter period of 2.5 μsec, so that the maxima of I_z and B_e coincided.

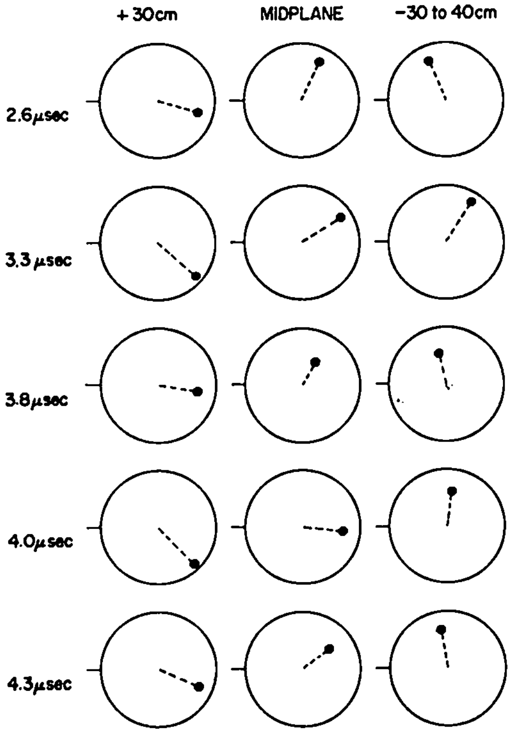

Fig. 61. Position of plasma in m = 1 Kruskal-Shafranov mode at six times and three axial positions in a single discharge.

The transverse motion of the central section of the plasma at $p_0 = 20$ mtorr, $B_0 = 0$ is indicated in Fig. 59 for various values of I_z (max); two stereoscopic views at right angles are given in each case. At the higher currents, the streak pictures show well-developed radial azimuthal motion. This is also seen in the interferograms of Fig. 60B, taken at times late in the discharge when the motion is well developed. The plasma is seen to occupy a semicircle which is interpreted as the end view of one half-wavelength of a helix formed by the plasma whose profile about its axis is unchanged (cf. Fig. 59). This is in contrast to Fig. 60C, taken late during the motion of Fig. 58 at 50 mtorr; here the motion driven by δ_0 is purely radial. The helix is observed to have the same orientation in all but one of ten cases, being displaced away from the coil feed slot at the midplane.

In order to elucidate the plasma distortion as a function of axial position, stereoscopic streak

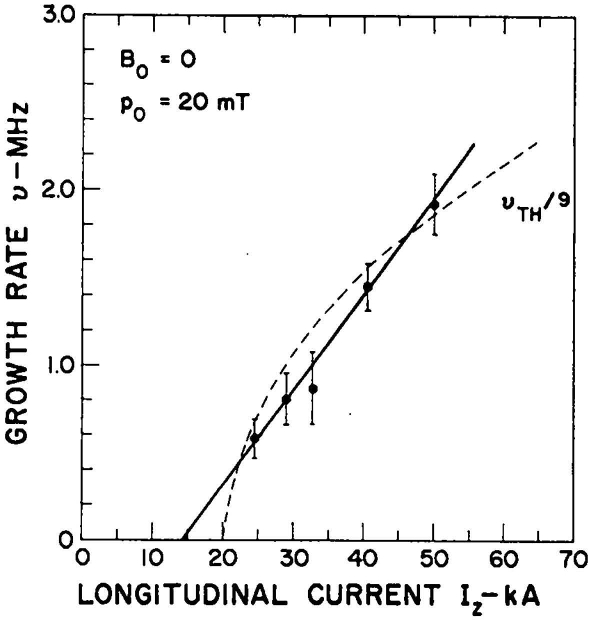

Fig. 62. Growth rate of K-S mode vs I_z. The points are experimental; dashed curve is theoretical divided by 9.

photographs were made by three streak cameras, one at the midplane and one on each side of the midplane at 30 cm and 30 or 40 cm. Figure 61 shows the position of the plasma column in a two-dimensional diagram as determined from the three stereoscopic streak photographs at the indicated times after the application of the main compression field. The circles correspond to the inside diameter of the discharge tube and the bar to the left indicates the coil current feed position. In general, the plasma column does not strike the discharge-tube wall due to the image currents induced in the compression coil. These become large as the plasma approaches the wall. The streak photographs confirm the data taken with two streak cameras and the interferograms of Fig. 60 which show that the plasma occupies a semicircle; the latter is the end view of approximately one half-wavelength of a helix formed by the plasma whose profile about its axis is unchanged. The present data show the helix to have almost the same orientation in most cases.

Growth rates were measured for a number of cases at each I_z value and the results are plotted in Fig. 62 as a function of I_z (max). For a higher filling pressure (p_0 = 50 mtorr) no sideways motion was observed, except at I_z = 50 kA, where the motion was small and slow.

It is concluded that this is the m = 1 Kruskal-Shafranov instability whose wavelength λ is twice the plasma length; the intercept of Fig. 62 at $I_z \approx$ 15 kA is identified as the Kruskal limit I_K. From the relation $I_K = (2 - \beta)\pi a^2 B_e/2\lambda$, derived from Eqs. 4 and 6, and $\beta = 0.25$, as an average value over all radii[13], and for B_e (av) = 80 kG it is calculated that $\lambda/a^2 \approx 150$ cm^{-1}. With $\lambda = 2\ell = 160$ cm, it is thus found that a = 1.0 cm, corresponding roughly to the toe of the density distribution.

The measured growth rates of Fig. 62 are a factor of 9 smaller than those predicted by Eq. 8 with $h_\delta = 0$. The line density is measured to be $\rho_\ell = 3.4 \times 10^{-8}$ g cm^{-1}. In Fig. 62 the dashed curve labelled $\nu_{TH}/9$ is a plot of $\nu/9$ computed from Eq. 8, using this value of ρ_ℓ. The lack of helical displacement at $p_0 \geq 50$ mtorr is attributed to the large value of a, so that the Kruskal limit is barely exceeded.

Plasma Halos

A halo-like luminosity has been observed surrounding the plasma core with colder plasmas. The observation of many such streak photographs shows that the halos are present with the colder plasma and absent with hot plasma. They are consistently present with only one-third of the primary capacitor bank energizing the 1-m compression coil.

Effect of Oscillating Longitudinal Current

Properties of the Current Channel

The current (with $\delta_0 = 0$) was driven by a 0.168-μF capacitor in the circuit of Fig. 63A, where L_s is an adjustable, calibrated coaxial inductor. The inductances L_1 and L_2, due to cables and connections, were determined from the frequencies at L_s = 620 nH and $L_s = \infty$ by using a copper tube (1.9-cm diam) along the compression-coil axis. Then (with the copper tube removed) the radius a of the current channel to the plasma was determined from its inductance L_L. In the preionization plasma a_1 = 3.4 cm and, with full magnetic compression at p_0 = 20 mtorr, a_2 = 1.4 cm.

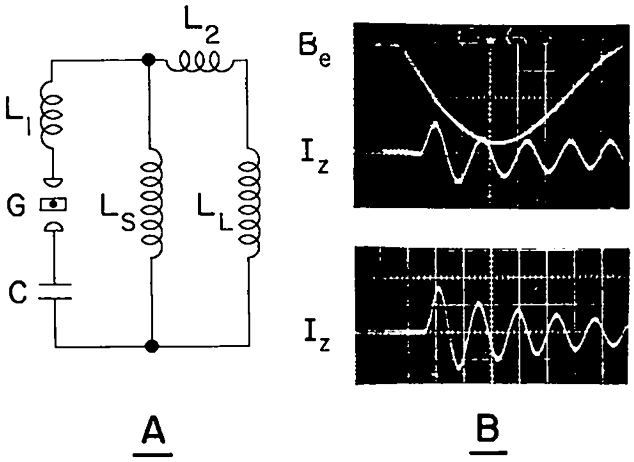

Fig. 63. A: Circuit for driving oscillating longitudinal current; B (upper): compression field B_θ and current I_z for compressed plasma; B (lower): I_z for preionized plasma; p_o = 20 mtorr for both. (Time scale: 1 μsec/div.)

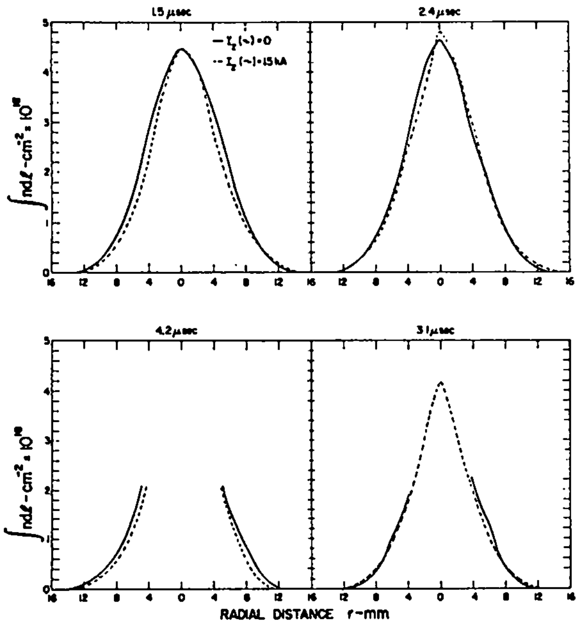

Fig. 64. Plasma density profiles without and with 0.63 MHz oscillating I_z.

These radii are significantly less than the discharge-tube internal radius of 4.3 cm, and a_2 corresponds both to the tail of the measured density distribution and to the value obtained earlier from the Kruskal limit. The agreement is good, considering the fact that a_2 is an overestimate which includes the effects of uncompressed plasma adjacent to the electrodes. An estimate of the correction for the

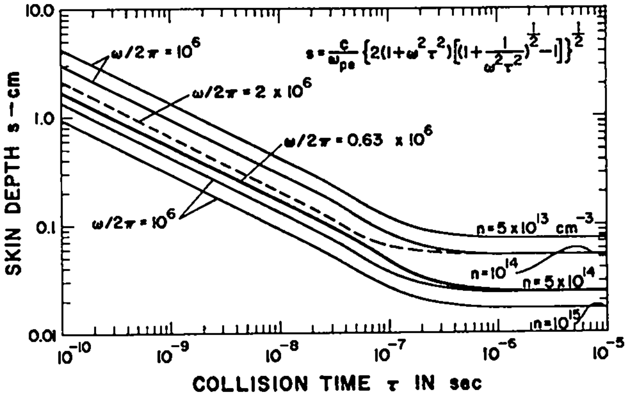

Fig. 65. Skin depth of oscillating I_z (or B_θ) vs collision time.

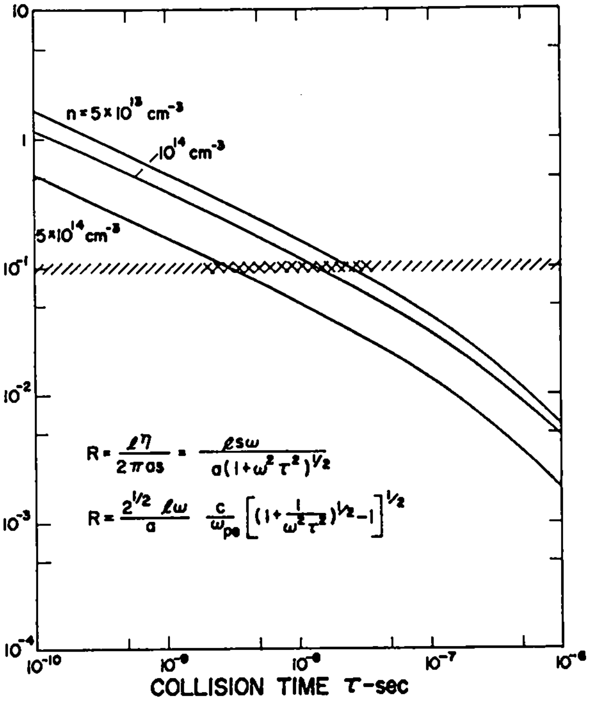

Fig. 66. Resistance of plasma column 90-cm long, 1-cm radius derived from Fig. 65; hatched line is observed plasma resistance.

ends gives the value a_2 = 1.0 cm for the compressed plasma. The current-carrying plasma has a density n lying between 10^{14} and $10^{15}/\text{cm}^3$.

The Q values of the circuit with L_L open-circuited, with the copper tube, with compressed plasma, and with preionized plasma (see oscillograms of Fig. 63B) were 29, 33, 17, and 11, corresponding to effective circuit resistances $(\omega CQ)^{-1}$ of 55, 50, 88, and 121 mΩ. Upon correcting for

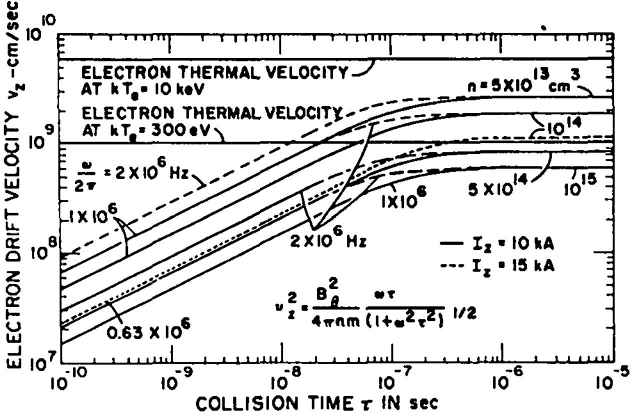

Fig. 67. Electron drift velocity vs collision time for various assumed ω and n.

the measured external circuit resistances in Fig. 63A, resistances of 148 and 141 mΩ are derived for the plasmas between electrodes in the preionized and compressed cases, respectively.

In order to arrive at a figure for the resistance of the compressed plasma, the plasma outside the coil is assumed to have the same resistance as the preionized plasma. Of the 130 cm between electrodes, 37 cm are assumed to be occupied by such plasma, whose resistance is therefore 43 mΩ. Thus the compressed-plasma resistance is 100 mΩ.

Plasma Density Profile

There is a possibility of anomalous diffusion induced by turbulence which might be caused by the streaming of electrons in the longitudinal current I_z. Therefore a comparison was made of the plasma density profiles (as observed with the M-Z interferometer) with and without I_z. The results are shown in Fig. 64 at various times during the discharge. There is no broadening of the profile induced by I_z. Streak photographs similarly show no difference between the cases with and without I_z.

Interpretation of the Current-Channel Resistivity

In order to derive a resistivity from the measured resistance of the plasma column the skin depth of the oscillating B_θ field must be known. This problem was treated earlier[14] in terms of a phenomenological collision time τ, to be thought of as between electrons and turbulences or, in a special case, between electrons and ions. The resulting skin depth, s, for various densities, ranging from collisionless to collision dominated, is shown in Fig. 65; the quantity c/ω_{pe} is the collisionless skin depth and ω is the angular collision frequency. With the expression given for s, the resistances R shown in Fig. 66 are derived for various assumed densities which are characteristic of the plasma density tail where the current is known to reside. The observed value of R corresponds to $\tau \approx 10^{-8}$ sec. From Fig. 65, the skinning is seen to be collision dominated.

The electrondrift velocity, v_z, can be derived[14] as a function of τ, as shown in Fig. 67. In the absence of turbulent heating the measured value of kT_e is 300 eV,[12] and the average value of v_z is seen to be well below the electron thermal velocity at $\tau \approx 10^{-8}$ sec. It is, however, greater than the ion thermal velocity of 4×10^7 cm/sec (corresponding to $kT_i \approx 2$ keV)[12] and the ion sound speed $[kT_e/m_i]^{\frac{1}{2}} = 1.2 \times 10^7$ cm/sec. Thus, on the average, ion sound might be expected to be unstable provided $kT_e/kT_i > 1$, which is not the case in the absence of oscillating I_z. It is to be noted that $\omega_{pi}^{-1} \approx 10^{-10}$ sec and so is much less than the derived value of τ.

Since the plasma is collision dominated, the diffusion coefficient can be expressed as

$$D = \frac{1}{2} \frac{v_e^2}{s\tau} , \qquad (10)$$

where the particular choice $\tau_B = 16/\omega_{ce}$ (ω_{ce} = electron cyclotron frequency) corresponds to Bohm diffusion. For Scylla IV parameters in the plasma tail $\tau_B \approx 10^{-11}$ sec. Thus the diffusion coefficient has about 10^{-3} of the Bohm value.

The possible consequence of this diffusion are shown in Fig. 68. If the sheath is assumed to advance with velocity v_D into the plasma tail by diffusion, expelling plasma from the moving layer of thickness s, then

$$v_D = D/s. \qquad (11)$$

The tail has a density gradient $n' \approx 2 \times 10^{15}/cm^4$, and v_D can also be expressed as

$$v_D = (dn/dt)/n'. \qquad (12)$$

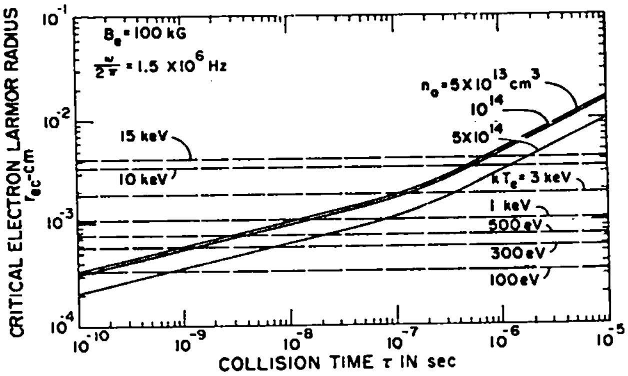

Fig. 68. Curves are (critical) electron Larmor radii (Eq. 16) for diffusion of the turbulent current layer; horizontal lines give radii for various electron temperatures in Scylla IV.

If it is assumed that the turbulent layer begins at some density n_o and advances to the value n, then since $s = s_o (n_o/n)^{\frac{1}{2}}$, the dimensionless scaling

$$\frac{d(n/n_o)}{d(t/\tau_o)} = (n/n_o)^{\frac{1}{2}} \qquad (13)$$

is found, where the characteristic diffusion time is

$$\tau_o = 2 s_o n_o \tau / n' r_e^2 \ . \qquad (14)$$

The solution of Eq. 13 for the time to advance from n_o to n is

$$\tau = 2 \left[(n/n_o)^{\frac{1}{2}} - 1 \right] \tau_o . \qquad (15)$$

The Larmor radius corresponding to $t = 10^{-3}$ sec is given by

$$r_{ec}^2 = \left[4\ s_o\ n_o \tau / t n' \right] \left[(n/n_o)^{\frac{1}{2}} - 1 \right] . \qquad (16)$$

Values of r_{ec} are plotted vs τ in Fig. 68 for various values of n_o in the tail of the density distribution to $n = 10^{15}/\text{cm}^3$. It is seen that electron temperatures in Scylla IV as large as 1 keV would still allow 10^{-3} sec before appreciable encroachment of the current layer on the plasma density distribution.

References

1. H. Griem and F. Ribe, USAEC Report TID-23705 (1966).
2. F. L. Ribe, W. E. Quinn, G. A. Sawyer, D. A. Baker, R. L. Morse, T.A. Oliphant, W. B. Riesenfeld, E. L. Kemp, R.S. Dike, and A.S. Rawcliffe, LASL Report LA-3487-MS (1966).
3. Status Report of the LASL CTR Program for 12-month Period Ending Oct. 31, 1967, LA-3831-MS.
4. F. Meyer and H. V. Schmidt, Z. Naturf. 13a 1005 (1958).
5. R. L. Morse, W. B. Riesenfeld and J. L. Johnson, Bull. Am. Phys. Soc., Ser. 2, 12, 1155 (1967)(Abstract); Plasma Phys. 10, 543 (1968).
6. F. A. Haas and J. A. Wesson, Phys. Rev. Letters 19, 833 (1967).
7. F. L. Ribe and W. B. Riesenfeld, Bull. Am. Phys. Soc., Ser 2, 13, 599 (1968) (Abstract); Phys. Fluids 11, 2035 (1968).
8. V. P. Gordienko, et al., Plasma Phys. 10, 449 (1968).
9. F. A. Haas and J. A. Wesson, Phys. Fluids 10, 2245 (1967).
10. F. A. Haas and J. A. Wesson, ibid., 9, 2472 (1966).
11. H. A. B. Bodin and A. A. Newton, Bull. Am. Phys. Soc., Ser 2, 12 1153 (1967)(Abstract).
12. E. M. Little, W. E. Quinn, and G.A. Sawyer, Phys. Fluids 8, 1168 (1965).
13. R. F. Gribble, E.M. Little, R. L. Morse, and W. E. Quinn, ibid., 11, 1221 (1968).
14. W. B. Riesenfeld, LASL Report LA-3831-MS, p. 82 et seq.

SCYLLA IA MEASUREMENTS OF THE PLASMA HALO

(H. Herold, V.A. Finlayson, J.D. Smith)

Measurements with the Old Spark-Gap and Triggering System

Measurements of the low-density plasma outside the high-β core of Scylla IA were first made under the following conditions: W = 60 kJ, coil diam = 10 cm, coil length = 10 cm, mirror ratio = 1.3. The old spark gaps and trigger system were used at a reduced charging voltage of 40 kV (compared to 50 kV maximum).

Results obtained with a CO_2-laser interferometer directed parallel to the discharge axis at a radius of 1.8 cm are shown in Fig. 69 for two filling pressures of deuterium. It is seen that for ~ 1.5 μsec a relatively high density exists at that radius (indicating a broad radial density profile). After this time the density levels off to minimum values of 8×10^{13} to $5 \times 10^{14}/cm^3$. This value of the halo density then decays with an e-folding time of about 30 μsec.

To get radial density profiles, the relative continuum intensities in a 50-Å band centered around 4460 Å (known to be free of impurity lines) were measured by means of a nine channel monochromator-detector system and the results were Abel-inverted. An example of the results for a discharge at 20 mtorr is seen in Fig. 70 , which gives radial density profiles at different times. It is seen that the halo plasma develops out of a relatively long existing broad-density profile. The main amount of plasma eventually contracts to a central core leaving outside a halo-like, low-density plasma cylinder. Then the central plasma core decays much faster (by end losses) than the plasma halo. If a $1/T_i$ dependence is assumed for the end loss e-folding time, which has been proved for collision-free and collision-dominated plasmas, a value of T_i of 100 to 200 eV is found in the halo. An attempt to measure T_e in the halo using the D_β to continuum ratio gave $T_e >> 10$ eV. These temperatures suggest that the halo plasma is separated in an early stage from the bulk of plasma, and is not created by ionization of neutrals left behind.

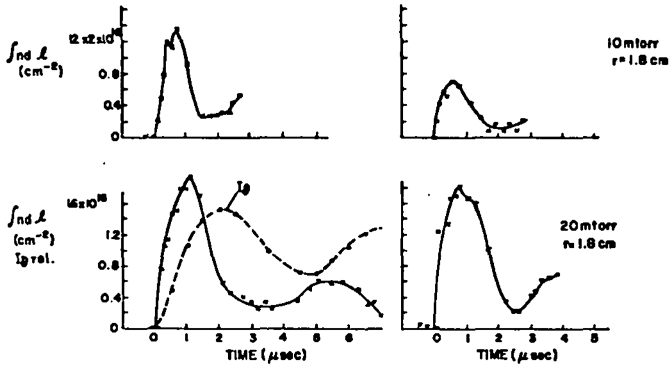

Fig. 69. Integrated density vs time at fixed radius in Scylla IA.

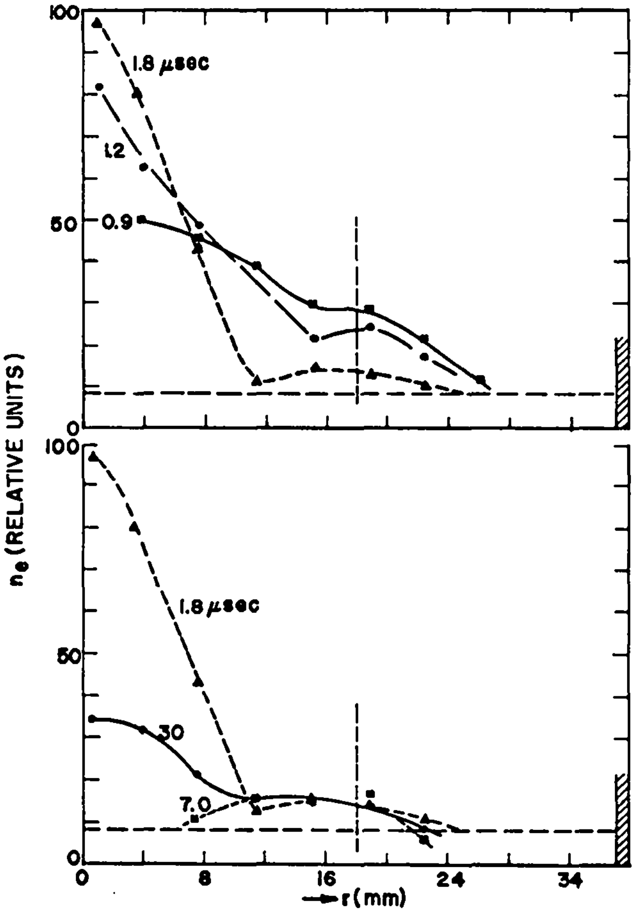

Fig. 70. Relative density profiles of Scylla IA plasma.

Measurements with the New Spark-Gap and Triggering System

With the hard-starting, spark-gap trigger system, described on p. 76 , the plasma properties have changed considerably. In particular, the plasma halo has diminished. In Fig. 71 radial density probiles before and after the rebuilding

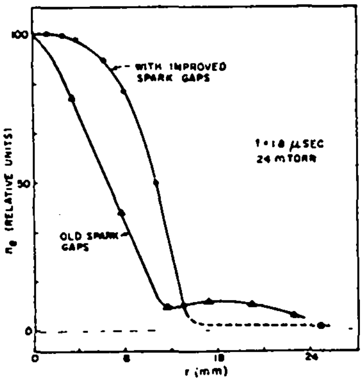

Fig. 71. Relative radial electron densities in Scylla IA before and after modification.

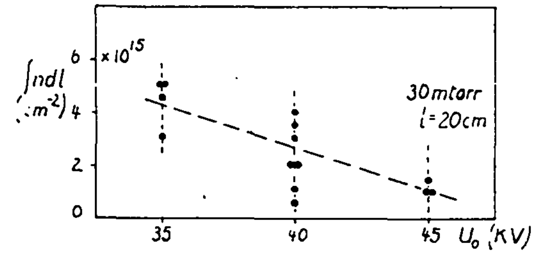

Fig. 72. Line density of the halo at r = 2.5 cm vs bank voltage, U_0.

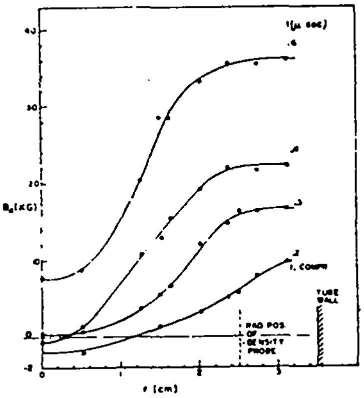

Fig. 73. Radial profiles of B_z for Scylla IA plasma (p_0 = 20 mtorr, U_0 = 40 kV).

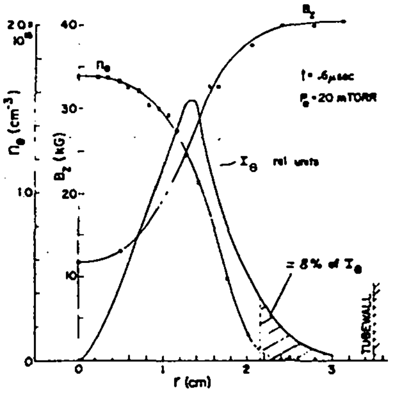

Fig. 74. Values of n_e, I_θ, and B_z vs radius at 0.6 μsec after start of main discharge.

are compared. The steeper density gradients and reduced halo can clearly be seen.

The halo density was remeasured using a gas-laser interferometer. Since the halo density was high enough and since the problem of beam bending by refraction is less severe for the shorter wavelength of the He-Ne laser, the latter was used instead of the CO_2 laser. Halo densities were measured at r = 2.5 cm with p_0 = 24 mtorr and 30 mtorr. At a charging bank voltage, U_0, of 40 kV the minimum halo densities (occurring at about B_z-maximum) were between 3×10^{13} and $3 \times 10^{14}/cm^3$. Within the big shot-to-shot deviations no difference could be found for the two filling pressures. To check the assumption that the halo development is influenced by the magnitude of dU/dt (t = 0), measurements were carried out at U_0 = 35 kV and 45 kV also. The result is shown in Fig. 72, which gives the measured minimum line densities of the halo as function of bank voltage. There is a tendency to lower halo densities with increasing voltage; however, the high shot-to-shot deviations and the rather poor statistics so far should not be disregarded. This would be in accordance with the observed reduction of plasma halo by the improvement of the spark gaps, i.e., higher dU/dt (t = 0).

To get the fraction of the total plasma current flowing in the halo, B_z was measured in the plasma. A B_z-probe with six coils (coil distance 0.5 cm, shielded with slotted hypodermic tubing, ceramic coated, over-all diam = 2.5 mm) was used. Figure 73 gives the radial B_z profiles at various times after the start of the main discharge and Fig. 74 gives an evaluation of I_θ at t = 0.6 μsec together with a density profile. It is seen that at this time, when a well-defined central plasma core has developed, about 8% of I_θ flows outside the high-density core, i.e., in a zone where $n_e \leq 5 \times 10^{14}$ /cm^3.

One somewhat strange observation should be mentioned in connection with these measurements. Figure 73 shows that there is reversed B_z field (up to 2 kG) present in the center of the plasma but only at about the time of the first and second maximum compression. Careful measurements of the field trapped in the PI-discharge show it is < 10 G and therefore cannot cause the observed reversed B_z.

DYNAMIC STABILIZATION EXPERIMENTS ON SCYLLA III INVOLVING KRUSKAL-SHAFRANOV, m = 1 MODES

(G.A. Sawyer, K.S. Thomas, M.H. Thomas, D.M. Weldon, E.L. Zimmermann)

Introduction

Experiments were performed on Scylla III to investigate the effects on plasma stability of running high-frequency alternating currents and direct currents down the z axis of the plasma. These experiments have relevance to Scyllac design in that stabilization of the Haas-Wesson instabilities predicted to occur in the "M and S" configuration used in Scyllac will probably require some form of dynamic stabilization. A study was made of the Kruskal-Shafranov (K-S) instability with quasidirect and high-frequency currents.

Scylla III Modification and Dynamic Stabilization Apparatus

A 1-m coil was attached to Scylla III and the previously used vacuum spark gap crowbar was replaced with a pair of dielectric switches. This has given the Scylla III device the following characteristics:

Half period	3.4	μsec
B_{max}	27	kG
Modulation due to crowbar	100	%

The dynamic stabilization apparatus consists essentially of 1 μF in high-Q capacitors and five parallel coils which form a multi-loop LC resonating circuit (Fig. 75). The inductance also serves as the primary of a transformer coupled to the plasma column as the secondary. To operate the device, the capacitor bank is charged up and then connected to the inductance by closing a dielectric switch. By a minor modification the bank can also serve as a quasi-dc source to excite K-S modes. The properties of the dynamic stabilization devices are given below:

τ (high-frequency)	1.3	μsec
τ (quasi-dc)	6	μsec
I_{max} (dc, V = 41 kV)	39	kA
I_{max} (high frequency, V = 45 kV)	33	kA

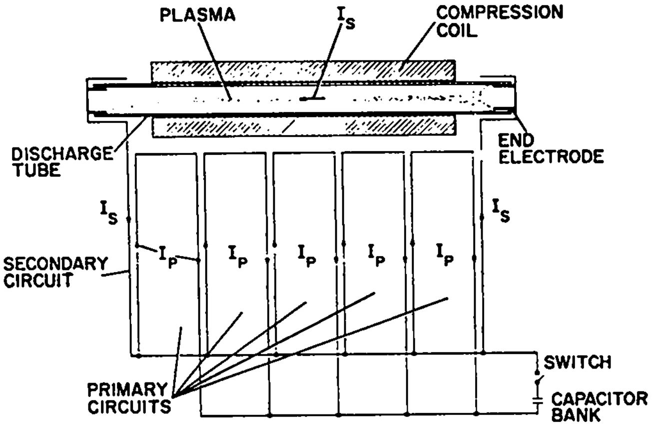

Fig. 75. Schematic of dynamic stabilization system.

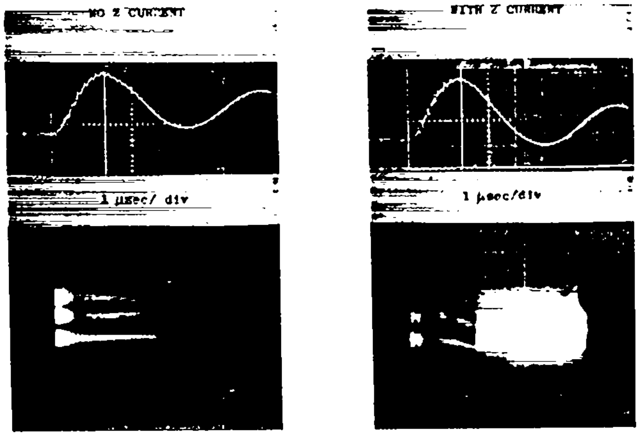

Fig. 76. Streak photographs showing m = 1 instability in Scylla III; oscillograms are B_z.

Apparatus

Three different methods were used to study the plasma: streak photography, holographic interferometry, and measurement of the ratio of current in the dynamic stabilization device to the z-current through the plasma. Streak pictures were taken at three points, one at the center of the coil and one 25-cm from each end of the coil. A system of mirrors collected light from all three slits and brought the images to a single streak camera. Only movement of the plasma in the horizontal plane was measured by streak photography.

The holographic interferometry was used to measure the density of the plasma column at various times after application of a z-current. Measurement of secondary and primary currents gave a rough indication of the effective radius of current through the plasma because the inductance of the secondary depends on the radius at which the current is being carried.

Results of Experiments

No Z-Current

A slight motion (1-2 cm in 4 μsec) of the whole plasma column toward the θ-pinch feed slot is observed with no z-current applied. This effect was identified as due to the dynamic stabilization feed plates connected to the ends of the discharge tube. It was eliminated by slotting the feed plates in the horizontal plane to allow passage of magnetic flux from the θ-pinch.

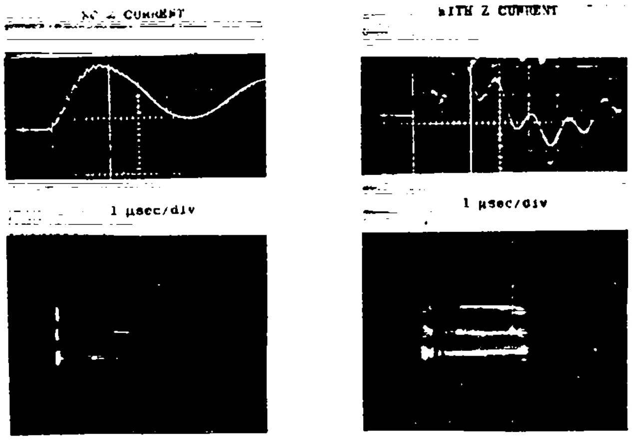

Fig. 77. Streak photographs showing plasma column with oscillating longitudinal current. (There is a high-frequency pickup in the B_z oscillogram on the right from the fast I_z circuit.)

Quasi-DC

Kruskal-Shafranov modes similar to the type found on Scylla IV were also found on Scylla III; the streak photograph in Fig. 76 shows an m = 1 instability driven by a longitudinal current of 35 kA. Growth rates are roughly the same order of magnitude as those found in Scylla IV. Interferograms showed that the plasma had a maximum density of the order of $2 \times 10^{16}/\text{cm}^3$ and that under the effect of a direct current in the z direction it tended to move upward and away from the θ-pinch feed slot. It also frequently appeared to be elliptical in cross section with the long axis vertical.

Oscillating Currents on Scylla III

The dynamic stabilization apparatus produced high-frequency currents of about 30 kA through the plasma with the voltages which could be safely put on the dynamic stabilization apparatus. Figure 77 shows that, even though the oscillating longitudinal current (30 kA) had a magnitude sufficient to excite the K-S mode in the quasisteady case, no instability occurred. This demonstrates the principle of dynamic stabilization.

Oscillating Currents

The dynamic stabilization apparatus was also run on Scylla IV. The feed point drift mentioned above, which was caused by asymmetry in the dynamic stabilization feed plates, was pronounced on Scylla IV. At this time Scylla IV had three axisymmetric bumps ($\Delta B_e/B_e = -0.22$), and the drift initiated a rapidly growing $m = 1$ Haas-Wesson instability. There was a slight indication that the dynamic stabilization z-current had a stabilizing effect on the instability. However, when the asymmetry was eliminated by slotting the feed plates, no instability, either Haas-Wesson or Kruskal, was observed up to currents of 30 kA at 800-kHz frequency for the collisionless plasmas being observed.

DIFFUSION AND TEMPERATURE LIMITATIONS IN $\beta \approx 1$ θ-PINCHES

(A. A. Newton)

In zero bias θ-pinches electron thermal conduction along the plasma to cold regions outside the coil has been shown to limit the electron temperature attainable.[1] A model has been constructed to explore this powerful cooling mechanism in reversed bias θ-pinches.

With reversed bias field early rapid diffusion generates a $\beta \approx 1$ plasma[2-5] with strong self-mirrors and a lifetime long compared to an ion transit time along the plasma. In this case particle loss is assumed to proceed by radial diffusion into a boundary layer or sheath and then by flow along the sheath which extends as a narrow cylinder to cold regions beyond the confines of the coil. Inside the sheath there is a $\beta \approx 1$ plasma with a cross-sectional area large compared to that of the sheath in the midplane but which collapses to zero near the ends of the coil.

Particle losses from this configuration have been analyzed[6], neglecting joule heating and thermal conduction. Thermal loss becomes important when the electron mean free path in the sheath exceeds $(m_e/m_i)^{\frac{1}{2}} L_e/2$ (L_e is the coil length).[1] As joule heating raises the temperature, the diffusion and dissipation rates decrease. Conduction losses increase steeply with temperature so that the latter should stabilize when joule heating balances the conduction loss, provided other sources and sinks are small. Thus the particle flux entering the sheath depends both on the resistivity and the pressure gradient and is determined by heat balance in addition to the continuity of radial and axial particle flow.

The coupled loss mechanisms can be analyzed dimensionally by seeking the equilibrium temperature at which joule heating equals the thermal loss and diffusion into the sheath equals the particle effusion loss. Consider a $\beta = 1$ plasma of radius R and length L, located in the midregion of the coil. It is bounded by a thin sheath of thickness Δ which collapses to a radius a ($a \ll R$) beyond the plasma and extends in a spindle for a distance ℓ to the cold regions outside the coil.

Magnetic flux is conserved through the sheath and spindle. The plasma and sheath are isothermal with $T_e = T_i$, and the temperature gradient is confined to the spindle. All sources and sinks of energy other than joule heating and thermal conduction are neglected, except for compression heating due to the plasma collapse which is set equal to the energy lost by effusion. The crowbarred condition, i.e., constant magnetic field, B, is assumed.

Then the power gain from joule heating $\sim \eta j^2 \, 2\pi R \Delta \ell$ (where η is the resistivity and $j \approx B/4\pi\Delta$) equals the heat loss along both spindles $\sim 2\pi a^2 K_e \, \partial T/\partial z$ ($K_e = K_o T^{\frac{5}{2}}$ is the thermal conductivity). The flux of particles entering the sheath by diffusion $\sim \eta n \, 2\pi RL/8\pi\Delta$ equals the effusion loss $\sim 2nv_z \pi a^2/4$, where n is the density. If the effusion velocity is thermal, i.e., $v_z = k^{\frac{1}{2}} T^{\frac{1}{2}}$, it follows that the equilibrium temperature is

$$T^3 = \frac{7}{16\pi} \frac{k^{\frac{1}{2}}}{K_o} B^2 \ell. \tag{1}$$

It is remarkable that T contains neither the magnitude nor the temperature dependence of η, so that any dissipative mechanism which leads to heating and diffusion as described above will produce the same result. Published data[2-5] are insufficiently detailed for a thorough test of Eq. 1, but it is noteworthy that the limiting temperature has not been exceeded.

N. J. Phillips[6] has found that the plasma lifetime is

$$\tau = \frac{15}{32}\left(\frac{VT}{k^{\frac{1}{2}}\eta_o}\right)^{\frac{1}{2}} , \tag{2}$$

where $V = \pi R^2 L$ is the plasma volume. The same result can be derived from the dimensional analysis using $\eta = \eta_o/T^{\frac{3}{2}}$, $\pi a^2 = 2\pi R\Delta$, and $\Delta^2 = \eta L/\pi v_z$, except that an additional factor ~ 6 appears. It is reasonable to conclude that Phillips's analytical result is valid in the presence of energy loss provided a temperature consistent with Eq. 1 is used. (Additional factors are possible in Eq. 1, although their effect is less important because the temperature occurs to the third power.)

Observed plasma lifetimes[2-5] agree with Eq. 2 to within a factor of ~ 2-3. Bohm diffusion over the whole plasma-sheath interface can be excluded since it leads to a decrease by a factor of ~ 5-10 in τ. The quoted interpretations of lifetimes using dimensional theory conflict on whether the diffusion is Bohm-like or classical. Clearly comparisons are only valid if made with a precise theory and a two-dimensional numerical calculation is to be preferred.

Finally it is worth noting that the limiting temperature of Eq. 1 precludes an open-ended pulsed thermonuclear reactor of reasonable dimensions even with the maximum magnetic fields presently attainable.

References

1. T. S. Green, et al., Phys. Fluids 10, 1665 (1967).
2. A. C. Kolb, et al., IAEA Conference, Culham I, 261 (1965).
3. A. Kaleck, et al., Proc. APS Topical Conf. on Pulsed High-Density Plasmas, Sept. 1967, LA-3770-MS Paper A-4.
4. E. A. McLean, et al., ibid., Paper A-5.
5. T. K. Allen, et al., ibid., Paper G-4.
6. N. J. Phillips, Proc. Phys. Soc. 77, 965 (1961).

HOLOGRAPHY

(F. C. Jahoda)

With the increasing use of holographic interferometry as a standard diagnostic technique on various Sherwood experiments it becomes increasingly desirable to be able to make multiple-frame interferograms in the course of a single discharge. Renewed attention has therefore been given to two potential methods.

In the first, a portion of a single ruby laser Q-switched giant pulse is stored in an optical delay line and then with appropriate optical elements after the delay line a second scene beam is superposed on the scene beam location of the undelayed direct pulse (i.e., sent through the plasma) while a second reference beam is displaced sufficiently from the undelayed reference beam to expose a different position of the hologram film. Two independent interferograms are thus produced by the usual method of two consecutive laser firings, with and without plasma present. The limitations are set by the intensity transmission and total delay time that can be achieved with the delay line.

With 3-in. diam high-reflectivity, dielectric mirrors, one plane mirror and one concave mirror of 10-m focal length, separated by about 5-m, 0.4-μsec delay (24 transits) was reached relatively easily. The finite size of the 45° entrance and exit mirrors to the delay cavity limits the number of nonoverlapping beam traversals between the main mirrors before the beam is obstructed by these subsidiary mirrors. In this case the intensity loss is severe but an interval of 0.2 μsec appears to be more practical. Larger mirrors of higher reflectivity or a more intense laser could improve on these times, but the method, at the moment, is cumbersome and inflexible and would be useful on a plasma only in the special circumstance that two such closely spaced interferograms are particularly desirable.

A second method promises much greater versatility. This is the so-called "live fringe" method, whereby a single holographic exposure is accurately replaced after development, and interference is produced between the reconstructed object (the original reference beam being now the reconstruction beam) and the object itself (now slightly altered by the presence of plasma, say) illuminated by what was the scene beam during the hologram recording. If the laser source is of sufficient duration, the time history of the changing interference structure can be followed with, e.g., an image-converter framing camera, observing the plasma directly through the hologram.

Several potential troubles in making this method workable have been overcome. Thus, photographic plates (rather than film) mounted in a special jig that goes through the dark-room processing and can be accurately repositioned have proved adequate in a CW He-Ne laser (long exposure times) version of this method.

Of more significance, the chilled Hughes ruby laser (used previously on Scylla IV), which stays on in excess of 100 μsec (some modulation but no dead time), makes good quality holograms despite there being no mode selection whatsoever, since both end mirrors are coatings on the ruby itself. To achieve this, however, the path lengths of reference and scene beams must be closely equal and a pinhole (0.04 in.) used that wastes most of the available laser energy. There is ample energy left in the time-integrated pulse to make the hologram, but the reconstructed image intensity is marginal for the framing time of the Beckman-Whitley image converter. Because these are only 1-frame units, in a working system several units must be used with further intensity losses due to beam splitting. Nevertheless, the threshold usefulness has been reached in the initial attempts, so that further effort on the reconstruction intensity seems justified and is in progress.

A single-frame live-fringe interferogram of an exploding wire has been produced with a giant-pulse ruby laser, where the intensity is sufficient to demonstrate the principle.

THREE ELECTRODE CASCADE SPARK-GAP DEVELOPMENT

(R. F. Gribble, D. Brown, C. F. Hammer, J. A. Meyer, T. D. Langham)

Introduction

Considerable effort has been devoted to revamping the start gap, presently in use in Scylla IV, with a view to providing a harder starting gap with less jitter for Scyllac. As previously used at 50-kV in Scylla IV, this gap was not "cascading" properly, resulting in a soft start of the θ-pinch (partially made up by the high voltage and large transfer efficiency). The gap has been redesigned and 36 were tested on Scylla IA with good results. On Scylla IV, 350 gaps with fast trigger are being installed for a large-scale test at 50 kV. The gap design is essentially final for Scyllac.

Gap Operating Modes

The four-electrode gap of the general Scylla variety (Fig. 78) has what may be called four modes of operation: simultaneous, fast swinging cascade, inverse cascade, and slow cascade. These define the sequence and manner in which the gaps operate. The three gaps in a four electrode switch are defined in the order in which they are intended to break down: gap zero, the illumination spark; gap 1, the first main breakdown caused by the trigger voltage; and gap 2, the connecting breakdown resulting from other factors, depending on the mode. Henceforth, "gap" will refer to gap 1 or 2, the upper gap will refer to that between the top or output electrode and the center electrode, and the lower gap is that between the center electrode and the load capacitor electrode. Further, ℓ_1 is the spacing of gap 1, and ℓ_2 is that of gap 2. Gap 1 is usually the lower one, and gap 2 is the upper one although this is not necessarily always the case.

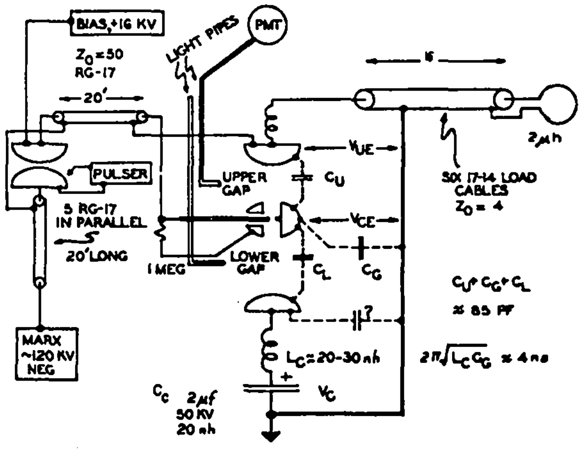

Fig. 78. Schematic diagram of apparatus for testing cascade spark gaps.

In the simultaneous mode, breakdown processes are begun simultaneously in both gaps as the center electrode is swung and both gaps connect within a few nsec of each other. This mode is desirable in that jitter and delay are minimal and the gaps start hard; the load cables are charged rapidly due to the low gap resistance. However, this operation is strongly dependent on capacitor voltage, trigger rise time, gap spacing, and pressure, and is very difficult to achieve for many gaps in parallel. The trigger voltage rise must be "faster" than breakdown processes.

The fast swinging cascade mode employed at Culham seems to be the most reliable method of operation. Here C_G (Fig. 78), charged to the trigger voltage, forms a closed loop with L_c, C_c and gap 1, the lower gap, as gap 1 conducts. When dI/dt in this circuit changes sign, the voltage across L_c adds positively to V_c, swinging the center electrode positive and rapidly overvolting gap 2 beyond V_c. However, in the old design C_G-L_c forms a 250-MHz ringing circuit and hence the overswing does not last long enough (half-period of 2 nsec) to produce a hard breakdown at the peak.

With $\ell_2 = \frac{1}{4}$ in. and a $\frac{3}{4}$-in. center electrode hole, the overswing produces a *sufficiently* high E-field for almost complete breakdown during the overswing, with the result that load current conduction begins within 10-30 nsec after the first overswing, depending on V_c and gap pressure.

In the slow-cascade Scylla IV mode the overswing following gap 1 (the lower gap) breakdown is not sufficient to cause immediate gap 2 breakdown, either because the amplitude is insufficient or the breakdown is too soft. But because the trigger cable is connected across the center and upper electrodes the trigger current flows through the load. While this current is increasing, the voltage developed across the load is such as to make the top electrode positive, decreasing the voltage across gap 2 (the center electrode is at + 48 kV). Gap 2 does not break down until the trigger current begins to decrease, making the top electrode negative and thus increasing the voltage across gap 2. But the changing voltage on the upper electrode is relatively slow (0.4-μsec half period, ~ 80-kV maximum), and hence gap 2 breakdown is soft. This mode and soft starting (much slower start than any fast cascade starting observed) has been realized with $\ell_1 = \ell_2 = \frac{1}{2}$ in., even with a fast trigger. The load voltage rise to peak on Scylla IV is 80 nsec. For fast θ-pinch operation it would be desirable to use a hard starting load spark gap.

The Culham group connect the trigger cable from center electrode to the load cable outer conductor, thus preventing trigger current from flowing into the load, since gap 1 is the lower gap. This would improve the operation of the LASL gap in the fast-cascade mode because it would prevent the initial drop across the load cables (about 16-kV for an 80-kV trigger) from reducing the gap 2 voltage on gap 1 breakdown. It has not been used, however, because such a trigger cable connection would result in an unfavorable prefire condition as the PI voltage appears across the load gap. This is due to the capacitive divider effect of the effective trigger cable capacitance connected across gap 1, the long gap. It is desirable that the PI voltage be divided across the gaps in the ratio of their spacing or at least it must appear across the long gap. Because, in the more desirable connection, the trigger current flows in the load, precise measurement of gap 2 delay of more than 48 nsec, i.e., the load cable double transit time, is difficult, as the voltage rise due to the reflected current has the same appearance as a soft starting gap 2. Reflections back from the trigger source 60 nsec following gap 1 breakdown also complicate the picture. These reflections frequently cause abrupt changes in light emission, although of lesser magnitude than the main load current.

The last mode to be discussed, the inverse cascade, occurs when gap 2 breaks down before gap 1, the unintended order.

Measurements of Gap Performance

A trigger circuit was built that can deliver to an open circuit RG-17 50-Ω coaxial cable a fast pulse of 60-nsec duration that rises to 300-kV in 4 nsec or less. For most of the work to date 160-kV pulses have been employed with this fast trigger; the behavior of the 50-kV load gap used in Scylla IA and several modifications of it have been studied. Pressurizing the gaps to 5 and 25 psig appears to be desirable.

The trigger circuit constructed for the work consists of five 50-Ω RG-17 charge cables, one RG-17 output cable, and a simple overvolted (but illuminated) two-electrode spark gap that connects the two sets of cables. A Marx circuit produces a rapidly rising voltage on the cables variable from 60 to 150 kV. The trigger gap consists of the top and bottom electrodes of an old original Scylla I gap and a porcelain insulator with a $\frac{1}{4}$-in. nylon spacer added. The gap spacing is $\frac{3}{4}$ in. Preillumination is provided by a small Scyllacita spark plug buried in the charge electrode. With the preillumination and 35-psig air in the gap, the output pulse is quite stable, having a value between 75 and 85 kV and a rise time of less than 4 nsec. When operating into a load spark gap the pulse doubles and is slowed by the RC of the cable Z and the electrode C (RC $\approx$ 5 nsec).

Only two types of measurements have been made on the gaps: voltage and light emitted. Capacitive voltage dividers are connected to the top and center electrodes of the gap and rigid light pipes are inserted in shallow holes in the gap insulators, as shown in Fig. 78, to observe the light emitted at each gap. The capacitive dividers were developed and constructed at LASL.

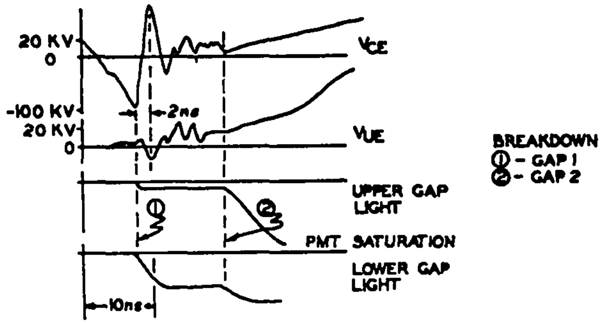

Fig. 79. Approximate waveforms for fast-cascade mode of three-electrode spark gap operation.

A 1500-pF ceramic feedthrough capacitor C is soldered into a BNC cable connector, and a resistor R of 10 kΩ is soldered between the feedthrough capacitor and the center conductor fitting of the connector. The outer end of the capacitor is soldered to a bare braided strip which is wrapped around a high-voltage cable to provide the small high-voltage capacitor of the divider. The rise time of the divider was measured to be 2 nsec with a 2-nsec rise time source. A faster source is being constructed to measure the response more accurately. The overshoot is small, and the e-folding fall time is RC.

To observe the light emission of the gaps, a selected 931 photomultiplier was installed in a double shielded housing. Gap breakdown is usually inferred from a sharp break in the PM signal; however, simultaneous observation of electrode voltages is frequently necessary due to ambiguities in the PM signal caused by cable reflections.

Results

Waveforms of fast swinging cascade operations are shown in Fig. 79; they were obtained at 500-torr gauge pressure, 48-kV capacitor voltage, and 80-kV trigger. The characteristic voltage overswing of the center electrode, which causes breakdown of the upper electrode and overall "hard" operation, is shown in the top oscillogram.

Use of air at pressures above atmospheric has several advantages. Obviously voltage hold-off is increased and prefiring is reduced as the pressure is increased. But more important is the fact that spark channel formation times are reduced with increasing pressure. This effect was clearly seen as a decrease of the delay from the start of the trigger to complete conduction and also a decrease in jitter as a function of pressure.

A summary of the observations is given below.

1. $V_C = +48$ kV, $V_{trigger} = 80$ kV, $\ell_1 = \ell_2 = \frac{1}{2}$ in., $\frac{1}{4}$-in. center hole. Slow cascade mode as in old Scylla IV. Ten shots in each run.

Run	Gap pressure, (torr)	Delay (nsec)	Jitter (nsec)
1	10	290	~ 20 ± 10
2	60	312	~ 20 ± 10
3	180	320	~ 20 ± 10
4	60	300	~ 20 ± 10

Note that delay is strongly dependent on pressure and that the trigger voltage appearing across the load was changing about eight times faster than it does for Scylla IV (80-kV peak component to 11 kV, same period).

2. Same as No. 1 but center electrode hole = $\frac{3}{4}$ in. diam.
   Same results as No. 1.

3. -80-kV fast trigger (~ 7 nsec), $\ell_1 = \frac{1}{2}$ in., $\ell_2 = \frac{1}{4}$ in., $\frac{3}{4}$ in. center hole.
   Best operation at 400-600 torr (8 to 15 psig) pressure
   Operating range: 40-50 kV
   Delay: 20-35 nsec. Jitter: 1-10 nsec
   Fast-cascade mode but never simultaneous mode
   Hard starting
   Prefires at $V_C = 53$ kV for pressures < 50 torr.

4. -80-kV slow trigger (~ 20 nsec) $\ell_1 = \frac{1}{2}$ in., $\ell_2 = \frac{1}{4}$ in., $\frac{3}{4}$ in. center hole
   $V_C = +48$ kV, 500 torr pressure
   Fast-cascade mode
   Medium hard starting
   Delay 43 to 58 nsec in five shots
   Operation is reliable at 48 kV, not at 42 kV.

5. Same as No. 4 but -40 kV slow trigger (~40 nsec)
   $V_C = 48$ kV, 500 torr pressure
   Delay, 78 to 110 nsec, five shots
   Operation at 48 kV very marginal
   Fast-cascade mode.

6. Same as No. 3 but ¼-in. center electrode hole instead of ¾ in.

Data have not been analyzed but delays and jitter appear to be 50% greater than that for a ¾-in. hole.

The inverse-cascade mode occurs when the trigger polarity is the same as V_C, the load capacitor potential, or in the case of $\ell_1/\ell_2 = 2$ at $V_C \leqslant 40$ kV, depending on the pressure. This occurs at 20 psi and $V_C = 40$ kV, and for all pressures where $V_C < 30$ kV. At 50 torr and $V_C = 32$ kV it occurs in about 50% of the shots. This mode is highly undesirable because the delay is from 50 to 300 nsec for $V_C = 48$ to 40 kV and the jitter is rather considerable. The cause for this mode is obvious for low V_C; the avalanche electric field is first reached in gap 2. For larger V_C at the higher pressures the mode is still possible because the breakdown field may still occur first in gap 2 even though the field was initially greater in gap 1. If V_{CE} is the center electrode potential to ground, the ratio of electric fields in the two gaps is $|E_{G2}/E_{G1}| \simeq 2V_{CE}/(V_C - V_{CE})$. The gap 2 field rapidly exceeds that of gap 1 at the higher pressures where the fast breakdown field is large.

At 600 torr and 48 kV, gap 1 rapidly conducts where V_{CE} reaches about -100 kV. At breakdown, then, for $\ell_1/\ell_2 = 2$, gap 2 has 4/3 the field of gap 1, but gap 1 breaks down first. Clearly the breakdown process in gap 1 begins sometime before $V_{CE} = -100$ kV. Since these conditions yielded the least delay and jitter, it is likely that breakdown had started in gap 2 by the time gap 1 had capitulated. At $V_C = 48$ kV and at a pressure somewhere between 15 and 20 psig, simultaneous mode operation must occur since, as was pointed out earlier, gap 2 broke down a few nsec before gap 1 at 20 psi, 48 kV, in still an essentially simultaneous mode.

The Selected Gap

The spark gap selected for testing in a multiple-capacitor, parallel system represents the least modification of existing designs. A standard center electrode is modified by enlarging the center hole from ¼ to ¾ in. diam, rounding the hole edge to ¼-in. radius of curvature, and adding an aluminum ring to the center electrode structure to increase the center electrode capacitance to ground by about 100 pF. The major change from existing design is reduced gap spacings in the ratio 2:1 and the use of air pressure > 1 atm. In addition, it was found that charging the load capacitor negatively greatly improved the gap performance over that for positive charge.

When using this center electrode geometry with a lower gap spacing of ½ in., upper ¼ in., gap pressure 14 psig, and load capacitor charge -59 kV, the average delay was 34 nsec, and the RMS jitter was 2 nsec in 50 samples taken from 1100 shots. The center electrode swing was 80 kV in 22 nsec to gap 1 breakdown. After 6 nsec the overswing reached a peak of -80 kV relative to the upper electrode. Gap 2 breakdown occurred 4-6 nsec after the overswing peak. The gap did not operate satisfactorily for positive charge < 55 kV, whereas its useful range extends down to 40 kV for negative charge. At 59 kV the delay was reduced by a factor of 2 and the RMS jitter by a factor of 5 by charging negatively.

Use of the grooved set of insulators was found to produce very good static hold-off. At 90 kV, 14 psig the gap would hold all day and at 20 psig it would take 95 kV indefinitely; however, at 2 psig the hold-off voltage was only about 55 kV.

Installation on Scylla IA

As a reliability test, the 36 Scylla IA gaps were modified to the selected gap specifications and the triggering system was replaced. Several minor problems were encountered in the triggering system, but these have been resolved. A difficulty with load gap prefiring was removed.

The load gap modification consisted of adding a capacitance ring to the center electrode, boring the center electrode hole to ¾-in. diam and shortening the upper gap by reducing the upper insulation length to 1.700 from 2.000 in. The capacitance ring consists of an aluminum tube 1½-in. long, 7.00-in. i.d. and 7.250-in. o.d. The ring increases the net center electrode capacitance to about 250 pF. By boring the center electrode hole to ¾ in. and rounding the edge to ¼-in.

curvature, the lower gap spacing was increased to 0.60 in. with a 2.000-in. insulator. The upper gap spacing is 0.30 in. with the 1.700-in. insulator. In addition, five $\frac{1}{8}$-in. x $\frac{1}{8}$-in. grooves were cut in both insulators. A $\frac{3}{16}$-in. tungsten pin was added to the center electrode to meet the spark plug pin for a spark plug gap of $\frac{1}{16}$ in. The 100-kΩ resistor connected between the spark plug and the center electrode was replaced with two series 75-Ω, 2-W carbon resistors to decrease the probability of a PI caused prefire. *After the interruption for* modification of the trigger system and the load gaps, plasma experiments were started again.

With the improved system the plasma properties have changed considerably, presumably as a result of the faster voltage rise. Under otherwise identical initial conditions as before (20-mtorr, 40-kV, Δt between PI and main bank = 14 μsec, PI about as effective as before) the neutron output has increased a factor of 2, which corresponds to an increase in T_i of about 150 eV. Streak pictures show a much better defined ingoing plasma sheath and a less diffuse plasma column. In addition, the plasma halo has diminished. Individual gap jitter for about 10 gaps monitored is < 2 nsec and the variation between the monitored gaps is less than 10 nsec. Part of this variation is due to different trigger cable lengths, and part is probably due to machining tolerances.

Trigger System for the 3-Meter Modified Scylla IV

A trigger system has been proposed for Scylla IV-3 that will employ components designed for Scyllac and provide a trial for the proposed Scyllac trigger system. Preliminary measurements indicate that the trigger gap will yield a pulse similar to that used in developing the fast load gap.

Three gap spacings have been tried on the submaster gap that employs Scylla I type electrodes. Near atmospheric pressure was used with a total gap spacing of 1 in. The gap inductance was about 100 nH. For $\frac{9}{16}$-in. spacing 20 psig was required and the inductance was 60 nH. For the third trial, gap spacings of $\frac{1}{8}$ and $\frac{1}{4}$ in. were used for a total of $\frac{3}{8}$ in. This gap broke down at 100 kV with 40 psig. The minimum operating gap pressure was 45 psig and the resulting gap inductance was about 45 nH; this gave a 28-nsec delay to the ~ 130-kV breakdown potential of gap 1 of the load gap (80 kV trigger + 50-kV capacitor charge).

Trigger transformers for triggatron buffer (10 kV) and for master gap trigger (100 kV) circuits were investigated. Two types of ferrite cores were tried for the triggatron circuit and Ferroxcube-144T500 cores were chosen. A 10-kV pulse was applied to the primary. With four primary and 12 secondary turns on two-stacked Ferroxcube cores the delay to 20 kV was 28 nsec. The other investigation involved the large laminated iron cores used for triggering master gaps. A total delay of 75 nsec to 100 kV was obtained with 20 kV applied to a one-turn primary with six secondary turns.

PIGGY-BACK CROWBAR DEVELOPMENT

(R. F. Gribble and J. A. Meyer)

The piggy-back crowbar switch development has been continued with renewed interest. The first version was impractical due to the rather large trigger energy requirement. It was hoped that by increasing the gap pressure this requirement would be reduced, but such was not the case. The Garching group have successfully utilized ferrite in a crowbar switch to isolate the trigger electrode for triggering in such a manner that the ferrite saturates when the switch closes, reducing the gap induction to a reasonable value. By adding toroidal ferrite cores to the original geometry, a crowbar switch with reasonable trigger energy requirements has resulted.

The new geometry also uses ferrite to introduce a saturating inductance in series with what was formerly the grounded electrode containing the trigger pin. Trigger current passing through the trigger pin and the ferrite inductance is initiated $\tau/2$ before the load current peak, where τ is the trigger period. The initial polarity of the trigger is the same as that of the load capacitor so that the first voltage spike produced by the ferrite does not break down the crowbar. Air surrounding the trigger pin in the crowbar is ionized during the first trigger half-period. When the trigger current reverses, the ferrite flux ideally switches saturation polarity, producing a voltage pulse across the crowbar gap and closing it. The advantages of this scheme over the Garching method are that the ferrite does not require biasing and the gap is heavily preionized. A high-voltage capacitor is required, however, since the magnitude of the closing pulse can be no greater than the potential across the trigger capacitor at the end of the first half-cycle.

Reasonable operation has been obtained with a 75-kV trigger capacitor delivering 10-kA peak. The crowbar was operated at 10 psig where 4 psig is the minimum pressure to prevent a crowbar prefire at the load gap firing. The data of Fig. 80 show the results obtained under these conditions.

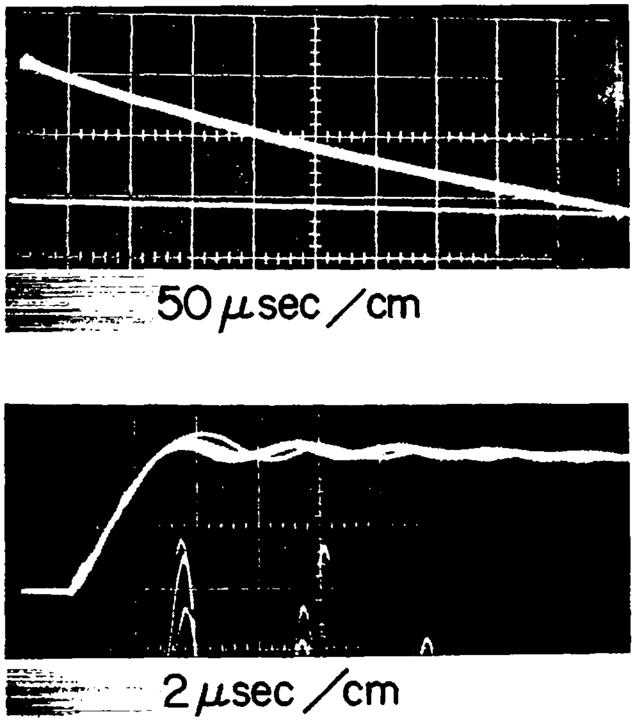

Fig. 80. Waveforms of piggy-back crowbar load current in a circuit with two capacitors and inductance scaled to the Scylla IV load.

EXPLODING-FOIL DIELECTRIC CROWBAR SWITCH DEVELOPMENT ON SCYLLA IA AND SCYLLA III

(V.A. Finlayson, G.A. Sawyer, J.D. Smith, M.H. Thomas, K.S. Thomas, E.L. Zimmermann)

Introduction

Development of the exploding-foil switch (see LA-3831-MS pp. 69, 77) to crowbar the current of Scylla IA has been completed during this report period. In its position at the rear of the collector plate the modulation is excessive for long-time crowbarring. However, it serves quite well as a device to prevent field reversal and loss of discharge tubes. A version of the switch, embedded in the collector plate for closer coupling, and hence giving lower modulation, has been tested on Scylla III.

The Scylla IA Experiments

Extensive parameter studies were made on the physical dimensions of the three switch parts consisting of the contact plate, the foil laminate, and die plate. First, various foil widths using 2-mil copper foil were studied beginning with those used by I. Henins and J. Marshall. The results are shown below as a function of closure time, i.e.,

Exploding Foil Width (in.)	Closure Time (μsec)
0.250	5.0 ± 0.1
0.312	6.2 ± 0.2
0.375	10.0 ± 0.6

the time from beginning of current flow in the foil to current flow in the crowbar switch. A slot width in the die plate of 0.250 in. was found to be the narrowest that would allow good metal flow into the slot. Since alignment is critical for 0.250-in. foil, the 0.312-in. foil was used, thus permitting some error in alignment.

Insulation for the foil laminate was studied next. The foil laminate must be insulated for the high-voltage inductive kick when the foil explodes. The copper foil is laminated between two pieces of $\frac{1}{32}$-in. polyethylene plastic at high temperature and pressure.

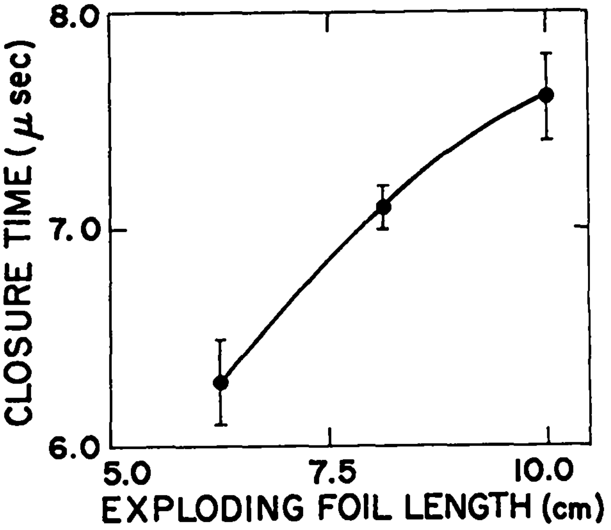

Fig. 81. Switch closure time vs foil length.

Tests have been made concerning the length of the exploding foil section, and values of foil length vs closure time are plotted in Fig. 81. All tests were conducted using a 14-μF capacitor at a charge voltage of 20 kV. The longer foil was characterized by longer closure time and less depth of penetration of metal into the slot. Closure was uniform, however, along the length of all switches tested; hence, it appears that longer switches could be used provided sufficient energy is supplied, as will be explained below.

Three criteria determine the contact plate thickness. First, it must be thin enough to be driven without too great resistance to the explosion, but it must be thick enough to both carry the current and make deep closure contact. From skin depth calculations, if half of the plate is driven into the slot, then 0.062-in. aluminum yields a penetration time of about 21 μsec whereas, 0.096-in. 1100-H17 aluminum gives a penetration time of about 100 μsec. Furthermore, the latter gives a better physical contact due to deeper penetration. Annealing of the aluminum is undesirable because it is softened so much that the plate tears when the switch is operated.

Since Scylla IA is a series machine with two crowbars, one for each side, a complication arises in the study of performance of the switch. If one

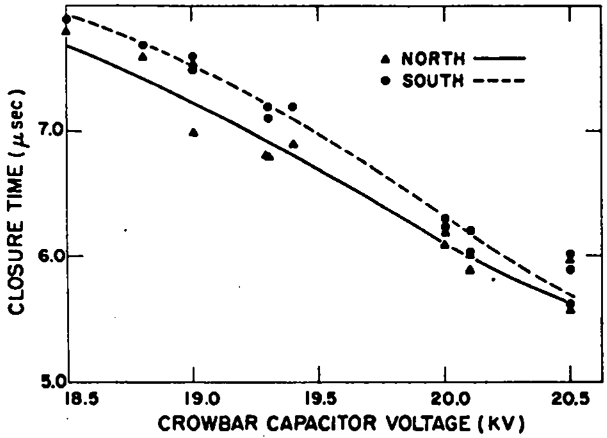

Fig. 82. Switch closure time vs crowbar capacitor voltage.

switch closes early, an overvoltage is produced on the other side of the machine causing the second switch to close sooner than normal. The effect of one switch on the other is seen in all the data so far collected. The foil is exploded using current from a 20-kV, 14-μF capacitor, and the closure time is taken from oscillograms of the foil current. The crowbar current breaks negative if the switch closes early in relation to peak current in the load coil or positive if closure is late. This arises from the fact that there is a two-loop circuit with the main bank in one loop. Modulation and e-folding time are measured on the oscillograms. On the basis of the definition

$$\text{Modulation} = \frac{I_{max} - I_{min}}{I_{max}} ,$$

the best modulation that can be obtained with the present geometry is 60%. When crowbarring 30 kV on the main bank, an e-folding time is ~ 800 μsec.

Figure 82 presents the results of crowbar charge voltage vs closure time. This plot shows the high degree of dependence of switch closure on energy. The two traces indicate the effect of slight energy differences in the two crowbar switch systems.

Exploding Foil

The jitter of the switch is indicated in the table given above for the present 0.312-in. wide foil. A problem closely related to this is the arcing in the switch as a function of closure time. The switch must be closed near peak current where the voltage is zero in order that arcing is kept at a minimum.

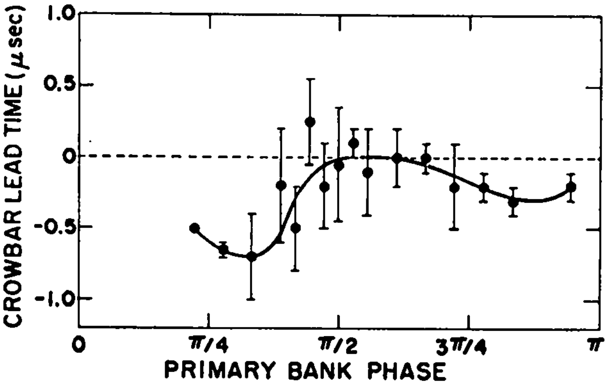

Fig. 83. Time variation in switch closure vs primary bank phase in Scylla IA.

The closure time and arcing are reduced by using less main insulation to be punctured. Earlier, 40 mils of polyethylene were used with a closure time of ~ 12.0 μsec. Presently three sheets of 6.0-mil polyethylene are used with the closure time of 6.2 ± 0.2 μsec and less arcing. Mylar (four sheets of 5 mils each) was tested, but the jitter was far too great, i.e., 6.0 ± 0.6 μsec.

Results of a study made in Scylla IA of closure time vs voltage across the switch are shown in Fig. 83. It will be noted that the switch will close up to 0.7 μsec sooner if closure is made with the main bank voltage across the crowbar switch. The effects of voltage on closure time and arcing are very significant at higher primary bank voltages.

Conclusion Concerning Scylla IA Operation

The present switch when closed near the peak of the load current is carrying ~2 MA with no arcing and an e-folding time of 800 μsec. The modulation, which is 80%, is due to the high inductance in the crowbar circuit, and it can be greatly reduced by putting the crowbar switch into the collector plate. Such experiments are described below.

The switch has been used in hundreds of main bank crowbar shots and has proven to be very reliable. The closure time is presently 5.75 ± 0.10 μsec; hence the jitter is very low from shot to shot.

Scylla III In-Plate Crowbar

An older model of solid dielectric crowbar switch had been used for several months on Scylla III. This switch was attached through an auxiliary collector plate and had 6-nH inductance resulting in nearly 100% modulation of the coil-current waveform.

An in-plate version of the solid dielectric switch with much lower inductance has now been installed. The current modulation has been reduced to ~15%; this is considered to be good performance. A side-on streak picture of the Scylla III discharge shows the plasma to remain stable with a slight wobble beginning at about 8 μsec.

Unfortunately, the switch is inconvenient to load and has suffered considerable damage from the explosive action of the arcing contacts when the switch is closing. This damage is difficult to repair in the in-plate geometry. It appears that the in-plate crowbar which has been planned for Scyllac will be only marginally capable of handling the large currents it must switch and will also be time consuming to load and maintain.

SCAN CONVERTER DEVELOPMENT

(R. F. Gribble, J. W. Lillberg, J. F. Trujillo)

Work has been continued on the scan converter (LA-3831-MS, p. 81) to provide a means of digitizing waveforms for the Scyllac computer control system. A block diagram of the scan-converter system is shown in Fig. 84. A prototype unit of six scan-converter tubes is well along toward completion. Problems encountered during this report period are summarized below.

The scan-converter logic chassis was constructed, as well as a tube simulator to debug the logic and sequential circuitry. A digital-to-analog converter provides a zero average value analog output voltage to relieve the problem of clamping read deflection voltages arising from capacitive coupling. Read analog circuitry was designed and constructed. The vertical read deflection amplifier has an open-loop gain of about 30,000; multiple feedback loops reduce the gain to 12 to provide a 60-V step response settling time to better than 0.2% in less than 400 nsec. The direct-coupled read current amplifier has been found to be stable, but signal-to-noise problems may require that the

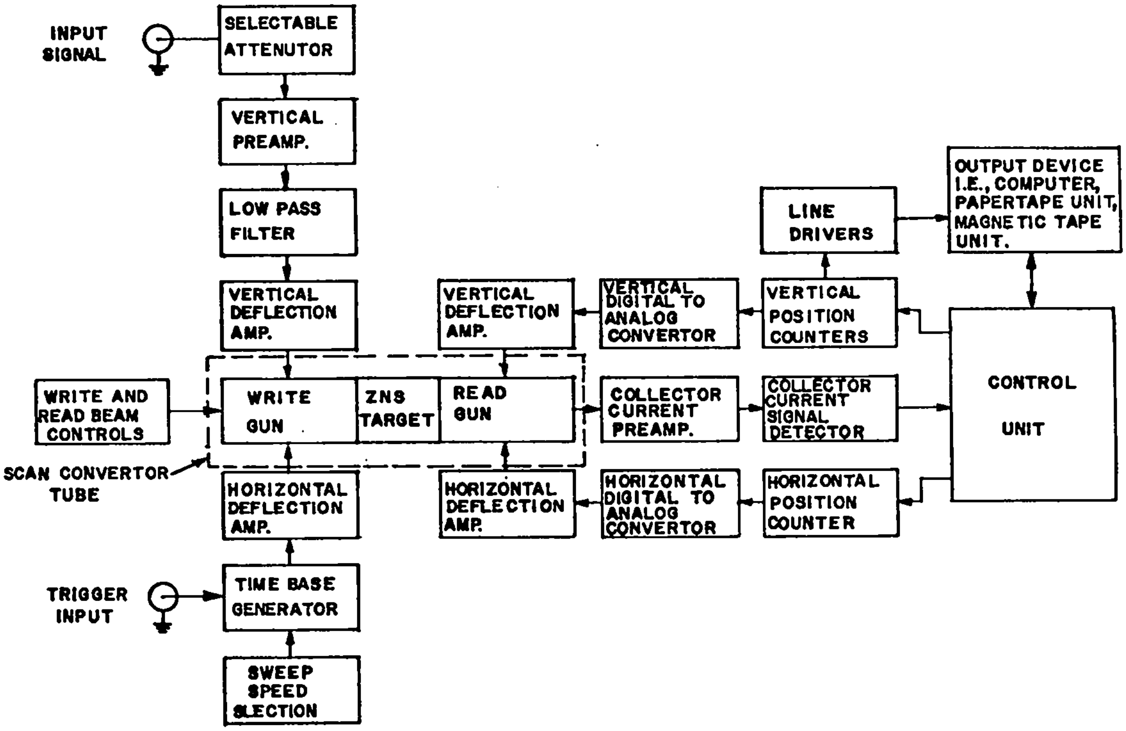

Fig. 84. Block diagram of scan-converter system.

clock frequency be reduced, depending on the actual signal available from the tube.

The problem of detecting a trace written on the target is not simple in that the read beam is gated and the secondary emission current pulse height is reduced where the beam strikes a "blank" portion of the target. Two detector schemes are being pursued. One uses a pulse height band detector: if the height is greater than an upper set value (beam striking a "blank" target) or if it is less than a lower set value (beam-off noise), the output is not triggered. The second uses a differential amplifier input to a Schmidt trigger to detect the difference between a reference pulse derived from the beam unblanking signal and the signal pulse. An output pulse is obtained only if the signal is less than the reference and only if the reference pulse is present. Both circuits will be built and tried on a tube.

Before one tube could be operated it was necessary to provide a read-beam detector, a read-beam horizontal deflection amplifier, a read-beam unblanking amplifier, layout and construction of these, final debugging of the logic chassis, and wiring of the tube module. The write circuitry is somewhat standard and straightforward.

Because of improved punched tape reading methods available at LASL, it was decided to use punched paper tape rather than IBM cards for the initial data recording. A fast Talley tape punch has been procured and the circuitry necessary to match it to the scan-converter logic has been constructed.

SCYLLAC ENGINEERING

(Scyllac Engineering Team)

The Title II drawings of the Scyllac building were completed and approved for bidding.

The three phases of Scyllac engineering, namely, component development, system development, and system design, proceeded on schedule. The development of the essential components, the 1.85-μF, 60-kV capacitor and the low-inductance, coaxial cable was completed. The development of a spark-gap crowbar switch is giving encouraging results. A new triggering system was developed that is expected to fire the 3240 primary spark gap which has an inductance of 30 nH. The prototype system was put into operation and immediately uncovered some deficiencies in the design of the cable terminating cartridge. By working in conjunction with the component development group, these deficiencies were eliminated. This sytem is also being used to evaluate the Scyllac triggering system. The general design of the collector plate was evaluated and certified.

In September 1968, the AEC released $5.135 million to begin the construction of Scyllac. Construction of the building began in Nov. 1968; it will cost about $2 million. The remaining $3 million is being used to order the components for the capacitor banks.

The design of the primary capacitor bank is about 60% complete. The entire charging system was designed and the components ordered. The structural hardware including the capacitor racks and machine platform was designed and ordered. The "start" spark gap was designed and about half the required number ordered. The collector plates for the machine were designed and ordered. About half the 1.85-μF, 60-kV capacitors and most of the low-inductance coaxial cable were ordered. The remaining design work will be completed in time to order the final components for the Scyllac system.

The new significant dates in the Scyllac schedule are given below, assuming the final increment of the Scyllac funds are available in FY-70.

Building	
Title I Preliminary Design Complete	Nov. 1967
Title II Final Design Complete	March 1968
Construction Begin	Nov. 1968
Construction Complete	Feb. 1970
Energy System	
Final Design Complete	Sept. 1969
Installation Begin	March 1970
Checkout Begin	July 1971
Experiments	
Begin	Jan. 1972

SUMMARY OF FUNDAMENTAL PLASMA GROUP ACTIVITIES

(H. Dreicer)

Members of this group are involved in two experimental programs dealing with steady-state plasmas. Considerable effort is also devoted to the underlying theoretical questions, and to the necessary equipment development.

The alkali Q-machine is being readied for a novel radioactive tracer experiment. When completed it should yield the cross section for resonant charge transfer between alkali ions and their parent background gas in a Q-machine, a subject which it is believed may be of interest in understanding the operation of these machines. A major advance in LASL's hot-plate technology now provides plates whose radial temperature profile can be easily controlled. This new degree of freedom promises more control in producing plasma quiescence.

The electron-cyclotron-heated (ECH) plasma machine has been in operation since April. The original hope that this device would develop into a second generation Q-machine, more versatile because the restrictions to alkali ions and to 0.25-eV energies are relaxed, was recently renewed. The reason is that a marked decrease has occurred in the plasma fluctuation level. The relation between this improvement and various equipment changes has not been established. Several experiments designed to measure the properties of the plasma column are under way.

Theoretical work is under way on several fronts to support the experiments. For example, there is research concerned with the penetration into Q-machine plasmas of the effects arising from hot-plate surface inhomogeneities. The Fokker-Planck boundary value computations on spatial relaxation due to Coulomb encounters are intimately connected with the velocity distributions which are established in Q-machine plasmas produced between end plates. Moreover, it is expected that the calculation of the microwave emission (or absorption) by electrons taking part in upper hybrid resonance is related in an important way to the operation of the ECH machine.

The task of improving the dc magnet power supplies has continued throughout the past year with the major engineering effort provided by LASL's Engineering Dept. Improvements have been made in the old induction voltage regulator which controls the 2.5-MW rectifier supply. Switch gear and a second induction voltage regulator were installed to permit the splitting of the 2.5-MW supply into two 1.25-MW supplies, and series transistor regulator banks have been installed on the 2.5-MW supply as well as on the 500-kW motor generator. J. McLeod, of this group, shared the major burden of electronic feedback control design and of its installation and testing. One staff member will be assigned to this important task until it is completed in 1969.

The group welcomes D. Mosher, a postdoctoral appointee, who came to LASL this past summer. N. Gardner and A. Mondragon have provided expert help in all phases of the group's experimental activities.

PROPOSAL FOR MEASURING THE RESONANT CHARGE-EXCHANGE CROSS SECTION OF POTASSIUM IONS AT Q-MACHINE ENERGIES

(H. Dreicer and D. B. Henderson)

The LASL alkali Q-machine is being prepared for a measurement of the charge exchange cross section which describes the probability of charge transfer from K atoms to K ions. The motivation for this work has been presented in the last Status Report[1] and elsewhere[2]. Standard measurements of such cross sections have not been carried out below 6 eV because of the difficulty of fashioning low-energy ion beams with any accuracy[2]. To avoid this problem it is proposed to utilize a single-ended Q-machine to produce a charge-neutralized, magnetically-confined ion beam whose energy is determined by the hot-plate temperature and hot-plate sheath drop as shown in Fig. 85.

Atomic beam nozzles located near the hot plate serve as the source of K atoms which are ionized by contact on the hot plate, and drift along the magnetic field to the cold collector. A second atomic beam nozzle is oriented to produce a relatively cold beam of K atoms which travel perpendicular to the magnetic field and traverse the ion beam. Any charge-exchange encounter which occurs in the region common to both beams causes the hot ion and cold atom involved to interchange their roles. As a result, a cold ion spirals

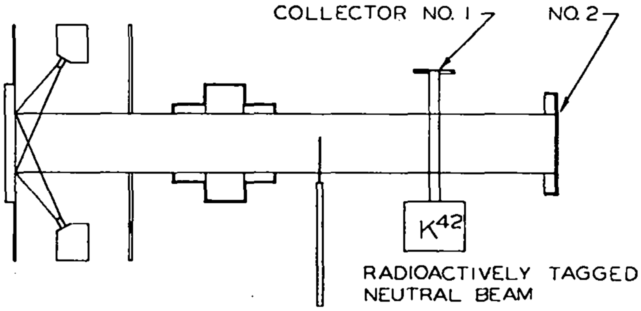

$$\sigma_x = \frac{1}{\int n\,d\ell} \times \frac{\text{ACTIVITY OF NO. 2}}{\text{ACTIVITY OF NO. 1}}$$

Fig. 85. Charge exchange measurement.

along the magnetic field towards the cold collector (No. 2 in Fig. 85) and a hot neutral joins the undisturbed cold atoms which impinge upon a second cold collector (No. 1). To determine that charge transfer has occurred it is necessary to distinguish the K particles in the two beams in a manner which permits their simple identification and separation at these two cold collectors. There appear to be two possible techniques to accomplish this: modification of one of the beams or use of a radioactive isotope in one of the two beams.

Potassium has a highly suitable radioisotope for this purpose: ^{42}K is easily produced in research reactors, is β active, and has a half-life of 12.5 h, a period sufficiently long to permit oven charging and machine operation, and yet sufficiently short to present no radioactivity cleanup problems. Measurements of the ion line density along the region traversed by the atomic beam and of the relative counting rates of the ^{42}K disintegration on the two cold collectors suffice to determine the charge-exchange cross section. Contributions from purely elastic encounters can be discriminated against by varying the solid angle subtended by the collector at the point of particle interaction. The reason is that for elastic scattering the original ion remains confined by the magnetic field after the collision whereas the scattered atom may go off in any direction.

In preparation for this and other Q-machine experiments, considerable component development has taken place on a hot-plate system, on factors affecting atomic-beam nozzle design, and on problems associated with the measurement of plasma density. These developments are described below in greater detail. D. Mosher is constructing Langmuir probes and precision probe drives. He has also determined, in a separate experiment, that surface diffusion of radioactive K atoms across the collectors in the charge exchange experiment will present no problem at room temperature. K. Wolfsburg (LASL J Division) has provided advice on questions of radiochemical analysis, counters, and ^{42}K production.

References

1. Status Report of the LASL CTR Program for 12-Month Period Ending Oct. 31, 1967 (LA-3831-MS).

2. H. Dreicer and D. B. Henderson, Phys. Rev. Letters, 20, 374 (1968).

ALKALI Q-MACHINE COMPONENT DEVELOPMENT: HOT PLATES

(H. Dreicer, D. B. Henderson, F. E. Wittman)

A description has already been given of how the control of hot-plate temperature profiles might be achieved by the use of a uniform electron bombardment beam surrounded by an annular one[1], and also of a three-stage bombardment system which might be capable of producing this electron beam configuration[1]. More recently, the modified system shown in Fig. 86 has been developed. It retains the three independently controlled electron beams featured in the earlier design, but requires only two high-power, high-voltage power supplies and a high-voltage control grid. This system has been operated successfully for long periods at a front hot-plate temperature of 2200-2300°K. Under these conditions the power required to operate a 3-in. diam plate varies from 10 to 12 kW depending upon the magnitude of the positive or negative temperature gradient which is programmed for the hot plate by control of the grid voltage.

In order to map the hot-plate temperature profile a two-color infrared pyrometer has been built which operates at 1.0 and 1.6 μ and utilizes detectors (silicon at 1.0 μ; indium arsenide at 1.6 μ) and their associated electronics, provided by J Division. The optical system constructed for this purpose is shown in Fig. 87. An Aero-Ektar objective lens collects hot-plate light coming through a 5-in. diam quartz window in the vacuum tank. A condensing lens at the first focus passes all of this light to the eyepiece lens, erecting a full-sized real image at the plane of the detector without any vignetting. Spatial resolution of the light emitted by the hot plate is 2 mm due to finite detector size. The light-chopping wheel is located near the first real image and operates with a 50% duty cycle at 960 Hz. This provides an ac signal at each of the two detectors.

Results of measurements made with the 1.0-μ detector are shown in Fig. 88, where the detector signal is given as a function of position along the horizontal diameter of the hot plate.

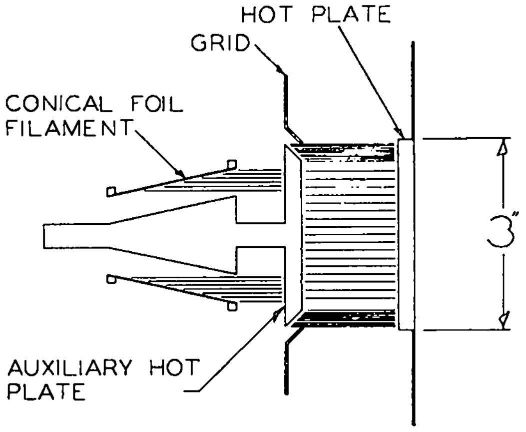

AS RUN FROM 5-13-68

Fig. 86. Hot-plate bombardment system schematic.

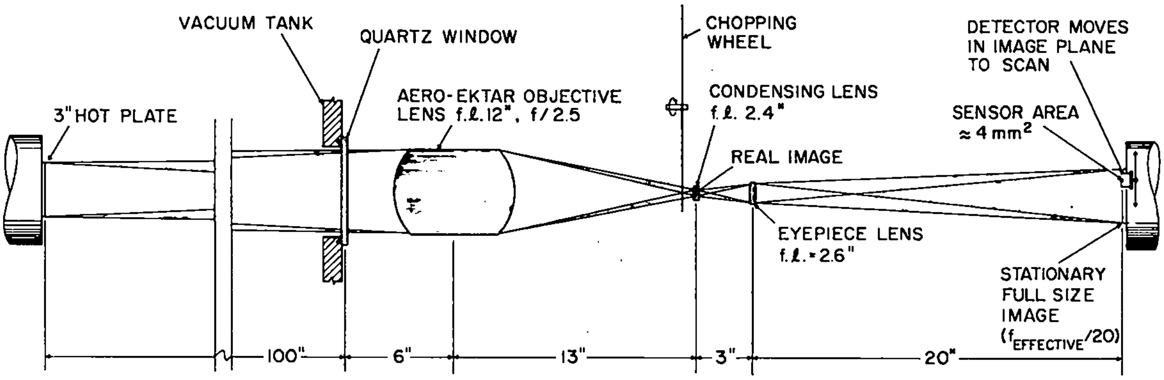

Fig. 87. Schematic of optical system used with two-color pyrometer.

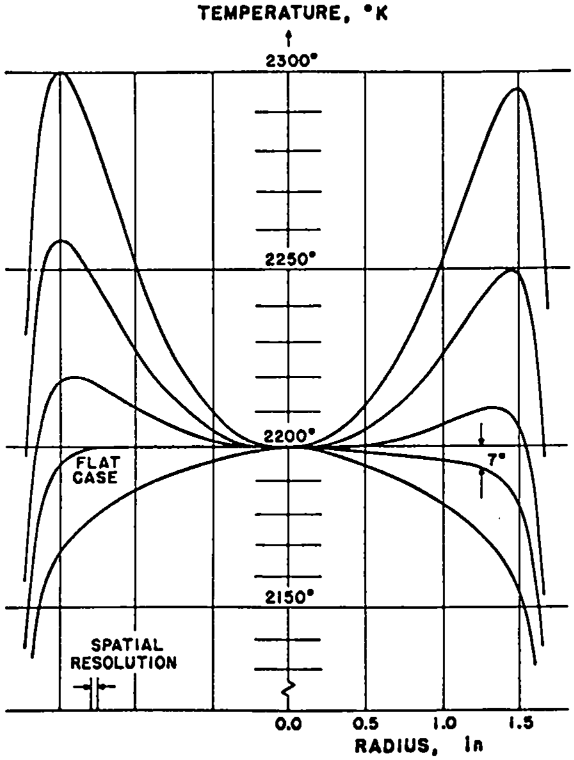

Fig. 88. Measured temperature as a function of position on hot plate.

The necessary calibration of this system against a black-body standard has not yet been carried out. Nevertheless a reasonable estimate of the temperature profile variations can be made in the following manner. The signal generated at the output of the detectors is given by

$$S = S_o \exp(-h\nu_o/kT) ,$$

where S_o includes the effects of solid angle, hot-plate emissivity, electronic gain, detector response, and transmission loss through the optical elements. The frequency ν_o represents the detector center frequency as determined by its filter characteristics. With a disappearing filament type of pyrometer the temperature T can be measured to about several percent. Thus S_o can be determined once S is measured, and this permits calibration of the variation of T across the hot plate with similar accuracy.

On the basis of the foregoing procedure, nearly isothermal hot-plate conditions were found, with 7°K temperature variations across 2.5 in. of the hot plate at 2200°K. The worst deviation appears to be due to misalignment of hot-plate parts at high temperature. Positive and negative temperature gradients as large as +100 and -50°K/in. have been easily achieved. Until the system is more adequately calibrated and operated as a two-color pyrometer to permit the elimination of the hot-plate emissivity factor and other common mode constants, results cannot be given with an accuracy > 10%, assuming that the emissivities quoted in the literature are also this accurate.[2]

In summary, a hot-plate system has been constructed, with a radial temperature profile which can be programmed over a wide range, including positive, negative, and nearly-zero temperature gradients. The programming procedure is simple, electronic, and requires no mechanical adjustments to the hot-plate system. This new degree of freedom is expected to be very useful in producing plasma quiescence. Recent results[3] on drift wave instabilities in Q-machine plasmas lend support to this expectation.

References

1. Status Report of the LASL CTR Program for 12-Month Period Ending Oct. 31, 1967 (LA-3831-MS).

2. W. H. Kohl, "Materials and Techniques for Electron Tubes," Reinhold Publishing Corp., 1960.

3. F. Perkins, Private Communication, Nov. 1968; also F. F. Chen and K. C. Rogers, Bull. Am. Phys. Soc., Ser. 2, 13, 1548 (1968) (Abstract).

ATOMIC BEAM NOZZLE DESIGN

(D. B. Henderson)

The charge-exchange cross-section measurement will require two atomic beam injection systems. One serves the hot plate which generates the plasma; the other provides the crossed radioactively tagged beam. The second must be very well collimated and baffled to avoid spurious collection of its atoms by collector 2 in Fig. 85. For this purpose, consideration has been given to a honeycomb nozzle[1] such as is shown in Figs. 89 and 90. Such a nozzle consists of many parallel tubes each of which has a length exceeding its diameter, and provides a well-collimated beam when it is operated at low gas pressure so that its diameter ≪ mean free path.[2] Compared to the conventional atomic-beam source, this nozzle appears to possess advantages when beams with a half-angle smaller than 3×10^{-3} rad are required or when efficiency is a paramount consideration. Provided larger angular emission is tolerated, higher intensities may be obtained with conventional nozzles by using baffles.

For the hot-plate, atomic-beam source it is planned to use a collection of conventional nozzles in order to allow higher fluxes. These simple nozzles will be spaced and directed to achieve desired plasma density profiles, a task requiring a knowledge of the distribution of efflux from a single simple nozzle at practical pressures and temperatures (for Q-machine injection). In order to measure this distribution and to verify the characteristics of the crossed beam nozzle, the apparatus shown in Fig. 91 has been assembled. The alkali vapor is conducted in through the heated tube marked A and the constant conductance turret assembly B to the nozzle C. The nozzle is rotated about its tip, changing the angle to the detector while preserving the detector distance and solid angle. Atoms travel to the detector through the liquid-nitrogen cooled tube D. A rotating chopping wheel E modulates the signal to the hot-wire detector (not visible) behind the wheel.

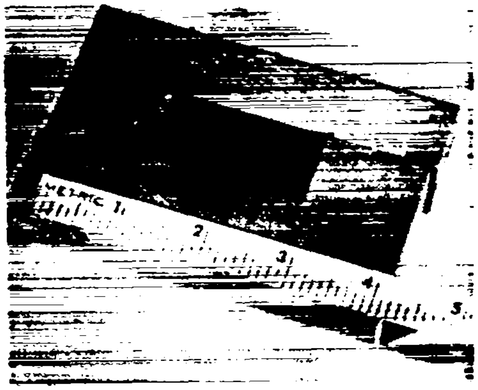

Fig. 89. Honeycomb nozzle.

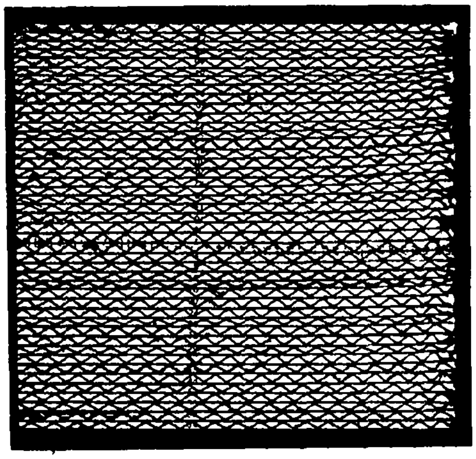

Fig. 90. Transmission photo of a portion of the honeycomb nozzle.

Temperature regulation through the four sheathed thermocouples and manual control of the radiant heaters has been satisfactory. A second scale-model chopping wheel on the outside of the vacuum-tank motion feedthrough modulates a light beam. With a lock-in amplifier, a signal phase-locked to the light signal has been obtained. This indicates that the alkali feed, nozzle, and detection systems all work as planned. Difficulty has been experienced with the rotation of the nozzle assembly inside the vacuum when it is heated to 350°C. With the solution of this technical problem, the measurements described above should be completed.

References

1. This nozzle design originated in the molecular beam laboratory of J. R. Zacharias, MIT, and was used by M. W. P. Standberg and H. Dreicer, Phys.Rev. 94, 1393 (1954).

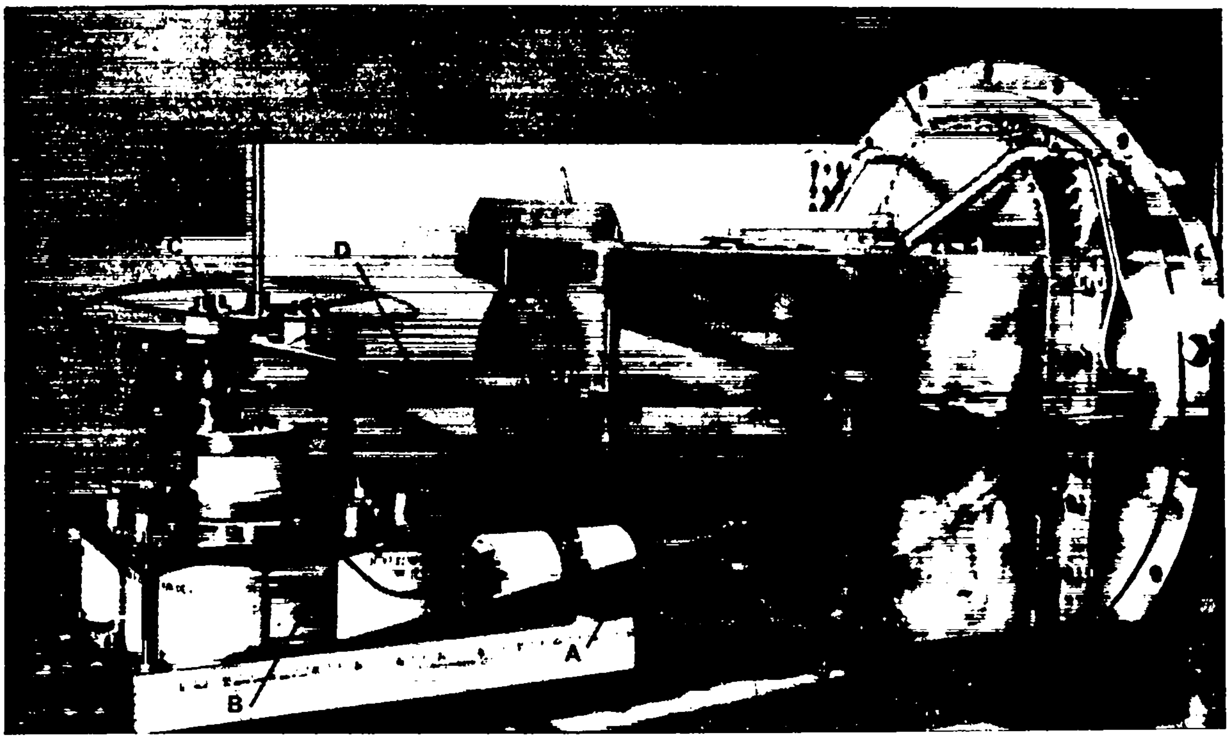

Fig. 91. Apparatus for measuring angular distribution of atoms emitted by nozzles.

2. J. A. Giordmaine and T. W. Wang, J. Appl. Phys. 31, 463 (1961).

EFFECT OF PLASMA ACCESS HOLES UPON MICROWAVE RESONATORS USED FOR DETERMINATION OF ELECTRON DENSITY

(H. Dreicer and W. Rich)

In the alkali Q-machine experiment, it is expected that plasma columns of low electron density and small radius R_p will be encountered. The latter is a condition which rules out the use of a microwave phase-shift interferometer for the measurement of electron density, because the ratio of R_p to microwave wavelength should be large compared to unity if microwave beam refraction and diffraction effects are to be avoided. For this reason, design has been started of microwave resonators for electron density determination. This technique, which depends upon a measurement of the resonant frequency shift when plasma is introduced into the resonator, is $\sim$ 25 years old. Nevertheless, the existing theory of this shift, when plasma is introduced through access holes in the resonator, is incomplete. The deficiency is related to the existence of microwave fringe fields, produced by the access holes, which cannot be expressed in analytical form, and have never been evaluated in any form.

The LASL LALA code, together with a new subroutine, has been used to evaluate both the frequency shift and the change in Q for resonators with access holes operating in the TM_{010} mode. The perturbation theory for plasma density determination using microwave resonators is based upon the following formula :

$$\frac{\Delta f}{f}\left(\frac{\omega_{po}}{\omega}\right)^2 = -\frac{1}{I_o}\int_{z=o}^{z_{max}}\int_{o}^{R_p} A(r)\,\frac{n(r)}{n(o)}\,E_r^2\,r\,dr\,dz - \frac{1}{I_o}\int_{o}^{z_{max}}\int_{o}^{R_p} C(r)\,\frac{n(r)}{n(o)}\,E_z^2\,r\,dr\,dz \qquad (1)$$

where

$$A(r) = \frac{1}{2}\,\frac{\Omega^2 - 1 - [V(r)]^2}{([\Omega^2 - 1] + [V(r)]^2)^2 + 4[V(r)]^2}$$

$$C(r) = \frac{-1}{2([V(r)]^2 + 1)}$$

$$I_o = \int_{z=o}^{z_{max}}\int_{o}^{R_c} (E_r^2 + E_z^2)\,r\,dr\,dz \quad ,$$

The quantity $\Delta(1/Q)(\omega_{po}/\omega)^2$ is given by Eq. 1 with B(r) replacing A(r) and D(r) replacing C(r).

$$B(r) = V(r)\,\frac{\Omega^2 + 1 + [V(r)]^2}{([\Omega^2 - 1] + [V(r)]^2)^2 + 4[V(r)]^2}$$

$$D(r) = -2C(r)\,V(r),$$

where

$\Delta(1/Q)$ = shift in 1/Q due to plasma electrons
$\Delta f/f$ = relative shift in cavity resonant frequency due to plasma electrons
ω_{po} = radian plasma frequency associated with maximum plasma density n(o)
E_z = axial electric field
E_r = radial electric field
ω = working (radian) frequency
n(r) = plasma density as a function of radius r.

R_p, R_c, and z_{max} are defined in Fig. 92.

Ω = ω_B/ω
ω_B = electron cyclotron (radian) frequency
V = ν/ω
ν = electron collision rate.

When n(r) is independent of r and the magnetic field is uniform, A, B, C, and D are constants, and only integrals over E_r^2 and E_z^2 are involved. These integrals,

$$I_1 = \int_{o}^{z_{max}}\int_{o}^{R_c} E_z^2\,r\,dr\,dz$$

and

$$I_2 = \int_{o}^{z_{max}}\int_{o}^{R_c} E_r^2\,r\,dr\,dz \quad ,$$

are shown in Figs. 92 and 93 as functions of R_p/R_c for several values of R_c/H, as well as for the case of a right circular cylinder of height 2H and radius R_c. With the help of these figures, the frequency shift and change in Q can be evaluated for two geometries. Since the LALA computations are very lengthy other geometries have not been investigated. Sufficient accuracy can be obtained, however, by interpolating on Figs. 92 and 93.

Although the radial electric integral is smaller than the axial electric integral the effect of the former on $\Delta f/f$ and $\Delta(1/Q)$ is very large near cyclotron resonance, and a considerable neighborhood about cyclotron resonance must in practice be avoided. This effect is

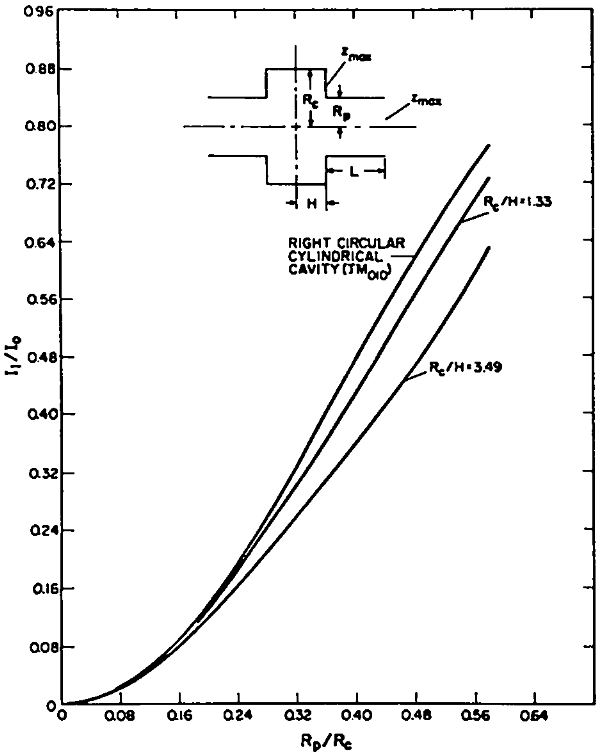

Fig. 92. I_1/I_0 as a function of R_p/R_c.

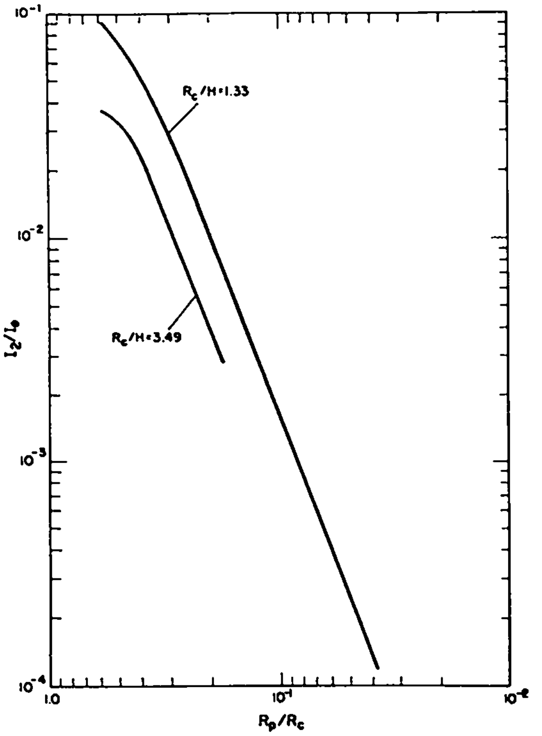

Fig. 93. I_2/I_0 as a function of R_p/R_c.

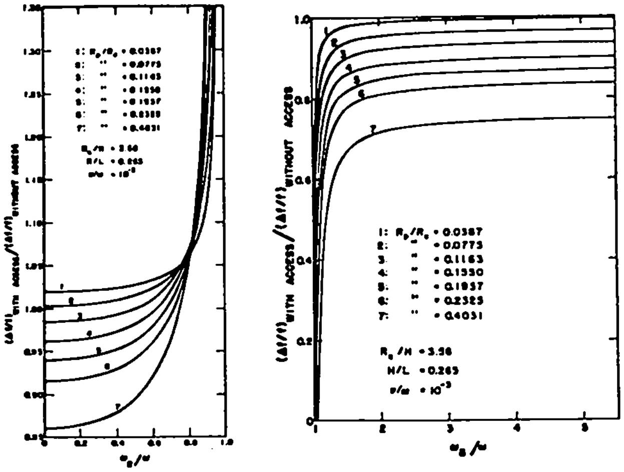

Fig. 94. Values of $\Delta f/f$ with and without access holes as functions of ω_B/ω.

shown in Fig. 94 where $\Delta f/f$ with and without access holes in the resonator is shown as a function of ω_B/ω with the ratio of plasma radius R_p to resonator radius R_c as a parameter. A similar plot of $\Delta(1/Q)$ can also be constructed with the help of the foregoing equations and Figs. 92 and 93.

PENETRATION OF END-PLATE EFFECTS

(H. Dreicer and D. B. Henderson)

A principal objective of the Q-machine development program at LASL has been aimed at providing controlled hot end-plate conditions. In this connection the nonequilibrium effects associated with the end plates have been studied at different temperatures, with different work functions, and subject to different neutral injection fluxes. Consideration has been given primarily to the collisionless limit in which the distribution functions are determined via the Vlasov equation from the distributions emitted by the hot plates. Trapped ions have been included by assuming them to be Maxwellian and to join smoothly to the nontrapped distribution.

In this treatment, a solution for the potential ϕ inside the bulk plasma may be obtained as a function of the net charge density n and of the various end-plate parameters. The effects of a discontinuity in end-plate parameters have been examined, for example, when the work function changes from one crystal grain to the next[1]. In this situation the $n(\phi)$ in the plasma has a corresponding jump in value across boundaries which are projected from the crystal grain boundaries on the end plates into the plasma. Then, using the Poisson equation, self-consistent solutions are obtained, the jump in plasma potential being spread over several Debye lengths, λ_D.

The effect of finite electron and ion Larmor radii, R_e and R_i, has been mocked up by taking $n(\phi)$ to be piecewise linear admixtures of the $n(\phi)$ intrinsic to each side of the boundary with the scale lengths being R_e and R_i. Roughly speaking, about half the potential change then occurs over a distance R_i on each side of the boundary and the remainder is concentrated in a distance of several R_e or λ_D at the boundary. The finite Larmor radius effects are essential for a physically plausible picture; without them there is a continuous potential, but discontinuous particle densities. Most of the results were obtained numerically, although an analytical solution is possible in those cases for which potential drops are large compared to kT/e. No results as general as these are known, although various workers have done many of the limiting cases. A more complete exposition will be presented in a Los Alamos Report.

Reference

1. Status Report of the LASL CTR Program for 12-Month Period Ending Oct. 31, 1967 (LA-3831-MS).

VELOCITY DISTRIBUTIONS ASSOCIATED WITH BOUNDED PLASMAS: SPATIAL RELAXATION

(H. Dreicer and J.D. Thomas (NMSU))

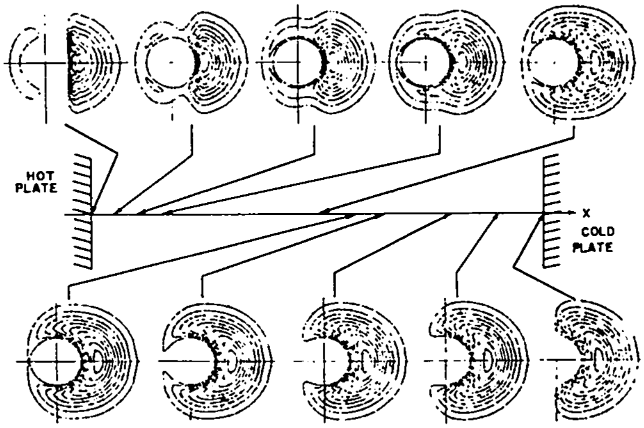

Fig. 95. Velocity space contours of constant velocity distribution function for various positions between the boundaries.

The Fokker-Planck boundary value problem for the Lorentz gas (i.e., electron-ion encounters only) was posed by one of the authors (H. Dreicer) in collaboration with W. B. Riesenfeld and described in the last Status Report[1]. This problem deals with the purely angular scattering of electrons on a random distribution of positive ions whose average density between two plane parallel boundaries is constant. Non-current-carrying eigenfunction solutions exist which are obtained by applying the method of separation to

$$\mu\frac{\partial f(x,\mu;v)}{\partial x} = A(v)\frac{\partial}{\partial\mu}\left[(1-\mu^2)\frac{\partial f}{\partial\mu}\right] \qquad (1)$$

with the boundary conditions

$$f(-1,\ \mu;\ v) = \alpha(\mu;v)$$

$$f(1,\ -\mu;\ v) = \beta(\mu;v),$$

where

$$A = a/\ell$$

and v = electron speed, a = actual half-spacing between plane parallel boundaries, ℓ = electron-ion mean free path for encounters (proportional to v^4),x = spatial position expressed in units of a, $\mu = \cos\theta$, where θ = angle between electron velocity and x axis. These eigenfunctions and the corresponding eigenvalues were computed numerically and described earlier[1]. In addition, there is a current-carrying solution to Eq. 1 which by inspection has the form

$$f = C + D(\mu - 2Ax),$$

where C and D are constants.

Unfortunately it has not been possible to prove the completeness of the non-current-carrying eigenfunctions. Attempts by W. B. Riesenfeld to utilize approximate analytic eigenfunctions to obtain a proof have also failed. In the absence of such a proof, further progress has depended upon the assumption that these eigenfunctions do form a complete set. Such an assumption is then sufficient to ensure the completeness of the entire solution which consists of the current-carrying and non-current-carrying parts.

General solutions to the problem have been obtained numerically; a least-squares procedure is employed to compute C, D, and the coefficients in the sum over eigenfunctions which is used to express the boundary conditions at x = ± 1.

Solutions are being presented in the form of contours of constant electron velocity distribution function in velocity space for any position between the boundaries. R. Frank (LASL C-Division) provided his Cal Comp plotting program for this purpose. A sample problem for which such contours are presented is shown in Fig. 95. In this case, $\alpha(\mu;v)$ is chosen to be a displaced Maxwellian distribution

$$\alpha(\mu;v) = \begin{cases} \exp\left[-\sigma(1+w^2) + 2\sigma\mu w\right] & ;\ \frac{1}{w} \le \mu \le 1 \\ 0 & ;\ 0 \le \mu \le \frac{1}{w} \end{cases}$$

and

$$\beta(\mu;v) = 0,$$

where $\sigma = mv_0^2/2kT$, v_0 = velocity displacement along x, and $w = v/v_0$.

For the results illustrated in Fig. 95, the quantities used are $\sigma = 0.5$ and $A = 1.0\ /w^4$. The boundary condition at $x = -1$ is intended to approximate the electrons emitted by a hot plate and accelerated by a sheath. The condition at $x = 1$ approximates a cold collector plate which emits no electrons. All electrons which are returned by collisions to the hot plate at $x = -1$ (i.e., whose μ is in the range $-1 \le \mu \le 0$), or which arrive at the cold plate in the range $0 \le \mu \le 1$, are absorbed. No electron-electron encounters are included. Each of the velocity space diagrams is associated with a given position along the x-axis. Each diagram consists of 10 contours which correspond to f values that vary in 10 equal increments between the maximum and zero. In all cases the smallest closed curve surrounds the point of maximum f. The decrease in the maximum f value from $x = -1$ to $x = 1$ is not documented in Fig. 95 to avoid loss of clarity.

Several other boundary conditions which have some application to Q-machine plasmas have been studied. Mirror boundary conditions which have reflection and absorption conditions over parts of the μ range are also being investigated.

Reference

1. Status Report of the LASL CTR Program for 12-Month Period Ending Oct. 31, 1967 (LA-3831-MS).

ECH-PLASMA EXPERIMENT

(H. Dreicer, J. McLeod, D. E. Michael)

The motivation behind the ECH-plasma experiment is the development of a reasonably quiescent plasma column which may utilize any ion species, operates at average electron energies far in excess of those possible in conventional thermally heated alkali Q-machines, and may be used in collisional or collisionless regimes. A simple analysis of the conditions under which a plasma column can be maintained in a steady quiescent state by electron cyclotron heating and ionization was presented in the last Status Report[1]. The main contention was that the most obvious microinstabilities, driven by velocity distribution anisotropies and double humps, might be avoided by limiting the average electron energy to tens of eV and by limiting the applied microwave power.

The first ECH column was produced in hydrogen (April, 1968) by feeding X-band microwave power to a 1-in. long Lisitano coil[2] located between two metallic floating end plates spaced 100 cm apart and oriented perpendicular to a nearly uniform, dc magnetic field. According to computations[1] and measurements, the spatial homogeneity between end plates is 1%; within the microwave coupling structure it is 0.02%.

These experiments were limited by electrical breakdown in the waveguide feeding the coupling structure. This difficulty was due to the high degree of magnetic field homogeneity which permitted cyclotron resonance to occur simultaneously in the waveguide and in the coupling structure. To avoid the destruction of waveguide vacuum windows which accompanies breakdown, two courses were thought to be practical after some experimentation. These were: orientation of the waveguide with the microwave electric field parallel to the applied magnetic field or transfer of the vacuum window to the boundary between the plasma column and the coupling structure. All the later experiments have used the latter alternative with a microwave coupling structure of LASL design (Fig. 96).

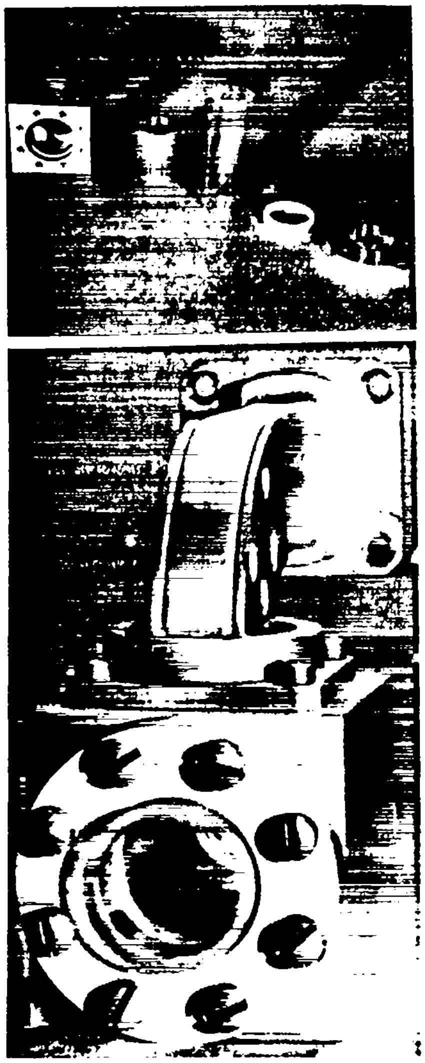

Fig. 96. Upper: Microwave coupling structure parts; lower: assembled microwave coupling structure.

The structure consists of a 1.125-in. i.d. closed loop of waveguide which surrounds the plasma column. The loop is formed in the E-plane so that one of the wide faces of the waveguide faces the plasma. This face has several simple slots across its width to radiate into the plasma. The structure is fed from one side by what would be an E-plane tee except that the cap of the tee is bent around to form the closed loop. The vacuum seal is made on a quartz tube which surrounds the plasma and fits inside the waveguide loop. All points at which microwave energy concentrates are thus outside the vacuum system where they can be pressurized if necessary, to prevent breakdown. The power level is now limited to 600 W by other microwave components and not by failure of the feed structure.

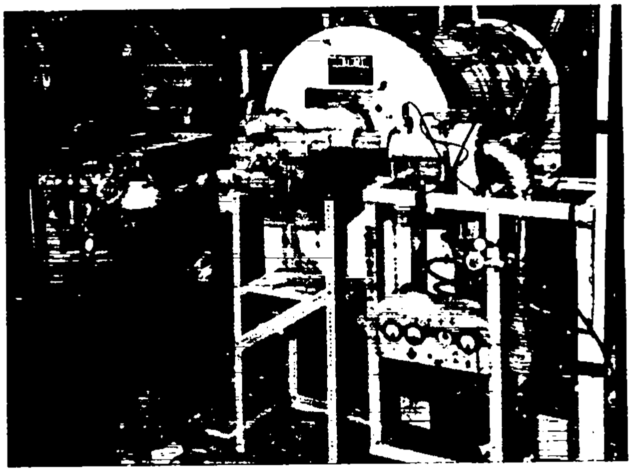

Fig. 97. ECH experimental arrangement.

The coupling structure is housed in an 8.5-in. i.d. vacuum tank and uses an 11-in. i.d., 6-ft long solenoid magnet powered by a motor generator. These components are shown in Fig. 97. Considerable effort has gone into stabilization of the magnet current. According to nuclear magnetometer measurements its long term (~ 10 min) stability is now 1 part in 10^4 with an superimposed 60-Hz hum component which amounts to 1G out of 3000 G. A description of the series transistor current regulator used for this purpose is given on p. 105.

Earlier microwave power sources have now been replaced by a Varian VA848 power amplifier which is fed from a low-power, phase-stabilized driver klystron. This system is capable of providing up to 2500 W, is highly stable, and can be amplitude-modulated to permit work in the afterglow. Plasma columns have been produced in hydrogen, helium, or argon, using from a few to several hundred W of microwave power, with the gas stream through the system controlled by a calibrated variable leak valve. A magnetically shielded ionization gauge, located outside of the

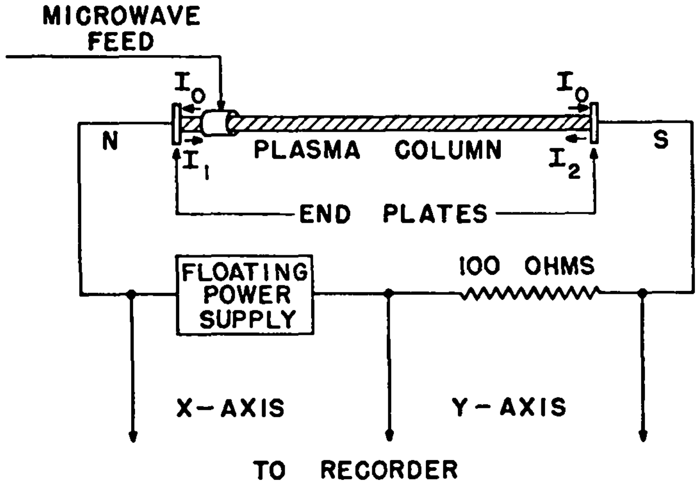

Fig. 98. Double probe circuit.

magnet, has been used to monitor the gas pressure which has ranged from 60 to 800 μtorr.

The major diagnostic tool so far has utilized the metallic end plates on which the plasma column terminates, arranged in the Langmuir double probe circuit shown in Fig. 98. It has been used to obtain a rough idea of the electron density and temperature for a variety of gas pressures, microwave powers, and various magnetic field ranges. When connected to an oscilloscope this double probe has also served as a sensor of noise upon which an estimate of quiescence has been based. The usual difficulty with a floating double probe in a magnetic field sensing only the plasma trapped within it, that is probably not representative of the remainder, is avoided by the use of these large disk electrodes between which the entire plasma is trapped. Since the entire plasma column including both electrodes is in a highly uniform magnetic field, no difficulties arise from the effects of mirrors or other gradients in the field. The penalty paid for the use of large probes is the lack of information on spatial distributions since only average values are obtained.

A Maxwellian distribution of electron velocities was assumed in interpreting the data, largely for lack of any more detailed information about the distribution function. The shapes of the current-voltage curves are compatible with the results of this assumption to the accuracy with which they can be determined. It is quite possible that other electron velocity distribution functions might fit the measured current-voltage curves so that the results to be presented are not yet unambiguous.

The electron saturation current could not be obtained directly in the usual way by observing the limiting current for large bias voltages, because the plasma was adversely affected by the bias voltage before complete saturation was reached. A small portion of the current-voltage curve near the point of inflection was analyzed for the first three nonzero terms in its expansion. The first and third order terms were combined to obtain temperature and density and the fifth order term, which could be obtained only approximately, was checked as a test of the applicability of the theory. A typical X-Y recorder curve of the current-voltage characteristic is shown in Fig. 99 for seven magnetic field values in the neighborhood of electron cyclotron resonance.* The point of inflection, which ought to be at zero voltage and current, is displaced somewhat, presumably because the two electrodes were not perfectly symmetrical with respect to the plasma.

Each electrode receives an electron current given by

$$I = \tfrac{1}{4} n e \bar{v} A \exp(-eV/kT),$$

where A is the cross section area of the plasma column, $\bar{v} = \sqrt{8kT/\pi m}$ is the mean electron velocity, V is the potential of the electrode relative to the plasma, n is the plasma density, and T is the electron temperature. The floating potential, V, is determined by the necessity of balancing the ion saturation current which is assumed to be unchanged by small changes in a potential that is attractive for the ions. Therefore, if I_1 and I_2 are the electric currents carried by electrons to the two end electrodes, then in the

---

*These values must be multiplied by a constant factor, close to unity, to obtain absolute magnetic field values.

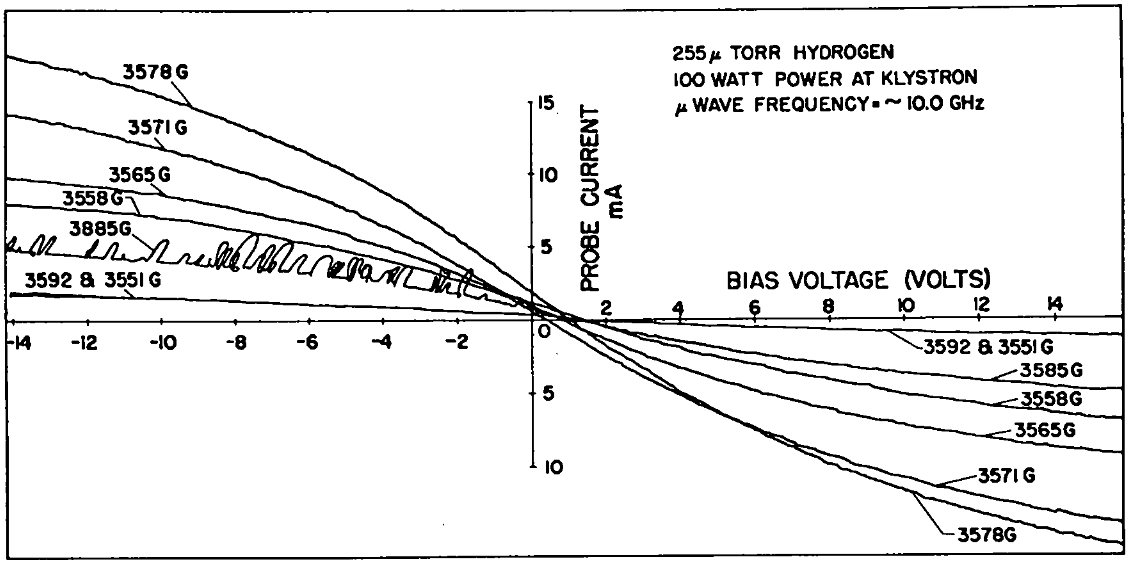

Fig. 99. Current-voltage characteristics of double probe.

steady state

$$I_1 + I_2 = 2I_0,$$

where I_0 is the unbiased electron (or ion) current to one electrode. Substitution from above gives

$$\exp(-eV_1/kT) + \exp(-eV_2/kT) = 2\exp(-eV_0/kT),$$

or if

$$\Delta V = V_2 - V_1$$

$$\exp(-eV_1/kT)[1 + \exp(-e\Delta V/kT)] = 2\exp(-eV_0/kT).$$

The net current flowing in the external circuit is

$$I_T = I_1 - I_2 = \tfrac{1}{4} ne\bar{v}A[\exp(-eV_1/kT) - \exp(-eV_2/kT)]$$

$$= \tfrac{1}{4} ne\bar{v}A \exp(-eV_1/kT)[1 - \exp(-e\Delta V/kT)]$$

and finally[3]

$$I_T = \tfrac{1}{2} ne\bar{v}A \exp(-eV_0/kT) \frac{1 - \exp(-e\Delta V/kT)}{1 + \exp(-e\Delta V/kT)}.$$

For small $e\Delta V/kT$, this expression is approximately equal to

$$I_T = \tfrac{1}{4} ne\bar{v}A \exp(-eV_0/kT)[(e\Delta V/kT) - \frac{1}{12}(e\Delta V/kT)^3 + \frac{1}{120}(e\Delta V/kT)^5 - \ldots].$$

If the measured value of $I_T = \alpha\Delta V - \beta(\Delta V)^3 + \ldots$ then

$$\alpha = \frac{ne^2A}{\sqrt{2\pi mkT}} \exp(-eV_0/kT),$$

$$\beta = \frac{ne^4A}{12(kT)^2\sqrt{2\pi mkT}} \exp(-eV_0/kT),$$

and

$$\frac{kT}{e} = \sqrt{\frac{\alpha}{12\beta}}$$

$$nA = \alpha \sqrt[4]{\frac{\alpha}{12\beta}} \sqrt{\frac{2\pi m}{e^3}} \exp(+eV_0/kT).$$

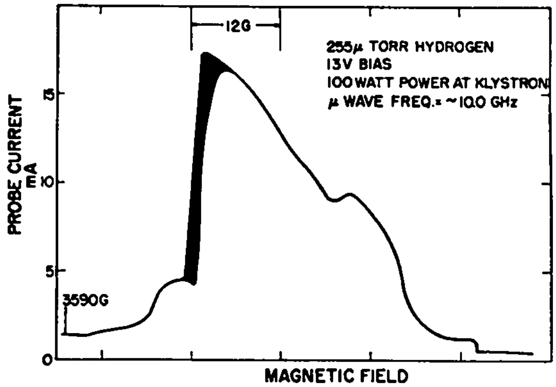

Fig. 100. Probe current as a function of magnetic field. Darkened portion is a region of large fluctuations in the current.

The factor $\exp(+eV_0/kT)$ has been assumed $\simeq \sqrt{M/m} = 60$ for H_2.

By utilizing these formulas, the curve in Fig. 99 for 3578 G (see footnote p. 99) yields an average plasma density of $10^{12}/cm^3$ and an electron temperature of 4 eV.

The same arrangement has also been used with fixed bias voltage to determine the range in magnetic field over which plasma is produced when the microwave frequency is held fixed. A typical plot of probe current as a function of magnetic field is shown in Fig. 100. A resonant phenomenon is clearly involved since probe current is not drawn outside of a narrow magnetic field range near the cyclotron resonant magnetic field. Whether this range is determined by spatial magnetic field inhomogeneity or by upper hybrid resonance effects has not yet been established.

It should be emphasized that very large uncertainties still exist in the parameters measured by the double probe, because the interpretation of the data is very sensitive to the assumption of a single Maxwellian velocity distribution all the way into the high-energy tail region. Since the relevant high-energy portion involved in the probe measurement may contain only a few percent of the electrons it is important to point out that no measurement has been made on the velocity distribution, and the use of a Maxwellian function is an outright assumption. Moreover, the probe interpretation is based upon a picture of the plasma column's sheath structure which has also not yet been verified by any measurement. The main virtue of the double probe is presently its ability to identify the presence of plasma and to serve as a noise probe. Recently, the value of this feature was established when, after various improvements made on the quality of the microwave power source and in the magnetic field stability, a marked decrease was observed in the level of fluctuation or noise.

Preparations are under way to make several other diagnostics measurements on these plasma columns before they are put to any other use.

References

1. Status Report of the LASL CTR Program for 12-Month Period Ending Oct. 31, 1967 (LA-3831-MS).
2. G. Lisitano, Proc. Seventh Internat. Conf. on Ionization Phenomena in Gases, 1, 464 (1966).
3. F. F. Chen, "Electric Probes," Chap. 4 in "Plasma Diagnostic Techniques," R. H. Huddleston and S. L. Leonard, eds., Academic Press, 1965.

ELECTROMAGNETIC RADIATION EMITTED BY UPPER HYBRID RESONANCE ELECTRONS

(H. Dreicer)

The electromagnetic radiation emitted by a magnetized plasma column into the extraordinary mode propagating normally to the magnetic field consists of the spectral lines at the cyclotron frequency and its harmonics superimposed upon a continuous background spectrum. Experimenters have concentrated their efforts mainly on the study of the harmonic emission with the result that the behavior of the background has received little attention. It is clear that the continuous spectrum should receive contributions from collision-induced bremsstrahlung. In many experimental situations, however, the collision rate is too small to account for the observations, and other radiation sources must be considered. In the collisionless limit, the main contributing factor appears to be the emission from electrons taking part in upper hybrid collective oscillations. No complete theory describing the shape of this continuous spectrum exists in this limit, although several authors have considered various aspects of the problem.[1-3]

Computations of this continuous spectrum have been made at LASL during the past year.[4] These apply to a collisionless plasma slab (thickness 2L); they take Budden tunneling through the evanescent layer into account, and utilize reflection and transmission coefficients as well as Kirchhoff's law to determine the emission from realistic density profiles.

It has been found that for a low-β plasma immersed in a static uniform magnetic field, the ratio of the power emitted by the upper hybrid electrons to that emitted by a black body at the electron temperature is given by the expression

$$P/P_B = 2\,\exp(-\pi\eta)[1-\exp(-\pi\eta)], \qquad (1)$$

where $\eta = \sqrt{2}(\omega_B/\omega)k\,|x_c - x_R|$, ω_B = electron cyclotron (radian) frequency, ω = radian frequency emitted, and $k = \omega/c$, and x_c and x_R are solutions of the dispersion relations

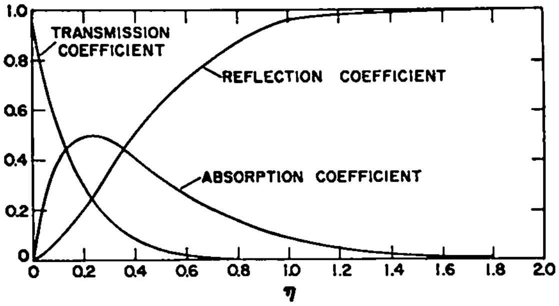

Fig. 101. Absorption, transmission, and reflection coefficient as a function of η.

$$[\omega_p(x_c)/\omega]^2 = 1 - (\omega_B/\omega)$$

$$[\omega_p(x_R)/\omega]^2 = 1 - (\omega_B/\omega)^2.$$

The quantity $\omega_p^2(x)$ is the local electron plasma frequency at the position x on the density profile.

Equation 1, by Kirchhoff's law, is also the absorption coefficient for radiation incident on the plasma slab, which is given as a function of η in Fig. 101 together with the reflection and transmission coefficients. The absorption maximum at $\eta \simeq 0.25$ makes clear the fact that P/P_B will possess a maximum as a function of ω_B/ω whenever variation of ω_B/ω causes η to increase or to decrease toward $\eta \simeq 0.25$ (or to pass through this point).

Some interesting comparisons can be made between the predicted emission and the available experimental observations. Figure 102 shows two spectra obtained at LASL at the frequencies ω_1 and ω_2 from a P.I.G. discharge operating in helium at 3 mtorr with $kL \geq 10$. At the higher frequency ($\omega_2 = 2\omega_1$), no background spectrum exists whereas at the lower frequency ω_1 the background spectrum peaks at about $\omega_B/\omega_1 \approx 1/9$. This peak in the background spectrum cannot be accounted for by summing the wings of the adjacent cyclotron harmonic lines which are superimposed on the background. Moreover it cannot be explained on the basis of simple bremsstrahlung. Transmission measurements made

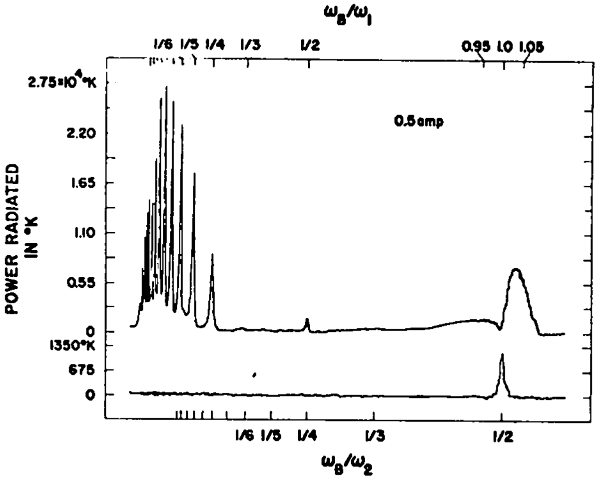

Fig. 102. Extraordinary wave power emitted as a function of ω_B/ω_1 and ω_B/ω_2.

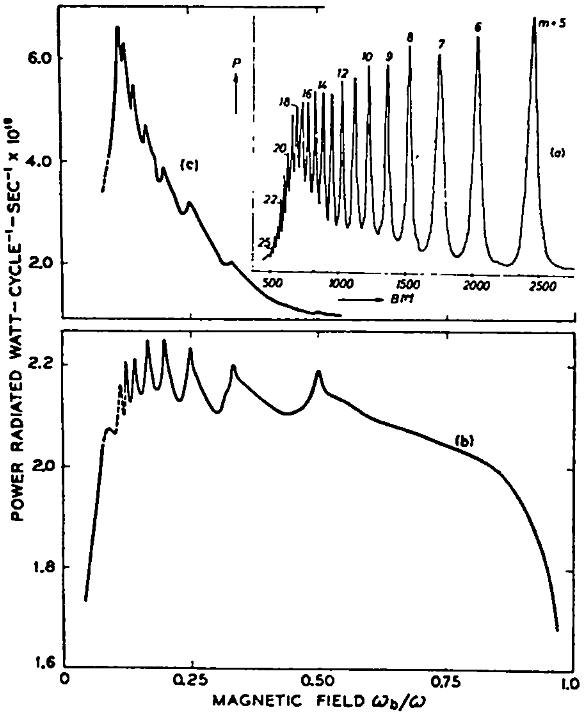

Fig. 103. Extraordinary wave power emitted from various plasmas as a function of ω_B/ω.

on the same plasma column indicate, however, that upper hybrid resonance electrons exist at the lower frequency ω_1 and are absent at ω_2. This observation provides some evidence that upper hybrid resonance electrons may indeed by responsible for the background spectrum.

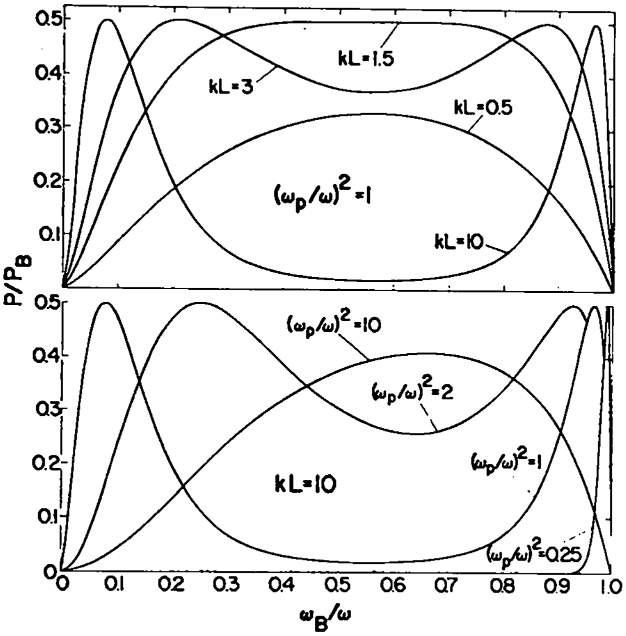

Fig. 104. Computed spectra.

Figure 103(a) shows some similar observations obtained by G. Landauer[5] on a plasma column of large kL. G. Bekefi et al.,[6] working with a low-pressure arc column, have also observed such a peak, shown in Fig. 103(c), at small ω_B/ω under conditions which probably amounted to $kL >> 1$, but this is not certain. Their measurements at $kL \simeq 0.5$ (Fig. 103(b)), which are characteristic of the spectra obtained whenever the plasma column is immersed in a waveguide, indicate a very broad background extending over nearly the entire ω_B/ω range.

The foregoing examples are to be compared with some spectra evaluated from Eq. 1 for a J_0 Bessel function profile. The results of such computations are shown in Fig. 104, where P/P_B is given as a function of ω_B/ω with the central value of $(\omega_p/\omega)^2$ and kL each treated as a parameter.

It should be emphasized that the theory represents a highly idealized situation, because the actual variation in plasma conditions with ω_B/ω is not included. Nevertheless, it appears highly probable that the peaks in the background spectrum observed at low ω_B/ω for large kL are indeed a manifestation of efficient Budden tunneling near $\omega_B/\omega \simeq 0$ where cutoff and hybrid resonance

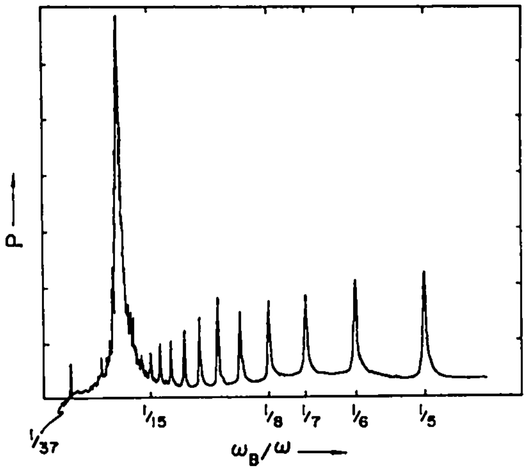

Fig. 105. Extraordinary wave power measured as a function of ω_B/ω (by G. Landauer).

layers merge, although the profile and electron density is such that the Budden tunneling is negligible for most of the ω_B/ω range. A particularly striking example of such an emission peak at kL = 14.5 was recently provided by G. Landauer[7] and is shown in Fig. 105. For small kL the evanescent region separating the cutoff and hybrid resonance layers is thin and this permits considerable tunneling of the radiation over nearly the entire ω_B/ω range as indicated in Fig. 103(b). Equation 1 also predicts that the emission will vanish for $\omega_B/\omega = 0$ and 1 as the same figure indicates.

Computations have also been made for high-β and for low-β plasmas immersed in non-uniform magnetic fields for which direct access to the upper hybrid resonance is possible.[8]

References

1. J. L. Hirshfield and S. C. Brown, Phys. Rev. 122, 719 (1961).
2. S. J. Buchsbaum, Physics Today 15, No. 12, 32 (1962).
3. A. F. Kuckes and A. Y. Wong, Phys. Fluids 8, 1161 (1965).
4. H. Dreicer, LA-DC-9540; see also Proc. NATO Advanced Study Inst. on Plasma Waves in Space and in the Lab., Røros, Norway, April 17-26, 1968.
5. G. Landauer, J. Nucl. Energy Pt. C 4, 395 (1962).
6. G. Bekefi, et al., Phys. Rev. Letters 9, 6 (1962). The writer is indebted to G. Bekefi for providing additional information about the experiment described in this reference.
7. Unpublished data supplied by G. Landauer in May 1968.
8. T. H. Stix, "The Theory of Plasma Waves," McGraw-Hill Book Co., New York, 1962.

MAGNET CURRENT REGULATION WITH SERIES TRANSISTORS

(J. McLeod)

A transistor regulator designed by the LASL Engineering Dept. and shown in Fig. 106, has been installed in series with the output of the 50-kW motor-generator magnet power supply and is now in service. The major feedback signal flow paths are shown in Fig. 107. The insertion of a fast electronic regulator into the high-current (2500 A) output circuit avoids the forcing problems inherent in the usual scheme of controlling a generator by means of its field winding. Field control is used to maintain the time average of the potential drop across the transistor regulator at its optimum value. Slow response is acceptable in this service and little field forcing is done.

The fastest and most active feedback loop senses the potential across the magnet and operates the transistors. Signal flow in the loop is not delayed by any of the various large inductances in other parts of the system and it can therefore respond to a transient very quickly. This fast loop maintains the magnet potential at that value which is required to provide zero current error as determined by comparing the shunt potential with the current set point. This is obtained by integrating the amplified current error. The current feedback loop thus contains a much faster potential feedback loop as a nested element. The current feedback need not be very fast since its principal purpose is to correct for changes in the magnet temperature; this is just as well since the signal flow is slowed by the magnet time constant. Stability tests indicate that the control loop holds the magnet current within a range of 0.01% of its value for 10 min. Longer term stability tests have not yet been conducted, but these would be relevant to the stability of the reference source and error amplifier and not to loop design.

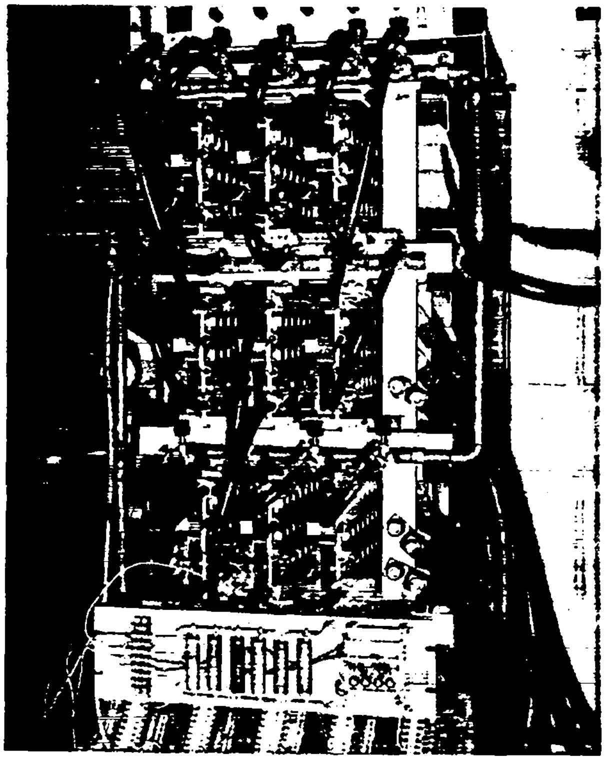

Fig. 106. Transistor regulator bank.

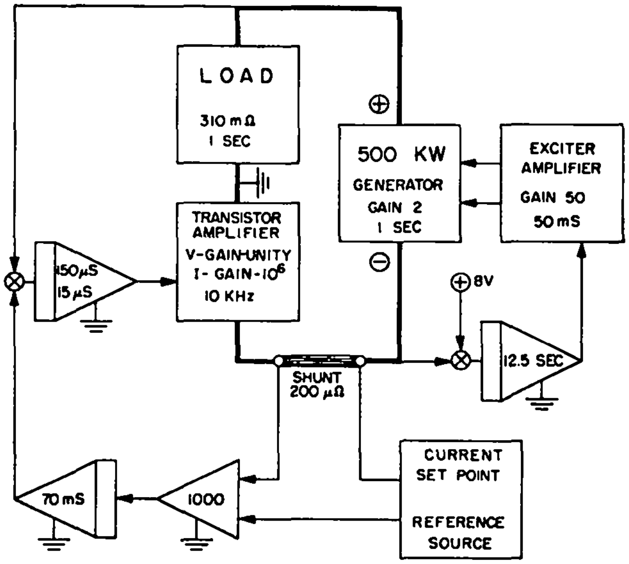

Fig. 107. Feedback schematic.

A similar regulator using roughly seven times as many transistors has also been constructed. Installation of this unit in series with the 2.5-MW rectifier magnet power supply has just been completed. A similar control loop is envisaged for this unit with the substitution of an induction voltage regulator on the incoming line for the field control available on the generator. A series pass element is the only feasible scheme

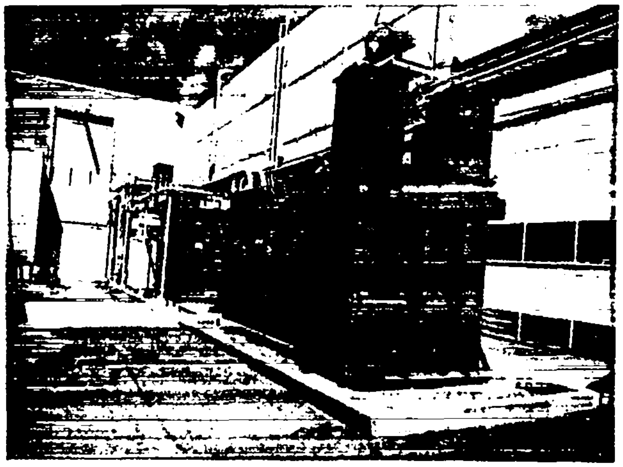

Fig. 108. Newly installed switch gear.

for regulating a big rectifier to 0.01%. Although other schemes might have been used successfully on the generator, it has been handled in the same way in order to gain experience for use on the larger regulator. It has proved possible to put the smaller regulator into service at a much earlier date and extensive tests of the static and high-frequency response of the transistors under actual operating conditions have been conducted using it.

Figure 108 shows the switch gear which has been installed in one of several steps taken to split the 2.5-MW supply into two 1.25-MW supplies.

SUMMARY OF THEORETICAL WORK

(W. B. Riesenfeld)

The chief emphasis in the past year's activities of the Sherwood theoretical group has been placed on two areas of investigation: (a) the numerical simulation of plasma through computer solution of the Vlasov equations for systems of sufficiently high symmetry, and (b) the study of high-β equilibrium and stability. The first of these efforts has developed to such an extent that it has been formalized by the appointment of R. L. Morse as Alternate Group Leader for the numerical simulation program. The high point of the year's activities was the Topical Conference on Numerical Simulation of Plasma, sponsored by the APS and organized by the LASL numerical simulation group. The Conference met at Los Alamos in Sep. 1968. Some of the contributions to the conference are summarized below.

The second effort, on high-β plasma analysis, has seen progress in the calculation of equilibrium and stability in linear and toroidal systems, using various models from thin-skin magnetohydrodynamics to self-consistent rigid rotor solutions of the Vlasov equations. In particular, the lateral displacement instability of a toroidal θ-pinch column of "bumpy" equilibrium has been analyzed in the magnetohydrodynamic approximation, growth rates have been calculated by a simple and elegant mathematical technique, and methods for dynamic stabilization have been proposed. Similar work has proceeded in checking the non-bumpy, rotational transform equilibrium recently suggested by the NYU group; this system is essentially a high-β extension of Stellarator equilibria treated at Princeton. This work is closely tied to the LASL Scyllac program. A brief listing of these and other activities of the mathematical physics group follows in the subsequent paragraphs.

1. The previously derived analytic equilibrium of a toroidal, corrugated MHD θ-pinch plasma of arbitrary β has been generalized to incorporate helical field lines of long pitch. The formalism has been adapted to analyze dynamic stabilization of the $m = 1$ mode, using interaction of Kruskal-Shafranov and Haas-Wesson perturba-

tions. This work has been published. An analysis of the toroidal equilibrium using rotationally transformed multipole fields has been made; recent NYU results have been derived by a different formalism employing special helical coordinates. In the high-β limit this equilibrium appears to be as m = 1 unstable as the "bumpy" equilibrium, but has a number of advantages over the latter.

2. The kinetic-bounce model has been used to study the stability of a rotating θ-pinch relative to m = 1 perturbations, with rigid rotor solutions of the Vlasov equations describing the equilibrium. In addition, the stability of a shear-free, finite-β plasma slab subject to artificial gravity (simulating curvature effects) has been studied, taking into account finite gyration radius effects through the Vlasov equations. The perturbations were described by finite resistivity fluid equations. These investigations are part of a continuing program of study of the equilibrium and stability of θ-pinches on models more realistic than MHD. Interest in the theory of z-pinches also has continued. Bounce model growth rates for the m = 0 and m = 1 modes of a unity-β, thin-skin z-pinch have been calculated and compared with the corresponding MHD results. Finally, the MHD stability properties of continuous flow pinches (see p. 23 et seq.) have been considered in a preliminary way.

The injected quadrupole design calculations have been completed, and the behavior of plasma in such a device has been analyzed by solving the two-dimensional anisotropic diffusion equation (classical and Bohm), the two-dimensional plasma flow and polarization equations, and the MHD equilibrium for high-β plasma. An analysis of MHD stability relative to interchange modes for this system is in progress.

3. The penetration of magnetic fields into nonlinear, hollow annular ferromagnetic conductors has been calculated to check the feasibility of using steel bolts in the Scyllac transmission line.

4. A method using Hamilton's variational principle has been devised to study nonlinear solutions of the Vlasov equations, particularly for streaming instabilities. This is a Lagrangian formulation which has also led to progress in application to linearized problems.

5. A calculation has been made of the fuel heating by reaction α particles as burnup proceeds to the 10% level in a fusion reactor. This work has important relevance to reactor feasibility studies.

6. Approximate analytic solutions have been found for the eigenfunctions and eigenvalues of the Fokker-Planck operator describing the one-dimensional electron velocity distribution function for bounded quiescent plasmas. The eigenvalues are in excellent agreement with the numerical values computed in connection with the alkali Q-machine work (see p. 86 et seq.).

7. An interesting application to an astrophysical problem has been made by modifying and adapting a previous Fokker-Planck code to treat the evaporation of stars from star clusters; an existing linear analysis is thereby extended into the nonlinear region of cluster contraction and heating.

NUMERICAL SOLUTIONS OF THE FOKKER-PLANCK EQUATION

(T. A. Oliphant)

For more than a year, numerical techniques have been applied to the solution of the Fokker-Planck equation for application to CTR and related problems. The basic mathematical procedure used is the spherical harmonic decomposition. Although the general formalism has been written down, the calculations so far have involved only a very few spherical harmonic terms. In fact the only really practical results have been obtained in cases of spherical symmetry in velocity space so that there is only one component for each plasma species.

The first application to CTR problems was a numerical calculation of the fuel heating by α particles as burnup proceeds in a fusion reactor. The fuel was assumed to be an equal mixture of deuterium and tritium. The relaxation and interaction of the ion, electron, and α-particle distribution functions were treated by solving the Fokker-Planck equation numerically for the α particles, and making a reasonable analytic parameterization for the remaining distribution functions. The resulting time dependences, which have been carried out to 10% burnup, are physically reasonable and satisfy the constraint of total energy conservation to 0.5% including bremsstrahlung losses.

The foregoing CTR code has also been adapted to the spherically symmetric star cluster contraction problem. This work extends the linear treatment of the problem (S. Chandrasekhar, 1943) to include the nonlinear effects introduced by the cluster contraction and the heating associated with it. The most noteworthy difference between the result obtained and that of Chandrasekhar is the prediction of a finite lifetime for star clusters. The initial decay rate for the total number of stars N(t) is slightly faster than Chandrasekhar's and it gets faster with time as nonlinear effects are felt more strongly. The function N(t) vanishes at 34.0 initial collision times.

LAGRANGIAN FORMULATION OF VLASOV SYSTEMS

(H. R. Lewis)

Numerical

(With J. Melendez)

Work is proceeding on the application of the Lagrangian formulation for Vlasov plasmas to the numerical solution of nonlinear problems.[1,2] The problem being considered first is that of the cold two-stream instability, and a preliminary report on that problem was presented at the APS Topical Conf. on Numerical Simulation of Plasma.[3] A method for calculating a class of difficult definite integrals that arise was devised in collaboration with J. Thomas (Visiting Staff Member).[4] It has been partially incorporated in the computer code with a resulting increase in speed. A further increase in speed is expected when the method is fully incorporated in the code. On the basis of some results obtained for the linearized equations, an effort is being made to find a set of variables for the nonlinear equations that do not exhibit time variations as rapid as those of the original variables.

Linearized Equations

An explicit set of variables has been found for the linearized Lagrangian formulation with an arbitrary one-dimensional velocity distribution that satisfy a system of second-order differential equations in time with constant coefficients and a time-dependent driving term. The existence of such variables was known before, but their explicit connection with the usual formulation is new. A particular solution has been found. Solution of the homogeneous equations would provide the solutions of the dispersion relation, and the possibility of using this as the basis of a practical numerical method of solving the dispersion relation is being investigated. The analysis can be extended to arbitrary physical situations in the Vlasov limit, and there appears to be the possibility of deriving a dispersion relation for nonuniform plasmas.

References

1. H. R. Lewis, Addendum to LASL report LA-3831-MS (Status Report of the LASL CTR Program for 12-month period ending Oct. 31, 1967), p. 1.
2. H. R. Lewis LASL Report LA-3803 (March 1968).
3. H. R. Lewis and K. J. Melendez, Proc APS Topical Conf. on Simulation of Plasma, Sept. 1968. LA-3990, Paper B-1.
4. J. D. Thomas and H. R. Lewis, LASL Preprint LA-DC 9864.

UTILITY COMPUTER CODES

(H. R. Lewis)

Los Alamos Scientific Laboratory reports describing three utility computer codes have been prepared. The titles and abstracts of the reports are given below.

LA-3877 - "Subroutines for Computing and Graphing Level Lines of Functions of two Variables."

FORTRAN subroutines for computing and graphing level lines of an arbitrary function of two variables are described. Instructions for using the subroutines are presented with an example and listings of the computer programs.

LA-3903 - "General Purpose Computer Code for Particle Trajectories and Other Problems."

Instructions for using a computer code for computing and graphing the solutions of a general system of not more than six first-order differential equations are presented with an example. The user is allowed very flexible control of the type and format of graphical output by means of data cards. A listing of the code is given in FORTRAN for the CDC 6600.

LA-3983 - "Use of Collineations for Interpolation on an Irregular Mesh."

A method is described for using collineations for interpolation on an irregular mesh whose elementary cells are quadrilaterals and whose mesh points are ordered in a way topologically equivalent to the ordering of the points of a rectangular mesh. First the irregular mesh is transformed to a rectangular mesh, and then interpolation is performed on the rectangular mesh. Listings of two computer programs that implement the method are given with examples. One of the programs uses bicubic spline interpolation on the rectangular mesh, and the other uses bilinear interpolation.

QUANTUM THEORY OF A CHARGED PARTICLE IN A TIME-VARYING ELECTROMAGNETIC FIELD

(H.R. Lewis and W.B. Riesenfeld)

The recently developed theory of explicitly time-dependent invariants and its application to the time-dependent harmonic oscillator[1-3] have been used to solve the problem of a charged particle moving quantum mechanically in a particular type of time-dependent electromagnetic field. The electromagnetic field is the axially symmetric classical field consisting of an arbitrarily time-dependent, uniform magnetic field, the associated induced electric field, and the electric field due to an arbitrarily time-dependent, uniform charge distribution. The dynamical variables of this system are simply related to those of the time-dependent harmonic oscillator by a noncanonical transformation. This noncanonical transformation is used to derive a class of invariants for the particle system from the invariants for the oscillator. These invariants for the particle system are not Hermitian. However, it turns out to be possible to derive from them a class of Hermitian invariants that are formally identical to the Hamiltonian for a particle in a uniform, time-independent magnetic field.

By using operator techniques, the eigenstates and eigenvalues of this class of Hermitian invariants are derived, and the phases for which the eigenstates are solutions of the Schrödinger equation are found. The results are a generalization of the well-known solution for a particle in a uniform, time-independent magnetic field. An article describing the theory of explicitly time-dependent invariants and its applications to time-dependent harmonic oscillators and to charged particles has been submitted for publication.[4]

References

1. H.R. Lewis, Jr., Phys. Rev. Letters 18, 510 (1967); 18, 636 (E) (1967).
2. H. R. Lewis, Jr., J. Math. Phys. (To be published).
3. H. R. Lewis, Jr., Phys. Rev. 172, 1313 (1968).
4. H. R. Lewis, Jr., and W. B. Riesenfeld, LASL Preprint LA-DC-9628.

QUADRUPOLE CALCULATIONS

(D. A. Baker, M.D.J. MacRoberts and L. W. Mann)

High-β Equilibria

Introduction

A study of quadrupole equilibria with finite pressure has been undertaken. In addition to being interesting in their own right, the finite pressure calculations will be useful in interpreting magnetic probe data which are obtained from the LASL quadrupole injection experiment.

Theory

The equations describing the equilibrium are the following:

$$\nabla \times \vec{B} = \mu_0 \vec{J} \qquad (1)$$

$$\nabla \cdot \vec{B} = 0 \qquad (2)$$

$$\vec{J} \times \vec{B} = \nabla p. \qquad (3)$$

Since the case of a pulsed, azimuthally symmetric, toroidal quadrupole is of interest, the approximation of perfectly conducting boundaries is used; the magnetic field is then subject to the condition that its normal component vanishes at the boundaries. To exploit the symmetry. cylindrical coordinates r, θ, z are introduced for which exist the following dependences for the magnetic field, current, and pressure: $\vec{B} = \hat{r}B_r(r,z) + \hat{z}B_z(r,z)$, $\vec{J} = \theta\vec{J}(r,z)$, and $p = p(r,z)$. An azimuthal field component B_θ is excluded. Equation 2 is asatisfied by introducing a stream function ψ such that

$$B_r = -\frac{1}{r}\frac{\partial\psi}{\partial z} \qquad (4)$$

$$B_z = \frac{1}{r}\frac{\partial\psi}{\partial r} \; . \qquad (5)$$

From these relations it follows that $\vec{B}\cdot\nabla\psi = 0$ so that the equation ψ = constant yields a flux surface. The boundary condition on $\vec{B}$ then reduces to the condition that ψ is constant along each boundary. From Eq. 3 it follows that $\vec{B}\cdot\nabla p = 0$ so that the pressure is constant along the flux surfaces and

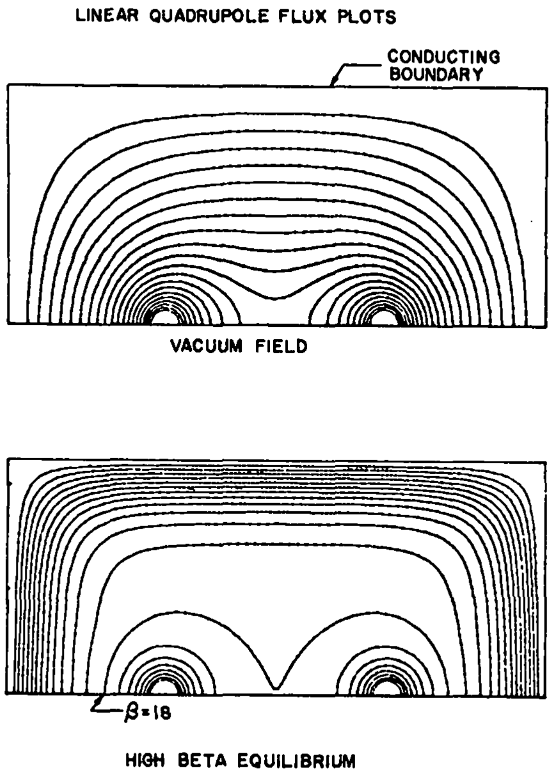

Fig. 109. Linear quadrupole flux plots. Upper: Vacuum field; Lower: High-beta equilibrium.

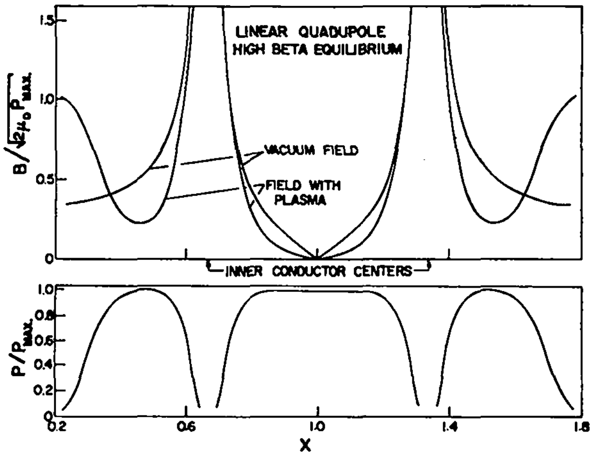

Fig. 110. Spatial distributions of field and plasma pressure for the linear quadrupole of Fig. 109.

therefore can be written as a function of ψ, $p = p(\psi)$. Upon expanding the cross product in Eq. 3 and substituting from Eqs. 4 and 5 the result is

$$\vec{J} \times \vec{B} = J_\theta(\hat{r}B_z - \hat{z}B_r) = \frac{J_\theta}{r} \nabla\psi = \nabla p = \frac{\partial p}{\partial \psi} \nabla\psi$$

from which it is seen that

$$J_\theta = r \frac{\partial p}{\partial \psi} . \qquad (6)$$

By substituting in this equation for J_θ from Eq. 1 and again using Eqs. 4 and 5, the differential equation for ψ is obtained,

$$r \frac{\partial}{\partial r} \left(\frac{1}{r} \frac{\partial \psi}{\partial r} \right) + \frac{\partial^2 \psi}{\partial z^2} + \mu_0 r^2 \frac{\partial p}{\partial \psi} = 0 . \qquad (7)$$

Once the pressure function, the conducting boundaries, and the values of ψ on these boundaries are assigned, the result is a well-posed boundary value problem. A difference equation corresponding to Eq. 7 is solved numerically using familiar techniques of successive over-relaxation.

Sample Equilibria

A sample flux plot of a high-β equilibrium for the case of a linear quadrupole having a rectangular outer boundary and small filamentary inner conductors is shown together with the corresponding vacuum case ($p = 0$) in Fig. 109. The pressure is a gaussian profile in ψ peaked on the separatrix and the field lines shown correspond to equal increments in flux. The expulsion of flux by the diamagnetic plasma is clearly evident. The β values given on the separatrix in the bridge region are the ratio of the plasma pressure to the local field pressure. The spatial distributions of field and pressure are shown in Fig. 110; a plot of the vacuum field is given for comparison. Similar plots for a toroidal quadrupole are shown in Figs. 111 and 112. A sequence of flux plots for increasing pressure values are shown in Fig. 111. The hashed lines correspond to one standard deviation of the gaussian pressure profile used. The profiles in Fig, 112 correspond to the lower left flux plot in Fig. 111. The displacement of the equilibrium configuration toward large radii is characteristic of toroidal geometries and is due to the $1/r$ drop off of the vacuum field.

MHD Stability

Preliminary investigations have been made into the magnitude of the plasma pressure that can

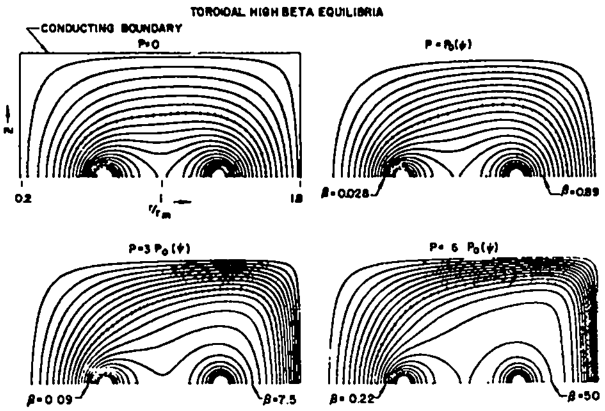

Fig. 111. Flux plots for a toroidal quadrupole for vacuum and three plasma pressures.

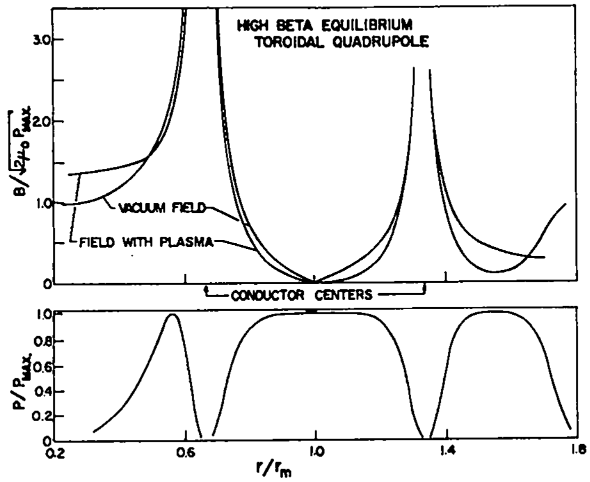

Fig. 112. Spatial distributions of field and plasma pressure corresponding to lower left of Fig. 111.

be introduced into the LASL quadrupole without causing the system to become MHD unstable to interchange flute modes. Calculations were made for the LASL geometry with the plasma pressure $p(\psi)$ a gaussian peaked on the separatrix. Inside ψ_{crit} (i.e., where $d/d\psi \int d\ell/B = 0$) it was found that the system was stable against interchange up to maximum pressures of $\sim 10^8$ newtons/m^2 when the vacuum field is just large enough to produce a maximum of 40 kG at the conducting rings. The 40 kG was the maximum field allowed in the design for strength of materials reasons. At the design plasma temperature of 2.5 keV this corresponds to a peak filling density of $4 \times 10^{13}/\text{cm}^3$. These results are subject to errors due to the finite mesh size particularly in the outer bridge region. Preparations are now being made to solve the eigenvalue equation required to determine complete MHD stability including, in particular, the troublesome ballooning modes.

Diffusion Calculations

To augment the equilibria calculations for a quadrupole, a computer program has been devised which solves the anisotropic two-dimensional diffusion equation

$$\nabla \cdot (\overset{\leftrightarrow}{D} \cdot \nabla n) = \partial n/\partial t$$

for the quadrupole fields. The diffusion tensor $\overset{\leftrightarrow}{D}$ may be any function of space and magnetic field provided the tensor becomes diagonal

$$\overset{\leftrightarrow}{D} = \begin{pmatrix} D_{\parallel} & 0 \\ 0 & D_{\perp} \end{pmatrix}$$

in a local orthogonal coordinate system with one axis aligned in the field direction. The calculations allow the determination of plasma profiles, wall fluxes, confinement times, etc., for a specified quadrupole geometry. The distribution of particle flux to the walls has been computed for classical and Bohm diffusion. The differences in these distributions are appreciable and may be useful in determining the type of diffusion occurring in experiments. The capability of using a finite $D_{\parallel}$ (for $D_{\parallel} = \infty$ the problem becomes one-dimensional) allows calculations for cold plasma and studies of the effect of a possible anomalous parallel diffusion for hot plasma.

Injection Calculations

One-dimensional analytic and computer calculations have been made of the time dependent polarization properties of a plasma stream in a transverse magnetic field[1]. For cases where the plasma-induced ΔB is negligible, it is found that the motion of the plasma is characterized by the values of the ion and electron dielectric constants, $K_{\pm} = 1 + nm/\epsilon_0 B^2$, as compared with unity. For the case $K_{\pm} \gg 1$, which applies to the LASL high-density injection experiments, the electrons oscillate at the upper hybrid frequency about a mean deflection which first sets up the average polarization E-field allowing a continuation of the plasma drift. Later, on a time scale of very nearly the lower hybrid frequency, the ions deflect and oscillate. The guiding centers of the electrons follow this ion motion and a constant average polarization E-field is maintained. The effects that appear when the plasma appreciably perturbs the magnetic field are presently being studied with a one-dimensional computer code. The analytic and numerical results are to be reported in a forthcoming paper.

A two-dimensional code for studying plasma injection is being developed. It is first planned to study the electron component of the motion at the early phase as moving plasma encounters a transverse field. It is believed that the electrons play an important role in the experimentally observed rapid field-plasma mixing.

Reference

1. D. A. Baker and L. W. Mann, Bull. Amer. Phys. Soc., Ser. 2, 13, No. 2 (1968)(Abstract.)

SUMMARY OF PLASMA SIMULATION ACTIVITIES

(R. L. Morse)

Introduction

Encouraging results have been obtained in four Sherwood problem areas by numerical simulation of plasma. These areas are: coaxial devices including the focus, guns, and continuous flow z-pinches; development of tearing, rotational, and mirror instabilities in θ-pinch and Astron-like plasmas; one - and two-dimensional (1- and 2-d) studies of electrostatic two-beam phenomena; and 2-d studies of collisionless shocks. These four projects have shared many numerical and computational techniques, but they will be discussed separately because of their great physical differences.

Coaxial Devices

All work in this area has been done under the assumption that the plasma as well as the apparatus is cylindrically symmetric, i.e., dependent only on the cylindrical coordinates r and z, and that the plasma can be treated as a classical fluid. The justification for these assumptions is a combination of theoretical foresight and experimental hindsight. The same basic 2-d, particle-in-cell (P.I.C.) type fluid code, which was written by D. Butler, was used to simulate both the focus and guns, which seem closely related to continuous flow z-pinches.

A time sequence of side-on photographs of a focus type plasma and a corresponding sequence of r,z particle plots from a simulation of that experiment was given in Fig. 30. Here a uniform filling of cold gas is driven away from a cylindrical electrode by a piston of B_θ magnetic field. This piston first appears at the rear of the electrode where an applied potential causes a discharge to the adjacent wall. As the discharge continues the magnetic piston ionizes and shock heats the filling gas and pushes it out and away from the electrode and along the electrode toward the blunt end. The curved shocked layer can be clearly seen in the photographs and the simulation plots.

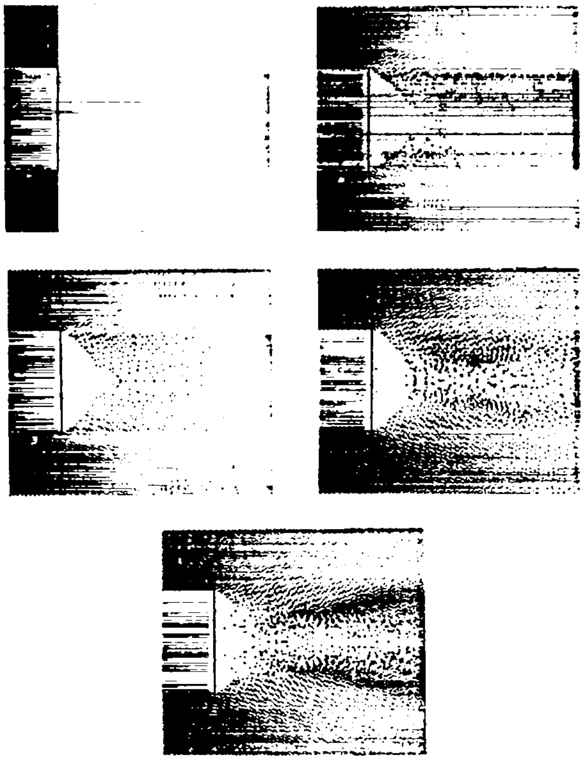

Fig. 113. Time sequence (upper left to bottom) of MHD simulation plots of plasma from a coaxial gun.

In the computations, B_θ and plasma do not mix; the vacuum form, $B_\theta \propto 1/r$, is used to obtain magnetic pressure at the otherwise free boundary behind the shock. After the shock passes the end of the electrode it collapses onto the axis of the system where it forms a small hot z-pinch called a plasma focus and a second shock which resembles a bubble. No effort was made to extend the computations to study details of the focus itself because it is felt that a microscopic plasma model is required. The implicit ideal MHD assumption in the computations limits them from showing some resistive blurring of the free boundary, but otherwise the simulation and experimental results are in good quantitative agreement. Apparently the computational technique would now be adequate to predict the effect of some changes in the experimental configuration.

More recent and less complete simulation work on plasma guns has shown qualitative agreement with gun experiments (see p. 23). Here, in contrast with the focus problem, the initial conditions are much less certain and more variable. Cold gas is puffed into an evacuated region between two coaxial electrodes and then ionized by an electrical discharge in such a way that the magnetic field of the discharge is frozen into the gas. For lack of a simulation of this complicated process, the simulation has been started arbitrarily with a vacuum magnetic field, $B_\theta \propto 1/r$, and a constant ratio of mass to flux throughout the region between the electrodes. This uniform gun filling is ended abruptly at the muzzle of the gun where an expansion into the outside vacuum starts at zero time. Figure 113 shows a time sequence of simulation particle plots starting with this expansion and developing a quasisteady flow pattern as more plasma flows through from back inside the gun (not shown).

An important feature of this quasisteady flow pattern is a standing shock which has been overlooked in the analytic work of A. I. Morozov on continuous flow z-pinches. The shock, which can be seen to surround the axis like a tube starting just beyond the tip of the electrode in Fig. 113, has been called a wake shock because of its strong resemblance to the standing shock in the wake of a blunt-ended body in hypersonic motion. Here cold magnetized plasma flows past the end of the electrode, expands toward the axis, is slowed (or refracted) in its radial motion and heated by the shock, and then flows along the axis through the region inside the shock. Figure 114 indicates a profile of the shock on top of which have been superimposed two radial profiles of specific internal plasma energy, I. It is this wake shock which has been seen experimentally and provides the major source of qualitative agreement with the simulations. An effort is now being made to increase the generality of these computations, in particular the input conditions, in order to make the simulations a useful machine design tool.

Tearing, Rotational, and Mirror Modes in θ-Pinch and Astron Plasmas

Work is being continued on the simulation of collisionless, confined plasma systems of the θ-pinch or Astron type in which one energetic particle species dominates the physics (hot ions

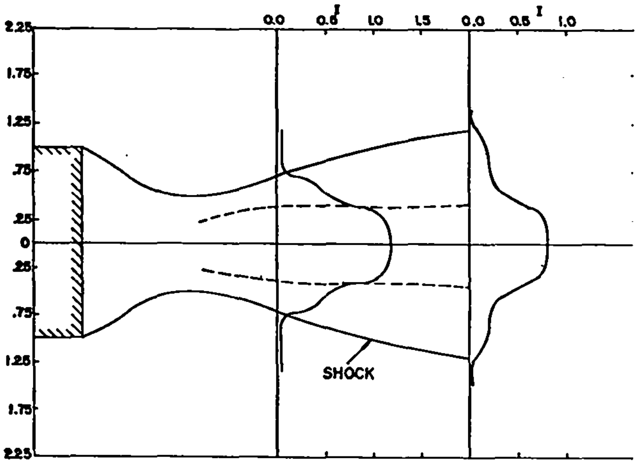

Fig. 114. Wake shock with temperature profiles for continuous flow from a plasma gun (corresponding to last frame in Fig. 113).

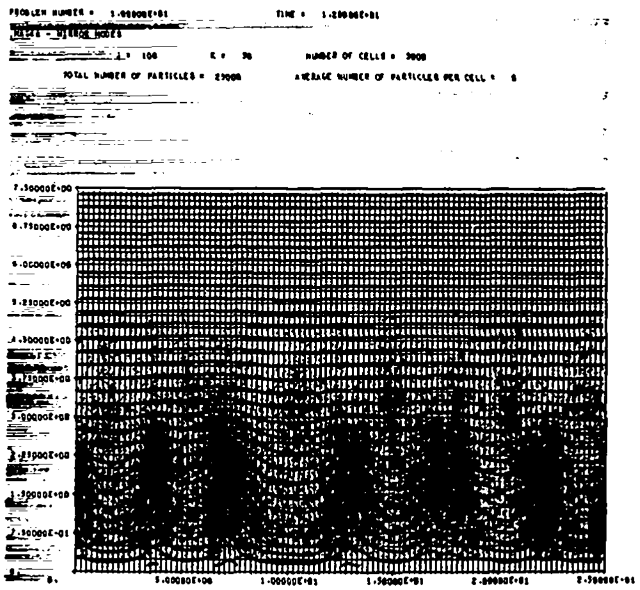

Fig. 115. Simulation plot showing fully developed mirror instability in a θ-pinch plasma. (Center axis is at bottom; heavy lines are magnetic field lines and lighter lines show the computational cells.

in a θ-pinch, injected electrons in Astron), the desired equilibrium is axisymmetric, and the magnetic field is predominantly B_r and B_z. The unstably growing modes of plasma deformation studied here are all of the m = 0 or axisymmetric type which can therefore be simulated in the two variables of the equilibria, r and z. However, all three particle velocities, v_r, v_θ, and v_z, must be handled explicitly and therein lies a difficulty. This phase space is five-dimensional; to treat this system in time by imposing a regular grid of sufficient resolution, Eulerian or Lagrangian, on the phase space would be much too large a task for any computer in existence or under development. Although the P.I.C. method was a convenience in the fluid computations described above, in these multidimensional collisionless problems the statistical advantages of P.I.C. are a necessity.

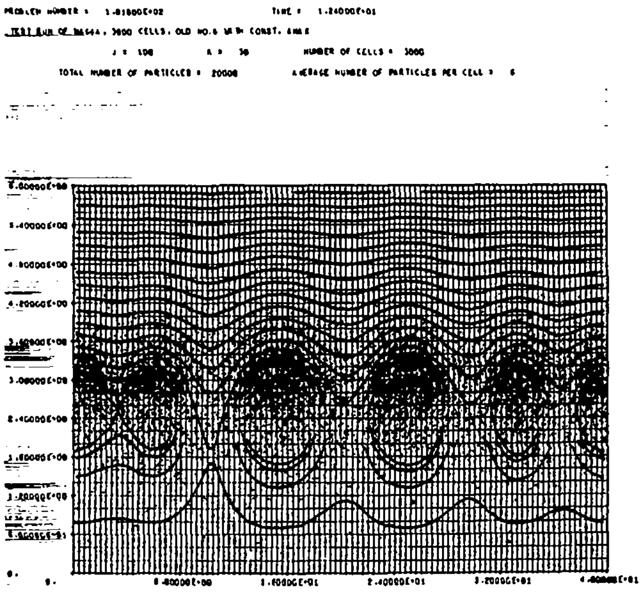

Fig. 116. Simulation plot showing fully developed tearing mode in an Astron-like plasma before coalescence.

Figure 115 shows an r,z plot of simulation particles (center axis at bottom) with magnetic lines superimposed, from a simulation of mirror instability in a θ-pinch plasma. Compression of the plasma has caused the perpendicular (r and θ) temperature to be much greater than the parallel (z) temperature and this in turn makes the plasma unstable to the growth of the lumpy, z-dependent structure seen in Fig. 115. The simulations show that these lumps partly remove the temperature imbalance, which seems to resolve an old question about end loss rates, and then by successive coalescence develop into longer wavelength lumps with surprisingly long life times. Since these lumps are not predicted by MHD theories, it is gratifying to report that something very similar has recently been seen by J.A. Phillips and H. J. Karr on the Columba machine at LASL.

Figure 116 is an r,z plot from a simulation of a plasma which started in equilibrium with a reversed magnetic field but no temperature imbalance. All broken field lines in the figure really connect in pairs (top and bottom) in the nearest adjacent column of cells. In the initial z-independent equilibrium, the magnitude of the reversed inside magnetic field was one-third that of the field at the outer wall. The tearing mode predicted by linear theory is seen in Fig. 116 at about full development. Subsequent coalescing of lumps proceeds as described above until here only one long lump of plasma remains. This result, together with a consistent modification of the distribution of particle velocities, appears to support the E-layer concept. In other runs, an open end and a mirror field have been included and have shown the development of a stationary, z-dependent equilibrium with reversed magnetic field. This result would seem to suit the needs of the Astron, for which a method for finding just such self-consistent equilibria has been sought.

Two-Beam Electrostatic Phenomena

(With C. Nielson)

In this oldest of collisionless plasma physics problems the distribution of electron velocities has two maxima which are sufficiently distinct to cause unstable growth of longitudinal electrostatic plasma oscillations. The frequency of these oscillations is so high that the heavy positive ions may be regarded as a fixed background of positive charge. The double maximum distributions considered range from the strongly unstable case of two distinct, equal beams to the gentle bump-on-tail case made famous by quasilinear theory. The direct physical applicability of the one-dimensional subset of such problems is limited to a few low-β machines, like that of J. Malmberg at Gulf General Atomic, which are contrived to contain two-beam electron distributions and look 1-d with respect to the resulting unstable oscillations. However, the nonlinear aspects of these 1-d problems have been studied extensively by plasma turbulence theorists because their basic simplicity allows more complete analysis and because an understanding of these simple problems seems a logical first step to understanding more complex systems.

At this time it appears that the solutions to these 1-d problems are available by simulation for all but very long times and some extreme limiting cases. The dominant feature of a wide range of cases is a single-mode structure which appears and saturates at about the wavelength where linear theory predicts a maximum growth rate. This is qualitatively similar to the early mirror and tearing mode behavior discussed above. As in those computations, the case of two equal beams shows successive coalescence toward longer-wavelength, single-mode structure whereas the bump-on-tail cases are unable to coalesce, for readily explicable reasons. In all cases the mode amplitude decays rapidly after saturation through a process of mixing in phase space which is related in an essential way to the existence of the single mode structure.

This picture is clearly not in agreement with quasilinear theory. Although it is too early to say whether or not such theory applies in the very gentle bump limit for which it was derived, it can now be said that it does not give the right answers for many of the more unstable cases to which it has been applied.

Again a P.I.C. simulation method has been used. In 1-d problems rather good statistics are possible; as many as 10^3 simulation particles per Debye length have been used. Figure 117 shows a set of diagnostics from a bump-on-tail case at 0, 4, and 40 plasma periods (T) after initial time. In each line the diagnostics left to right are (1) a phase space plot (v_x vs x) of the simulation particles, (2) the electrostatic field energy in the different numbered Fourier modes (small mode numbers correspond to long wavelengths), (3) the distribution of electron velocities, $f(v_x)$, independent of x, and (4) the electrostatic potential as a function of x. The plots at T = 4.0, which is about the time of saturation, show the clear trapped particle regions in phase space associated with the strong single mode structure of the potential. The T = 40.0 plots show that the electrostatic oscillations have essentially died out, the vortex structure in phase space has disappeared and the bump on the tail of the velocity distribution has damped.

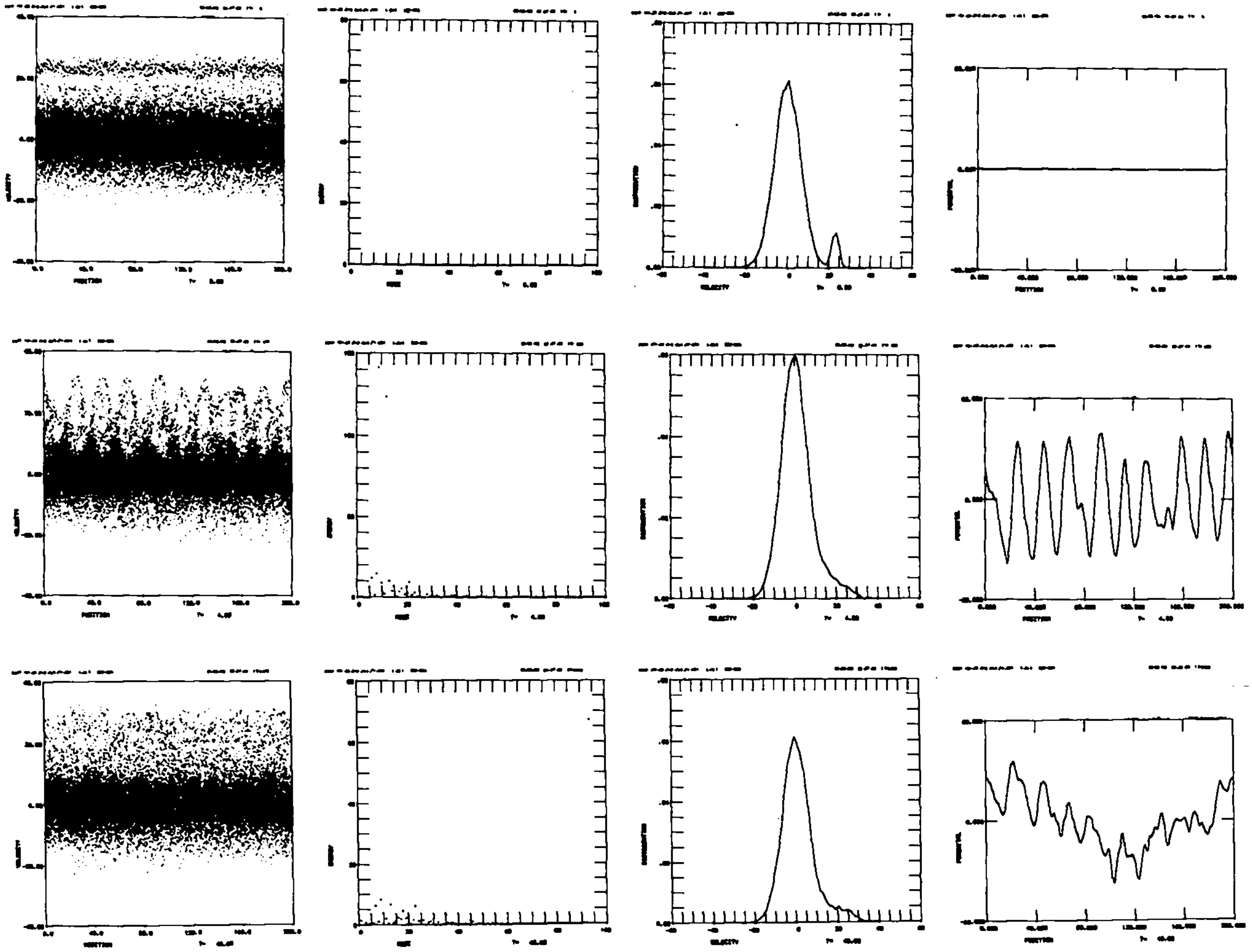

Fig. 117. Diagnostics of one-dimensional electrostatic bump-on-tail problem at T = 0, 4, and 40 plasma periods after initial time.

Two-Dimensional Studies of Collisionless Shocks

(With C. Shonk)

For this work a numerical model has been (and is being) developed with the following properties: all physical quantities depend on the coordinates x and y; the magnetic field has one component, B_z which in general is time dependent; the electric field has two components, E_x and E_y, which together may be both electrostatic and inductive; ions are treated microscopically by P.I.C. methods; electrons are treated as a fluid which is adiabatically tied to magnetic field lines, i.e., it moves according to first-order drifts; and the fields are determined in such a way that charge neutrality is maintained at all times to within truncation error. This last condition does not mean that the electrostatic fields are suppressed; it means, rather, that the Debye length is small. These simulations differ in an essential way from all the others reported above. In some sense all of the others were one-species calculations; this model definitely contains two active species and as a result is much more complicated.

In the language of collisionless shock work, the length scale here is c/ω_{pi} (rather than c/ω_{pe}). When simulated collisionless shocks are driven into a quiescent magnetized plasma by a magnetic piston, the front of the disturbance first forms plane and thin, and then thickens with the formation of a gross lumpy structure which

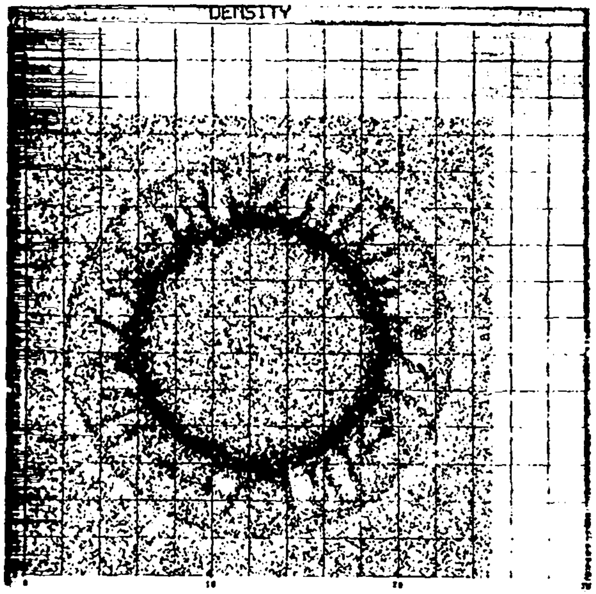

Fig. 118. x,y plot of simulation particles in θ-pinch implosion showing "venetian blind" structure.

resembles a cross section through a set of venetian blinds lying in the plane of the shock front. The continuing development of this technique is now being aided by a linear theory of the mode structure. The wavelength of this structure is about c/ω_{pi} and in a θ-pinch implsion these venetian blinds would resemble radially directed fingers curving slightly in the proper sense for ion trajectories in the B_z field. Figure 118 shows a frame from such a θ-pinch simulation. End-on photographs of θ-pinch implosions obtained by O. Freidricks of the University of Texas and E. Hinz of Jülich tentatively appear to show such structure. However, careful comparisons have not yet been made and the absence of such structure in the high-temperature Scylla IA at LASL raises some questions.

PUBLICATIONS

Allis, W.P., "Exact Nonlinear Waves in a Collisionless Plasma," Bull. Am. Phys. Soc., Ser 2, 13, 201 (1969)(Abstract).

Atkinson, D. W. and Phillips, J. A., "Some Observations on the Flow of a Tenuous Plasma in a Magnetic Field," Culham Laboratory, 1967. CLM-R 72.

Atkinson, D. W. and Phillips, J. A., "Plasmascope Observations of Plasma in a Magnetic Field," Culham Laboratory, 1968. CLM-R 82

Armstrong, T. P. and Freidberg, J. P., "Persistently Recurring Nonlinear Waves Arising from the Two Stream Instability," Proc. APS Topical Conf. on Pulsed High-Density Plasmas, Sept. 1967. LA-3770, Paper A-6.

Baker, D. A. and Mann, L. W., "Transient Polarization Calculations of a Plasma Stream in a Transverse Magnetic Field," Bull. Am. Phys. Soc., Ser 2, 13, 317 (1968)(Abstract).

Baker, D. A. and Mann, L. W., "Formation and Transport of a Saturation Shock in a Ferromagnetic Conductor," ibid., Ser. 2, 13, 875 (1968) (Abstract).

Bernstein, I.D., and Dreicer, H., "Kinetic Theory of Electron Diffusion," ibid., Ser. 2, 13, 806 (1968)(Abstract).

Bekefi, G., Dreicer, H., Fowler, T.K., Guest, G.E., Perkins, W.A., Stix, T.H., and Ware, A.A., "Report of Ad Hoc Panel on Fusion Research on Low-β Plasmas Confined in Open-Ended Magnetic Geometries," USAEC Report TID-24254, March, 1968.

Bottoms, P.J., Mather, J.W., and Williams, A. H., "Neutron Energy Distribution in the Dense Plasma Focus (DPF)," Bull. Am. Phys. Soc., Ser 2, 13, 493 (1968)(Abstract).

Bottoms, P.J., Henson, R. M., and Mather, J.W., "Current Sheath Resistance Measurements and a Dynamical Study of the Dense Plasma Focus," ibid., Ser. 2, 12, 713 (1967)(Abstract).

Bottoms, P. J., Carpenter, J. P., Mather, J.W., Ware, K. D., and Williams, A. H., "On The Mechanism of Neutron Production from the Dense Plasma Focus ," DTIE, 1968. CONF-680805-2 MN.

Brousseau, A.T., "Model-10 Precision Delay Trigger Generator," LA-3964-MS (1968).

Burkhardt, L.C., DiMarco, J.N., Hammel, J.E., Henson, R.M., and Karr, H. J., "Magnetic Shielding of Current Feeds in Plasma Containment Systems," Phys. Fluids, 11, 1562 (1968).

Butler, T. D., Henins, I., Marshall, J., and Morse, R. L., "Coaxial Snowplow Discharge," Proc. APS Topical Conf. on Pulsed High-Density Plasmas, Sept. 1967, LA-3770, Paper C-7. Abstract in Bull. Am. Phys. Soc., Ser 2, 12, 1157 (1967).

Butler, T.D., Cook, J. L., and Morse, R. W., "MHD Simulation of Co-Axial Plasma Flow," Proc. APS Topical Conf. on Numerical Simulation of Plasma, Sept., 1968. LA-3990, Paper C-6.

Butler, T. D., and Morse, R. L., "Numerical Study of a Coaxial Accelerator," Bull. Am. Phys. Soc., Ser. 2, 13, 878 (1968)(Abstract).

Daehler, M., "Twelve-Channel Triple-Etalon Fabry-Perot Spectrometer," Program Opt. Soc. Am., Spring Meeting 1968. p. 29 (Abstract).

Daehler, M., and Ribe, F. L., "Cooperative Light Scattering from θ-Pinch Plasmas," Phys. Rev., 161, 117 (1967).

Daehler, M. and Roesler, F. L., "High Contrast in a Polyetalon Fabry-Perot Spectrometer," Appl. Opt., 7, 1240 (1968).

Dickman, D. O., Morse, R. L., and Nielson, C. W., "Numerical Simulation of Axi-Symmetric Collisionless, Finite β Plasma," Proc. APS Topical Conf. on Numerical Simulation of Plasma, Sept. 1968. LA-3990, Paper C-2.

Dickman, D. O. and Morse, R. L., "Turbulent Dissipation of Pressure Anisotropy in High Beta Plasmas," Bull. Am. Phys. Soc., Ser. 2, 13, 284 (1968)(Abstract).

DiMarco, J. N., Burkhardt, L.C., and Karr, H. J., "Confinement of Energetic Plasma in the Caulked Stuffed Cusp Experiment," ibid., Ser. 2, 13, 277 (1968)(Abstract).

Dreicer, H., "Perturbation Analysis of Cyclotron Resonance in the Electromagnetic Field of a TE_{011} Mode," ibid., Ser. 2, 13, 271 (1968) (Abstract).

Dreicer, H., "Transmission and Emission of Radiation by a Magnetized Laboratory Plasma," DTIE, 1968, LA-DC-9540; to be published in Proc. NATO Advanced Study Institute on Plasma Waves in Space and in the Laboratory.

Dreicer, H., Book Review: "Electrons, Ions, and Waves: Selected Works of William Phelps Allis, " S. C. Brown, Ed. Science, 158, 482 (1967).

Dreicer, H. and Henderson, D. B., "Particle Losses in Quiescent Cesium Plasmas Due to Resonant Charge Exchange and Hot Plate Surface Inhomogeneities," Bull. Am. Phys. Soc., Ser. 2, 13, 880 (1968)(Abstract).

Dreicer, H. and Henderson, D. B., "Particle Losses Due to Charge Exchange in Cesium Plasmas," Phys. Rev. Letters, 20, 374 (1968).

Finlayson, V. A., "Exploding Foil Driven Switch for Short-Circuiting a Theta-Pinch Foil," Bull. Am. Phys. Soc., Ser. 2, 13, 557 (1968)(Abstract).

Forman, P.R., and Kunkel, W.B., "Determination of Neutral-Atom Density in a Highly Ionized Decaying Hydrogen Plasma," Phys. Fluids, 11, 1528 (1968).

Freidberg, J. L., and Morse, R. L., "Z-Dependent Marginal Stability of the Rigid Rotor Model of a High-Theta Pinch," Proc. APS Topical Conf. on Pulsed High-Density Plasmas, Sept. 1967. LA-3770, Paper B-7.

Gribble, R. F., Little, E.M., and Quinn, W. E., "Faraday Rotation Measurements on the Scylla IV Theta Pinch," ibid., paper A-3; abstract published in Bull. Am. Phys. Soc., Ser. 2, 12, 1154 (1967).

Hammel, J.E., and Rode, D. L., "Fractional-Fringe-Shift Laser Interferometer," LA-3730 (1967).

Hammel, J. E. and Kewish, R. W., "Experiment on Plasma Stream Interactions Through Polarization Electric Fields," Bull. Am. Phys. Soc., Ser. 2, 13, 317 (1968)(Abstract).

Henderson, D. B. and Dreicer, H., "Q-Machine End Plate Profiles," ibid., Ser. 2, 13, 288 (1968) (Abstract).

Herold, H. G. and Jahoda, F. C., "Measurement of Plasma Density Outside the Plasma Column in a Theta Pinch by Means of a Carbon Dioxide-Laser Interferometer," ibid., Ser. 2, 13, 877 (1968) (Abstract).

Henins, I. and Marshall, J., "Fast Metallic Contact Solid Dielectric Switch for High Voltage and Current," Rev. Sci. Instr., 39, 1481 (1968).

Henins, I. and Marshall, J., "Use of a Bare Magnetic Plasma Guide Field Coil in Vacuum," Bull. Am. Phys. Soc., Ser. 2, 13, 275 (1968)(Abstract).

Henins, I. and Marshall, J., "Study of Coaxial Snowplow Discharge," ibid., Ser. 2, 13, 878 (1968)(Abstract).

Henins, I., Henry, P.S., Lohr, J.M., and Marshall, J., "Coaxial Gun Development," Proc. APS Topical Conf. on Pulsed High-Density Plasmas, Sept. 1967, LA-3770, Paper E-2; abstract published in Bull. Am. Phys. Soc., Ser. 2, 12, 1159 (1967).

Jahoda, F. C., "Holographic Plasma Diagnostics," LA-3968-MS (1968).

Jahoda, F. C., "Holographic Diagnostics: Interferometry: Moire-Schlieren," Bull. Am. Phys. Soc., Ser 2, 13, 265 (1968)(Abstract).

Johnson, John L., Morse, R.L., and Riesenfeld, W.B., "Hydromagnetic Equilibrium of a Finite Beta Toroidal Plasma Column," Proc. APS Topical Conf. on Pulsed High-Density Plasmas, Sept. 1967. LA-3770, Paper B-2; abstract published in Bull. Am. Phys. Soc., Ser. 2, 12, 1155 (1967).

Johnson, Jerald L, Morse, R. L., and Riesenfeld, W.B., "Hydromagnetic Equilibrium of a Thin-Skin, Finite-Beta Toroidal Plasma Column," LA-3778 (1968).

Karr, H. J., Burkhardt, L.C., and DiMarco, J.N., "Plasma Injection and Trapping in the Caulked-Stuffed Cusp Experiment," Bull. Am. Phys. Soc., Ser. 2, 13, 277 (1968)(Abstract).

Kemp, E. L., "Design of Scyllac, a 15-Meter Theta-Pinch Machine," Fifth Symp. on Fusion Tech., Culham Lab., 1968 No. 59; also in DTIE, 1968.CONF-680710-4 MN.

Kemp, E. L., Quinn, W. E., Ribe, F. L., and Sawyer, G. A., "15-M Scyllac Theta Pinch," Proc. APS Topical Conf. on Pulsed High-Density Plasmas, Sept. 1967. LA-3770, Paper G-1; abstract published in Bull. Am. Phys. Soc., Ser. 2, 12, 1161 (1967).

Lewis, H. R., "The Motion of aTime Dependent Harmonic Oscillator, and of a Charged Particle in a Class of Time-Dependent Axially Symmetric Electromagnetic Fields," Phys. Rev., 172, 1313 (1968).

Lewis, H. R., "Classical and Quantum Systems with Time-Dependent Harmonic-Oscillator-Type Hamiltonians," Phys. Rev. Letters, 18, 636 (1967)(Erratum).

Lewis, H. R., "Solution of the Equations of Motion for a Particle in an Arbitrarily Time-Dependent Uniform, Axially Symmetric Magnetic Field," Bull. Am. Phys. Soc., Ser. 2, 13, 311 (1968) (Abstract).

Lewis, H. R., "Class of Exact Invariants for Classical and Quantum Time-Dependent Harmonic Oscillators," LA-DC-9020 (1967).

Lewis, H. R., "Hamilton's Principle and Numerical Solution of the Vlasov Equations," LA-3803 (1968).

Lewis, H. R., "Subroutines for Computing and Graphing Level Lines of Functions of Two Variables," LA-3877 (1968).

Lewis, H. R., "General Purpose Computer Code for Trajectories and Other Problems," LA-3903 (1968).

Lewis, H. R. and Melendez, K. J., "Numerical Investigation of the Two-Stream Instability via Hamilton's Principle," Proc. APS Topical Conf. on Numerical Simulation of Plasma, Sept. 1968, LA-3990, Paper B-1.

Little, E. M., Newton, A.A., Quinn, W. E. and Ribe, F. L., "Linear Theta-Pinch Experiments Related to the Stability of a Toroidal Theta-Pinch of Large Aspect Ratio," DTIE, 1968. CONF-680805-20 MN.

Little, E. M., Quinn, W. E. and Ribe, F. L., "Observation of Kruskal-Shafranov Modes on a Theta-Pinch Plasma Column," Bull. Am. Phys. Soc., Ser. 2, 13, 877 (1968)(Abstract).

Marshall, J. and Henins, I., "Plasma Production by a Coaxial Gun," ibid., Ser. 2, 13, 878 (1968) (Abstract).

Mather, J. W. and Bottoms, P. J., "Characteristics of the Dense Plasma Focus Discharge," Phys. Fluids, 11, 611 (1968).

Mather, J. W., Bottoms, P. J., and Williams, A. H., "Some Characteristics of the Dense Plasma Focus," Bull. Am. Phys. Soc., Ser. 2, 12, 1156 (1967)(Abstract).

Mather, J. W., "Intense Source of Neutrons from the Dense Plasma Focus," Gmelin, 1967. AED-CONF. 67-182-005.

McLeod, J. J. and Dreicer, H., "Properties of ECH Q-Machines," Bull. Am. Phys. Soc., Ser. 2, 13, 289 (1968)(Abstract).

Mjolsness, R. C. and Petschek, A. G., "Electron Distribution Function in a Plasma with Excitation Collisions," Phys. Fluids, 10, 1511 (1967).

Morse, R. L., "Ballooning of $\beta = 1$ Plasmas with Sharp Boundaries," ibid., 10, 236 (1967).

Morse, R. L., Adiabatic Time Development of Linear Theta-Pinch Plasma Profiles," ibid., 10, 1560 (1967).

Morse, R. L., "Adiabatic End Loss from a θ-Pinch," ibid., 11, 1558 (1968).

Morse, R. L., Compiler, "Proc. of APS Topical Conf. on Numerical Simulation of Plasmas," Sep. 1968, LA-3990.

Morse, R. L., "Sheath Stability," Proc. APS Topical Conf. on Pulsed High-Density Plasmas, Sept. 1967, LA-3770, Paper F-3; abstract published in Bull. Am. Phys. Soc., Ser. 2, 12, 1161 (1967).

Morse, R. L., and C. W. Nielson, "Numerical Simulation of Warm Two-Beam Plasma," Proc. APS Topical Conf. on Numerical Simulation of Plasma, Sept. 1968. LA-3990, Paper A-4.

Morse, R. L., Equilibria of Collisionless Plasma," LA-3844-MS (1968).

Morse, R. L., Riesenfeld, W. B, and Johnson, John L., "Hydromagnetic Equilibrium of a Thin Skin Finite Beta Toroidal Plasma Column," Plasma Phys., 10, 543 (1968).

Newton, A. A. and Marshall, J., "Plasma Convection, Concentration and Heating by Flux Annihilation," Bull. Am. Phys. Soc., Ser. 2, 13, 878 (1968)(Abstract).

Oliphant, T. A., "Computer Simulation of the Theta Pinch," Proc. APS Topical Conf. on Pulsed High-Density Plasmas, Sept. 1967. LA-3770, Paper F-2; abstract published in Bull. Am. Phys. Soc., Ser. 2, 12, 1160 (1967).

Oliphant, T. A., "Calculation of High-Beta Toroidal Plasma Equilibrium," LA-3749 (1967).

Oliphant, T. A., "Numerical Study of a High-Beta Toroidal Plasma Equilibrium, " Bull. Am. Phys. Soc., Ser. 2, 13, 319 (1968)(Abstract).

Oliphant, T. A. and Hoyt, M. S. "Structure of a Magnetically Driven Plane Shock Wave in a Plasma," LA-3674 (1967).

Phillips, J. A., Schofield, A. E., and Tuck, J. L., "Columba - A High Temperature Z-Pinch Experiment," Proc. APS Topical Conf. on Pulsed High-Density Plasmas, Sept. 1967. LA-3770, Paper G-3; abstract published in Bull. Am. Phys. Soc., Ser. 2, 12, 1162 (1967).

Ribe, F. L., Compiler, "Proc. APS Topical Conf. on Pulsed High-Density Plasmas," Sept. 1967, LA-3770.

Ribe, F. L., "High-Beta Plasmas in Theta Pinches and Cusp Experiments, "Nucl. Fission, 7, 81 (1967).

Ribe, F. L. and Riesenfeld, W. B., "Unstable, Transverse-Displacement Mode of a Bumpy Plasma Column and its Possible Stabilization," Phys. Fluids 11, 2065 (1968).

Sawyer, G. A., Finlayson, V. A., Jahoda, F. C., and Thomas, K. S., "Measurement of β, N, and T_i in High- and Low-Pressure Theta-Pinch Operation," ibid., 10, 1564 (1967).

Schofield, A. E. and Holm, R. C., "Overvoltage protection circuit for Condenser Discharge System," U.S. Patent 3,368,135 (1968).

Shonk, C. R., and Morse, R. L., "Two-Dimensional Simulation of Shock Waves in Collisionless Plasmas," Proc. APS Topical Conf. on Numerical Simulation of Plasma, Sept. 1968. LA-3990, Paper C-3.

Shonk, C. R. and Morse, R. L., "Numerical Simulation of the Compression of a High Beta Plasma," Bull. Am. Phys. Soc., Ser. 2, 13, 598 (1968)(Abstract).

Thomas, K. S." Measurement of Theta-Pinch End Loss Using a Gas Laser Interferometer," Proc. APS Topical Conf. on Pulsed High-Density Plasmas, Sept. 1967. LA-3770, Paper D-3; also published in Phys. Fluids, 11, 1125 (1968); abstract published in Bull. Am. Phys. Soc., Ser. 2, 12, 1158 (1967).

Thomson, D. P., Caird, R. S., Ewing, K. J., Finlayson, V. A., Fowler, C. M., Garn, W. B., Kemp, E. L., Kewish, R. W., Sawyer, G. A., and Tuck, J. L., "Characteristics of the Scyllacita Theta-Pinch," LA-3863-MS (1968).

Thomson, D. B., Caird, R. S., Ewing, K, J., Fowler, C. M., Garn, W. B., Crawford, J. C., and Damerow, R. A., "Explosive Generator-Powered Theta-Pinch." Proc. APS Topical Conf. on Pulsed High-Density Plasmas, Sept. 1967. LA-3770, Paper H-3; abstract published in Bull. Am. Phys. Soc., Ser. 2, 12, 1163 (1967).

Tuck, J. L., "Energy Sources of the Future with Emphasis on the Light Elements," DTIE, 1968. CONF-680502-2 MN.

Tuck, J. L., "Monte Carlo and Computer Plasma Simulation Studies of the Inhibition of End Loss from a Theta-Pinch by Nonadiabatic 'Rough' Magnetic Walls," DTIE, 1968. CONF-680805-11 MN.

Tuck, J. L., "Reduction of Plasma Loss from Open-Ended Magnetic Confinement Systems by Magnetically Rough Walls," Phys. Rev. Letters, 20, 715 (1968).

Tuck, J. L., Proc. of APS Topical Conf. on Numerical Simulation of Plasma, Sept. 1968, LA-3990, Opening Remarks.

Baker, D.A. and Freidberg, J.P., "Optimization of the $\int d\ell/B$ Stable Region in a Linear Quadrupole," LA-4017 (1968).

Finlayson, V.A., "Characteristics of the Scylla 1A Theta Pinch with Crowbar," LA-4042 (1968).

Lewis, H.R., "Use of Collineations for Interpolation on an Irregular Mesh," LA-3983 (1968).

Suydam, B. R., "Stationary Axisymmetric Flow of a Hot Plasma," LA-4015-MS (1968).

Suydam, B.R., "Stability of Slowly Tapered Axisymmetric Plasma Flows," LA-4034-MS (1968).